A process-based, idealized study of salt and sediment dynamics in well-mixed estuaries

Wei, Xiaoyan

DOI
10.4233/uuid:ac9cac89-36a8-457d-8c3e-cee73091aa93

Publication date
2017

Document Version
Final published version

Citation (APA)
Wei, X. (2017). *A process-based, idealized study of salt and sediment dynamics in well-mixed estuaries*. [Dissertation (TU Delft), Delft University of Technology]. https://doi.org/10.4233/uuid:ac9cac89-36a8-457d-8c3e-cee73091aa93

A PROCESS-BASED, IDEALIZED STUDY OF SALT AND SEDIMENT DYNAMICS IN WELL-MIXED ESTUARIES

A PROCESS-BASED, IDEALIZED STUDY OF SALT AND SEDIMENT DYNAMICS IN WELL-MIXED ESTUARIES

Proefschrift

ter verkrijging van de graad van doctor
aan de Technische Universiteit Delft,
op gezag van de Rector Magnificus prof. ir. K.C.A.M. Luyben,
voorzitter van het College voor Promoties,
in het openbaar te verdedigen op
donderdag, 1 juni 2017 om 12:30 uur

door

Xiaoyan WEI

Master of Science in Harbour, Coastal and offshore Engineering, Hohai University,
Nanjing, Jiangsu, China,
geboren te Anhua, Hunan, China.

Dit proefschrift is goedgekeurd door de

promotor: prof. dr. ir. A.W. Heemink
copromotor: dr. H.M. Schuttelaars

Samenstelling promotiecommissie:

Rector Magnificus,	voorzitter
Prof. dr. ir. A.W. Heemink	Delft University of Technology, promotor
Dr. H.M. Schuttelaars	Delft University of Technology, copromotor
Onafhankelijke leden:	
Dr. R.W. Geyer	Woods Hole Oceanographic Institution
Prof.dr. H.E. de Swart	Utrecht University
Prof.dr.ir. C.W. Oosterlee	Delft University of Technology
Prof.dr.ir. Z.B. Wang	Delft University of Technology
Prof.dr.ir. H.H.G. Savenije	Delft University of Technology

This research was funded by the China Scholarship Council (CSC).

Keywords: salt intrusion, tidal advection, lateral processes, gravitational circulation, estuarine turbidity maximum, sediment transport, well-mixed

ISBN 978-94-6186-828-2

An electronic version of this dissertation is available at
`http://repository.tudelft.nl/`.

Curiosity has its own reason for existence.

Albert Einstein

Contents

Summary

Estuaries are important ecosystems accommodating a large variety of living species. Estuaries are also important to people by their demand of freshwater for drinking, irrigation, and industry. Due to natural changes and human activities, the estuarine water quality, influenced by both salinity and turbidity (the cloudiness or haziness of water), has been greatly changed in many estuaries and may continue to change in the future. To predict and control the salt intrusion and the occurrence of high turbidity levels, it is essential to understand the physical mechanisms governing the estuarine dynamics. To that end, this thesis provides a systematical investigation of the dominant physical processes which result in salt intrusion and the formation of the Estuarine Turbidity Maxima (ETM's) in well-mixed estuaries.

To evaluate the importance of processes varying at the tidal timescale for the residual salt balance, a width-averaged semi-analytical model is developed. This model resolves the width-averaged water motion and salinity, while parameterizing all lateral processes in a prescribed diffusion term. It is found that the salt transport contribution due to the temporal correlations between the horizontal tidal velocities and tidal salinities (tidal advective diffusion) can be explicitly obtained after calculating the tidal water motion. The tidal advective diffusion dominates the residual landward salt transport in the Scheldt estuary, but is less important than other (unresolved) processes in the Delaware and the Columbia estuaries. This implies that the lateral processes, which are not explicitly resolved because the model is width-averaged, are probably important in the Delaware and the Columbia estuaries.

To explore the contribution of lateral processes to the residual salt transport, the width-averaged model is extended to a three-dimensional model using a semi-analytical iterative approach, resolving both longitudinal and lateral processes on the tidal timescale. This model allows for a systematic investigation of the relative importance of each physical process to residual salt transport including the effects of lateral processes, which are associated with estuarine convergence, Coriolis force and lateral bathymetric variations. The tidal advective diffusion is found to strongly dominate the residual landward salt transport in a schematized estuary representative for the Delaware estuary, highlighting the important role of lateral processes in maintaining the salt intrusion. Estuarine circulation, including the gravitational circulation, is only important for the lateral salinity distribution, not for the along-channel salt intrusion. It is also found that including the Coriolis force or lateral bathymetric variations strongly enhances the lateral circulations, while the inclusion of the estuarine convergence alone does not result in a strong lateral

circulation.

To systematically investigate the physical processes of the sediment transport and trapping in well-mixed estuaries, a semi-analytical three-dimensional sediment model is integrated with the hydro-salinity model mentioned above, dynamically resolving the effects of salt intrusion on sediment dynamics. The estuaries are assumed to be in morphodynamic equilibrium, where the tidally-averaged sediment deposition and erosion balance each other. It is found that, in a schematized system representative for the Delaware estuary (but neglecting the Coriolis force), the ETM is located near the salt intrusion limit. Sediments are transported from the downstream (upstream) region to the ETM through the channel (over the shoals), and transported from the ETM to the downstream (upstream) region over the shoals (through the channel). The seaward sediment transport induced by the river flow and the tidal return flow is mainly balanced by the landward sediment transport related to the internally-generated bottom M_4 tidal velocity, spatial settling lag effects and gravitational circulation. The sediment transport pattern and the relative importance of different processes strongly depend on the settling velocity and river discharge. For example, the ETM moves towards the riverside with increasing settling velocity or decreasing river discharge. The contribution of the gravitational circulation to the sediment transport increases significantly with increasing river discharge, which tends to trap fine-grained sediments in the lower estuary over the shoals, and coarse-grained sediments in the channel near the salt intrusion limit.

Samenvatting

Estuaria zijn belangrijke ecosystemen die een grote verscheidenheid aan flora en fauna huisvesten. Estuaria zijn ook belangrijk voor de lokale bevolking, vanwege de grote vraag aan zoet water uit estuarine waterlopen voor drinkwater, irrigatie en industrie. Door natuurlijke variaties en menselijke activiteiten is de waterkwaliteit, onder invloed van zowel saliniteit en turbiditeit, sterk veranderd in vele estuaria. Deze verandering zal waarschijnlijk ook in de toekomst doorzetten. Daarom is het van groot belang om de fysische mechanismen te begrijpen die een rol spelen bij de estuarine dynamica, en om zoutindindringing en hoge turbiditeit niveaus te voorspellen en te reguleren. In het kader hiervan biedt dit proefschrift een systematische studie naar de dominante fysische mechanismen die verantwoordelijk zijn voor zoutindringing, en het estuarine turbiditeitsmaximum (ETM) in goed-doorgemengde estuaria.

In de zoutbalans is de sterkte van processen die variëren op de getij-tijdschaal vergeleken met de sterkte van getijgemiddelde processen. Hiervoor is een breedtegemiddeld semi-analytisch model ontwikkeld voor de waterbeweging en saliniteit, waarbij laterale processen worden geparametriseerd in een voorgeschreven diffusieve term. Het blijkt dat de bijdrage aan het zouttransport door de tijdscorrelatie van het horizontale getij en de getijvariërende saliniteit (getij-advectieve diffusie) expliciet berekend kan worden door gebruik te maken van de getijwaterbeweging. De getij-advectieve diffusie is het dominante mechanisme in het residuele landinwaartse zouttransport in het Schelde estuarium, maar is minder belangrijk dan andere, onbepaalde, mechanismen in de Delaware en Columbia estuaria.

Om de bijdrage door laterale processen aan het residuele zouttransport te onderzoeken is het breedtegemiddelde model uitgebreid naar een drie-dimensionaal model. Dit model maakt gebruik van een semi-analytische, iteratieve aanpak en lost zowel de tijdsvariërende als ruimtelijke (laterale en longitudinale) processen op. Dit model maakt het mogelijk om systematisch de relatieve sterkte van elk afzonderlijk fysisch mechanisme dat bijdraagt aan het residuele zouttransport te onderzoeken, inclusief de effecten van laterale processen die worden veroorzaakt door geometrische convergentie, Coriolis en laterale variaties van de bathymetrie. De getij-advectieve diffusie blijkt een sterk dominante rol te spelen in het residuele landinwaarste zouttransport in een geschematiseerd estuarium dat representatief is voor het Delaware estuarium. Dit benadrukt het belang van laterale processen bij het in stand houden van de zoutindringing. Estuarine circulatie, waaronder gravitationele circulatie, is alleen van belang voor de laterale verdeling van zout en niet voor de verdeling van zout in de langsrichting. Ook blijkt dat het meenemen van Coriolis en laterale variaties van de bathymetrie de laterale circulatie versterkt, terwijl de het meenemen van alleen geometrische convergentie niet leidt tot een sterke laterale circulatie.

Om de fysische mechanismen die leiden tot sedimenttransport en -invanging in goed-doorgemengde estuaria systematisch te onderzoeken, is er een semi-analytisch drie-dimensionaal model geïntegreerd in het eerdergenoemde model voor de waterbeweging en saliniteit. Hierdoor kan het effect van zoutindringing op de sedimentdynamica dynamisch worden opgelost. Er wordt verondersteld dat de gemodelleerde estuaria in morfodynamisch evenwicht zijn, zodat de getijgemiddelde depositie en erosie van sediment gelijk zijn. In een geschematiseerd estuarium dat representatief is voor het Delaware estuarium (echter zonder Coriolis), blijkt dat het ETM zich bevindt bij het punt van maximale zoutindringing. Het sediment wordt door de diepere geulen (over de platen) van benedenstrooms (bovenstrooms) getransporteerd naar de locatie van het ETM en wordt over de platen (door de diepere geulen) vanaf de ETM-locatie stroomafwaarts (stroomopwaarts) getransporteerd. Het zeewaartse sedimenttransport veroorzaakt door de rivierafvoer en getij-terugstroming wordt voornamelijk gecompenseerd door het landwaartse transport veroorzaakt door het intern gegenereerde M_4 getij, sediment advectie ('spatial settling lag') en gravitationele circulatie. De sedimenttransportpatronen en de relatieve sterkte van de verschillende mechanismen hangt sterk af van de valsnelheid en rivierafvoer. Het ETM beweegt bijvoorbeeld bovenstrooms als de valsnelheid wordt verhoogd of de rivierafvoer wordt verlaagd. De bijdrage van de gravitationele circulatie aan het sedimenttransport wordt significant vergroot als ook de rivierafvoer wordt vergroot. Dit leidt tot invanging van fijn sediment op de platen in het benedenstroomse deel van het estuarium en invanging van grover sediment in de diepere geulen bij het punt van maximale zoutindringing.

Chapter 1

Introduction

Estuaries, which are coastal bodies of water connecting the riverine and marine environment, are among the most important ecosystems in the world. Apart from that, estuaries also accommodates world's largest harbors and a large number of industries, hence they are also economically important. Conditions of estuaries (water quality, morphology, etc.) can change significantly by natural causes such as typhoons, floods/droughts, and sea level rise, and human activities such as dam constructions and channel deepening. Therefore, in order to sustain the economic development and the great diversity of living species, we have to be able to predict estuarine responses to natural variations or anthropogenic impacts, so that proper measures can be taken to reduce possible negative effects. To reach that, a good understanding of the dominant physical mechanisms of estuarine dynamics is needed.

This thesis aims to improve our understanding of the dominant physical mechanisms controlling the behavior of salinity and suspended sediment concentration (SSC) in estuarine environments. These two factors are very important for the estuarine water quality, and changes in the sediment dynamics can also result in changes of the navigational depth due to sediment erosion or deposition. In section 1.1, a definition of an estuary is given, and the strong implications of salinity and SSC to estuarine water quality and environment are explained. In section 1.2, the influence of natural variations and human activities on estuaries is introduced. In section 1.3, the Delaware estuary is introduced as an example of an important well-mixed system with complex estuarine dynamics. Section 1.4 introduces the present knowledge regarding physical mechanisms of the transport of salt and sediment. In section 1.5, the knowledge gap concerning the salt and sediment dynamics is introduced, and the main research questions are formulated. In section 1.6, the main assumptions adopted in this thesis are discussed. The outline of this thesis is given in section 1.7.

1.1 Estuaries

An estuary is often defined as a semi-enclosed coastal body of water which connects a river with the open sea (Dyer 1997). The water motion at the seaward side of the estuary is generally forced by the tides, that result from the gravitational forces exerted by the moon and the sun (Platzman 1971). At the landward side of the estuary, there are usually rivers discharging into the estuary as a result of terrestrial runoff. In the region where the freshwater and the saline seawater meet, vertical salinity differences in the water column are often found. Depending on the relative strengths of tides and river discharge, the vertical salinity difference can vary significantly from estuary to estuary. This vertical structure is used to categorize estuaries as salt-wedge estuaries, strongly stratified estuaries, partially mixed estuaries, or well-mixed estuaries (Pritchard 1955, Cameron and Pritchard 1963, Valle-Levinson 2010). As shown in Fig. 1.1, in salt-wedge estuaries, the fresher water in the upper layers is separated from a wedge-shaped saltier layer near the bottom. The top-to-bottom salinity difference is large in strongly stratified estuaries, moderate in partially mixed estuaries, and small in well-mixed estuaries. This thesis will focus on well-mixed estuaries.

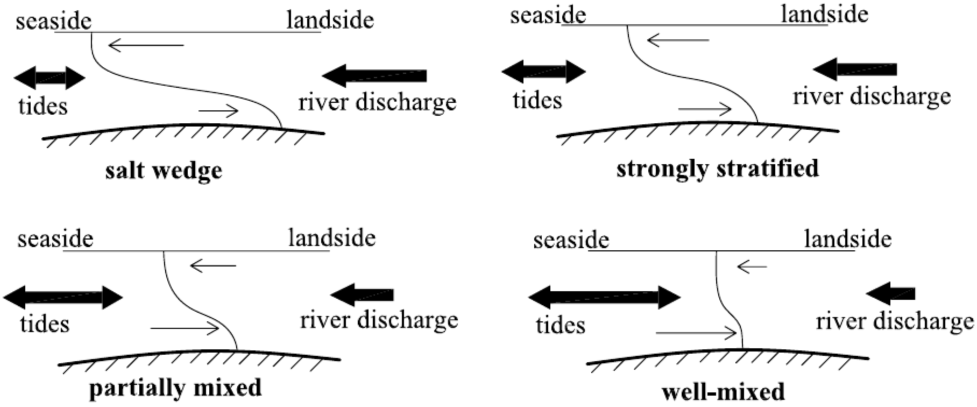

Figure 1.1: Vertical salinity differences in estuaries of different mixing conditions, with different magnitudes of tidal forcing and river discharge.

The estuarine water quality is not only important to the great diversity of estuarine species, but also for human lives because estuaries are usually surrounded by densely populated cities, providing huge amounts of fresh water for drinking, irrigational and industrial purposes. In this thesis, I will focus on two important factors controlling the estuarine water quality, namely, the salinity and turbidity (the cloudiness or haziness of water).

The longitudinal and lateral salt dynamics are of great importance for the functioning of estuaries. Salt intrusion, and the resulting salinity changes, can greatly affect the fresh water supply in deltas for drinking, industrial and irrigation purposes, see for example the discussion of Dai *et al.* (2011) concerning the Yangtze estuary and Gong and Shen

(2011) concerning the Pearl River estuary. Moreover, since in most estuaries, fresh water supply from the upper river exceeds fresh water losses by evaporation or freezing, salt intrusion results in a horizontal salinity gradient, with the salinity consistently decreasing from the ocean toward the head of the estuary (i.e, positive estuaries, see Valle-Levinson (2010)). This salinity gradient plays an important role in the estuarine water motion, thus significantly influencing the transport of nutrients, pollutants, sediment, and other waterborne materials in estuaries.

Turbidity is strongly related to high suspended sediment concentrations (SSC). Transport processes in estuaries can result in sediments being trapped at specific locations, forming an estuarine turbidity maximum (ETM), a region with a larger SSC than that observed in the upstream or downstream. These high concentrations of sediment within the ETM can significantly influence the estuarine functioning. First of all, an ETM can be a locus of contaminants (Jay *et al.* 2015), thus seriously affecting the water quality and threatening fresh water intake. Secondly, high turbidity levels within the ETM regions can result in a reduced light availability and oxygen in the water column, negatively affecting the primary production and thus the estuarine food webs (de Jonge *et al.* 2014). For this reason, high SSC is likely to hinder the production of phytoplankton and zooplankton, thus reducing the ecological value of the estuary.

Apart from the strong implications of ETM's on water quality, they are also of great significance for morphological and economical reasons. This is related to the fact that ETM's are often locations of long-term sediment deposition, thus requiring frequent dredging to maintain the navigation channel at appropriate water depths (Jay *et al.* 2015). Furthermore, high SSC also greatly influences the water density, further contributing to the estuarine circulation in highly turbid estuaries (Talke *et al.* 2009). Finally, the vertical structure of salinity and SSC can greatly affect the vertical density structure, and hence the vertical turbulent mixing (Simpson *et al.* 1990, Geyer 1993), which in turn influences the water motion, and the transport of salt and SSC.

1.2 Natural variations and anthropogenic interventions

Estuaries are strongly impacted by variations of forcing conditions in the ocean and the river basin due to climate changes, and anthropogenic perturbations in the delta.

Natural variations related to climate changes can have a large impact on estuarine dynamics. These changes include short-term events such as storms and typhoons, seasonal variations such as floods and droughts (changes in river runoff), and long-term variations such as sea level rise. The influence due to these changes have been evidenced in many estuaries worldwide. Concerning the short-term events, wind-related sediment resuspension was found to contribute significantly to the sediment transport and deposition in the Peel-Harvey estuary (Gabrielson and Lukatelich 1985) and the Ems estuary (de Jonge *et al.* 2014). On the intermediate timescale, variations in river discharges due to seasonal floods or droughts greatly affect the salt intrusion and sediment concentrations in the Hudson River estuary (Woodruff *et al.* 2001). Moreover, the abnormally strong salt intrusion in the Yangtze estuary in 2006 is attributed to the extreme low river discharge caused by the extreme drought (Dai *et al.* 2011); and an enhanced salt intrusion was found in the Pearl River estuary during dry seasons (Gong and Shen 2011). Variations in river discharge are also responsible for the significant variations of the ETM location and the magnitude of sediment concentrations in the Ems estuary (Chernetsky *et al.* 2010, de Jonge *et al.* 2014). On the long timescale, sea level rise has a potential impact on enhancing salt intrusion and exacerbate sediment erosion (Hilton *et al.* 2008, Nicholls and Cazenave 2010).

Human activities can also strongly influence the estuarine dynamics. To accommodate the fast economic development and rapid growth of human population in deltas, the size and frequency of human activities have been consistently increasing. To name a few, many estuaries are drained for agricultural uses, filled to create harbors or expand urban areas (land reclamation), dammed for hydropower and preventing floods, and dredged to maintain ship navigation (Nichols *et al.* 1986). These activities have posed a great threat to the estuarine habitats. A good example is the construction of the Three Gorges Dam in China, the largest dam in the world. This construction greatly reduces the supply of fresh water and sediment to the Yangtze estuary, which results in a stronger salt intrusion and riverbed scouring (Yang *et al.* 2006, Stone 2008). Channel deepening is the most common human activity in estuaries worldwide for the maintenance of ship navigation, which is responsible for the increased tidal range, enhanced salt intrusion and turbidity levels (Schuttelaars *et al.* 2013, de Jonge *et al.* 2014). Examples of estuaries experiencing intensive deepening include the Ems estuary between the Netherlands and Germany (Jonge 1983), the Delaware estuary in the US (DiLorenzo *et al.* 1993), the Yangtze estuary (Dai *et al.* 2013) and Pearl River estuary in China (Zhang *et al.* 2010). In the Pearl River estuary, for instance, over 8.7×10^8 m^3 of sand was excavated between 1983 to 2003 (Luo *et al.* 2007), resulting in an enhanced salt intrusion: the salt water intruded 10-20 km more landward in the 2000s compared to the 1980s. In the Ems estuary, intensive human interventions were carried out in the past few decades, such as land reclamation and channel deepening. This has resulted in a dramatic increase in the tidal range from 1970s to 1990s (see Fig. 1.2a) and suspended sediment concentration from 1970s to 2000s (see Fig. 1.2b), especially in the upper reach of the Ems estuary, significantly increasing flooding risks and deteriorating the estuarine water quality.

1.3 An example: the Delaware estuary

The Delaware estuary is one of the largest well-mixed estuaries in the world, and is used in this thesis as the main example to illustrate the estuarine dynamics in well-mixed systems. Millions of people live in the delta region around the Delaware estuary, with their daily life strongly influenced by and impacting the estuarine water quality.

The Delaware estuary, stretching from Trenton (the landward limit of the fresh tidal river) to Cape May and Cape Henlopen (the estuarine mouth in the Delaware Bay), is about 215 km long (see Fig. 1.3). The estuarine bathymetry is characterized by shallow flanks and a deep channel, with a mean water depth of 8 m (Aristizábal and Chant 2013). The estuarine width is approximately 18 km at the mouth of the Delaware bay, increases to ~40 km in the bay and then decreases landward. The M_2 tide is the dominant tidal

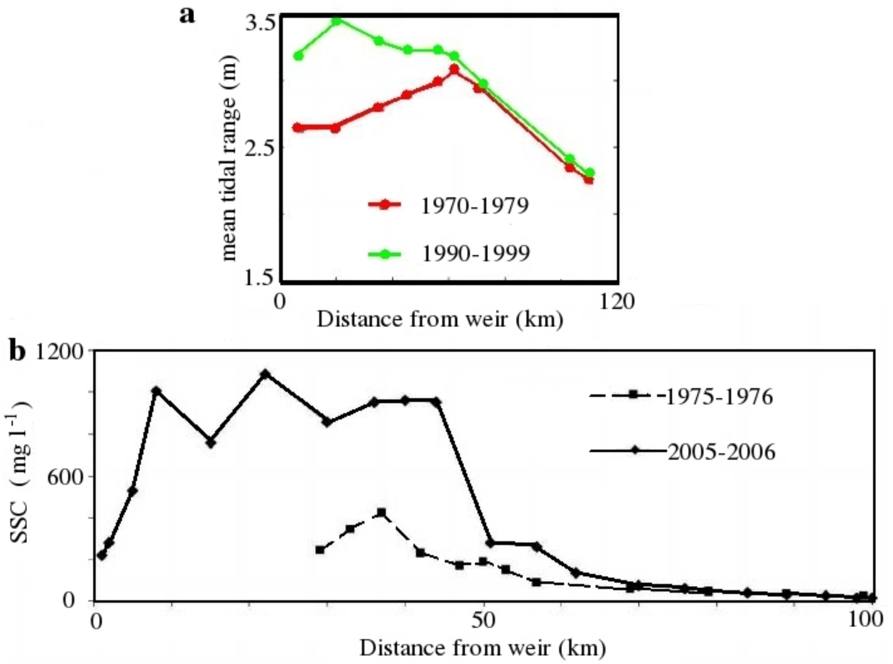

Figure 1.2: The mean tidal range and suspended sediment concentration (SSC) along the Ems estuary. This plot is based on Schuttelaars *et al.* (2013), and reprinted with permission.

constituent in the Delaware estuary, with a tidal amplitude of about 0.7 m at the mouth (Garvine *et al.* 1992). The annual mean freshwater discharge is 330 m^3 s^{-1}, more than half of which is discharged by the Delaware River, and the rest is mainly discharged by the Schuylkill and Christina river tributaries, with an annual mean flow of ~77 m^3 s^{-1} and 19 m^3 s^{-1}, respectively (Mansue and Commings 1974). These tributaries contribute to over 80% of the total sediment load to the Delaware estuary. According to daily observations (monitored by U.S. Geological Survey), the salt intrusion limit is usually located between 80 and 120 km from the estuarine mouth, with a typical vertical salinity variation of 1 psu (Garvine *et al.* 1992). Later, it was found that the vertical stratification can reach up to 10 psu in the channel, but the water column is consistently well-mixed on the flanks (Aristizábal and Chant 2013).

Observations of McSweeney *et al.* (2016) revealed complex three-dimensional structures of salinity and SSC near the ETM of the Delaware estuary (see Fig. 1.4). According to their observations, an ETM is found near the landward limit of salt intrusion at ~100 km from the mouth. The vertical stratification is smaller than 5 psu except at ~50-70 km from the mouth, where the top-to-bottom salinity difference is as large as 10 psu. The suspended sediment concentrations are highest in the ETM zone, extending from 70 km to 120 km up-estuary from the mouth. The salinities are larger in the channel than on the flanks, while the vertical stratification decreases from 4 psu in the deep channel to 1 psu on the flanks (see Fig. 1.4b). The suspended sediment concentrations are larger

Figure 1.3: A map of the Delaware estuary (source: http://delawareestuary.org/estuary-map). The red lines qualitatively show the locations of axial surveys and the mooring transect reported in McSweeney *et al.* (2016).

on the flanks than in the channel, and the highest SSC in the cross-section is found on the flank near Delaware. This highlights the complexity of the dynamics in the Delaware estuary, and the potential importance of both longitudinal and lateral processes in the

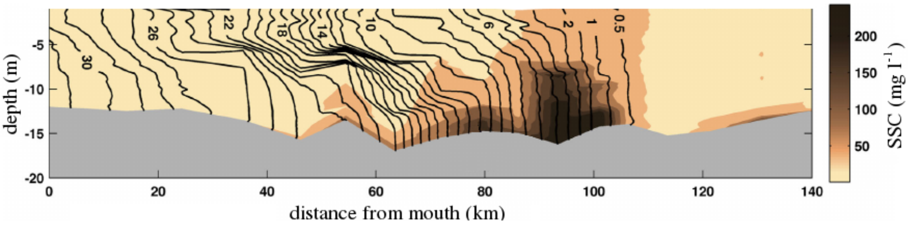

(a) The longitudinal-vertical distribution of salinity and SSC at the mid-axis

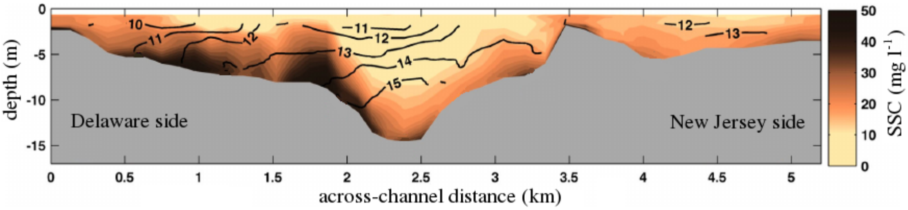

(b) The cross-sectional distribution of salinity and SSC

Figure 1.4: The observed distributions of salinity and sediment concentration in the Delaware estuary. The figures are based on McSweeney *et al.* (2016), and reprinted with permission.

maintenance of salt intrusion and the ETM. The tidal river and lower bay are characterized by lower sediment concentrations with small sediment sizes, while the sediment size increases towards the ETM, and decreases further landward (Gibbs *et al.* 1983).

1.4 Present knowledge

Many studies have investigated the physical mechanisms resulting in salt intrusion and sediment transport and trapping in estuaries. Field observations are often used to demonstrate the structures of salinity and SSC in estuaries, which are decomposed to get insight into physical processes of the salt and sediment transport (Fischer 1972, Hughes and Rattray 1980, Lerczak *et al.* 2006, Sommerfield and Wong 2011, McSweeney *et al.* 2016). However, due to limited observations available for financial and technical reasons, the investigation of the mechanisms driving the highly dynamic spatio-temporal patterns of salt and sediment transport, is usually done by employing process-based idealized models.

Existing process-based idealized models are either complex numerical models, such as width-averaged numerical models (Festa and Hansen 1978, Geyer 1993) and three-dimensional models (Lin and Kuo 2003, Lerczak and Geyer 2004, Ralston and Stacey 2005, Ralston *et al.* 2010, Gong and Shen 2011, Ralston *et al.* 2012), or theoretical models, for example the cross-sectionally integrated (1D) models of Friedrichs and Aubrey (1988), Friedrichs *et al.* (1998), the width-averaged (2DV) models of (Hansen and Rattray 1965, McCarthy 1993, MacCready 2004, Chernetsky *et al.* 2010), the depth-averaged models of Li and O'Donnell (1997), Valle-Levinson *et al.* (2000), the cross-sectional models of Nunes and Simpson (1985) and Huijts *et al.* (2006), and the three-dimensional models of Winant (2008), Ensing *et al.* (2015) and Kumar *et al.* (2017). The former type of models, the so-called simulation models, are more suited to do complex experiments for a specific estuary. These models take into account most details of realistic estuarine bathymetry and geometry and forcing conditions, and include all known physical processes, thus allowing for a quantitative comparison with observations. However, due to all complex details included in these models, they are often very expensive to run, thus difficult to use for sensitivity analysis. Another drawback is that these models need intensive calibration before applying to a new situation with a changed condition, in which the calibration can be invalid (Schuttelaars *et al.* 2013). More importantly, due to the complexity of numerical models, it is difficult to assess the influence of each specific physical process from the model results. Therefore, analyzing the underlying mechanisms is difficult using this type of models. The theoretical models, however, are specifically designed for investigating physical mechanisms systematically. By using basic assumptions and a simplified bathymetry and geometry, these models can be used to identify the dominant physical mechanisms for a group of estuaries with similar characteristics. Moreover, these models are usually fast in calculation and efficient to perform sensitivity studies.

Idealized models have been already used successfully to examine the processes driving the tidal and tidally-averaged (residual) water motion, the salt transport processes, and sediment transport and trapping processes along and across the estuary. Below, the existing knowledge concerning the water motion and residual salt transport processes obtained by prior idealized modelling work is introduced in section 1.4.1; in section 1.4.2, the present knowledge of sediment transport and trapping processes is briefly discussed.

1.4.1 Water motion and salt transport

The hydrodynamic processes, including both the tidal water motion and the tidally-averaged water flow (also known as estuarine circulation, or exchange flow) play an important role in the estuarine transport of salt, sediment, and passive contaminants (Chatwin 1975, 1976). The tidal flow is dominantly forced by external tides, and is strongly influenced by estuarine geometry, bathymetry and bottom friction (Hansen and Rattray 1965, Friedrichs and Madsen 1992, Friedrichs and Aubrey 1994, Lanzoni and Seminara 1998, Friedrichs 2010, Toffolon and Savenije 2011).

The estuarine circulation, though its magnitude is usually much smaller than the tidal velocities, is crucial for the distribution and estuarine transport of waterborne materials (Geyer and MacCready 2014). A well-established mechanism that results in the along-channel estuarine circulation is related to the along-channel density gradient as a result of salt intrusion. This mechanism was theoretically calculated by Hansen and Rattray (1965) assuming rectangular cross-sections, which results in a circulation featuring a landward residual current near the bottom and a seaward current near the top. This mechanism formulates the classical salt balance in estuaries, where the up-estuary transport by gravitational circulation is balanced by the down-estuary transport by the river flow (MacCready 2004, MacCready and Geyer 2010, Geyer and MacCready 2014).

Gravitational circulation can be strongly modified by across-channel bathymetric variations, exhibiting remarkable lateral characteristics with landward residual currents concentrated in the channel and seaward currents over the shallows. This was systematically investigated using theoretical idealized models (Wong 1994, Friedrichs and Hamrick 1996), in which lateral circulations were neglected. Friedrichs and Hamrick (1996) also reported the potential significance of the nonlinear advection of the along-channel momentum by along-channel tidal flow to the along-channel residual circulation. This is supported by Huijts *et al.* (2009) who included lateral flows using a cross-sectional analytical model. The nonlinear advection of the along-channel momentum by lateral tidal flow can strongly affect the along-channel circulation, as observed in Lacy and Monismith (2001) and confirmed by both theoretical studies (Nunes and Simpson 1985, Huijts 2011) and idealized numerical models (Lerczak and Geyer 2004), where this process is referred to as differential advection. Many other processes also affect the along-channel estuarine circulation, thus playing an important role in salt transport. Among these, one important process is related to the tidally varying intensity of turbulence (i.e., tidal straining), as a result of vertical or lateral salinity differences (Simpson *et al.* 1990, Burchard and Hetland 2010, Cheng *et al.* 2010, Burchard *et al.* 2014), which is found to result in a significant residual circulation especially in well-mixed estuaries (Burchard and Schuttelaars 2012). By employing an idealized cross-sectional (2D) numerical model, Schulz *et al.* (2015) found that the tidal straining effects on the residual circulation is strong in narrow estuaries, and increases with increasing depth-to-width ratio. The contribution of the tidal straining on salt transport is studied using an idealized numerical model by Cheng *et al.* (2013), who found this process contributes to a landward salt transport in estuaries with strong tides, and a seaward salt transport in estuaries with weak tides.

Lateral estuarine circulations, also known as secondary estuarine circulation, and usually associated with lateral depth variations, curvature, density gradients, winds, Coriolis deflection (Becherer 2014, Becherer *et al.* 2015), can also play an important role in the landward salt transport. Lateral estuarine circulations were found to greatly contribute to the along-channel salt transport by Fischer (1972) and Smith (1977). Later, Hughes and Rattray (1980) found the correlation between the temporally and laterally varying water depths, velocities and salinities largely contributes to the along-channel salt transport, confirming the potential importance of lateral processes and processes at the tidal timescale. The temporal correlation between the along-channel velocities and salinities was found to dominate the salt transport in the North Inlet, South Carolina (Kjerfve 1986), and was systematically investigated using a 2DV analytical model by McCarthy (1993) for well-mixed estuaries.

1.4.2 Sediment transport

Sediment transport and trapping mechanisms have been intensively investigated in the past few decades. In the classical theory, the formation of ETM is attributed to the convergence of sediment transport due to a down-estuary transport by river discharge and an up-estuary transport due to the salinity-induced gravitational circulation (Postma 1967, Festa and Hansen 1978). This mechanism is qualitatively sketched in Fig. 1.5: the river flow induces a seaward sediment flux at all water depths, contributing to a significant seaward sediment transport. The gravitational circulation, however, induces a landward transport near the bottom and a seaward transport near the surface. Due to larger sediment concentrations near the bottom than at the surface, the landward sediment transport near the bottom exceeds the seaward transport in the upper layers, resulting in a landward sediment transport integrated over the depth. The convergence of sediment transports due to these two processes hence leads to the formation of the ETM. Observational studies (Fugate *et al.* 2007, Sommerfield and Wong 2011, McSweeney *et al.* 2016) have shown remarkable complex lateral structures of suspended sediment concentration and sediment transport patterns, highlighting the importance of lateral processes such as differential advection and lateral circulations to the cross-channel and along-channel sediment transport. Other processes can also play an important role, including tidal velocity asymmetry (Allen *et al.* 1980, Jay and Musiak 1994, Friedrichs *et al.* 1998, Burchard and Baumert 1998), settling lag effects (de Swart and Zimmerman 2009, Chernetsky *et al.* 2010), tidal straining (Jay and Musiak 1996, Scully and Friedrichs 2003), sediment-induced stratification (Winterwerp 2011) and currents related to turbidity-induced density gradients (Talke *et al.* 2009, Lacy *et al.* 2014). For cohesive sediments, particle aggregation (i.e., flocculation) can also significantly affect the entrapment of sediment (van Leussen 1999, Winterwerp 2011).

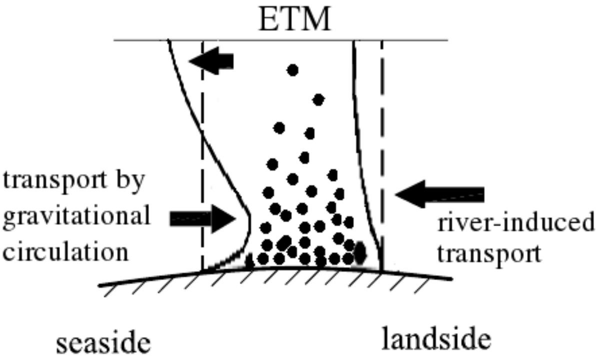

Figure 1.5: This sketch shows the classical mechanism of the ETM formation due to contributions of gravitational circulation and river-induced flow.

1.5 Research questions

Previous discussion has shown that idealized process-based theoretical models are effective tools to investigate the mechanisms of estuarine dynamics. Therefore, this type of models will be used to investigate the contributions of the potentially important processes of salt intrusion and sediment transport (and trapping) in well-mixed estuaries.

Due to the nonlinear coupling of water motion and salinity, in most of the existing theoretical models, the salinity effects on water motion and salinity/sediment transport is either ignored (Li and O'Donnell 1997) or diagnostically included using a prescribed salinity (see, for example, Friedrichs *et al.* (1998), Talke *et al.* (2009), Chernetsky *et al.* (2010), Huijts *et al.* (2006, 2011), Kumar *et al.* (2017), de Jonge *et al.* (2014)). For this reason, the dynamical effects of salinity on water motion and transport of salt or sediment are not identified using these models. Hansen and Rattray (1965) analytically resolved the coupled water motion and salinity in a width-averaged model, which is extended by MacCready (2004). However, in both models, the processes at the tidal timescale, which can be significant for salt and sediment transport, are neglected. McCarthy (1993) analytically solved the dynamically coupled width-averaged water motion and salinity equation for well-mixed estuaries (with an exponentially converging width and a constant water depth), resolving processes at the tidal timescale. Nevertheless, this model is limited to estuaries with a horizontal bed and converging width. Besides, the tidally averaged density, which is a real number, was taken to be complex, thus yielding inconsistent results. Moreover, all models discussed above focus on either longitudinal processes or lateral processes, even though both processes (especially the interactions between them) can be important for residual circulations and transport of salt and sediment, resulting in a relatively poor understanding of the three-dimensional processes of salt and sediment transport in estuaries.

Therefore, to fill in this knowledge gap and improve understanding of the salt and sediment transport mechanisms in well-mixed estuaries, this thesis addresses the following three research questions:

*Q*1: Can we quantify the residual salt transport contribution induced by processes at the tidal timescale in well-mixed estuaries of an arbitrary geometry and bathymetry? How does this contribution vary with estuarine bathymetry, geometry and friction parameters? How significant is this contribution in natural well-mixed estuaries?

*Q*2: Under what conditions are lateral processes important for the residual salt transport in well-mixed estuaries? Can we identify the three-dimensional structure of residual salt fluxes induced by each physical process?

*Q*3: What is the influence of salt intrusion on sediment transport and trapping in well-mixed estuaries? What are other potentially important processes governing the occurrence and variations of estuarine turbidity maximum? How do the sediment transport processes change with different sediment properties (such as settling velocity) and forcing conditions (such as river discharge)?

1.6 Main assumptions

The estuarine water motion strongly controls the transport of salt and sediments. Meanwhile, due to the feedback of salinity and SSC on the water density, the water motion is also be affected by salinity and SSC through the baroclinic pressure and vertical mixing in the momentum equations. To enable an (semi-) analytical solution and a systematic investigation of the dominant physical processes of the salt and sediment transport, it is assumed that estuaries are well-mixed and tidally dominated. This means the tidal forcing is much stronger than the river flow, and the top-to-bottom salinity difference is at least one order of magnitude smaller than the bottom salinity, ignoring the salinity-induced stratification. The influence of SSC on the water density is also assumed to be negligible. Moreover, the effects of flocculation and hindered settling are not considered.

1.7 Outline of this thesis

In chapter 2, a width-averaged (2DV) semi-analytical model is developed to investigate the salt dynamics resolving processes in the longitudinal and vertical directions and processes at the tidal timescale, extending the model of McCarthy (1993). By using a perturbation method, the width-averaged water motion and salinity are explicitly calculated at the tidal time scale. The residual salt transport contribution due to the temporal correlation between tidal salinities and tidal velocities (tidal advective diffusion) is the focus in this chapter, while all lateral processes are parameterized in a prescribed diffusion coefficient. The sensitivity of the tidal advective diffusion to friction parameters and estuarine shape is also studied. The 2DV model is applied to three estuaries under well-mixed conditions: the Delaware, Scheldt and Columbia estuaries.

In chapter 3, a three-dimensional (3D) semi-analytical model is developed by extending the 2DV model in chapter 2, such that the temporal and spatial (both longitudinal and lateral) variabilities of the water motion and salinity are dynamically resolved. Using this model, the contributions of various longitudinal and transverse processes to the residual salt transport are assessed individually. The salt dynamics in a schematized estuary, representative for the Delaware, is systematically investigated. The salt transport contributions due to tidal advective diffusion, gravitational circulation, and other residual flow components are identified and individually discussed. Then, the influences of estuarine convergence, bathymetry, and Coriolis force on the salt transport processes are explored.

In chapter 4, a 3D semi-analytical model is introduced, incorporating the 3D salinity module in chapter 3 and the sediment module of Kumar *et al.* (2017), thus allowing for a systematic study of the salinity effects on the sediment transport. The sediment transport and trapping mechanisms are explored for a schematized estuary representative for the Delaware estuary, but neglecting Coriolis force. The influence of Coriolis deflection on sediment dynamics is studied subsequently by including Coriolis force, followed by a sensitivity study of the sediment transport and trapping processes to settling velocity and river discharge.

In chapter 5, conclusions of this thesis are summarized, together with some recommendations for future research.

References

Allen, G. P., J. Salomon, P. Bassoullet, Y. Du Penhoat, and C. De Grandpre, *Effects of tides on mixing and suspended sediment transport in macrotidal estuaries,* Sedimentary Geology **26**, 69–90 (1980).

Aristizábal, M., and R. Chant, *A numerical study of salt fluxes in Delaware Bay estuary,* Journal of Physical Oceanography **43**, 1572–1588 (2013).

Becherer, J., *Estuarine circulation in well-mixed tidal inlets*, Ph.D. thesis (2014).

Becherer, J., M. T. Stacey, L. Umlauf, and H. Burchard, *Lateral circulation generates flood tide stratification and estuarine exchange flow in a curved tidal inlet,* Journal of Physical Oceanography **45**, 638–656 (2015).

Burchard, H., and H. Baumert, *The formation of estuarine turbidity maxima due to density effects in the salt wedge: A hydrodynamic process study,* Journal of Physical Oceanography **28**, 309–321 (1998).

Burchard, H., and R. D. Hetland, *Quantifying the contributions of tidal straining and gravitational circulation to residual circulation in periodically stratified tidal estuaries,* Journal of Physical Oceanography **40**, 1243–1262 (2010).

Burchard, H., E. Schulz, and H. M. Schuttelaars, *Impact of estuarine convergence on residual circulation in tidally energetic estuaries and inlets,* Geophysical Research Letters **41**, 913–919 (2014).

Burchard, H., and H. M. Schuttelaars, *Analysis of tidal straining as driver for estuarine circulation in well-mixed estuaries,* Journal of Physical Oceanography **42**, 261–271 (2012).

Cameron, W. M., and D. W. Pritchard, *Estuaries,* In M. N. Hill (ed.), The Sea **2**, 306–324 (1963).

Chatwin, P., *On the longitudinal dispersion of passive contaminant in oscillatory flows in tubes,* Journal of Fluid Mechanics **71**, 513–527 (1975).

Chatwin, P., *Some remarks on the maintenance of the salinity distribution in estuaries,* Estuarine and Coastal Marine Science **4**, 555–566 (1976).

Cheng, P., H. E. Swart, and A. Valle-Levinson, *Role of asymmetric tidal mixing in the subtidal dynamics of narrow estuaries,* Journal of Geophysical Research: Oceans **118**, 2623–2639 (2013).

Cheng, P., A. Valle-Levinson, and H. E. De Swart, *Residual currents induced by asymmetric tidal mixing in weakly stratified narrow estuaries,* Journal of Physical Oceanography **40**, 2135–2147 (2010).

Chernetsky, A. S., H. M. Schuttelaars, and S. A. Talke, *The effect of tidal asymmetry and temporal settling lag on sediment trapping in tidal estuaries,* Ocean Dynamics **60**, 1219–1241 (2010).

Dai, Z., A. Chu, M. Stive, X. Zhang, and H. Yan, *Unusual salinity conditions in the Yangtze estuary in 2006: impacts of an extreme drought or of the Three Gorges Dam?* Ambio **40**, 496–505 (2011).

Dai, Z., J. T. Liu, G. Fu, and H. Xie, *A thirteen-year record of bathymetric changes in the north passage, Changjiang (Yangtze) estuary,* Geomorphology **187**, 101–107 (2013).

DiLorenzo, J. L., P. Huang, M. L. Thatcher, and T. O. Najarian, *Dredging impacts on Delaware estuary tides,* in *Proceedings of the 3rd International Conference on Estuarine and Coastal Modeling III* (1993) pp. 86–104.

Dyer, K., *Estuaries: a physical introduction wiley,* New York (1997).

Ensing, E., H. E. de Swart, and H. M. Schuttelaars, *Sensitivity of tidal motion in well-mixed estuaries to cross-sectional shape, deepening, and sea level rise,* Ocean Dynamics **65**, 933–950 (2015).

Festa, J. F., and D. V. Hansen, *Turbidity maxima in partially mixed estuaries: A two-dimensional numerical model,* Estuarine and Coastal Marine Science **7**, 347–359 (1978).

Fischer, H., *Mass transport mechanisms in partially stratified estuaries,* Journal of Fluid Mechanics **53**, 671–687 (1972).

Friedrichs, C. T., *Barotropic tides in channelized estuaries,* Contemporary Issues in Estuarine Physics , 27–61 (2010).

Friedrichs, C. T., B. Armbrust, and H. E. de Swart, *Hydrodynamics and equilibrium sediment dynamics of shallow, funnel-shaped tidal estuaries,* Physics of Estuaries and Coastal Seas , 315–327 (1998).

Friedrichs, C. T., and D. G. Aubrey, *Non-linear tidal distortion in shallow well-mixed estuaries: a synthesis,* Estuarine, Coastal and Shelf Science **27**, 521–545 (1988).

Friedrichs, C. T., and D. G. Aubrey, *Tidal propagation in strongly convergent channels,* Journal of Geophysical Research: Oceans (1978–2012) **99**, 3321–3336 (1994).

Friedrichs, C. T., and J. M. Hamrick, *Effects of channel geometry on cross sectional variations in along channel velocity in partially stratified estuaries,* Buoyancy Effects on Coastal and Estuarine Dynamics , 283–300 (1996).

Friedrichs, C. T., and O. S. Madsen, *Nonlinear diffusion of the tidal signal in frictionally dominated embayments,* Journal of Geophysical Research: Oceans **97**, 5637–5650 (1992).

Fugate, D. C., C. T. Friedrichs, and L. P. Sanford, *Lateral dynamics and associated transport of sediment in the upper reaches of a partially mixed estuary, Chesapeake Bay, USA,* Continental Shelf Research **27**, 679–698 (2007).

Gabrielson, J., and R. Lukatelich, *Wind-related resuspension of sediments in the peel-harvey estuarine system,* Estuarine, Coastal and Shelf Science **20**, 135–145 (1985).

Garvine, R. W., R. K. McCarthy, and K.-C. Wong, *The axial salinity distribution in the Delaware estuary and its weak response to river discharge,* Estuarine, Coastal and Shelf Science **35**, 157–165 (1992).

Geyer, W. R., *The importance of suppression of turbulence by stratification on the estuarine turbidity maximum,* Estuaries **16**, 113–125 (1993).

Geyer, W. R., and P. MacCready, *The estuarine circulation,* Annual Review of Fluid Mechanics **46**, 175 (2014).

Gibbs, R. J., L. Konwar, and A. Terchunian, *Size of flocs suspended in Delaware Bay,* Canadian Journal of Fisheries and Aquatic Sciences **40**, s102–s104 (1983).

Gong, W., and J. Shen, *The response of salt intrusion to changes in river discharge and tidal mixing during the dry season in the Modaomen estuary, China,* Continental Shelf Research **31**, 769–788 (2011).

Hansen, D. V., and M. Rattray, *Gravitational circulation in straits and estuaries,* Estuarine and Coastal Marine Science **23**, 104–122 (1965).

Hilton, T., R. Najjar, L. Zhong, and M. Li, *Is there a signal of sea-level rise in Chesapeake Bay salinity?* Journal of Geophysical Research: Oceans **113** (2008).

Hughes, F., and M. Rattray, *Salt flux and mixing in the Columbia River estuary,* Estuarine and Coastal Marine Science **10**, 479–493 (1980).

Huijts, K., *Modelling the transverse distribution of velocity and suspended sediment in tidal estuaries,* (2011).

Huijts, K., H. M. Schuttelaars, H. E. de Swart, and C. Friedrichs, *Analytical study of the transverse distribution of along-channel and transverse residual flows in tidal estuaries,* Continental Shelf Research **29**, 89–100 (2009).

Huijts, K., H. M. Schuttelaars, H. E. de Swart, and A. Valle-Levinson, *Lateral entrapment of sediment in tidal estuaries: An idealized model study,* Journal of Geophysical Research: Oceans **111** (2006).

Huijts, K. M., H. E. de Swart, G. P. Schramkowski, and H. M. Schuttelaars, *Transverse structure of tidal and residual flow and sediment concentration in estuaries,* Ocean Dynamics **61**, 1067–1091 (2011).

Jay, D., and J. Musiak, *Internal tidal asymmetry in channel flows: Origins and consequences,* Mixing in Estuaries and Coastal Seas , 211–249 (1996).

Jay, D., S. Talke, A. Hudson, and M. Twardowski, *Estuarine turbidity maxima revisited: Instrumental approaches, remote sensing, modeling studies, and new directions,* Developments in Sedimentology **68**, 49-109 (2015).

Jay, D. A., and J. D. Musiak, *Particle trapping in estuarine tidal flows,* Journal of Geophysical Research: Oceans **99**, 20445–20461 (1994).

Jonge, V. d., *Relations between annual dredging activities, suspended matter concentrations, and the development of the tidal regime in the Ems estuary,* Canadian Journal of Fisheries and Aquatic Sciences **40**, s289–s300 (1983).

de Jonge, V. N., H. M. Schuttelaars, J. E. van Beusekom, S. A. Talke, and H. E. de Swart, *The influence of channel deepening on estuarine turbidity levels and dynamics, as exemplified by the Ems estuary,* Estuarine, Coastal and Shelf Science **139**, 46–59 (2014).

Kjerfve, B., *Circulation and salt flux in a well mixed estuary,* Physics of shallow estuaries and bays , 22–29 (1986).

Kumar, M., H. M. Schuttelaars, and P. C. Roos, *Three-dimensional semi-idealized model for estuarine turbidity maxima in tidally dominated estuaries,* Ocean Modelling **113**, 1–21 (2017).

Lacy, J. R., S. Gladding, A. Brand, A. Collignon, and M. Stacey, *Lateral baroclinic forcing enhances sediment transport from shallows to channel in an estuary,* Estuaries and Coasts **37**, 1058–1077 (2014).

Lacy, J. R., and S. G. Monismith, *Secondary currents in a curved, stratified, estuarine channel,* Journal of Geophysical Research: Oceans **106**, 31283–31302 (2001).

Lanzoni, S., and G. Seminara, *On tide propagation in convergent estuaries,* Journal of Geophysical Research **103**, 30793–30812 (1998).

Lerczak, J. A., and W. R. Geyer, *Modeling the lateral circulation in straight, stratified estuaries,* Journal of Physical Oceanography **34**, 1410–1428 (2004).

Lerczak, J. A., W. R. Geyer, and R. J. Chant, *Mechanisms driving the time-dependent salt flux in a partially stratified estuary,* Journal of Physical Oceanography **36**, 2296–2311 (2006).

van Leussen, W., *The variability of settling velocities of suspended fine-grained sediment in the Ems estuary,* Journal of Sea Research **41**, 109–118 (1999).

Li, C., and J. O'Donnell, *Tidally driven residual circulation in shallow estuaries with lateral depth variation,* Journal of Geophysical Research: Oceans **102**, 27915–27929 (1997).

Lin, J., and A. Y. Kuo, *A model study of turbidity maxima in the York River estuary, Virginia,* Estuaries **26**, 1269–1280 (2003).

Luo, X.-L., E. Y. Zeng, R.-Y. Ji, and C.-P. Wang, *Effects of in-channel sand excavation on the hydrology of the Pearl River Delta, China,* Journal of Hydrology **343**, 230–239 (2007).

MacCready, P., *Toward a unified theory of tidally-averaged estuarine salinity structure,* Estuaries **27**, 561–570 (2004).

MacCready, P., and W. R. Geyer, *Advances in estuarine physics,* Annual Review of Marine Science **2**, 35–58 (2010).

Mansue, L. J., and A. B. Commings, *Sediment transport by streams draining into the Delaware estuary* (US Government Printing Office, 1974).

McCarthy, R. K., *Residual currents in tidally dominated, well-mixed estuaries,* Tellus A **45**, 325–340 (1993).

McSweeney, J. M., R. J. Chant, and C. K. Sommerfield, *Lateral variability of sediment transport in the Delaware estuary,* Journal of Geophysical Research: Oceans (2016).

Nicholls, R. J., and A. Cazenave, *Sea-level rise and its impact on coastal zones,* science **328**, 1517–1520 (2010).

Nichols, F. H., J. E. Cloern, S. N. Luoma, and D. H. Peterson, *The modification of an estuary.* Science(Washington) **231**, 567–573 (1986).

Nunes, R., and J. Simpson, *Axial convergence in a well-mixed estuary,* Estuarine, Coastal and Shelf Science **20**, 637–649 (1985).

Platzman, G. W., *Ocean tides and related waves,* Mathematical Problems in the Geophysical Sciences **1**, 239–291 (1971).

Postma, H., *Sediment transport and sedimentation in the estuarine environment,* (1967).

Pritchard, D. W., *Estuarine circulation patterns,* (1955).

Ralston, D. K., W. R. Geyer, and J. A. Lerczak, *Structure, variability, and salt flux in a strongly forced salt wedge estuary,* Journal of Geophysical Research: Oceans **115** (2010).

Ralston, D. K., W. R. Geyer, and J. C. Warner, *Bathymetric controls on sediment transport in the Hudson River estuary: lateral asymmetry and frontal trapping,* Journal of Geophysical Research: Oceans **117** (2012).

Ralston, D. K., and M. T. Stacey, *Longitudinal dispersion and lateral circulation in the intertidal zone,* Journal of Geophysical Research: Oceans **110** (2005).

Schulz, E., H. M. Schuttelaars, U. Gräwe, and H. Burchard, *Impact of the depth-to-width ratio of periodically stratified tidal channels on the estuarine circulation,* Journal of Physical Oceanography **45**, 2048–2069 (2015).

Schuttelaars, H. M., V. N. de Jonge, and A. Chernetsky, *Improving the predictive power when modelling physical effects of human interventions in estuarine systems,* Ocean & Coastal Management **79**, 70–82 (2013).

Scully, M. E., and C. T. Friedrichs, *The influence of asymmetries in overlying stratification on near-bed turbulence and sediment suspension in a partially mixed estuary,* Ocean Dynamics **53**, 208-219 (2003).

Simpson, J. H., J. Brown, J. Matthews, and G. Allen, *Tidal straining, density currents, and stirring in the control of estuarine stratification,* Estuaries **13**, 125–132 (1990).

Smith, R., *Long-term dispersion of contaminants in small estuaries,* Journal of Fluid Mechanics **82**, 129–146 (1977).

Sommerfield, C. K., and K.-C. Wong, *Mechanisms of sediment flux and turbidity maintenance in the Delaware estuary,* Journal of Geophysical Research: Oceans **116** (2011).

Stone, R., *Three Gorges Dam: into the unknown,* Science **321**, 628–632 (2008).

de Swart, H. E., and J. Zimmerman, *Morphodynamics of tidal inlet systems,* Annual review of fluid mechanics **41**, 203–229 (2009).

Talke, S. A., H. E. de Swart, and H. M. Schuttelaars, *Feedback between residual circulations and sediment distribution in highly turbid estuaries: an analytical model,* Continental Shelf Research **29**, 119–135 (2009).

Toffolon, M., and H. H. Savenije, *Revisiting linearized one-dimensional tidal propagation,* Journal of Geophysical Research: Oceans **116** (2011).

Valle-Levinson, A., *Contemporary issues in estuarine physics* (Cambridge University Press, 2010).

Valle-Levinson, A., K.-C. Wong, and K. M. Lwiza, *Fortnightly variability in the transverse dynamics of a coastal plain estuary,* Journal of Geophysical Research: Oceans **105**, 3413–3424 (2000).

Winant, C. D., *Three-dimensional residual tidal circulation in an elongated, rotating basin,* Journal of Physical Oceanography **38**, 1278–1295 (2008).

Winterwerp, J. C., *Fine sediment transport by tidal asymmetry in the high-concentrated Ems River: indications for a regime shift in response to channel deepening,* Ocean Dynamics **61**, 203–215 (2011).

Wong, K.-C., *On the nature of transverse variability in a coastal plain estuary,* Journal of Geophysical Research: Oceans **99**, 14209–14222 (1994).

Woodruff, J. D., W. R. Geyer, C. K. Sommerfield, and N. W. Driscoll, *Seasonal variation of sediment deposition in the Hudson River estuary,* Marine Geology **179**, 105–119 (2001).

Yang, Z.-S., H.-J. Wang, Y. Saito, J. Milliman, K. Xu, S. Qiao, and G. Shi, *Dam impacts on the Changjiang (Yangtze) River sediment discharge to the sea: The past 55 years and after the Three Gorges Dam,* Water Resources Research **42** (2006).

Zhang, W., X. Ruan, J. Zheng, Y. Zhu, and H. Wu, *Long-term change in tidal dynamics and its cause in the Pearl River Delta, China,* Geomorphology **120**, 209–223 (2010).

Chapter 2

Salt dynamics in well-mixed estuaries: importance of advection by tides

Understanding salt dynamics is important to adequately model salt intrusion, baroclinic forcing and sediment transport. In this chapter, the importance of the residual salt transport due to tidal advection in well-mixed tidal estuaries is studied. The water motion is resolved in a consistent way with a width-averaged analytical model, coupled to an advection-diffusion equation describing the salt dynamics. The residual salt balance obtained from the coupled model shows that the seaward salt transport driven by river discharge is balanced by the landward salt transport due to tidal advection and horizontal diffusion. It is found that the tidal advection behaves as a diffusion process, and this contribution is named tidal advective diffusion. *The horizontal diffusion parameterizes processes not explicitly resolved in our model, and is called the* prescribed diffusion. *The tidal advective diffusion results from the correlation between the tidal velocity and salinity, and can be explicitly calculated with the dominant semi-diurnal water motion. The sensitivity analysis shows that tidal advective diffusivity increases with increasing bed roughness and decreasing vertical eddy viscosity. Furthermore, tidal advective diffusivity reaches its maximum with moderate water depth, and moderate convergence length. The relative importance of tidal advective diffusion is investigated using the residual salt balance, with the prescribed diffusion coefficient obtained from the measured salinity field. The tidal advective diffusion dominates the residual salt transport in the Scheldt estuary, and other processes significantly contribute to the residual salt transport in the Delaware estuary and the Columbia estuary.* [1]

---

[1] This chapter is based on:
Wei, X., Schramkowski, G.P., Schuttelaars, H.M., 2016. Salt dynamics in well-mixed estuaries: importance of advection by tides. *Journal of Physical Oceanography*, **46**(5), pp.1457-1475.

2.1 Introduction

The spatial and temporal variations of salinity significantly influence residual water motion through the gravitational and tidal straining circulation (Burchard *et al.* 2011, Geyer and MacCready 2014), thus affecting both tidal and residual transport of sediment, pollutants and other waterborne materials. Hence, a good understanding of salt dynamics is critical to simulating, forecasting and controlling salt intrusion in estuaries, for example, to maintain sufficient fresh-water supply in deltas.

The salinity structure in tidal estuaries is maintained by the competing influences of river flow which tends to drive salt water seaward, the gravitational circulation which tends to drive salt water landward, and a down-gradient salt flux due to shear dispersion, tidal pumping and other processes (MacCready 2004). To identify different driving processes for the estuarine salt flux, many researchers decomposed the current and salinity fields (spatially and temporally) using both short term and long term time series of data (Fischer 1972, Hughes and Rattray 1980, Bowen and Geyer 2003, Lerczak *et al.* 2006). However, as the results strongly depend on the methods of decomposition (Rattray and Dworski 1980), it is difficult to get insight into physical mechanisms resulting in the residual salt transport from various decomposition methods.

The pursuit of theoretically identifying transport processes in flow dates back to the 1950s (Taylor 1953, 1954), when they resolved contaminant dispersion in a straight circular tube under a steady pressure gradient. To identify the main salt transport processes in estuaries, many analytical models have been developed (Hansen and Rattray 1965, MacCready 2004). After tidally averaging all the physical quantities, their model results highlight the significant contribution of gravitational circulation to residual salt transport. To assess the tidal contribution to salt transport, McCarthy (1993) developed a coupled model of the tidal water motion and salinity at the tidal time-scale for well-mixed estuaries. There, the residual salt transport due to river discharge is balanced by the transport resulting from tidal oscillatory dispersion, and horizontal diffusive buoyancy transport.

In this chapter, the salt dynamics in well-mixed estuaries will be investigated at the tidal time-scale, extending the model from McCarthy (1993). We will focus on the tidal oscillatory dispersion contribution to the residual salt transport, which is parameterized as an along-channel diffusivity in classical theories (Geyer and MacCready 2014), and will be called the tidal advective diffusion in this chapter. The main contribution of this chapter is to show the sensitivity of the tidal advective diffusion to friction parameters and estuarine shape, and its relative importance to the residual salt transport in natural estuaries.

The chapter is structured as follows: section 2.2 introduces the width-averaged model, coupling hydrodynamics with salt dynamics; the solution method is introduced in section 2.3. Section 2.4.1 discusses the sensitivity of the tidal advective diffusivity to varying friction parameters and estuarine shape. In section 2.4.2, the relative importance of tidal advective diffusion to the residual salt transport is studied for three estuaries, i.e., the Delaware estuary, the Scheldt estuary and the Columbia estuary. In section 2.5, the sensitivity of the tidal advective diffusivity to model parameters is explained and discussed, followed by a discussion of other important salt transport processes and the model limitations. Conclusions are drawn in section 2.6.

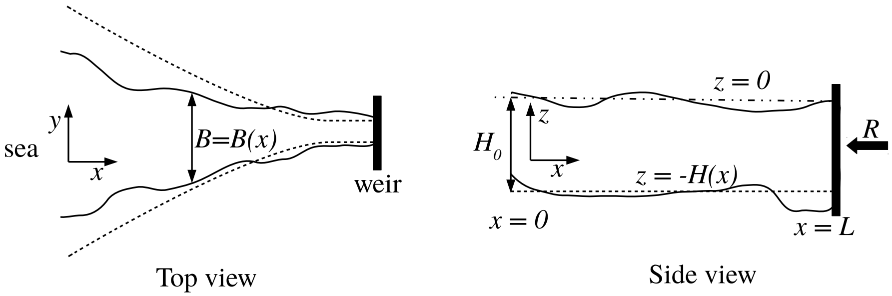

Figure 2.1: The top view and the side view of the estuary, with x the longitudinal coordinate positive in the landward direction, y the transverse coordinate, and z the vertical coordinate positive in the upward direction. Here $H(x)$ is the water depth of the estuary and $B = B(x)$ the estuarine width. H_0 is the estuarine depth at the mouth. R is the river discharge from upstream. The dashed lines represent an estuary with an exponentially converging width and a horizontal bed, which is used for parameter sensitivity study.

2.2 Model description

To investigate the residual along-channel salt transport for estuaries that are tidally dominated and well-mixed, the approach taken by McCarthy (1993) is followed. However, a different expression for the tidal salinity component is obtained by considering the tide-averaged salinity as a real number instead of a complex number (see Eq. (2.15) and appendix 2.C for details), a different seaward boundary condition is used, and a weir is prescribed at the landward side. Furthermore, the model is extended for estuaries with an arbitrary depth and width (see Fig. 2.1).

The water motion is described by the width-averaged continuity equation, and the longitudinal momentum equation,

$$\frac{\partial u}{\partial x} + \frac{\partial w}{\partial z} + \frac{1}{B}\frac{dB}{dx}u = 0, \tag{2.1}$$

$$\frac{\partial u}{\partial t} + u\frac{\partial u}{\partial x} + w\frac{\partial u}{\partial z} = -\frac{g}{\rho_c}\int_z^{\eta}\frac{\partial \rho}{\partial x}dz - g\frac{\partial \eta}{\partial x} + \frac{\partial}{\partial z}\left(A_v\frac{\partial u}{\partial z}\right). \tag{2.2}$$

Here t denotes time, u and w denote the longitudinal and vertical velocity components, η the free surface elevation, ρ_c the background density taken to be 1000 kg m^{-3}, ρ the along-channel density and g the acceleration of gravity. The vertical eddy viscosity is denoted by A_v, which is assumed to be constant both in time and space.

The boundary conditions at the free surface (z=η) are the kinematic and stress-free boundary conditions:

$$w = \frac{\partial \eta}{\partial t} + u\frac{\partial \eta}{\partial x} \quad \text{and} \quad A_v\frac{\partial u}{\partial z} = 0. \tag{2.3}$$

At the bottom ($z = -H(x)$), the normal water flux vanishes,

$$w = -\frac{dH}{dx}u. \tag{2.4}$$

A partial slip condition is prescribed using a linearized bed stress (Schramkowski and de Swart 2002, Chernetsky *et al.* 2010), defined at ~1 m just above the real bed (Schramkowski *et al.* 2010),

$$A_v \frac{\partial u}{\partial z} = su, \tag{2.5}$$

where the slip parameter (or bottom friction parameter) s, depending on the bed roughness, is assumed to be constant both in time and space. In general, s can vary from zero in frictionless cases (free-slip) to large values in strongly frictional cases (no-slip).

The water motion is driven by a prescribed semi-diurnal tidal elevation (M_2) at the entrance ($x = 0$),

$$\eta(t,0) = a_{M_2} \cos(\sigma t), \tag{2.6}$$

where a_{M_2} is the constant amplitude of the M_2 tidal constituent, and σ the M_2 tidal frequency.

At the weir ($x = L$), a constant river discharge R is prescribed,

$$B(L) \int_{-H}^{\eta(t)} u(L,z,t) dz = -R. \tag{2.7}$$

The density ρ is assumed to depend only on salinity, and follows from the linear equation of state: $\rho = \rho_c(1 + \beta_s S)$, with $\beta_s = 7.6\times10^{-4}$ psu^{-1}. Here S is the width-averaged salinity, that is obtained from solving

$$\frac{\partial S}{\partial t} + u\frac{\partial S}{\partial x} + w\frac{\partial S}{\partial z} = \frac{\partial}{\partial x}\left(K_h \frac{\partial S}{\partial x}\right) + K_h \frac{1}{B}\frac{dB}{dx}\frac{\partial S}{\partial x} + \frac{\partial}{\partial z}\left(K_v \frac{\partial S}{\partial z}\right). \tag{2.8}$$

Here K_h and K_v are the longitudinal and vertical eddy diffusivity coefficients, respectively, both assumed to be constant in time and space. The vertical eddy diffusivity K_v is assumed to be equal to the vertical eddy viscosity A_v, which varies from small values in strongly-stratified cases to large values in well-mixed cases.

Instead of prescribing a constant background salinity and a zero background salinity gradient at the estuarine mouth as required by McCarthy (1993), only the tidally averaged salinity at the estuarine mouth is prescribed to be a constant S_m in this model,

$$\bar{S} = S_m \qquad \text{at } x = 0. \tag{2.9}$$

Here the overbar ($^-$) indicates tidally averaged quantities. It is required that the residual salt transport vanishes at the weir,

$$\overline{\int_{-H}^{\eta} \left(-uS + K_h \frac{\partial S}{\partial x}\right) dz} = 0 \qquad \text{at } x = L. \tag{2.10}$$

Furthermore, the salt flux through the sea surface and the bottom has to vanish:

$$K_v \frac{\partial S}{\partial z}\bigg|_{z=\eta} = K_v \frac{\partial S}{\partial z}\bigg|_{z=-H} = 0. \tag{2.11}$$

2.3 Perturbation method

The system of equations, given by Eqs. (2.1)-(2.11), will be solved using an asymptotic approximation of all physical variables with a small parameter ε, the ratio of the M_2 tidal amplitude to the water depth at the estuarine entrance (McCarthy 1993, Chernetsky *et al.* 2010). In this procedure, a scaling analysis is first used to make the equations dimensionless. Next, the various terms in the governing equations are ordered with respect to ε. As a next step, the physical variables are asymptotically expanded in ε,

$$\Phi \quad = \Phi_0 + \varepsilon\Phi_1 + \varepsilon^2\Phi_2 + ... \tag{2.12}$$

with Φ any of the physical variables (η, u, w, S). The subscript 0 denotes the leading order, 1 the first order, and so on. Finally, terms at the same order of ε are collected in the dimensionless governing equations, and are required to balance. This results in a system of dimensional equations at each order of ε (see appendix 2.A for details), which can be solved separately.

To obtain the leading order salinity distribution and assess the importance of residual salt transport by the tidal buoyancy contribution, the leading order water motion has to be solved, together with the leading order and first order salinity equation, and the depth-integrated second order salinity equation. The leading order hydrodynamic equations and corresponding solutions for rectangular basins and exponentially convergent estuaries are presented by Ianniello (1979) and Chernetsky *et al.* (2010), and for estuaries with an arbitrary geometry in appendix 2.B.

The salinity equation in leading order reads

$$\frac{\partial S_0}{\partial t} = K_v \frac{\partial}{\partial z}\left(\frac{\partial S_0}{\partial z}\right), \tag{2.13}$$

which, together with the boundary condition (2.11), yields a steady, vertically homogeneous unknown background salinity field $S_0 = S_0(x)$. Here the leading order salinity is taken to be real. This is different from McCarthy (1993), who allows the leading order density field to be a complex quantity (for a discussion see appendix 2.C). The salinity equation at the first order reads

$$\frac{\partial S_1}{\partial t} + u_0 \frac{dS_0}{dx} = K_v \frac{\partial^2 S_1}{\partial z^2}. \tag{2.14}$$

Since S_0 is a function of x only, the salinity at first order S_1 can be written as

$$S_1 = \Re\left\{\hat{S}_1 e^{i\sigma t}\right\}, \qquad \text{with } \hat{S}_1 = \frac{d\hat{\eta}_0}{dx}\frac{dS_0}{dx} S_z(x,z), \tag{2.15}$$

and $\hat{S}_1$ is the complex amplitude of the first order salinity. Solutions of $S_z(x,z)$ can be obtained analytically from Eq. (2.14) for estuaries of any bathymetry $H(x)$ (see appendix 2.C).

Finally, the tidally averaged, and vertically integrated $O(\varepsilon^2)$ salinity equation is derived,

$$-\frac{d}{dx}B(x)\int_{-H(x)}^{0} \overline{S_1 u_0}\, dz + \frac{d}{dx}B(x)\int_{-H(x)}^{0} K_h \frac{dS_0}{dx} dz = -R\frac{dS_0}{dx}. \tag{2.16}$$

Given a horizontal eddy diffusivity K_h, the only unknown in Eq. (2.16) is dS_0/dx. Thus, the tidally averaged salinity profile S_0, consistent with the tidal motion, river discharge and geometrical parameters can be obtained. Note that the contribution due to the width-averaged and depth-integrated exchange flow induced by gravitational circulation is resolved but absent in Eq. (2.16). This is because the width-averaged and depth-integrated residual Eulerian flow $\int_{-H}^{0} \bar{u}_1 dz$, together with the Stokes drift $\eta_0 u_0|_{z=0}$, equals the width-averaged river discharge $-R/B$ (McCarthy 1993). The insignificance of gravitational circulation in well-mixed systems is in agreement with MacCready and Geyer (2010), and has been observed in the North Inlet where almost no gravitational circulation is found by Kjerfve (1986).

Nevertheless, the absence of gravitational circulation in the width-averaged and depth-integrated residual salt balance in this model does not imply that gravitational circulation does not contribute to residual salt transport. In well mixed estuaries, contributions of exchange flows due to gravitational circulation and other processes can result in a significant transport of salinity due to variations in the lateral direction. In this model, these contributions are not resolved explicitly but parametrized in the prescribed diffusion.

By substituting the solutions for S_1 and u_0 into (2.16), it yields

$$\frac{d}{dx}\left\{\left(-\frac{1}{2}\Re\left(\int_{-H(x)}^{0}\hat{S}_1\hat{u}_0^* dz\right)\left(\frac{dS_0}{dx}\right)^{-1}+K_h H(x)\right)\frac{dS_0}{dx}\right\}=-\frac{R}{B(x)}\frac{dS_0}{dx}, \tag{2.17}$$

with $\hat{u}_0^*$ the complex conjugate of $\hat{u}_0$. Integrating Eq. (2.17) with respect to x, and using the condition that no net residual salt transport is allowed at the weir, it yields

$$(K_h^{\text{adv}}+K_h)\frac{dS_0}{dx}=-\frac{R}{H(x)B(x)}S_0. \tag{2.18}$$

The tidally averaged transport of salinity by tidal advection behaves as a diffusive process, with K_h^{adv} the corresponding diffusivity coefficient given by

$$K_h^{\text{adv}}=-\frac{1}{2}\Re\left\{\frac{1}{H(x)}\int_{-H}^{0}\hat{S}_1\hat{u}_0^* dz\right\}\left(\frac{dS_0}{dx}\right)^{-1}. \tag{2.19}$$

Hereafter this diffusive contribution will be called *tidal advective diffusion*. The diffusive contribution parametrized by the horizontal eddy diffusivity K_h will be called the *prescribed diffusion*. The tidal advective diffusivity K_h^{adv} measures the contribution of residual salt transport due to tidal advective diffusion, called the tidal buoyancy contribution by McCarthy (1993). Equation (2.19) shows that the tidal advective diffusion originates from the temporal correlation between the tidal velocity and salinity, and can be calculated explicitly with the given M_2 tidal information. On the other hand, K_h is necessary to parameterize all unresolved processes of residual salt transport in the width-averaged model (the most important unresolved processes are discussed in section 2.5.5). Since the processes are not resolved, K_h has to be prescribed.

After solving (2.18), the leading order salinity is easily obtained as

$$S_0(x)=S_m e^{-\int_0^x f_s dx}, \text{ with } f_s=\frac{R}{H(x)B(x)}\frac{1}{K_h+K_h^{\text{adv}}}. \tag{2.20}$$

2.4 Results

Substituting the solutions of u_0 and S_1 (see Eqs. (2.57) and (2.58)) into Eq. (2.19) yields

$$K_h^{\text{adv}} = -\frac{1}{2}\Re\left\{\frac{1}{H(x)}\left|\frac{d\hat{\eta}_0}{dx}\right|^2 \int_{-H(x)}^{0} S_z(x,z)U^*(x,z)dz\right\}. \tag{2.21}$$

Equation (2.21) suggests that K_h^{adv} is proportional to $|d\hat{\eta}_0/dx|$ squared which is proportional to a_{M_2} (see Eq. (2.50)), and is independent of river discharge. The dependence of K_h^{adv} on the slip parameter (s), vertical eddy viscosity and diffusivity (A_v), estuarine depth (H) and convergence length (L_b) is more complex, as can be seen from Eqs. (2.57), (2.50) and (2.61). Therefore, the sensitivity of K_h^{adv} to s, A_v, H and L_b are investigated in section 2.4.1. In Section 2.4.2, the importance of tidal advective diffusion to residual salt transport is studied using field data for three estuaries, i.e., the Delaware, Scheldt and Columbia estuaries. To justify the well-mixed assumption, the top-to-bottom salinity difference ($\triangle S$) is required to be at least one order of magnitude smaller than the bottom salinity (S_{bottom}) in the region of salt intrusion, $\triangle S/S_{\text{bottom}} \leq O(\varepsilon)$. The Delaware estuary is considered to be well-mixed because the vertical difference of salinity is much smaller than the salinity at the bottom in most of the salt intrusion region (Garvine *et al.* 1992). The Scheldt estuary is well-mixed especially in the seaward part, with only a small local vertical salinity gradient (Peters and Wollast 1976). The stratification in the Columbia estuary is weak in the studied period of 24-26 October in 1980, during spring tides with low river discharges (Jay and Smith 1990b). These three different estuaries are also representative for systems with different bathymetry and geometry profiles. The geometry of the Delaware estuary can be approximated with a horizontal bed and an exponentially varying width with a constant convergence length. The geometry of the Scheldt estuary can be captured by splitting the estuary into two sections using a different convergence length per section, along with a significant bathymetric variations along the channel. In contrast, both the geometry and bathymetry of the Columbia estuary show complex variations.

2.4.1 Parameter sensitivities

In this section, we focus on idealized estuaries with a horizontal bed, and an exponentially decreasing width (see dashed lines in Fig. 2.1) which is given by

$$B(x) = B_0 e^{-\frac{x}{L_b}}, \tag{2.22}$$

with B_0 the estuarine width at the entrance, and L_b the estuarine convergence length. The estuarine convergence length L_b represents the along-channel change of the estuarine geometry: small values of L_b correspond to strongly convergent estuaries, while for L_b very large, the estuary becomes prismatic. The default parameter values for the sensitivity analysis are representative for the Scheldt estuary, as listed in Table 2.1.

Table 2.1: Default values of model parameters.

Variable	a_{M_2}	L	H	L_b	s	A_v
Unit	m	km	m	km	m s^{-1}	m^2 s^{-1}
Value	2	200	10	50	0.01	0.008

Sensitivity of K_h^{adv} to s and A_v

In Fig. 2.2a, the sensitivity of K_h^{adv} to the slip parameter s is shown. It reveals that when increasing s from 0.0001 m s^{-1} to 0.1 m s^{-1}, K_h^{adv} increases from almost zero to more than 100 m^2 s^{-1}, and K_h^{adv} becomes almost independent of s for large values of s.

The tidal advective diffusivity K_h^{adv} is very sensitive to the vertical eddy viscosity A_v, as shown in Fig. 2.2b. The largest value of $K_h^{\text{adv}}(\sim 4\times10^4$ m^2 $s^{-1})$ is found when A_v is about 10^{-3} m^2 s^{-1}, while K_h^{adv} is much smaller ($K_h^{\text{adv}} \sim 10^2$ m^2 s^{-1}) for default A_v (see the dashed line in Fig. 2.2b). Larger values of A_v result in smaller magnitudes of K_h^{adv}. Notice that this thesis focuses on well-mixed estuaries, hence A_v cannot be too small to ensure that the top-to-bottom salinity difference is not too large ($\triangle S/S_{\text{bottom}} \le O(\varepsilon)$). Generally, the well-mixed assumption can be justified by requiring an approximate balance between the vertical mixing of salinity and its rate of change, as suggested by Eq. (2.13). Hence, A_v is constrained by $A_v/\sigma H_0^2 \gtrsim O(1)$, scaling t and z with the tidal period σ^{-1} and the water depth H_0, respectively. With the default values from Table 2.1, $A_v \gtrsim 10^{-2}$ m^2 s^{-1} is required for the estuary to be well-mixed.

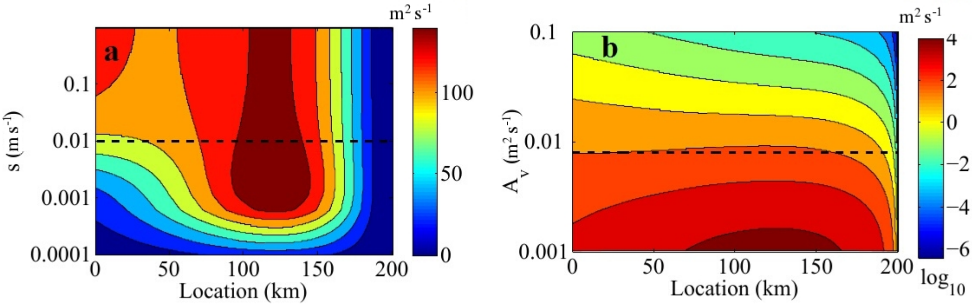

Figure 2.2: The tidal advective diffusivity K_h^{adv} with varying s and A_v. Here the dashed lines represent the default values for the slip parameter ($s = 0.01$ m s^{-1}) and vertical eddy viscosity ($A_v = 0.008$ m^2 s^{-1}). The y axis is logarithmic in both figures.

To explain the observed parameter dependency of K_h^{adv} (calculated using the depth-integrated residual salt transport), the residual salt flux due to tidal advective diffusion (hereafter it is called the tidal advective salt flux, abbreviated as $TASF$) at each location (x, z) is calculated for different s and A_v, using a constant residual salinity gradient

$$\frac{dS_0}{dx} = -2\times10^{-4} \text{ psu m}^{-1}, \tag{2.23}$$

which is representative for the Scheldt estuary. The residual tidal advective salt flux $TASF$ at a certain location (x,z) is given by

$$\frac{1}{2}\Re\left\{\hat{S}_1(x,z)\hat{u}_0^*(x,z)\right\} = \frac{1}{2}|\hat{S}_1||\hat{u}_0|\cos(\phi_u - \phi_s). \tag{2.24}$$

Here $S_1 = |\hat{S}_1|e^{-i\phi_s}$, $\hat{u}_0^* = |\hat{u}_0|e^{i\phi_u}$, with $|\cdot|$ the absolute values of the tidal salinity S_1 and velocity u_0, and ϕ_u, ϕ_s are the phases of the complex amplitudes of u_0 and S_1. Equation (2.24) shows that $TASF$ depends not only on the magnitudes of u_0 and S_1, but also on their phase difference ($\triangle\phi = \phi_s - \phi_u$). Integrating $TASF$ from bottom to top gives the residual tidal advective salt transport at location x. In case that $\hat{S}_1$ and $\hat{u}_0$ are exactly out of phase ($\triangle\phi = 90°$), there is no residual salt transport due to tidal advective diffusion. This will be discussed in more detail in Section 2.5.

In essence, $TASF$ is resulting from the temporal correlation between u_0 and S_1. In frictionless estuaries, the two-dimensional flow behaves like a one-dimensional flow (vertically uniform) with no turbulence or shear generated (see Figs. 2.3a, b). In this case, the peak tidal velocities proceed large S_1 and small S_1 by exactly 90° (see Fig. 2.3b), and no tidal advective salt transport is produced after one tidal cycle as the salt imported into the estuary during flood is exported out during ebb. In natural estuaries with bed friction, the bottom-induced turbulence is transferred throughout most of the water column, resulting in a vertically varying u_0 and S_1 (see Figs. 2.3c-d). In this case, the magnitude of u_0 near the top exceeds that near the bottom (see Fig. 2.3c), because currents in upper layers experience less resistance from the bed friction. Meanwhile, the peak tidal velocities near the bottom leads those near the top (see Fig. 2.3d), owing to larger shear stress near the bottom. Therefore, since S_1 is mainly forced by u_0 as suggested by Eq. (2.14), S_1 becomes larger near the top than the bottom, and large S_1 at upper layers leads that at lower layers. As a result, S_1 slightly catches up with u_0 in the upper layer ($\triangle\phi < 90°$), so that large S_1 coincides more with flood velocities and small S_1 coincides more with ebb velocities, resulting in a landward $TASF$ in the upper layer. On the other hand, S_1 lags more behind u_0 in the lower layer ($\triangle\phi > 90°$), thus large S_1 coincides more with ebb velocities and small S_1 coincides more with flood velocities, resulting in a seaward $TASF$ in the lower layer. Since the amplitudes of u_0 and S_1 are larger in the upper layers than the bottom, the landward $TASF$ in upper layers exceeds the seaward $TASF$ near the bottom, resulting in a net landward salt transport integrated over the depth. This mechanism has been observed by Bowen and Geyer (2003).

Slip parameter

In Fig. 2.4 (left column), $TASF$ throughout the estuary is shown for $s = 0.1$ m s^{-1}, 0.01 m s^{-1}, and 0.001 m s^{-1}, respectively. Landward $TASF$ is found at the top and seaward $TASF$ at the bottom for all s. It means that tidal advective diffusion drives salt landward in the upper layer and transports salt seaward near the bottom. This result confirms the previous analysis, and is consistent with the measurements in the Hudson estuary (Bowen and Geyer 2003), where a landward oscillatory salt transport is found near the surface, and a seaward (or near zero) transport at the bottom.

The magnitude of $TASF$ increases significantly when s decreases from 0.1 to 0.001 m s^{-1}. Concerning $|\hat{S}_1||\hat{u}_0|$, Fig. 2.4 (middle column) shows its largest values are found

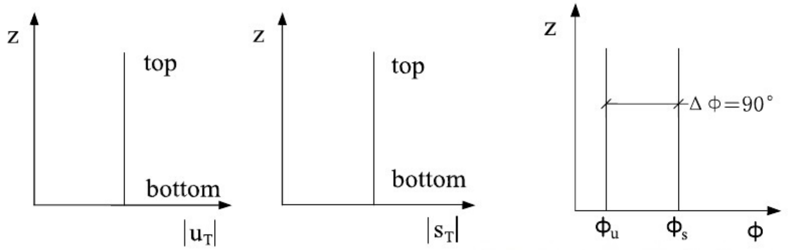

(a) Amplitudes in frictionless case

(b) Phases in frictionless case

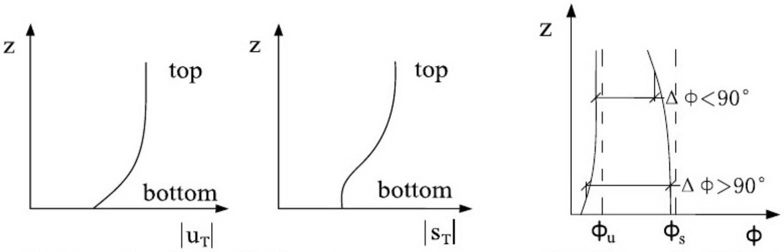

(c) Amplitudes in frictional case

(d) Phases in frictional case

Figure 2.3: The amplitudes (a, c) and phases (b, d) of the tidal velocity u_T and salinity s_T in frictionless (a, b) and frictional cases (c, d). In this model, M_2 tidal constituent is considered, hence, $u_T = u_0$ and $s_T = S_1$.

near the surface, decreasing towards the bottom. With s decreasing from 0.1 m s^{-1} to 0.001 m s^{-1}, $|\hat{S}_1||\hat{u}_0|$ increases at all depths, and becomes vertically more homogeneous.

For estuaries with a horizontal bed, ϕ_u and ϕ_s are constant along the channel, hence $\triangle\phi$ only varies in the vertical direction. For all the three slip parameters, $\triangle\phi$ is smaller than 90° at the top and larger than 90° near the bottom, consistent with Fig. 2.3d. This results in a landward tidal advective salt transport in the upper layer and seaward transport near the bottom. The right column of Fig. 2.4 also shows that $\triangle\phi$ becomes closer to 90° at all depths for decreasing s, with $\cos(\phi_u - \phi_s)$ getting smaller. This observation, together with the fact that $|\hat{S}_1||\hat{u}_0|$ becoming more vertically uniform, leads to a smaller K_h^{adv} for decreasing s (see Fig. 2.2a), even though the magnitude of $TASF$ increases at all depths.

Eddy viscosity

Figure 2.5 shows $TASF$, $|\hat{S}_1||\hat{u}_0|$ and $\triangle\phi$ for two different values of the vertical eddy viscosity: $A_v = 0.03$ m^2 s^{-1} and 0.001 m^2 s^{-1}. The tidal advective salt flux increases significantly when A_v decreases from 0.03 to 0.001 m^2 s^{-1} (see Fig. 2.5, left column). This increase corresponds well with the strong increase of K_h^{adv}, as can be seen in Fig. 2.2b. Figure 2.5, middle column, displays a strong increase of $|\hat{S}_1||\hat{u}_0|$ for decreasing A_v, with $|\hat{S}_1||\hat{u}_0|$ becoming less vertically homogeneous. Furthermore, the maximum values of $|\hat{S}_1||\hat{u}_0|$ move from the mouth to a more landward location. The phase difference $\triangle\phi$ for different values of A_v is shown in the right column of Fig. 2.5. For $A_v = 0.03$ m^2 s^{-1}, $\triangle\phi$ is very close to 90° with a small change from 89° at the top to 92° at the bottom. For

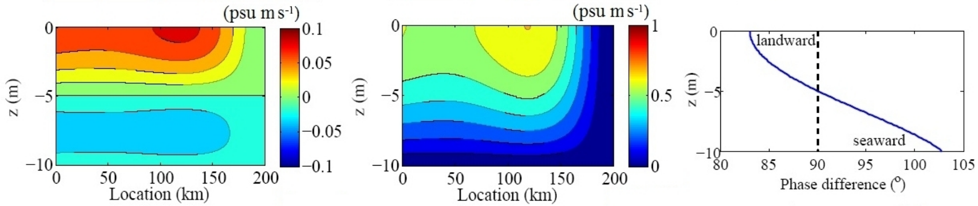

(a) $TASF$ for $s = 0.1$ m s^{-1} (b) $|\hat{S}_1||\hat{u}_0|$ for $s = 0.1$ m s^{-1} (c) $\Delta\phi$ for $s = 0.1$ m s^{-1}

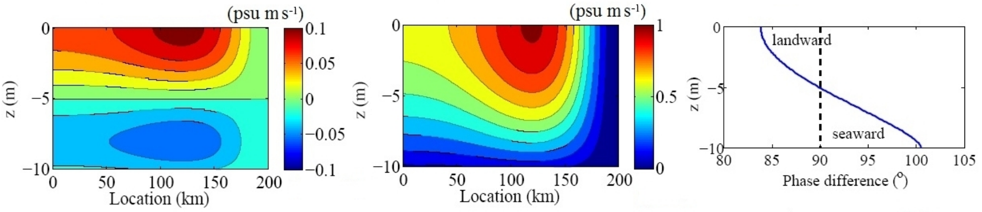

(d) $TASF$ for $s = 0.01$ m s^{-1} (e) $|\hat{S}_1||\hat{u}_0|$ for $s = 0.01$ m s^{-1} (f) $\Delta\phi$ for $s = 0.01$ m s^{-1}

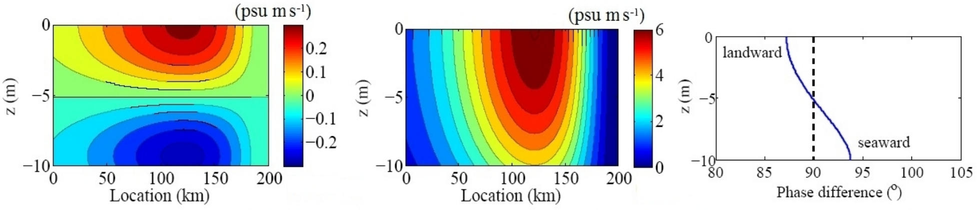

(g) $TASF$ for $s = 0.001$ m s^{-1} (h) $|\hat{S}_1||\hat{u}_0|$ for $s = 0.001$ m s^{-1} (i) $\Delta\phi$ for $s = 0.001$ m s^{-1}

Figure 2.4: $TASF$, $|\hat{S}_1||\hat{u}_0|$, and $\Delta\phi$ for different values of slip parameter, $s = 0.1$ m s^{-1} (top row), 0.01 m s^{-1} (middle row), and 0.001 m s^{-1} (bottom row). Note that different color scales are used for $TASF$ and $|\hat{S}_1||\hat{u}_0|$ for $s = 0.001$ m s^{-1}. The dashed line in the right column shows the phase difference of $\Delta\phi = 90°$.

$A_v = 0.001$ m^2 s^{-1}, $\Delta\phi$ strongly deviates from 90°, varying from 80° at the top to 135° at the bottom. The magnitude of $\cos(\phi_u - \phi_s)$ is much larger in the latter case. Therefore, the significant increase of K_h^{adv}, is due to the overall effects of increasing magnitude and larger vertical variations of $|\hat{S}_1||\hat{u}_0|$, together with the altered $\Delta\phi$.

Sensitivity of K_h^{adv} to H and L_b

Since the water motion is strongly affected by estuarine geometry and bathymetry (Friedrichs and Aubrey 1994, Lanzoni and Seminara 1998, Prandle 2003), the sensitivity of K_h^{adv} to estuarine depth (H) and convergence length (L_b) is investigated.

The influence of H on K_h^{adv} is shown in Fig. 2.6a. The maximum values for K_h^{adv} are found in estuaries with $H \sim 16$ m, and K_h^{adv} decreases sharply when estuaries become either deeper or shallower. In Fig. 2.6b, the influence of L_b on K_h^{adv} is shown. In most of the estuary, K_h^{adv} first increases when L_b decreases from 1000 km to 40 km, and then

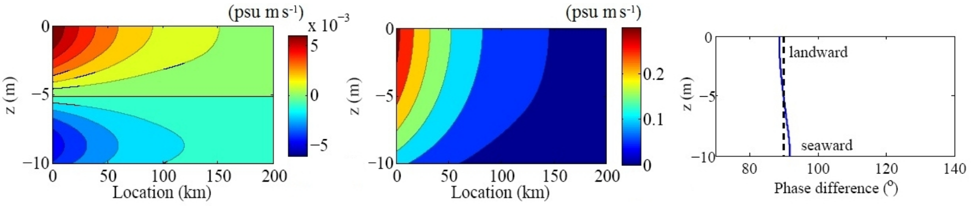

(a) $TASF$ for $A_v = 0.03$ m^2 s^{-1} (b) $|\hat{S}_1||\hat{u}_0|$ for $A_v = 0.03$ m^2 s^{-1} (c) $\Delta\phi$ for $A_v = 0.03$ m^2 s^{-1}

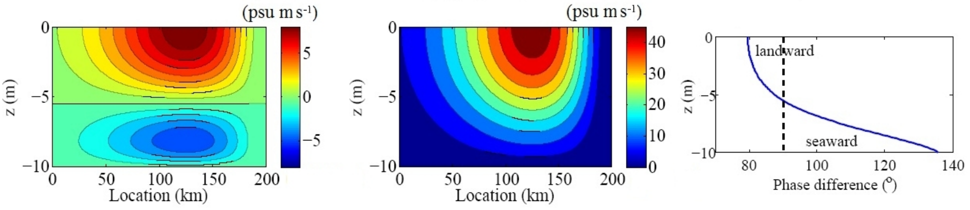

(d) $TASF$ for $A_v = 0.001$ m^2 s^{-1} (e) $|\hat{S}_1||\hat{u}_0|$ for $A_v = 0.001$ m^2 s^{-1} (f) $\Delta\phi$ for $A_v = 0.001$ m^2 s^{-1}

Figure 2.5: $TASF$, $|\hat{S}_1||\hat{u}_0|$, and $\Delta\phi$ for different values of vertical eddy viscosity, $A_v = 0.03$ (the top row), and 0.001 m^2 s^{-1} (the bottom row). Note the color scale differences used in (a), (b), and (d), (e), since $TASF$ and $|\hat{S}_1||\hat{u}_0|$ change magnitude significantly with changing A_v.

decreases when L_b is further decreased from 40 km to 10 km. The change of K_h^{adv} with L_b is very gradual for L_b larger than 100 km, while the change is dramatic for small values of L_b. Near the estuarine mouth, K_h^{adv} monotonically decreases for decreasing L_b. Results in Fig. 2.6 suggest that K_h^{adv} is more sensitive to H than L_b.

It is found that $TASF$ significantly decreases when the estuary becomes very deep, accompanied with a decreasing and vertically more uniform $|\hat{S}_1||\hat{u}_0|$ (plots not shown). Furthermore, $\Delta\phi$ strongly deviates from 90° in deep estuaries but very close to 90° in shallow estuaries. The estuarine convergence length (L_b) influences $TASF$ only through the tidal amplitudes $|\hat{S}_1||\hat{u}_0|$, which increases with L_b till $L_b \sim 50$ km, and then decreases for further increasing L_b. Meanwhile, $\Delta\phi$ does not change with L_b.

2.4.2 Applications

As the tidal advective salt transport varies significantly with model parameters, its importance will be quantified for three estuaries: the Delaware, Scheldt, and Columbia estuaries. The length of these estuaries, and their depth and width profiles are obtained from observations, as are the amplitude and phase of the M_2 sea surface elevation. The friction parameters s and A_v result from calibrating the M_2 sea surface elevation with observations. To this end, the difference between the simulated and observed M_2 tidal elevation in the salt intrusion region is first evaluated using a cost function f_{cost} based on least square fit (Davies and Jones 1996),

$$f_{\text{cost}} = \sum_{i=1}^{i=N} \sqrt{(\Delta\hat{\eta}_i)^2 + 2\hat{\eta}_i^{\text{obs}}\hat{\eta}_i^{\text{mod}}(1-\cos\Delta\Phi_i)} \quad , \tag{2.25}$$

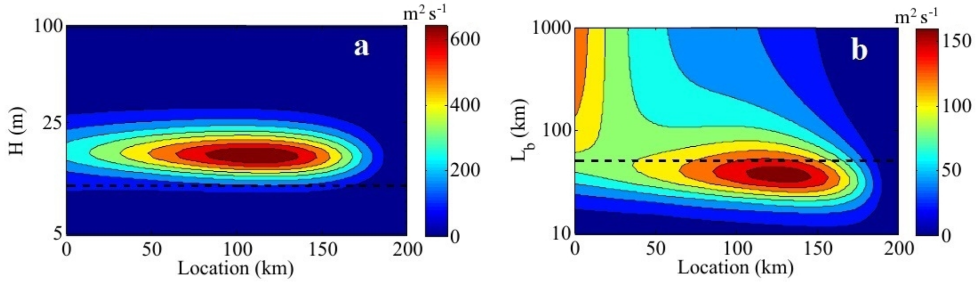

Figure 2.6: K_h^{adv} with varying H and L_b. Here the y axis is logarithmic in both figures.

with $\triangle\hat{\eta}_i = \hat{\eta}_i^{\mathrm{obs}} - \hat{\eta}_i^{\mathrm{mod}}$, $\triangle\Phi_i = \Phi_i^{\mathrm{obs}} - \Phi_i^{\mathrm{mod}}$. Here $\hat{\eta}^{\mathrm{obs}}$ and Φ^{obs} are the observed M_2 tidal amplitude and phase, $\hat{\eta}^{\mathrm{mod}}$ and Φ^{mod} are the simulated M_2 tidal amplitude and phase, and the subscript i indicates the numbering of the observed location. A range of A_v and s values are used in this procedure, with more than one combination of A_v and s producing approximately the same f_{cost} close to the minimum. As a next step, different combinations of A_v and s values are used to calculate the M_2 tidal elevation for the whole estuary, and the combination giving the best fit is selected as the final A_v and s values by visual inspection.

Then, using observed tidally averaged salinity profiles, the total diffusivity

$$K_h^{\mathrm{total}} = K_h + K_h^{\mathrm{adv}} \tag{2.26}$$

can be obtained by applying Eq. (2.18). Since K_h^{adv} can be explicitly calculated, K_h follows directly from $K_h = K_h^{\mathrm{total}} - K_h^{\mathrm{adv}}$. The ratio $r_s = K_h^{\mathrm{adv}} / K_h^{\mathrm{total}}$ is used to quantify the relative importance of the residual salt transport due to tidal advective diffusion.

The Delaware estuary

The geometry of the Delaware estuary can be approximated as an exponentially converging channel with a constant convergence length of $L_b = 42$ km (and $B_0 = 39$ km) and a constant water depth of 8 m (Kuijper and Van Rijn 2011), see blue lines in Fig. 2.7a. The tidal data of the Delaware estuary is taken from Friedrichs and Aubrey (1994). The tidally averaged salinity data for the central part (blue dots in Fig. 2.7b) are obtained from Kuijper and Van Rijn (2011), while the salinity at the entrance (blue dot circled by a red line in Fig. 2.7b) is taken from Garvine *et al.* (1992). Here, the salt intrusion length is about 150 km. The river discharge is taken to be ~72 m^3 s^{-1} (Kuijper and Van Rijn 2011, Savenije 2012). The M_2 sea surface elevation of the Delaware estuary is best fitted with the observed data using $s = 0.039$ m s^{-1} and $A_v = 0.005$ m^2 s^{-1} (see Fig. 2.8a and Table 2.2). In general, the M_2 tidal water levels are well reproduced by the model, with an almost constant M_2 tidal amplitude in the first 150 km and an amplification in the most landward part. The simulated M_2 phase corresponds well with the observed data throughout the Delaware estuary.

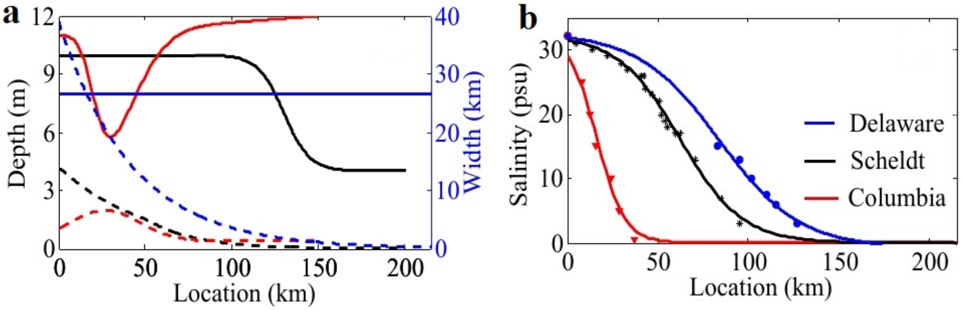

Figure 2.7: (a) The geometry and bathymetry of the Delaware estuary (see blue lines), Scheldt estuary (see black lines), and Columbia estuary (see red lines), with solid lines for water depth and dashed lines for estuarine width. (b) The observed residual salinity (dots) for the three estuaries, together with a fitted hyperbolic tangent profile of salinity for each (solid lines). Different colors represent for different estuaries: blue for the Delaware estuary, black for the Scheldt estuary, and red for the Columbia estuary.

Table 2.2: Model parameters for each estuary from calibration of M_2 tidal data.

Variable	Unit	Columbia	Scheldt	Delaware
a_{M_2}	m	2.05	2	0.75
L	km	150	200	215
R	m^3 s^{-1}	3800	90	72
s	m s^{-1}	0.035	0.0099	0.039
A_v	m^2 s^{-1}	0.0060	0.0085	0.0050

Using these observations, K_h^{adv}, K_h, and K_h^{total} are calculated within the region of salt intrusion (x <150 km), as shown in Fig. 2.8b. The tidal advective diffusivity K_h^{adv} remains approximately 20 m^2 s^{-1} in the seaward reach, and slightly increases to ~ 30 m^2 s^{-1} in the central region. The prescribed diffusivity K_h first decreases from ~180 m^2 s^{-1} at the mouth to 50 m^2 s^{-1} at x = 80 km. Next, it gradually increases to ~70 m^2 s^{-1} in the landward direction. As a result, K_h^{total} decreases from ~200 m^2 s^{-1} at the mouth to about 70 m^2 s^{-1} at x =80 km, and slightly increases landward. The ratio r_s increases from ~0.1 at the estuarine mouth to ~0.3 in the central region (see Fig. 2.8b). This suggests that in the central region of salt intrusion, tidal advective diffusion is an important process but not the dominant one for the residual salt transport in the Delaware estuary.

The Scheldt estuary

The width of the Scheldt estuary can be described by two exponentially converging parts, with a convergence length of about 50 km in the downstream reach (up to 50 km from the mouth), and 28 km in the landward section of the estuary (Kuijper and Van Rijn 2011) (see black dashed line in Fig. 2.7a). The water depth of the Scheldt estuary decreases

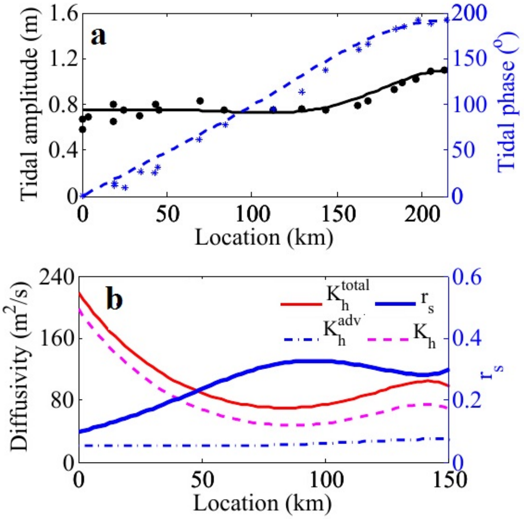

Figure 2.8: (a) The modelled M_2 sea surface amplitude (see black solid line) and phase (blue dashed line) versus the observed M_2 tidal surface amplitude (black dots) and phase (blue stars) in the Delaware estuary. (b) Diffusivity (K_h^{adv}, K_h, and K_h^{total}) and the ratio r_s in the region of salt intrusion.

from 10 m at the seaward side to less than 5 m at the landward side (Savenije and Veling 2005) (see black solid line in Fig. 2.7a). The tidal data is taken from Savenije (1993), and the salinity data from Kuijper and Van Rijn (2011), with a salt intrusion length of ~ 100 km (see black dots and line in Fig. 2.7b) for a river discharge of about 90 m^3 s^{-1} (Savenije 2012).

The M_2 sea surface elevation in the Scheldt estuary is best fitted with the observed data for s = 0.0099 m s^{-1} and A_v = 0.0085 m^2 s^{-1} (see Fig. 2.9a and Table 2.2). In general, the M_2 tidal properties are well reproduced by the model, with an amplification in the first 120 km and an abrupt damping in the landward part. The M_2 phase is slightly overestimated in the seaward part of the Scheldt estuary. Along the Scheldt estuary, K_h^{adv} remains around ~ 10^2 m^2 s^{-1} in the region of salt intrusion (x < 100 km, see Fig. 2.9b). The highest K_h (320 m^2 s^{-1}) is found near the estuarine mouth. It significantly decreases to ~10 m^2 s^{-1} at around x = 60 km, and slightly increases again in the landward direction. The total diffusivity, therefore, decreases from more than 400 m^2 s^{-1} at the mouth to about 100 m^2 s^{-1} at x = 50 km, and then increases gradually. As shown in Fig. 2.9b, the relative contribution of the tidal advective diffusion is higher than 0.50 (with a maximum of 0.7) except in the region close to the estuary mouth and near the end of the salt intrusion. Hence, tidal advective diffusion is a dominant process for residual salt transport in the central salt intrusion region of the Scheldt estuary, whereas the contribution of all other parametrized processes is small.

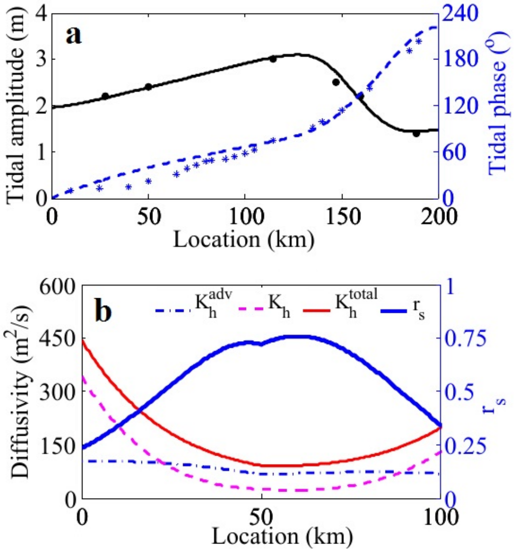

Figure 2.9: (a) The modelled M_2 sea surface amplitude (see black solid line) and phase (blue dashed line) versus the observed M_2 tidal surface amplitude (black dots) and phase (blue stars) in the Scheldt estuary. (b) Diffusivity (K_h^{adv}, K_h, and K_h^{total}) and the ratio r_s in the region of salt intrusion.

The Columbia estuary

For the Columbia estuary, the geometry and the tidal data are taken from Giese and Jay (1989). The width and depth of the Columbia estuary is highly variable (see red lines in Fig. 2.7a). The salt intrusion length is about 40 km (see red dots and line in Fig. 2.7b) according to the observations from Jay and Smith (1990b), with a river discharge of ~ 3800 $\text{m}^3\ \text{s}^{-1}$.

The M_2 sea surface elevation is best matched by the model using $s = 0.035\ \text{m s}^{-1}$ and $A_v = 0.006\ \text{m}^2\ \text{s}^{-1}$ (see Fig. 2.10a and Table 2.2). The M_2 tidal amplitude is reasonably well reproduced while the M_2 phase is slightly underestimated in the landward part of the Columbia estuary. It implies the friction in the landward part of the estuary is underestimated. However, the general M_2 tidal properties are well reproduced, with a small increase of the M_2 tide in the first 10 km and a consistent decrease afterwards.

Giese and Jay (1989) show that in the Columbia estuary, tidal constituents of S_2, K_1, O_1, P_1 and N_2 are all non-negligible compared to M_2, even though the M_2 tidal constituent is most significant. Here, all these contributions are included by linearly adding up their tidal amplitudes, resulting in an equivalent tidal amplitude $a_{M_2}^{\text{eqv}}$. The equivalent tidal frequency is taken to be M_2 tidal frequency. An equivalent tidal amplitude at the entrance $a_{M_2}^{\text{eqv}} = 2.05$ m is used to assess the salt transport contribution of tidal advective diffusion for the Columbia estuary, according to a one-year record by Giese and Jay (1989).

The three diffusion coefficients, K_h^{adv}, K_h and K_h^{total}, and the ratio r_s are shown in Fig. 2.10b. The tidal advective diffusion K_h^{adv} varies from 800 $\text{m}^2\ \text{s}^{-1}$ at the mouth to

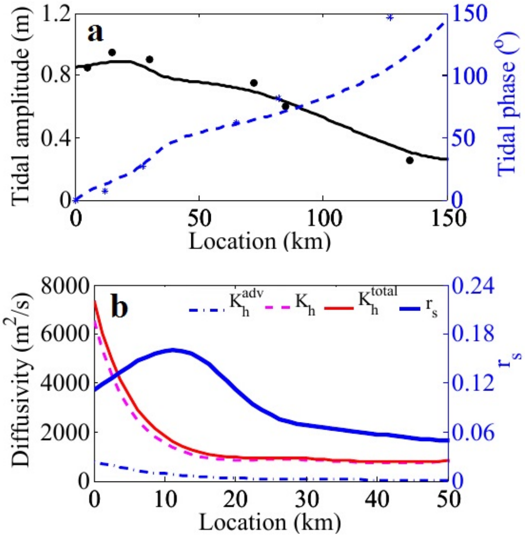

Figure 2.10: (a) The modelled M_2 sea surface amplitude (see black solid line) and phase (blue dashed line) versus the observed M_2 tidal surface amplitude (black dots) and phase (blue stars) in the Columbia estuary. (b) Diffusivity (K_h^{adv}, K_h, and K_h^{total}) and the ratio r_s in the region of salt intrusion.

50 m^2 s^{-1} at the end of salt intrusion. The prescribed diffusion coefficient K_h decreases from 6500 m^2 s^{-1} to 850 m^2 s^{-1}. As a result, K_h^{total} drops from about 7000 m^2 s^{-1} at the mouth to about 900 m^2 s^{-1} at the end of salt intrusion, and the tidal advective diffusion coefficient K_h^{adv} is much smaller than K_h. The relative contribution of the tidal advective diffusion r_s is ~ 0.16 at about $x = 10$ km, which is close to the result of Hughes and Rattray (1980). They found the $\bar{A}(\overline{u_0 S_1})$ is about 0.22 of the total salt transport processes at Clatsop Spit section (~ 10 km away from the estuary mouth) during low discharges. Here u_0 and S_1 are the cross-sectionally averaged tidal velocity and salinity, and $\bar{A}$ the tidally averaged area of the cross-section. The relatively low magnitude of r_s suggests that the lateral processes and lateral variations of longitudinal processes parameterized in the present model are probably significant in the Columbia estuary.

2.5 Discussion

It has been found that the contribution of salt transport by tidal advection acts as a horizontal diffusive process with a diffusivity K_h^{adv}. This diffusivity is similar to the virtual coefficient of diffusion obtained in the classical work of Taylor (1953, 1954). The similarity arises because the cross-sectional mixing time is short, and the effect of horizontal diffusivity is small compared to vertical diffusivity.

The values of A_v obtained for the three estuaries are much smaller than the approximated value using a simple boundary layer approximation for a well-mixed system: $A_v \sim \kappa\sqrt{su}(z + H + z_0)$, with κ the Von Karman constant and z_0 the roughness height. This deviation can be explained by the procedure for calibrating the M_2 tidal surface elevation. As mentioned previously, A_v and s for a real estuary are chosen by minimizing the difference between the simulated and observed M_2 tidal elevation. However, in reality, the observed M_2 tidal elevation is affected by many factors such as wind, lateral processes, asymmetric mixing, and the nonlinear impact of higher harmonics (Jones and Davies 1996), which are not considered in the present width-averaged model. Hence, A_v and s obtained from the calibration procedures are actually effective vertical eddy viscosity and slip parameters, parameterizing all processes unresolved in the model, and they can not be directly related using the above-mentioned simple boundary layer approximation.

In this section, the sensitivity of K_h^{adv} to model parameters will be explained by making an estimate of its magnitude in terms of dimensionless parameters. Substituting the tidal velocity and salinity into Eq. (2.19) yields an estimate of K_h^{adv} (see details in appendix 2.D):

$$K_h^{\mathrm{adv}} \approx \frac{8}{945}\frac{g^2}{\sigma^3}\left|\frac{d\hat{\eta}_0}{dx}\right|^2 |\alpha|^2 \frac{1}{Stk^6}, \tag{2.27}$$

with $\alpha = \left(\cosh(\delta) + \dfrac{i}{\delta s^*}\sinh(\delta)\right)^{-1}$, $s^* = \dfrac{s}{\sigma H}$, $\delta = (1+i)/Stk$ and $Stk = \sqrt{\dfrac{2A_v}{\sigma H^2}}$.

Stk is the Stokes number, defined as the ratio of the frictional depth to the water depth (Souza 2013). Equation (2.27) is derived by assuming a small $|\delta|$ ($< \sqrt{2}$) for well mixed systems (see appendix 2.D for detail). This equation suggests that K_h^{adv} can be directly estimated using the M_2 sea surface gradient, the effective turbulence and friction parameters. The tidal advective diffusivity K_h^{adv} is proportional to the M_2 sea surface gradient squared, and it is affected by the Stokes number and the dimensionless slip parameter s^*.

To calculate the estimated K_h^{adv}, the sea surface elevation is first calibrated to obtain the effective s and A_v for each estuary. Then, the parameters α and Stk at each longitudinal position can be calculated using the bathymetry profiles of the three estuaries from section 2.4.2. After that, the estimated K_h^{adv} at every location of each estuary can be obtained from Eq. (2.27). The accuracy of this estimate is shown in Fig. 2.11, where the analytical solution of K_h^{adv} evaluated from Eq. (2.19) is compared with the estimated K_h^{adv} for the Delaware estuary, the Scheldt estuary and the Columbia estuary. In general, the estimated values agree well with the analytical solutions, with less than 5% difference between them for all three estuaries. It indicates that Eq. (2.27) is indeed a good estimate of K_h^{adv}, both for estuaries with a horizontal bed and those with non-uniform bathymetry. With this estimate of K_h^{adv}, the sensitivity of K_h^{adv} to the dimensionless slip parameter, the Stokes number, estuarine depth and convergence length can be explained.

2.5.1 Influence of the dimensionless slip parameter

The dimensionless slip parameter (s^*) affects K_h^{adv} mainly through the parameter α, while the influence of s^* through the sea surface gradient is minor. For large values of s^*, approaching a no-slip boundary condition, α approaches to $1/\cosh\delta$. This implies that increasing s^* further does not change K_h^{adv} since the flow hardly changes when s^* approaches to infinity. On the other hand, for very small values of s^*, a free slip condition is approximated, and α becomes proportional to s^*. In this case, K_h^{adv} approaches to zero

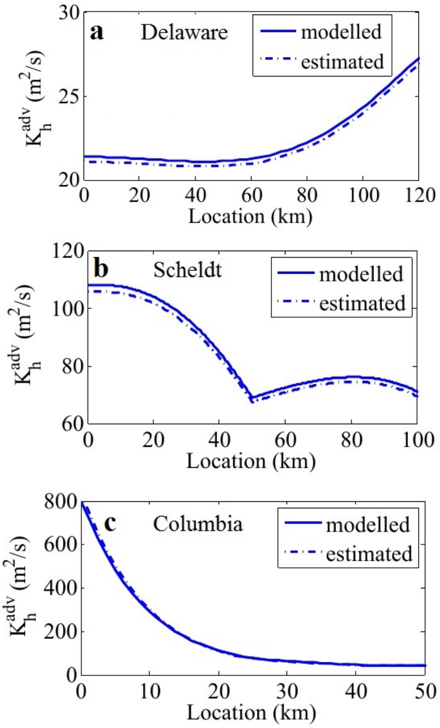

Figure 2.11: The comparison of K_h^{adv} from the model (see solid lines) with the estimated K_h^{adv} using Eq. (2.27) (see dash-dotted lines) for the Delaware estuary, the Scheldt estuary, and the Columbia estuary.

as s^* approaches to zero. For s^* between these two limits, increasing s^* will increase α (see Eq. (2.66)), resulting in an increase of K_h^{adv}, as observed in Fig. 2.2a.

2.5.2 Influence of the Stokes number

The Stokes number (Stk) determines the height of bottom-friction influence (Souza 2013), thus is crucial for the vertical structures of u_0 and S_1. Equation (2.27) shows K_h^{adv} is proportional to Stk^{-6}, which partly explains the strong sensitivity of K_h^{adv} on A_v.

Apart from the proportionality of K_h^{adv} to Stk^{-6}, Stk also affects K_h^{adv} through α and the sea surface gradient. The influence of Stk on α can be clearly seen by taking s^* to be large, but δ not too small, in which case α can be approximated as $1/\cosh(\delta)$. However, for small δ, Stk hardly affects α: α only depends on the dimensionless slip parameter as $s^*/(s^*+i)$. The influence of Stk on the sea surface gradient, however, is only through affecting the complex wave number (see Eq. (2.50) in appendix 2.B). For both large and small values of δ, the wave number is hardly depending on δ, hence independent of Stk. Since we focus on relatively small values of δ (well-mixed estuaries), the influence of K_h^{adv} through α and the sea surface gradient is smaller than that through Stk^{-6}.

2.5.3 Influence of estuarine depth

The influence of H on K_h^{adv} can be explained using Stk and s^*. When a shallow estuary becomes moderately deep (H varies from 5 m to 16 m), the increase of depth results in a decrease of Stk, and a strong increase of K_h^{adv} (see Fig. 2.6a). However, when the estuary becomes much deeper ($|\delta| >> \sqrt{2}$), the dependency of K_h^{adv} on Stk^{-6} is no longer valid (as Eq. (2.27) breaks down), increasing H is equivalent to decreasing s^*. In this case, u_0 and S_1 become almost uniform in the vertical ($\alpha \to 0$), and K_h^{adv} approaches to zero.

2.5.4 Influence of the estuarine convergence length

From Eq. (2.27) it follows that the estuarine convergence length (L_b) influences K_h^{adv} only through altering the sea surface gradient. To better understand this influence, an asymptotic solution for the sea surface gradient is obtained for very weakly converging and very strongly converging estuaries, using analytical solutions for estuaries with a horizontal bed (see appendix 2.B for these solutions).

For weakly converging estuaries (L_b is large), the complex amplitude of the sea surface gradient is approximately given by

$$\frac{d\hat{\eta}_0}{dx} \approx a_{M_2} e^{\frac{x}{2L_b}} \frac{k_0}{2} \frac{\sinh\left[\frac{k_0}{2}(x-L)\right]}{\cosh(\frac{k_0 L}{2})}, \tag{2.28}$$

with $k_0 = \sqrt{4\sigma^2\delta/(gH(\alpha\sinh\delta - \delta))}$ the complex wave number for large values of L_b. In this case, the complex amplitude of the sea surface gradient exponentially decreases with L_b, which results in the significant decrease of K_h^{adv} (proportional to the square of the magnitude of $d\hat{\eta}_0/dx$) when L_b increases from 40 km to 1000 km, as shown in Fig. 2.6b. However, for very strongly convergent estuaries, the complex amplitude of the sea surface gradient is approximately given by

$$\frac{d\hat{\eta}_0}{dx} \approx a_{M_2} \frac{k_0^2 L_b}{2}. \tag{2.29}$$

Since $d\hat{\eta}_0/dx$ linearly decreases with L_b, K_h^{adv} tends to decrease when L_b varies from 40 km to 10 km. Near the estuarine mouth, K_h^{adv} consistently decreases with L_b as $d\hat{\eta}_0/dx$ near the mouth decreases for L_b varying from 1000 km to 10 km.

2.5.5 Other salt transport processes

The estuarine circulation due to salinity-driven gravitational circulation (Hansen and Rattray 1965, MacCready 2004) and tidal straining (Burchard and Hetland 2010) are other potentially important salt transport processes. Gravitational circulation dominates the estuarine circulation in many estuaries, and is usually much more significant in strongly stratified cases than in partially mixed estuaries (Jay and Smith 1990c). In partially mixed and weakly stratified estuaries, the exchange flow is dominated by tidal straining (Burchard and Baumert 1998, Burchard *et al.* 2011). Besides estuarine circulation, there are other significant salt transport processes: lateral advection of the longitudinal momentum (Lerczak *et al.* 2006); tidal advective diffusion due to temporal correlation between the tidally-varying velocity and salinity, also known as tidal oscillatory transport (Bowen and Geyer 2003); and the correlations between the tidal velocity and salinity, and the tidal variation of the cross-sectional area (Hughes and Rattray 1980). In partially mixed systems like the Hudson estuary, the residual salt transport induced by estuarine circulations dominates over the tidal oscillatory transport. Contrary to estuaries with pronounced vertical stratification, residual salt transport induced by estuarine circulations can be negligible in weakly stratified and well-mixed estuaries (Jay and Smith 1990a). In the North Inlet (Kjerfve 1986), for instance, the landward salt transport mainly results from the correlation between the tidally-varying velocity, salinity and water depth. Instead of calculating each of these processes explicitly, the present width-averaged model resolves only the width-averaged tidal advective diffusion while parameterizing all other processes in the prescribed diffusion.

2.5.6 Model limitations

Many processes such as lateral processes and tidal straining are not taken into account in the present model. By using a constant vertical eddy viscosity, for example, the asymmetric tidal mixing (tidal straining) is assumed to be very small, though tidal mixing is usually larger during spring tide than neap tide in real estuaries, potentially affecting the tidal velocity and salinity. It means that, including significant asymmetric tidal mixing can result in a different salt transport contribution induced by tidal advective diffusion. Moreover, by taking a constant partial slip parameter, the model excludes the influence of local bed friction variations on water motion and salt dynamics. More importantly, by neglecting the lateral processes which can be significant in well-mixed estuaries such as the Delaware estuary (Aristizábal and Chant 2013, McSweeney *et al.* 2016), gravitational circulation drops out from the main residual salt balance integrated over the cross-section. Therefore, to investigate most of the salt dynamics using the model developed in this chapter, the model is preferably applied to well-mixed, tidally dominated estuaries where lateral processes and tidal straining are not significant. However, in other estuaries where the above-mentioned conditions are not exactly satisfied, the present model can be used to estimate the salt transport contribution due to the width-averaged tidal advective diffusion.

2.6 Conclusion

The importance of tidal advective diffusion on the residual salt transport in well-mixed estuaries is studied by coupling the width-averaged shallow water equations and the salinity equation in a consistent way. This coupled system of equations is solved using a perturbation method, in which the physical quantities are expanded in a small parameter: the ratio of the M_2 tidal amplitude to the water depth at the estuarine mouth. The salt balance equation shows that the seaward residual salt transport driven by river discharge is balanced by the landward salt transport due to tidal advection and diffusive processes, which parameterizes unresolved processes. It is found that the salt transport due to tidal advection behaves effectively as a diffusive term. Therefore, we use the term *tidal advective diffusion* for this contribution. The tidal advective diffusion results from the temporal correlation between the tidal velocity and salinity, and can be calculated explicitly after solving the tidal water motion.

For estuaries in which the water motion is mainly forced by a M_2 tidal constituent, the tidal advective diffusivity is calculated after calibrating the M_2 tidal data using the partial slip parameter and the vertical eddy viscosity. Sensitivity analysis shows that the tidal advective diffusivity increases with increasing slip parameter, decreasing vertical eddy viscosity, and it reaches its maximum for moderate water depth and moderate convergence length. To understand this sensitivity, an estimate of the tidal advective diffusivity is made. This estimate reveals that the tidal advective diffusivity is proportional to the amplitude of sea surface gradient squared, and it depends on the Stokes number and the dimensionless slip parameter. Results show that the influences of slip parameter and eddy viscosity on the tidal advective diffusivity are mainly through the parameter α and the Stokes number, with the influence of the Stokes number being more significant. The estuarine depth influences the tidal advective diffusivity through both changing the dimensionless slip parameter and Stokes number; while the influence of the estuarine convergence length on the tidal advective diffusivity is only through altering the along-channel sea surface gradient. Furthermore, tidal advective diffusion transports salt landward near the surface and seaward near the bottom, with the tidal advective transport over the complete water column being always non-negative.

Using the residual salt balance, the prescribed diffusivity is obtained from the measured salinity field. The relative importance of the tidal advective diffusion is quantified for three estuaries: the Delaware, Scheldt and Columbia estuaries. The tidal advective diffusion dominates the residual salt transport processes in the central part of the Scheldt estuary, where up to 70% of the total residual salt transport is attributed to this process. In the Delaware estuary and the Columbia estuary, tidal advective diffusion contributes up to 30% and 16% to the total residual salt transport, respectively. It suggests that the width-averaged tidal advective diffusion is less important than other processes such as lateral processes in the Delaware estuary and the Columbia estuary.

2.A Scaling analysis

A perturbation method is used to analytically solve Eqs. (2.1)-(2.11). First of all, variables are scaled with their typical scales (see Table 2.3), where dimensionless variables are denoted by a tilde (~). The governing equations (2.1) and (2.2) are transformed into their dimensionless form. In Table 2.3, * means that the density gradient scale ($\triangle_\rho = \rho_s - \rho_r$) is defined as the density difference between the seaward and landward side (McCarthy 1993), with ρ_s and ρ_r the density of sea water and river flow. The dimensionless water motion equations read

$$\frac{\partial \tilde{u}}{\partial \tilde{x}} + \frac{\partial \tilde{w}}{\partial \tilde{z}} + \frac{1}{\tilde{B}} \frac{d\tilde{B}}{d\tilde{x}} \tilde{u} = 0 \quad , \tag{2.30}$$

$$\frac{\partial \tilde{u}}{\partial \tilde{t}}+\frac{U}{\sigma L_b}\tilde{u}\frac{\partial \tilde{u}}{\partial \tilde{x}}+\frac{U}{\sigma L_b}\tilde{w}\frac{\partial \tilde{u}}{\partial \tilde{z}}=\frac{\triangle_\rho H_0}{U\sigma L_b}\frac{g}{\rho_c}\frac{\partial \tilde{\rho}}{\partial \tilde{x}}(\tilde{z}-\frac{a_{M_2}}{H_0}\tilde{\eta})-\frac{a_{M_2}}{U\sigma L_b}g\frac{\partial \tilde{\eta}}{\partial \tilde{x}}+\frac{A_v}{\sigma H_0^2}\frac{\partial^2 \tilde{u}}{\partial \tilde{z}^2}=0 \quad , \tag{2.31}$$

with U the typical scale of the M_2 tidal velocity in the longitudinal direction and L_b the typical length scale. For estuaries with an exponentially decreasing width, L_b is equivalent to the estuarine convergence length (see Eq. (2.22)).

Table 2.3: Scales of physical variables

Variable	Typical scale	Symbol	Expression
t	M_2 tidal frequency	σ	$\sigma^{-1}\tilde{t}$
η	M_2 tidal amplitude	a_{M_2}	$a_{M_2}\tilde{\eta}$
x	estuarine convergence length	L_b	$L_b\tilde{x}$
z	water depth at mouth	H_0	$H_0\tilde{z}$
H	water depth at mouth	H_0	$H_0\tilde{H}$
B	estuarine width at mouth	B_0	$B_0\tilde{B}$
u	see Chernetsky et al (2010)	$U=\frac{\sigma a_{M_2}L_b}{H}$	$U\tilde{u}$
w	see Chernetsky et al (2010)	$W=\frac{H_0}{L_b}U$	$W\tilde{w}$
ρ'_x	*	ρ'_x	$\triangle_\rho\tilde{\rho}'_x$
S	salinity at mouth	S_m	$S_m\tilde{S}$

The corresponding dimensionless boundary conditions at the free surface are given by:

$$\tilde{w}=\frac{\partial \tilde{\eta}}{\partial \tilde{t}}+\frac{a_{M_2}}{H_0}\tilde{u}\frac{\partial \tilde{\eta}}{\partial \tilde{x}} \text{ and } A_v\frac{\partial \tilde{u}}{\partial \tilde{z}}=0 \text{ at } \tilde{z}=\frac{a_{M_2}}{H_0}\tilde{\eta}. \tag{2.32}$$

The dimensionless boundary conditions at the bottom read,

$$\tilde{w}=-\tilde{u}\frac{\partial \tilde{H}}{\partial \tilde{x}} \text{ and } \frac{\partial \tilde{u}}{\partial \tilde{z}}=\frac{sH_0}{A_v}\tilde{u} \quad \text{at } \tilde{z}=-\tilde{H}. \tag{2.33}$$

At the entrance of the estuary, the dimensionless boundary condition reads

$$\tilde{\eta}=\cos(\sigma\tilde{t}) \qquad \text{at } \tilde{x}=0, \tag{2.34}$$

while at the end of estuary, it is given by,

$$\int_{-\tilde{H}}^{\tilde{\eta}}\tilde{u}d\tilde{z}=\frac{R}{B_0H_0U}\frac{1}{\tilde{B}} \qquad \text{at } \tilde{x}=1. \tag{2.35}$$

The dimensionless salinity equation is also derived,

$$\frac{\partial \tilde{S}}{\partial \tilde{t}}+\frac{U}{\sigma L_b}\tilde{u}\frac{\partial \tilde{S}}{\partial \tilde{x}}+\frac{W}{\sigma H_0}\tilde{w}\frac{\partial \tilde{S}}{\partial \tilde{z}}=\frac{K_h}{\sigma L_b^2}\frac{\partial}{\partial \tilde{x}}\frac{\partial \tilde{S}}{\partial \tilde{x}}+\frac{K_v}{\sigma H_0^2}\frac{\partial}{\partial \tilde{z}}\frac{\partial \tilde{S}}{\partial \tilde{z}}+\frac{K_h}{\sigma L_b^2}\frac{1}{\tilde{B}}\frac{d\tilde{B}}{d\tilde{x}}\frac{\partial \tilde{S}}{\partial \tilde{x}}, \tag{2.36}$$

with

$$\tilde{S} = 1 \qquad \text{at } \tilde{x} = 0. \tag{2.37}$$

This boundary condition is different from McCarthy (1993), who required no salinity gradient at the estuarine mouth. No residual salt transport is required at the weir,

$$\overline{-\int_{-\tilde{H}}^{\tilde{\eta}} \tilde{u}\tilde{S} d\tilde{z} + \frac{K_h}{UL_b}\int_{-\tilde{H}}^{\tilde{\eta}} \frac{\partial \tilde{S}}{\partial \tilde{x}} d\tilde{z}} = 0 \text{ at } \tilde{x} = 1, \tag{2.38}$$

where the overbar ($^{-}$) means tidally averaged quantities. Moreover, no salt flux is allowed through the free surface or through the bottom,

$$K_v \frac{\partial \tilde{S}}{\partial \tilde{z}}\bigg|_{\tilde{z}=\tilde{\eta}} = K_v \frac{\partial \tilde{S}}{\partial \tilde{z}}\bigg|_{\tilde{z}=\tilde{H}} = 0. \tag{2.39}$$

As a next step, the order of magnitudes of the above scaling parameters is provided in terms of ε for the governing equations and the boundary conditions, as summarized in Table 2.4. Here $U/\sigma L_b = O(\varepsilon)$ follows from integrating the continuity equation over depth and requiring an approximate balance between the resulting contributions (Chernetsky *et al.* 2010).

Table 2.4: Order of magnitude of scaling parameters

Dimensionless parameters	Order
a_{M_2}/H_0	$O(\varepsilon)$
$U/\sigma L_b = W/\sigma H_0$	$O(\varepsilon)$
$\triangle_\rho H_0^2 g/\rho_c U\sigma L_b$	$O(\varepsilon)$
$a_{M_2} g/U\sigma L_b$	$O(1)$
$A_v/\sigma H_0^2 = K_v/\sigma H_0^2$	$O(1)$
sH_0/A_v	$O(1)$
$R/B(L)H_0U$	$O(\varepsilon)$
$K_h/\sigma L_b^2$	$O(\varepsilon^2)$
K_h/UL_b	$O(\varepsilon)$

Substituting the scaled variables into Eqs. (2.30), (2.31) and (2.36) yields:

$$\frac{\partial \tilde{u}}{\partial \tilde{x}} + \frac{\partial \tilde{w}}{\partial \tilde{z}} + \frac{1}{\tilde{B}}\frac{d\tilde{B}}{d\tilde{x}}\tilde{u} = 0, \tag{2.40}$$

$$\frac{\partial \tilde{u}}{\partial \tilde{t}} + \varepsilon\tilde{u}\frac{\partial \tilde{u}}{\partial \tilde{x}} + \varepsilon\tilde{w}\frac{\partial \tilde{u}}{\partial \tilde{z}} = -\varepsilon\int_{\tilde{z}}^{\tilde{\eta}} \frac{\partial \tilde{\rho}}{\partial \tilde{x}} d\tilde{z} - \frac{\partial \tilde{\eta}}{\partial \tilde{x}} + \frac{\partial^2 \tilde{u}}{\partial \tilde{z}^2},$$

$$\frac{\partial \tilde{S}}{\partial \tilde{t}} + \varepsilon\tilde{u}\frac{\partial \tilde{S}}{\partial \tilde{x}} + \varepsilon\tilde{w}\frac{\partial \tilde{S}}{\partial \tilde{z}} = \varepsilon^2\frac{\partial^2 \tilde{S}}{\partial \tilde{x}^2} + \varepsilon^2\frac{1}{\tilde{B}}\frac{d\tilde{B}}{d\tilde{x}}\frac{\partial \tilde{S}}{\partial \tilde{x}} + \frac{\partial^2 \tilde{S}}{\partial \tilde{z}^2}.$$

The dimensionless boundary conditions in terms of ε can also be obtained using Table 2.4. After that, all the physical variables are expanded in power series of the ε. By substituting the expanded variables from Eq. (2.12) into Eq. (2.40), and their boundary conditions, and collecting the terms of the same order of ε, each system of equations of different orders of ε can be obtained.

2.B The leading order water motion

The leading order dimensional equations for the water motion are:

$$\frac{\partial u_0}{\partial x}+\frac{\partial w_0}{\partial z}+\frac{1}{B}\frac{dB}{dx}u_0=0, \tag{2.41}$$

$$\frac{\partial u_0}{\partial t}=-g\frac{\partial \eta_0}{\partial x}+A_v\frac{\partial^2 u_0}{\partial z^2}. \tag{2.42}$$

The free surface elevation is at $O(\varepsilon)$, thus the boundary condition at the sea surface is given at $z=0$ in the leading order system, hence

$$w_0=\frac{\partial \eta_0}{\partial t} \text{ and } A_v\frac{\partial u_0}{\partial z}=0,$$

and at the bottom $(z=-H)$,

$$w_0=-u_0\frac{dH}{dx} \text{ and } A_v\frac{\partial u_0}{\partial z}=su_0,$$

The leading order system is forced by a M_2 tide at the entrance,

$$\eta_0=a_{M_2}\cos(\sigma t),$$

and no water transport in the leading order is allowed at the end of estuary $(x=L)$,

$$\int_{-H}^{0}u_0 dz=0.$$

The leading order hydrodynamic system allows solutions of the following form:

$$(u_0,w_0,\eta_0)=\Re\{\hat{u}_0(x,z),\hat{w}_0(x,z),\hat{\eta}_0(x)e^{i\sigma t}\}, \tag{2.43}$$

where $\Re$ means only the real parts of the solutions are used, and $\hat{u}_0$, $\hat{w}_0$, $\hat{\eta}_0$ are the complex amplitudes of u_0, w_0, η_0, respectively. Substituting Eq. (2.43) into (2.41) and (2.42) yields

$$\frac{\partial \hat{u}_0}{\partial x}+\frac{\partial \hat{w}_0}{\partial z}+\frac{1}{B}\frac{dB}{dx}\hat{u}_0=0, \tag{2.44}$$

$$i\sigma\hat{u}_0+g\frac{d\hat{\eta}_0}{dx}-A_v\frac{\partial^2 \hat{u}_0}{\partial z^2}=0. \tag{2.45}$$

Solving Eq. (2.45) using the corresponding boundary conditions regarding u_0 yields

$$\hat{u}_0=\frac{g}{i\sigma}\frac{d\hat{\eta}_0}{dx}(\alpha\cosh\delta\frac{z}{H}-1), \tag{2.46}$$

$$\text{with } \delta=\frac{1+i}{Stk}, \text{ and } \alpha=(\cosh\delta+\frac{A_v}{sH}\delta\sinh\delta)^{-1}.$$

Here $Stk=\sqrt{\frac{2A_v}{\sigma}}/H$ is the Stokes number.

By substituting Eq. (2.46) into Eq. (2.44), and applying the boundary conditions regarding w_0, we derive a second-order ordinary differential equation,

$$T_1(x)\frac{d^2\hat{\eta}_0}{dx^2} - T_2(x)\frac{d\hat{\eta}_0}{dx} - T_3(x)\hat{\eta}_0 = 0, \tag{2.47}$$

$$\begin{aligned}
\text{with}\quad T_1(x) =& \frac{\alpha\sinh\delta - \delta}{\delta}H,\\
T_2(x) =& -\frac{1}{B}\frac{dB}{dx}T_1(x) - \frac{\sinh\delta}{\delta}\frac{d\alpha}{dx}H\\
& -(\alpha\cosh\delta - 1)\frac{dH}{dx},\\
T_3(x) =& \frac{\sigma^2}{g}.
\end{aligned}$$

Eq. (2.47) can be solved together with the boundary conditions of η_0. Note that T_1 and T_2 are functions of x for a spatially varying bathymetry, thus hereafter a finite difference method is used to obtain $\hat{\eta}_0$ for a depth-varying estuary. In this sense, the model is solved semi-analytically. However, Eq. (2.47) can be solved analytically for estuaries with a horizontal bed and an exponentially converging width,

$$B = B_0 e^{-\frac{x}{L_b}}, \tag{2.48}$$

with B_0 the width at the entrance, and L_b the estuarine convergence length. The analytical solutions of the sea surface elevation and the longitudinal sea surface gradient read

$$\hat{\eta}_0 = \frac{a_{M_2} e^{\frac{x}{2L_b}} (-\sinh(\frac{k}{2}(x-L)) + L_b k\cosh(\frac{k}{2}(x-L)))}{\sinh(\frac{kL}{2}) + kL_b\cosh(\frac{kL}{2})}, \tag{2.49}$$

$$\frac{d\hat{\eta}_0}{dx} = \frac{a_{M_2} e^{\frac{x}{2L_b}} \sinh\left(\frac{k}{2}(x-L)\right)(-\frac{1}{2L_b} + \frac{k^2L_b}{2})}{\sinh\left(\frac{kL}{2}\right) + kL_b\cosh\left(\frac{kL}{2}\right)}, \tag{2.50}$$

with $k = \sqrt{1/L_b^2 + 4\sigma^2\delta/(gH(\alpha\sinh\delta - \delta))}$ the complex wave number.

2.C The analytical solution for salinity

The dimensional salinity equation in the first order is

$$\frac{\partial S_1}{\partial t} + u_0\frac{\partial S_0}{\partial x} = K_v\frac{\partial^2 S_1}{\partial z^2}, \tag{2.51}$$

with

$$S_1 = \Re\left\{\hat{S}_1 e^{i\sigma t}\right\}. \tag{2.52}$$

The leading order salinity S_0 is taken to be real. Note that this is different from McCarthy (1993), who allows the leading order density to be complex, resulting in an incorrect expression for density (see Eq. (19) in McCarthy (1993)). The correct expression reads

$$\rho_1 = \Re\left\{A'(x)\rho(z)\Re(\rho_0'(x))e^{i\sigma t}\right\}, \tag{2.53}$$

where ρ_0' and $A'(x)$ are the along-channel gradient of the tidally averaged density and tidal surface elevation, respectively, ρ_1 is the tidal density, and $\rho(z)$ determines the depth dependency of the tidal salinity which can be analytically derived (McCarthy 1993). Hence it was erroneously assumed by McCarthy (1993) that

$$\Re\left\{u_0\Re(\rho_0'(x))\right\} = \Re\left\{\hat{u}_0\rho_0'(x)e^{i\sigma t}\right\}, \tag{2.54}$$

whereas it is equal to

$$\Re\left\{\hat{u}_0 e^{i\sigma t}\Re(\rho_0'(x)\right\}. \tag{2.55}$$

This means that the correct expressions are obtained by replacing $\rho_0'(x)$ with $\Re(\rho_0'(x))$, i.e., by taking $\rho_0(x)$ to be real. Substituting Eq. (2.52) into (2.51) gives

$$i\sigma\hat{S}_1 + \hat{u}_0\frac{\partial S_0}{\partial x} = K_v\frac{\partial^2\hat{S}_1}{\partial z^2}. \tag{2.56}$$

As u_0 can be solved independently of salinity (see Eq. (2.46)), and can be written as

$$\hat{u}_0 = U(x,z)\frac{g}{i\sigma}\frac{d\hat{\eta}_0}{dx}, \quad \text{with } U(x,z) = \alpha\cosh\delta\frac{z}{H} - 1. \tag{2.57}$$

Equation (2.56) suggests S_1 can be written as

$$\hat{S}_1 = S_z(x,z)\frac{d\hat{\eta}_0}{dx}\frac{dS_0}{dx}, \tag{2.58}$$

here S_z measures how the vertical structure of the tidal saliniry is influenced by the vertical profile of the tidal velocity, and it relates the gradients of the tidal elevation and subtidal salinity with the tidal salinity. Substituting Eqs. (2.57) and (2.58) into (2.56) yields

$$\frac{\partial^2 S_z}{\partial z^2} - \frac{i\sigma}{K_v}S_z = \frac{ig}{K_v\sigma}(1-\alpha\cosh\delta\frac{z}{H}). \tag{2.59}$$

Notice that the no salt flux through the free surface and the bottom is equivalent to zero vertical gradient of S_z,

$$\left.\frac{\partial S_z}{\partial z}\right|_{z=0} = \left.\frac{\partial S_z}{\partial z}\right|_{z=-H} = 0. \tag{2.60}$$

Using Eqs. (2.59) and (2.60), $S_z(x,z)$ can be solved analytically for estuaries of any bathymetry $H(x)$. The analytical solution reads

$$S_z(x,z) = \frac{g}{\sigma^2}\left(-1+\frac{\alpha}{2}(1+\delta\frac{\cosh\delta}{\sinh\delta})\cosh\delta\frac{z}{H} - \frac{\alpha}{2}\delta\frac{z}{H}\sinh\delta\frac{z}{H}\right). \tag{2.61}$$

2.D The estimation of K_h^{adv}

To derive an estimate of K_h^{adv}, the complex amplitudes of the M_2 tidal velocity ($\hat{u}_0$) and salinity ($\hat{S}_1$) are decomposed into a depth-averaged part and the deviation from this depth average:

$$\hat{u}_0 = <\hat{u}_0(x)> + \hat{u}_0'(x,z), \tag{2.62}$$

$$\hat{S}_1 = <\hat{S}_1(x)> + \hat{S}_1'(x,z). \tag{2.63}$$

Here $<\cdot>$ means averaging over depth, and $'$ the deviation from the depth average. Averaging Eq. (2.14) over depth using boundary condition (2.11) shows that the depth averaged M_2 salinity is 90° out of phase with the depth-averaged tidal velocity. This implies that the tidal advective diffusivity only results from the correlation between the depth varying parts of the tidal velocity and salinity. Then, $\hat{u}_0'^*$ and $\hat{S}_1' \cdot (dS_0/dx)^{-1}$ (used in Eq. (2.19)) are written in terms of $\hat{\eta}_0$ and S_0 (see appendix 2.B & 2.C for details),

$$\hat{u}_0' = \frac{g\alpha}{i\sigma}\frac{d\hat{\eta}_0}{dx}\left[\cosh\left(\frac{\delta z}{H}\right) - \frac{\sinh(\delta)}{\delta}\right], \tag{2.64}$$

$$\hat{S}_1' = \frac{g\alpha}{2\sigma^2}\frac{d\hat{\eta}_0}{dx}\frac{dS_0}{dx}\left[\left(1+\delta\frac{\cosh(\delta)}{\sinh(\delta)}\right)\cosh\left(\frac{\delta z}{H}\right) - \frac{\delta z}{H}\sinh\left(\frac{\delta z}{H}\right) - 2\frac{\sinh(\delta)}{\delta}\right], \tag{2.65}$$

with $\delta = (1+i)/Stk$. Here

$$Stk = \sqrt{\frac{2A_v}{\sigma H^2}}$$

is the Stokes number. The parameter α depends on both δ and the dimensionless partial slip parameter $s^* = s/\sigma H$, and is given by

$$\alpha = \left(\cosh(\delta) + \frac{i}{\delta s^*}\sinh(\delta)\right)^{-1}. \tag{2.66}$$

Hence, K_h^{adv} can be analytically solved using only the M_2 tidal motion, as

$$K_h^{\mathrm{adv}} = \frac{1}{4}\frac{g^2}{\sigma^3}\left|\frac{d\hat{\eta}_0}{dx}\right|^2 |\alpha|^2 F, \tag{2.67}$$

where F is the vertical integral given by

$$F = -\frac{1}{H}\int_{-H}^{0}\left(\cosh\left(\frac{\delta z}{H}\right) - \frac{\sinh(\delta)}{\delta}\right)\left(\cosh\left(\frac{\delta z}{H}\right)\left(1+\delta\frac{\cosh(\delta)}{\sinh(\delta)}\right) - \frac{\delta z}{H}\sinh\left(\frac{\delta z}{H}\right) - 2\frac{\sinh(\delta)}{\delta}\right)dz. \tag{2.68}$$

Since F depends only on δ for a given H, and $|\delta|$ is small for well-mixed estuaries, it yields an estimation of F after using Taylor expansion:

$$F \approx \frac{32}{945}Stk^{-6}. \tag{2.69}$$

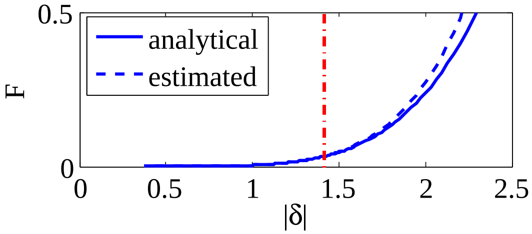

Figure 2.12: The comparison of the analytical solution of F (see the solid blue line) with the estimated F using Eq. (2.69) (see the blue dashed line). The red dash-dotted line represents the absolute value of $|\delta| = \sqrt{2}$.

As pointed out by Souza (2013), that boundary layer increases with Stk, and it covers the entire water column (estuary being well-mixed) when Stk approaches unity. Hence, the well-mixed assumption has to be valid when $|\delta|$ ($= \sqrt{2}/Stk$) is smaller than $\sqrt{2}$. Fig. 2.12 shows that the estimated F using Eq. (2.69) agrees well with the analytical results obtained from Eq. (2.68). It means that Eq. (2.69) is a good estimate of F for well-mixed estuaries. Substituting Eq. (2.69) into Eq. (2.67) yields an estimate of the tidal advective diffusivity:

$$K_h^{\text{adv}} \approx \frac{8}{945}\frac{g^2}{\sigma^3}\left|\frac{d\hat{\eta}_0}{dx}\right|^2 |\alpha|^2 \frac{1}{Stk^6}. \tag{2.70}$$

References

Aristizábal, M., and R. Chant, *A numerical study of salt fluxes in Delaware Bay estuary,* Journal of Physical Oceanography **43**, 1572–1588 (2013).

Bowen, M. M., and W. R. Geyer, *Salt transport and the time-dependent salt balance of a partially stratified estuary,* Journal of Geophysical Research: Oceans (1978–2012) **108** (2003).

Burchard, H., and H. Baumert, *The formation of estuarine turbidity maxima due to density effects in the salt wedge: A hydrodynamic process study,* Journal of Physical Oceanography **28**, 309–321 (1998).

Burchard, H., and R. D. Hetland, *Quantifying the contributions of tidal straining and gravitational circulation to residual circulation in periodically stratified tidal estuaries,* Journal of Physical Oceanography **40**, 1243–1262 (2010).

Burchard, H., R. D. Hetland, E. Schulz, and H. M. Schuttelaars, *Drivers of residual estuarine circulation in tidally energetic estuaries: Straight and irrotational channels with parabolic cross section,* Journal of Physical Oceanography **41**, 548–570 (2011).

Chernetsky, A. S., H. M. Schuttelaars, and S. A. Talke, *The effect of tidal asymmetry and temporal settling lag on sediment trapping in tidal estuaries,* Ocean Dynamics **60**, 1219–1241 (2010).

Davies, A., and J. Jones, *Sensitivity of tidal bed stress distributions, near bed currents, overtides and tidal residuals to frictional effect in the eastern Irish Sea,* Journal of Physical Oceanography **26**, 2554–2575 (1996).

Fischer, H., *Mass transport mechanisms in partially stratified estuaries,* Journal of Fluid Mechanics **53**, 671–687 (1972).

Friedrichs, C. T., and D. G. Aubrey, *Tidal propagation in strongly convergent channels,* Journal of Geophysical Research: Oceans (1978–2012) **99**, 3321–3336 (1994).

Garvine, R. W., R. K. McCarthy, and K.-C. Wong, *The axial salinity distribution in the Delaware estuary and its weak response to river discharge,* Estuarine, Coastal and Shelf Science **35**, 157–165 (1992).

Geyer, W. R., and P. MacCready, *The estuarine circulation,* Annual Review of Fluid Mechanics **46**, 175 (2014).

Giese, B., and D. Jay, *Modelling tidal energetics of the Columbia River estuary,* Estuarine, Coastal and Shelf Science **29**, 549–571 (1989).

Hansen, D. V., and M. Rattray, *Gravitational circulation in straits and estuaries,* Estuarine and Coastal Marine Science **23**, 104–122 (1965).

Hughes, F., and M. Rattray, *Salt flux and mixing in the Columbia River estuary,* Estuarine and Coastal Marine Science **10**, 479–493 (1980).

Ianniello, J. P., *Tidally induced residual currents in estuaries of variable breadth and depth,* Journal of Physical Oceanography **9**, 962–974 (1979).

Jay, D., and J. Smith, *Residual circulation in shallow, stratified estuaries. II. weakly-stratified and partially-mixed systems,* Journal of Geophysical Research **95**, 733–748 (1990a).

Jay, D. A., and J. D. Smith, *Circulation, density distribution and neap-spring transitions in the Columbia River estuary,* Progress in Oceanography **25**, 81–112 (1990b).

Jay, D. A., and J. D. Smith, *Residual circulation in shallow estuaries: I. highly stratified, narrow estuaries,* Journal of Geophysical Research: Oceans (1978–2012) **95**, 711–731 (1990c).

Jones, J., and A. Davies, *A high-resolution, three-dimensional model of the M2, M4, M6, S2, N2, K1 and O1 tides in the eastern Irish Sea,* Estuarine, Coastal and Shelf Science **42**, 311–346 (1996).

Kjerfve, B., *Circulation and salt flux in a well mixed estuary,* Physics of shallow estuaries and bays , 22–29 (1986).

Kuijper, K., and L. C. Van Rijn, *Analytical and numerical analysis of tides and salinities in estuaries; part II: salinity distributions in prismatic and convergent tidal channels,* Ocean Dynamics **61**, 1743–1765 (2011).

Lanzoni, S., and G. Seminara, *On tide propagation in convergent estuaries,* Journal of Geophysical Research **103**, 30793–30812 (1998).

Lerczak, J. A., W. R. Geyer, and R. J. Chant, *Mechanisms driving the time-dependent salt flux in a partially stratified estuary,* Journal of Physical Oceanography **36**, 2296–2311 (2006).

MacCready, P., *Toward a unified theory of tidally-averaged estuarine salinity structure,* Estuaries **27**, 561–570 (2004).

MacCready, P., and W. R. Geyer, *Advances in estuarine physics,* Annual Review of Marine Science **2**, 35–58 (2010).

McCarthy, R. K., *Residual currents in tidally dominated, well-mixed estuaries,* Tellus A **45**, 325–340 (1993).

McSweeney, J. M., R. J. Chant, and C. K. Sommerfield, *Lateral variability of sediment transport in the Delaware estuary,* Journal of Geophysical Research: Oceans (2016).

Peters, J., and R. Wollast, *Role of the sedimentation in the self-purification of the Scheldt estuary,* in *Proceedings of the Third Federal Inter-agency Sedimentation Conference, Denver, Colo* (1976) p. 3.

Prandle, D., *Relationships between tidal dynamics and bathymetry in strongly convergent estuaries,* Journal of Physical Oceanography **33**, 2738–2750 (2003).

Rattray, M., and J. Dworski, *Comparison of methods for analysis of the transverse and vertical circulation contributions to the longitudinal advective salt flux in estuaries,* Estuarine and Coastal Marine Science **11**, 515–536 (1980).

Savenije, H. H., *Composition and driving mechanisms of longitudinal tidal average salinity dispersion in estuaries,* Journal of hydrology **144**, 127–141 (1993).

Savenije, H. H., *Salinity and tides in alluvial estuaries* (2nd completely revised edition: salinityandtides.com, pp139, 2012).

Savenije, H. H., and E. J. Veling, *Relation between tidal damping and wave celerity in estuaries,* Journal of Geophysical Research: Oceans (1978–2012) **110** (2005).

Schramkowski, G. P., and H. E. de Swart, *Morphodynamic equilibrium in straight tidal channels: combined effects of coriolis force and external overtides,* Journal of Geophysical Research: Oceans (1978–2012) **107**, 20–1 (2002).

Schramkowski, G. P., H. E. de Swart, and H. M. Schuttelaars, *Effect of bottom stress formulation on modelled flow and turbidity maxima in cross-sections of tide-dominated estuaries,* Ocean Dynamics **60**, 205–218 (2010).

Souza, A., *On the use of the Stokes number to explain frictional tidal dynamics and water column structure in shelf seas,* Ocean Science **9**, 391–398 (2013).

Taylor, G., *Dispersion of soluble matter in solvent flowing slowly through a tube,* in *Proceedings of the Royal Society of London A: Mathematical, Physical and Engineering Sciences*, Vol. 219 (The Royal Society, 1953) pp. 186–203.

Taylor, G., *The dispersion of matter in turbulent flow through a pipe,* in *Proceedings of the Royal Society of London A: Mathematical, Physical and Engineering Sciences*, Vol. 223 (The Royal Society, 1954) pp. 446–468.

Chapter 3

Three-dimensional salt dynamics in well-mixed estuaries: influence of estuarine convergence, Coriolis and bathymetry

Understanding the dominant mechanisms of the three-dimensional salt dynamics is of great importance to better predict salt intrusion, baroclinic forcing and residual circulation. A semi-analytical three-dimensional model is set up to dynamically calculate the coupled water motion and salinity for idealized well-mixed estuaries, and prognostically investigate the influence of each physical process on the residual salt transport. As a study case, a schematized estuary with an exponentially converging width and a channel-shoal structure is considered. It is found that the temporal correlation between tidal velocities and salinities is the dominant landward salt transport process. The residual salt transport as a result of gravitational circulation is locally significant, but the transport integrated over the cross-section is small. The impacts of the estuarine geometry, bathymetry and Coriolis force on the salt dynamics are studied using three experiments (I-III), in which the impact of each of these factors is studied in separation. In experiment I, a convergent estuary without bathymetric variations or Coriolis force is considered. In this case, the temporal correlation between tidal velocities and salinities is the only landward salt transport process. In experiment II, Coriolis effects are included. This results in a significant residual salt transport cell due to advection of the tidally averaged salinity by residual circulation, with salt imported from the left side of the estuary and exported on the right (looking seaward). In experiment III, a lateral channel-shoal structure is included while the Coriolis effects are excluded. It is found that the advection of the tidally averaged salinity by gravitational circulation results in *a significant landward salt transport through the channel and a seaward salt transport over the shoals.* [1]

3.1 Introduction

Estuaries are dynamically complex systems that are important from both an economical and ecological point of view. To be able to address issues related to these aspects, a good understanding of the physical processes resulting in the estuarine exchange flow is fundamental, as this flow drives long-term transport of sediment and other suspended particle matter in estuaries. Since the exchange flow is significantly affected by the salt dynamics, it is key to improve our understanding of the essential three-dimensional processes that result in the spatially and temporally varying salinity field.

Salt transport processes can vary significantly from estuary to estuary, since estuaries are subject to different forcing conditions and have different geometries and bathymetries (Fischer 1972). The classical subtidal salt balance, in which the river-induced seaward transport is balanced by the landward transport due to the longitudinal-vertical gravitational circulation and dispersion, is extensively described in literature (see for example Hansen and Rattray (1965), MacCready (2004), MacCready and Geyer (2010)). In this way, both lateral processes and processes that vary on the tidal timescale are parameterized. This classical balance is challenged in partially to well-mixed estuaries where gravitational circulation is relatively weak (Jay and Smith 1990), and other processes are likely to dominate. In well-mixed estuaries, for instance, the tidal oscillatory transport due to temporal correlations on the tidal timescale between the longitudinal velocity and salinity can be the predominant salt import mechanism (McCarthy 1993, Wei *et al.* 2016). The tidal oscillatory salt transport is also significant in partially stratified estuaries such as the Hudson estuary especially during neap tides (Chen *et al.* 2012, Wang *et al.* 2015). Even in salt wedge estuaries such as the Merrimack River, the landward salt transport is mainly associated with the tidal oscillatory processes, rather than with the steady sheared gravitational circulation (Ralston *et al.* 2010). This confirms the potential importance of considering residual salt transport contribution due to tidal processes (Hughes and Rattray 1980, Geyer and MacCready 2014).

Apart from the importance of processes on the tidal timescale, the transverse circulation (also known as secondary estuarine circulation), is also of great importance for estuarine salt transport (Fischer 1972, Dyer 1974, Smith 1977). Significant transverse circulations are observed in well-mixed, partially mixed and stratified estuaries (Nunes and Simpson 1985, Becherer *et al.* 2015, Valle-Levinson *et al.* 2000, Lacy and Monismith 2001). These circulations are usually associated with lateral variations in bathymetry (Nunes and Simpson 1985, Valle-Levinson *et al.* 2000), Coriolis effects (Lerczak and Geyer 2004, Valle-Levinson 2010), lateral density gradients (Huijts *et al.* 2006, 2011) and curvature-induced centrifugal forces (Lacy and Monismith 2001, Buijsman and Ridderinkhof 2008). Transverse circulations are also affected by the estu-

---

[1] This chapter is based on:
Wei, X., Kumar, M., Schuttelaars, H.M., in press. Three-dimensional salt dynamics in well-mixed estuaries: influence of estuarine convergence, Coriolis and bathymetry. *Journal of Physical Oceanography*.

arine width-to-depth ratio (Schulz *et al.* 2015) and temporal/lateral variations of mixing (tidal and lateral straining, see Burchard *et al.* (2011), Becherer *et al.* (2015)).

To investigate the influence of transverse processes on estuarine salt transport, the salt flux is usually decomposed into different contributions associated with transverse and vertical steady or oscillatory shear, using velocities and salinities from measurements (Fischer 1972, Dyer 1974, Hughes and Rattray 1980, West *et al.* 1990, Guymer and West 1992) or numerical models (Oey *et al.* 1985, Ralston and Stacey 2005, Ralston *et al.* 2010). This decomposition method, however, strongly depends on the quality and quantity of the measurements, and the resolution and accuracy of numerical models. Moreover, it is difficult to relate the shear-induced salt transport to a specific physical process since the shearing itself can be a result of the interplay of many different processes.

To unravel the dominant salt transport mechanisms, idealized theoretical models are appropriate tools, as they are specifically developed to investigate the influence of each physical process in isolation. This type of models has been successfully used to gain insight into the influence of lateral processes on water motion (Nunes and Simpson 1985, Li and O'Donnell 1997, Wong 1994, Valle-Levinson *et al.* 2003, Kumar *et al.* 2016) and lateral sediment trapping (Huijts *et al.* 2006, 2009, 2011). Existing idealized theoretical models aiming at understanding the salt dynamics (explicitly including processes on the tidal timescale), however, are limited to width-averaged models (McCarthy 1993, Wei *et al.* 2016). In these models, the coupled width-averaged water motion and salinity are dynamically resolved while the lateral processes are parameterized as diffusion. Since these models do not resolve the lateral dynamics, the relative importance of the transverse circulation on the residual salt balance can not be investigated.

In this chapter, we therefore develop a three-dimensional idealized model by extending the model of Wei *et al.* (2016). This model is specifically aiming at dynamically resolving the temporal and spatial (both longitudinal and lateral) variabilities of the water motion and salinity (i.e., prognostic in salinity, including lateral processes). With this model, the influence of each physical process on the residual salt balance is systematically investigated. As a first step, the estuaries are assumed to be well-mixed, i.e., the top-to-bottom salinity difference is much smaller compared to the bottom salinity, and the effects of tidal straining are assumed to be small. The nonlinear system of the three-dimensional water motion and salinity is solved at the tidal time-scale, employing a perturbation method to analytically obtain the vertical structures of the physical quantities, and a finite element method to calculate their horizontal variations. An iterative approach is used to calculate the coupled gravitational circulation and salinity field. Using this model, the influence of each of the longitudinal/transverse processes on the residual salt transport is investigated.

The chapter is structured as follows: the equations governing the coupled water motion and salinity (see section 3.2.1), and the solution method (see section 3.2.2) are introduced in Section 3.2; in Section 3.3, the salt dynamics for the default experiment representative for the Delaware estuary (see section 3.3.1), and the influences of estuarine width convergence, bathymetry, and Coriolis force on salt transport processes (see section 3.3.2) are investigated; in section 3.4, the three-dimensional salt fluxes induced by the tidal advective diffusion (see section 3.4.1) and gravitational circulation (see section 3.4.2) are analyzed considering the influence of the estuarine width convergence, Coriolis and bathymetry, respectively; conclusions are drawn in Section 3.5.

3.2 Model description

3.2.1 Governing equations

To investigate the salt dynamics and transport mechanisms in tidal estuaries, an idealized three dimensional model is developed for estuaries that are assumed to be tidally dominated and well-mixed. The shape of the estuary (i.e., its geometry) is arbitrary (see Fig. 3.1). The seaward boundary ($\partial_S\Omega$) is connected with the open sea and forced by tides. A weir is assumed to be located at the landward boundary denoted by $\partial_R\Omega$, where a river flows into the estuary. The closed boundaries ($\partial_C\Omega$) are impermeable. The undisturbed water level is located at $z = 0$, and the free surface elevation is denoted by $z = \eta$. The estuarine bed is located at $z = -H(x, y)$, with H an arbitrary function of the horizontal coordinates (x, y).

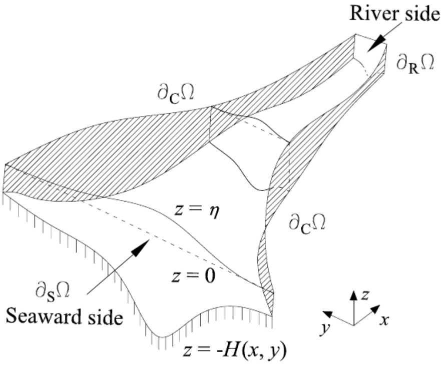

Figure 3.1: A three-dimensional sketch of an estuary, with x and y the horizontal coordinates, and z the vertical coordinate, positive in the upward direction. The seaward, river and closed boundaries are denoted by $\partial_S\Omega$, $\partial_R\Omega$ and $\partial_C\Omega$, respectively. The free surface elevation and the estuarine bottom are located at $z = \eta$ and $z = -H(x, y)$, respectively. A sketch for an estuary with a more general geometry and bathymetry can be found in Kumar *et al.* (2016) in Fig. 1.

The water motion is described by the three-dimensional shallow water equations, assuming hydrostatic equilibrium and using the Boussinesq approximation (Cushman-Roisin and Beckers 2011):

$$\frac{\partial u}{\partial x} + \frac{\partial v}{\partial y} + \frac{\partial w}{\partial z} = 0, \tag{3.1}$$

$$\frac{\partial u}{\partial t}+\nabla\cdot(\mathbf{U}u)=-g\frac{\partial\eta}{\partial x}-\frac{g}{\rho_c}\int_z^\eta\frac{\partial\rho}{\partial x}dz'+fv+\frac{\partial}{\partial z}\left(A_v\frac{\partial u}{\partial z}\right)+\frac{\partial}{\partial x}\left(A_h\frac{\partial u}{\partial x}\right)+\frac{\partial}{\partial y}\left(A_h\frac{\partial u}{\partial y}\right),\tag{3.2}$$

$$\frac{\partial v}{\partial t}+\nabla\cdot(\mathbf{U}v)=-g\frac{\partial\eta}{\partial y}-\frac{g}{\rho_c}\int_z^\eta\frac{\partial\rho}{\partial y}dz'-fu+\frac{\partial}{\partial z}\left(A_v\frac{\partial v}{\partial z}\right)+\frac{\partial}{\partial x}\left(A_h\frac{\partial v}{\partial x}\right)+\frac{\partial}{\partial y}\left(A_h\frac{\partial v}{\partial y}\right).\tag{3.3}$$

Here t denotes time, $\mathbf{U}=(u,v,w)$ is the velocity vector, with u, v and w the velocity components in x, y and z directions, respectively. The acceleration of gravity is denoted by g. Parameters A_v and A_h are respectively the vertical and horizontal eddy viscosity coefficients. The Coriolis parameter is denoted by f, and the estuarine water density is denoted by ρ. The density is assumed to depend only on the salinity S as $\rho=\rho_c(1+\beta_s S)$, with β_s =7.6×10^{-4} psu^{-1} and ρ_c the background density, taken to be 1000 kg m^{-3}. To dynamically calculate the density, the salinity equation has to be solved:

$$\frac{\partial S}{\partial t}+\nabla\cdot(\mathbf{U}S)=\frac{\partial}{\partial x}\left(K_h\frac{\partial S}{\partial x}\right)+\frac{\partial}{\partial y}\left(K_h\frac{\partial S}{\partial y}\right)+\frac{\partial}{\partial z}\left(K_v\frac{\partial S}{\partial z}\right).\tag{3.4}$$

Here K_h and K_v are the horizontal and vertical eddy diffusivity coefficients, respectively. The vertical eddy diffusivity K_v is assumed to be equal to the vertical eddy viscosity A_v.

At the seaward boundaries, the water motion is forced by a prescribed sea surface elevation that consists of a semi-diurnal constituent (M_2) and a residual water level (M_0):

$$\eta(x,y,t)=a_{M_2}(x,y)\cos[\sigma t-\varphi(x,y)]+a_{M_0}(x,y)\qquad\text{at }(x,y)\in\partial_S\Omega,\tag{3.5}$$

where $a_{M_2}(x,y)$ and $\varphi(x,y)$ are the prescribed amplitude and phase of the semi-diurnal tidal elevation at the seaward boundary $\partial_S\Omega$, with $\sigma\sim 1.4\times10^{-4}s^{-1}$ the M_2 tidal frequency. The residual water level $a_{M_0}(x,y)$ is prescribed at $\partial_S\Omega$, where a_{M_0} averaged over the seaward boundary vanishes. Furthermore, the tidally averaged salinity is prescribed at the seaward boundary and is denoted by S_e,

$$\overline{S}(x,y)=S_e(x,y)\qquad\text{at }(x,y)\in\partial_S\Omega,\tag{3.6}$$

where the overbar $\bar{\cdot}$ denotes a tidal average.

At the free surface, the kinematic and stress-free boundary conditions are prescribed:

$$w=\frac{\partial\eta}{\partial t}+u\frac{\partial\eta}{\partial x}+v\frac{\partial\eta}{\partial y},\tag{3.7}$$

$$A_v\frac{\partial u}{\partial z}=A_v\frac{\partial v}{\partial z}=0\qquad\text{at }z=\eta.\tag{3.8}$$

At the bottom, the normal velocity is required to vanish and a partial slip condition is applied. Here, a linear relationship between the bed shear stress and the velocity at the top of the bottom boundary layer is used (Schramkowski and de Swart 2002),

$$w=-\frac{\partial H}{\partial x}u-\frac{\partial H}{\partial y}v,\tag{3.9}$$

$$A_v\left(\frac{\partial u}{\partial z},\frac{\partial v}{\partial z}\right)=s(u,v)\qquad\text{at }z=-H(x,y).\tag{3.10}$$

The slip parameter s depends on the bed roughness, and can vary from 0 in frictionless cases (free slip) to large values in strongly frictional cases (no slip). The vertical eddy viscosity A_v is assumed to be constant in time and depth, neglecting the temporally and vertically varying salinity-induced stratification effects. At the free surface and the bottom, the salt flux is required to vanish,

$$K_v \frac{\partial S}{\partial z}\bigg|_{z=\eta} = K_v \frac{\partial S}{\partial z}\bigg|_{z=-H} = 0. \tag{3.11}$$

Since the main aim of the model is to analyze the salt dynamics at the estuarine scales, the boundary layers where viscous effects are dominant are not resolved (see Winant (2008) for a detailed discussion). Instead of prescribing a velocity at each location of the closed boundaries and the river boundaries, the normal component of the water transport and the tidally-averaged salt transport integrated over the depth are prescribed. At the closed boundaries, the tidally-averaged water/salt transport integrated over the water depth is required to vanish due to impermeability. At the river boundary $\partial_R\Omega$, a river discharge R is prescribed and the tidal discharge is assumed to vanish; the tidally-averaged depth-integrated salt transport through the river boundary is also required to vanish. The resulting conditions read

$$\int_{-H}^{\eta} (u,v)dz \cdot \vec{\mathbf{n}}_h = 0 \quad \text{at } (x,y) \in \partial_C\Omega, \tag{3.12}$$

$$\int_{\partial_R\Omega} \left[\int_{-H}^{\eta} (u,v)\,dz \cdot \vec{\mathbf{n}}_h\right] ds = R \quad \text{at } (x,y) \in \partial_R\Omega. \tag{3.13}$$

$$\left[\overline{\int_{-H}^{\eta}\left(-uS + K_h\frac{\partial S}{\partial x}\right)dz}\ ,\overline{\int_{-H}^{\eta}\left(-vS + K_h\frac{\partial S}{\partial y}\right)dz}\right]\cdot \vec{\mathbf{n}}_h = 0 \text{ at } (x,y) \in \partial_C\Omega \text{ or } \partial_R\Omega. \tag{3.14}$$

Here $\vec{\mathbf{n}}_h$ is the horizontal unit normal vector pointing outwards. The depth-integrated river transport per unit width R_i is assumed to be proportional to the local water depth:

$$R_i(x,y) = \frac{R \cdot H(x,y)}{\int_{\partial_R\Omega} H(x,y)ds} \quad \text{at } (x,y) \in \partial_R\Omega. \tag{3.15}$$

No boundary conditions for the temporally varying salinity transport are prescribed at $\partial_S\Omega$, $\partial_R\Omega$ or $\partial_C\Omega$, as the horizontal and vertical structure of the time-dependent salinity will be directly related to the tidally-averaged salinity field (a detailed discussion will follow in section 3.2.2).

3.2.2 Solution method

Perturbation method

The system of equations (3.1)-(3.15) is solved using an asymptotic expansion of the physical variables in a small parameter ε, which is the ratio of the mean M_2 tidal amplitude ($a_{M_2}^m$) and the mean water depth (H_0^m) obtained by averaging a_{M_2} and H over the seaward boundary ($\partial_S\Omega$). To make a consistent expansion, as a first step, the governing equations are made dimensionless and a scaling analysis is performed to order various terms in the equations with respect to this small parameter ε. As a next step, the physical variables are written as asymptotic expansions in ε,

$$\Gamma = \Gamma_0 + \varepsilon\Gamma_1 + \varepsilon^2\Gamma_2 + \ldots \quad , \tag{3.16}$$

where Γ represents any of the physical variables (η, u, v, w, S). The subscript denotes the order in the expansion. Finally, all terms of the same order in ε are collected and required to balance, resulting in a system of equations at each order of ε.

Using this perturbation approach, the salinity equation at leading order becomes (see details in appendix 3.A)

$$\frac{\partial S_0}{\partial t} = \frac{\partial}{\partial z}\left(K_v \frac{\partial S_0}{\partial z}\right). \tag{3.17}$$

Since there is no horizontal transport of salt at this order, the boundary conditions given in Eq. (3.14) at $\partial_C\Omega$ or $\partial_R\Omega$ are automatically satisfied. The remaining boundary conditions read

$$\overline{S}_0 = S_e(x,y) \qquad \text{at } (x,y) \in \partial_S\Omega, \tag{3.18a}$$

$$K_v \frac{\partial S_0}{\partial z} = 0 \quad \text{at } z = -H \text{ and } z = 0. \tag{3.18b}$$

It is found that the leading-order salinity field S_0 is time-independent and vertically homogeneous (McCarthy 1993, Wei *et al.* 2016), i.e., the tidally-averaged salinity is an unknown function of the horizontal coordinates (x, y):

$$S_0 = S_0(x,y). \tag{3.19}$$

To get a closed formula for S_0, the first-order salinity equation, and the depth-integrated, tidally averaged second-order salinity equation have to be solved. The first-order salinity equation reads

$$\frac{\partial S_1}{\partial t} + u_0 \frac{\partial S_0}{\partial x} + v_0 \frac{\partial S_0}{\partial y} = K_v \frac{\partial^2 S_1}{\partial z^2}, \tag{3.20}$$

which reveals that the temporal and vertical variations of the first order salinity S_1 are forced by the advection of the leading order salinity S_0 by the leading order horizontal velocities u_0 and v_0. The leading order velocities are driven by the M_2 sea surface elevation that is prescribed at the seaward boundary. This tidal motion is independent of salinity, and can be calculated explicitly by numerically solving a two-dimensional wave equation for the leading-order free surface elevation η_0 (Kumar *et al.* 2016). Then, the horizontal tidal velocities are expressed as

$$u_0 = C_1 \frac{\partial \eta_0}{\partial x} + C_2 \frac{\partial \eta_0}{\partial y}, \quad v_0 = -C_2 \frac{\partial \eta_0}{\partial x} + C_1 \frac{\partial \eta_0}{\partial y}, \tag{3.21}$$

where C_1 and C_2 are analytical expressions that describe the vertical structure of the velocity fields (for details see Appendix 3.B and Kumar *et al.* (2016)). The boundary conditions for salinity equation at this order read:

$$\overline{S}_1 = 0 \quad \text{at } (x,y) \in \partial_S \Omega, \tag{3.22a}$$

$$\left(\int_{-H}^{0} \overline{u_0 S_0}\, dz, \int_{-H}^{0} \overline{v_0 S_0}\, dz \right) \cdot \vec{\mathbf{n}}_h = 0 \text{ at } (x,y) \in \partial_C \Omega \text{ or } \partial_R \Omega, \tag{3.22b}$$

$$K_v \frac{\partial S_1}{\partial z} = 0 \quad \text{at } z = -H \text{ and } z = 0. \tag{3.22c}$$

Since the leading order water motion only consists of an M_2 tidal consistent, and the leading order salinity field is time independent, the first order salinity field consists only of a M_2 tidal consistent as well. Hence, the tidally averaged salt transport at O(ε) vanishes, and boundary conditions (3.22a) and (3.22b) are automatically satisfied. By substituting (3.21) into (3.20) and applying boundary condition (3.22c), an analytical expression for the first order salinity S_1 is obtained:

$$S_1 = S_{z_1} \left(\frac{\partial \eta_0}{\partial x} \frac{\partial S_0}{\partial x} + \frac{\partial \eta_0}{\partial y} \frac{\partial S_0}{\partial y} \right) + S_{z_2} \left(\frac{\partial \eta_0}{\partial y} \frac{\partial S_0}{\partial x} - \frac{\partial \eta_0}{\partial x} \frac{\partial S_0}{\partial y} \right). \tag{3.23}$$

Equation 3.23 shows that the horizontal structure of S_1 is directly related to the gradients of the leading-order water elevation and salinity, while its vertical structure, denoted by S_{z_1} and S_{z_2}, is explicitly calculated (for details see Appendix 3.C).

Next, the tidally-averaged, depth-integrated salinity equation at O(ε^2) is derived:

$$\nabla \cdot \begin{pmatrix} \int_{-H}^{0} \overline{u_0 S_1}\, dz \\ \int_{-H}^{0} \overline{v_0 S_1}\, dz \end{pmatrix} + \nabla \cdot \begin{pmatrix} \left[\int_{-H}^{0} \overline{u}_1\, dz + \left(\overline{\eta_0 u_0} \right)|_{z=0} \right] S_0 \\ \left[\int_{-H}^{0} \overline{v}_1\, dz + \left(\overline{\eta_0 v_0} \right)|_{z=0} \right] S_0 \end{pmatrix} - \nabla \cdot \begin{pmatrix} H K_h \partial S_0 / \partial x \\ H K_h \partial S_0 / \partial y \end{pmatrix} = 0, \tag{3.24}$$

i.e., the divergence of the depth-integrated residual salt transport due to all processes has to vanish at each location. The tidally averaged salt transport at this order is a result of advection of the first order salinity S_1 by the leading-order tidal flow (u_0, v_0) (first term), and the leading order salinity S_0 by the first-order residual flow (u_1, v_1) together with transport due to the time-varying sea surface elevation (second term), and diffusive processes (third term).

At the closed boundaries $\partial_C \Omega$ and the river boundaries $\partial_R \Omega$, the normal component of the depth-integrated residual salt transport at O(ε^2) has to vanish,

$$\begin{bmatrix} \int_{-H}^{0} \overline{u_0 S_1}\, dz + \left(\int_{-H}^{0} \bar{u}_1\, dz + \overline{\eta_0 u_0}|_{z=0} \right) S_0 - H K_h \frac{\partial S_0}{\partial x} \\ \int_{-H}^{0} \overline{v_0 S_1}\, dz + \left(\int_{-H}^{0} \bar{v}_1\, dz + \overline{\eta_0 v_0}|_{z=0} \right) S_0 - H K_h \frac{\partial S_0}{\partial y} \end{bmatrix} \cdot \vec{\mathbf{n}}_h = 0 \quad \text{at } (x,y) \in \partial_C \Omega \text{ or } \partial_R \Omega, \tag{3.25}$$

while at the seaward boundary, the tidally-averaged salinity S_0 is prescribed (see Eq. (3.18a)),

$$S_0 = S_e \quad \text{at } (x,y) \in \partial_S \Omega. \tag{3.26}$$

By substituting the expressions for the leading order tidal velocities, Eq. (3.21), and the first order salinity, Eq. (3.23), into Eq. (3.24), an elliptic partial differential equation for S_0 is obtained:

$$-\nabla \cdot \left(H \mathbf{K}_{\mathbf{h}}^{\text{total}} \nabla S_0 \right) + \nabla \cdot (\mathbf{F} S_0) = 0. \tag{3.27}$$

Here

$$\mathbf{K_h^{\text{total}}} = \begin{pmatrix} K_h + K_{h11}^{\text{adv}} & K_{h12}^{\text{adv}} \\ K_{h21}^{\text{adv}} & K_h + K_{h22}^{\text{adv}} \end{pmatrix} \tag{3.28}$$

is the effective total diffusivity tensor and **F** the residual water transport vector. The entries in $\mathbf{K_h^{\text{total}}}$ consist of the prescribed horizontal eddy diffusivity (K_h), and the tidal advective diffusion coefficients (K_{h11}^{adv}, K_{h12}^{adv}, K_{h21}^{adv}, K_{h22}^{adv}), which are induced by the temporal correlation between the leading-order horizontal tidal velocities and the first-order salinity (Wei *et al.* 2016). The tidal advective diffusion coefficients are explicitly evaluated using the leading order water motion:

$$\begin{aligned} K_{h11}^{\text{adv}} = &-\frac{1}{2H}\Re\left\{\left|\frac{\partial\hat{\eta}_0}{\partial x}\right|^2 \int_{-H}^{0} C_1^* S_{z_1}\,dz + \frac{\partial\hat{\eta}_0}{\partial x}\frac{\partial\hat{\eta}_0^*}{\partial y}\int_{-H}^{0} C_2^* S_{z_1}\,dz\right\} \\ &-\frac{1}{2H}\Re\left\{\frac{\partial\hat{\eta}_0}{\partial y}\frac{\partial\hat{\eta}_0^*}{\partial x}\int_{-H}^{0} C_1^* S_{z_2}\,dz + \left|\frac{\partial\hat{\eta}_0}{\partial y}\right|^2 \int_{-H}^{0} C_2^* S_{z_2}\,dz\right\}, \end{aligned} \tag{3.29}$$

$$\begin{aligned} K_{h12}^{\text{adv}} = &-\frac{1}{2H}\Re\left\{\frac{\partial\hat{\eta}_0}{\partial y}\frac{\partial\hat{\eta}_0^*}{\partial x}\int_{-H}^{0} C_1^* S_{z_1}\,dz + \left|\frac{\partial\hat{\eta}_0}{\partial y}\right|^2 \int_{-H}^{0} C_2^* S_{z_1}\,dz\right\} \\ &+\frac{1}{2H}\Re\left\{\left|\frac{\partial\hat{\eta}_0}{\partial x}\right|^2 \int_{-H}^{0} C_1^* S_{z_2}\,dz + \frac{\partial\hat{\eta}_0}{\partial x}\frac{\partial\hat{\eta}_0^*}{\partial y}\int_{-H}^{0} C_2^* S_{z_2}\,dz\right\}, \end{aligned} \tag{3.30}$$

$$\begin{aligned} K_{h21}^{\text{adv}} = &-\frac{1}{2H}\Re\left\{\frac{\partial\hat{\eta}_0}{\partial x}\frac{\partial\hat{\eta}_0^*}{\partial y}\int_{-H}^{0} C_1^* S_{z_1}\,dz - \left|\frac{\partial\hat{\eta}_0}{\partial x}\right|^2 \int_{-H}^{0} C_2^* S_{z_1}\,dz\right\} \\ &-\frac{1}{2H}\Re\left\{-\frac{\partial\hat{\eta}_0}{\partial y}\frac{\partial\hat{\eta}_0^*}{\partial x}\int_{-H}^{0} C_2^* S_{z_2}\,dz + \left|\frac{\partial\hat{\eta}_0}{\partial y}\right|^2 \int_{-H}^{0} C_1^* S_{z_2}\,dz\right\}, \end{aligned} \tag{3.31}$$

$$\begin{aligned} K_{h22}^{\text{adv}} = &-\frac{1}{2H}\Re\left\{\left|\frac{\partial\hat{\eta}_0}{\partial y}\right|^2 \int_{-H}^{0} C_1^* S_{z_1}\,dz - \frac{\partial\hat{\eta}_0}{\partial y}\frac{\partial\hat{\eta}_0^*}{\partial x}\int_{-H}^{0} C_2^* S_{z_1}\,dz\right\} \\ &-\frac{1}{2H}\Re\left\{\left|\frac{\partial\hat{\eta}_0}{\partial x}\right|^2 \int_{-H}^{0} C_2^* S_{z_2}\,dz - \frac{\partial\hat{\eta}_0}{\partial x}\frac{\partial\hat{\eta}_0^*}{\partial y}\int_{-H}^{0} C_1^* S_{z_2}\,dz\right\}. \end{aligned} \tag{3.32}$$

Here $\Re\{\cdot\}$ indicates that the real part is used. The complex amplitude of the M_2 tidal surface elevation is denoted by $\hat{\eta}_0$, and the asterisk (*) denotes the conjugate of a complex variable. Here, K_{h11}^{adv} and K_{h12}^{adv} measure the longitudinal and lateral diffusion, respectively, due to the temporal correlation between u_0 and S_1; K_{h21}^{adv} and K_{h22}^{adv} measure the longitudinal and lateral diffusion due to the temporal correlation between v_0 and S_1. Inclusion of these advective diffusivities in the effective diffusivity tensor shows that in a tidally averaged model, diffusion is generally non-isotropic. The tidal advective diffusion coefficients K_{h12}^{adv}, K_{h21}^{adv} and K_{h22}^{adv} are associated with lateral processes/variations in the leading-order water motion due to geometrical features such as estuarine width convergence, Coriolis deflection and lateral bathymetric variations. In case of no lateral variations of the tidal surface elevation and no Coriolis forcing, i.e., $\partial\hat{\eta}_0/\partial y = 0$ and

$f = 0$, these three diffusion coefficients vanish, and $K_{h_{11}}^{\mathrm{adv}}$ becomes identical to the width-averaged tidal advective diffusivity K_h^{adv} as used in Wei *et al.* (2016). The prescribed horizontal diffusivity K_h parameterizes unresolved processes such as mixing induced by river bends and tidal straining.

The residual water transport in the longitudinal and lateral directions is given by

$$\mathbf{F} = \left(\int_{-H}^{0} \bar{u}_1 \, dz + \overline{\eta_0 u_0}|_{z=0}, \ \int_{-H}^{0} \bar{v}_1 \, dz + \overline{\eta_0 v_0}|_{z=0} \right). \tag{3.33}$$

The first-order residual velocity ($\bar{u}_1$, $\bar{v}_1$) consists of various contributions including tidal rectification of the leading order M_2 tide (denoted by AD), density driven gravitational circulation (GC), the stress-free surface condition (NS), river discharge (RD), and a return flow (TRF). Hence, $\mathbf{F}$ is decomposed into various components:

$$\mathbf{F} = \mathbf{F}^{\mathrm{RD}} + \mathbf{F}^{\mathrm{TRF}} + \mathbf{F}^{\mathrm{AD}} + \mathbf{F}^{\mathrm{NS}} + \mathbf{F}^{\mathrm{GC}}. \tag{3.34}$$

All contributions to $\mathbf{F}$, except for $\mathbf{F}^{\mathrm{GC}}$, are calculated explicitly (without information of the salinity field) by numerically solving a two-dimensional equation for that specific contribution to the residual free surface elevation (see section 3.2.2), while the vertical structure is obtained analytically (see details in Appendix 3.D and Kumar *et al.* (2017)). The residual contribution $\mathbf{F}^{\mathrm{GC}}$ due to the gravitational circulation,

$$\mathbf{F}^{\mathrm{GC}} = \mathbf{B} \nabla \bar{\eta}_1^{\mathrm{GC}} - \mathbf{C} \nabla S_0, \tag{3.35}$$

itself depends on salinity S_0 (here $\mathbf{B}$ and $\mathbf{C}$ are 2×2 matrices, whose elements are known functions of the horizontal coordinates, see details in Appendix 3.D.2). Hence, to obtain S_0, the coupled system of equations, given by

$$\nabla \cdot \left[\left(H \mathbf{K}_{\mathbf{h}}^{\mathrm{total}} + S_0 \mathbf{C} \right) \nabla S_0 \right] - \nabla \cdot \left(S_0 \mathbf{B} \nabla \bar{\eta}_1^{\mathrm{GC}} \right) = \nabla \cdot \left(\tilde{\mathbf{F}} S_0 \right), \tag{3.36}$$

$$\nabla \cdot (\mathbf{B} \nabla \bar{\eta}_1^{\mathrm{GC}}) - \nabla \cdot (\mathbf{C} \nabla S_0) = 0, \tag{3.37}$$

has to be solved simultaneously. Here Eq. (3.36) follows from substituting Eqs. (3.34) and (3.35) into Eq. (3.27), and Eq. (3.37) follows from requiring the divergence of the horizontal residual water transport by gravitational circulation to vanish (see Appendix 3.D.2 for details). Note that, since the leading and first order water motion (except for gravitational circulation) can be calculated explicitly, the only unknown variables in this system of equations are the leading order salinity field S_0 and $\bar{\eta}_1^{\mathrm{GC}}$.

Numerical method

All physical variables of water motion and salinity will be calculated using a standard finite element method (Gockenbach 2006). As a first step, the weak form of the equations is derived. These equations are all two-dimensional (as the vertical structure of all physical variables is derived analytically). Hence, the domain is discretized in the horizontal directions using triangles, and the unknown variables are approximated using polynomial basis functions. Then, these approximations are substituted into their weak form. The numerical solution method for the leading order tidal motion and the first-order residual flow components (except for gravitational circulation) are discussed in detail in Kumar *et al.* (2017, 2016). However, as the gravitational circulation and the tidally averaged salinity field are coupled, the solution procedures as discussed in Kumar *et al.* (2017, 2016) cannot be used, and an iterative approach has to be taken. In order to eliminate any accuracy loss that results from taking derivatives of S_0 and $\bar{\eta}_1^{\mathrm{GC}}$, a special iteration scheme is adopted, in which no information of the gradients of S_0 or $\bar{\eta}_1^{\mathrm{GC}}$ from the previous iteration step is required. This iterative scheme reads

$$\nabla\cdot\left[\left(H\mathbf{K}_{\mathbf{h}}^{\mathrm{total}}+S_0^{(k)}\mathbf{C}\right)\nabla S_0^{(k+1)}\right]-\nabla\cdot\left(S_0^{(k)}\mathbf{B}\nabla\bar{\eta}_1^{\mathrm{GC}^{(k+1)}}\right)=\nabla\cdot\left(\tilde{\mathbf{F}}S_0^{(k)}\right), \tag{3.38}$$

$$\nabla\cdot\left(\mathbf{C}\nabla S_0^{(k+1)}\right)-\nabla\cdot\left(\mathbf{B}\nabla\bar{\eta}_1^{\mathrm{GC}^{(k+1)}}\right)=0, \tag{3.39}$$

where the superscripts k and k+1 denote the physical variables at the $(k)^{\mathrm{th}}$ and $(k+1)^{\mathrm{th}}$ iteration step, respectively.

The weak form of Eqs. (3.38) and (3.39) is derived by multiplying these equations with a test function V, integrating them over the domain Ω, and applying the no normal salt transport boundary conditions and integration by parts:

$$\iint_\Omega\left(H\mathbf{K}_{\mathbf{h}}^{\mathrm{total}}+S_0^{(k)}\mathbf{C}\right)\nabla S_0^{(k+1)}\cdot\nabla V\,dxdy-\iint_\Omega S_0^{(k)}\mathbf{B}\nabla\bar{\eta}_1^{\mathrm{GC}^{(k+1)}}\cdot\nabla V\,dxdy$$
$$=\iint_\Omega\tilde{\mathbf{F}}S_0^{(k)}\cdot\nabla V\,dxdy, \tag{3.40}$$

$$\iint_\Omega\mathbf{C}\nabla S_0^{(k+1)}\cdot\nabla V\,dxdy-\iint_\Omega\mathbf{B}\nabla\bar{\eta}_1^{\mathrm{GC}^{(k+1)}}\cdot\nabla V\,dxdy=0. \tag{3.41}$$

Next, the unknown sea surface elevation related to the gravitational circulation and salinity are approximated using Lagrangian basis functions ϕ_j:

$$\bar{\eta}_1^{\mathrm{GC}^{(k+1)}}=\sum_{j=1}^{N_f}\bar{\eta}_{1_j}^{\mathrm{GC}^{(k+1)}}\phi_j,\quad S_0^{(k+1)}=\sum_{j=1}^{N_f}S_{0_j}^{(k+1)}\phi_j, \tag{3.42}$$

where the ϕ_j's are chosen to be quadratic polynomials, which are equal to 1 at node j and 0 at other nodes, and N_f is the total number of nodes. Substituting (3.42) into (3.40) and (3.41), and taking $V=\phi_i$, the following system of equations (for i=1, 2, ..., N_f) is found:

$$\sum_{j=1}^{N_f}S_{0_j}^{(k+1)}\iint_\Omega\left(H\mathbf{K}_{\mathbf{h}}^{\mathrm{total}}+S_0^{(k)}\mathbf{C}\right)\nabla\phi_j\cdot\nabla\phi_i-\sum_{j=1}^{N_f}\bar{\eta}_{1_j}^{\mathrm{GC}^{(k+1)}}\iint_\Omega S_0^{(k)}\mathbf{B}\nabla\phi_j\cdot\nabla\phi_i$$
$$=\iint_\Omega\tilde{\mathbf{F}}S_0^{(k)}\cdot\nabla\phi_i, \tag{3.43}$$

$$\sum_{j=1}^{N_f}S_{0_j}^{(k+1)}\iint_\Omega\mathbf{C}\nabla\phi_j\cdot\nabla\phi_i-\sum_{j=1}^{N_f}\bar{\eta}_{1_j}^{\mathrm{GC}^{(k+1)}}\iint_\Omega\mathbf{B}\nabla\phi_j\cdot\nabla\phi_i=0. \tag{3.44}$$

This system of equations is linear in the unknown coefficients $\bar{\eta}_{1_j}^{\mathrm{GC}^{(k+1)}}$ and $S_{0_j}^{(k+1)}$ using a known $S_0^{(k)}$. The iterative procedure is stopped when the relative difference between the solutions from the $(k+1)^{\mathrm{th}}$ and k^{th} iteration step,

$$\sqrt{\left(\frac{\iint_{\Omega}\left(X^{(k+1)}-X^{(k)}\right)^2 dxdy}{\iint_{\Omega}\left(X^{(k)}\right)^2 dxdy}\right)}, \tag{3.45}$$

becomes smaller than 5×10^{-4}, with $X=\left(S_0,\ \bar{\eta}_1^{\mathrm{GC}}\right)$. To start the iteration, a prescribed salinity field (e.g., $S_0^{(1)}=0$) is used. When solving this coupled system of equations, special care has to be taken of the seaward boundary, since numerical instabilities can occur when using an arbitrary prescribed water level at this boundary (Chen and Sanford 2009), see detailed procedures in Appendix 3.E.

3.3 Results

In this chapter, schematized estuaries with a simplified geometry and bathymetry are studied. The estuarine width B is assumed to decrease exponentially in the landward direction,

$$B = B_0 e^{-x/L_b}, \tag{3.46}$$

with B_0 the estuarine width at the seaward entrance and L_b the estuarine convergence length (see Fig. 3.2). The seaward boundary is located at $x=0$, and the landward boundary is located at $x=L$. The mid-axis of the idealized estuary is located at $y=0$, and the lateral boundaries at $y=\pm B/2$.

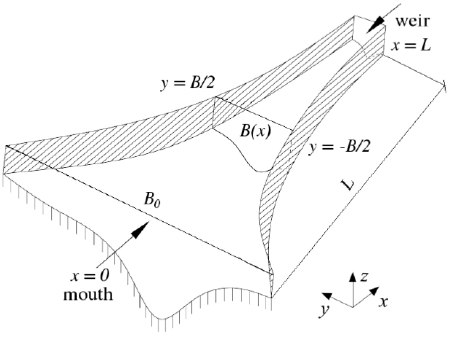

Figure 3.2: A three-dimensional sketch of an idealized estuary, where x is the longitudinal coordinate pointing towards the landward direction, and y the lateral coordinate towards the right bank (looking seaward). The estuarine mouth (seaward boundary) is located at $x=0$ and the weir (landward boundary) at $x=L$. The side walls (lateral boundaries) are located at $y=\pm B/2$.

In this geometry, the contribution of each physical process to the along-channel residual salt transport can be obtained by integrating Eq. (3.24) from the left bank of the channel ($y=y_1$) to the right bank ($y=y_2$), and subsequently integrating from the weir located at $x=L$ (where the cross-sectionally integrated longitudinal salt transport vanishes) to any longitudinal location x,

$$\int_{y_1}^{y_2} S_0 F_1 dy + \int_{y_1}^{y_2}\int_{-H}^{0} \overline{S_1 u_0} dz dy = \int_{y_1}^{y_2} H K_h \frac{\partial S_0}{\partial x} dy. \tag{3.47}$$

Here F_1 is the longitudinal component of the depth-integrated residual water transport. Substituting the decomposition of the residual transport Eq. (3.34) into (3.47) yields

$$\underbrace{\int_{y_1}^{y_2} S_0 F_1^{\mathrm{AD}} dy}_{\mathrm{AD}} + \underbrace{\int_{y_1}^{y_2} S_0 F_1^{\mathrm{GC}} dy}_{\mathrm{GC}} + \underbrace{\int_{y_1}^{y_2} S_0 F_1^{\mathrm{RD}} dy}_{\mathrm{RD}} + \underbrace{\int_{y_1}^{y_2} S_0 F_1^{\mathrm{TRF}} dy}_{\mathrm{TRF}} + \underbrace{\int_{y_1}^{y_2} S_0 F_1^{\mathrm{NS}} dy}_{\mathrm{NS}}$$
$$+ \underbrace{\int_{y_1}^{y_2}\int_{-H}^{0} \overline{S_1 u_0} dz dy}_{\mathrm{TASF}} - \underbrace{\int_{y_1}^{y_2} H K_h \frac{\partial S_0}{\partial x} dy}_{\mathrm{DIF}} = 0. \tag{3.48}$$

This expression shows that the cross-sectionally integrated tidally-averaged salt transport due to tidal rectification (AD), gravitational circulation (GC), river discharge (RD), tidal return flow including Stokes' drift (TRF), the stress-free surface condition (NS), tidal advective salt transport (TASF), and diffusion (DIF) balance each other, and their relative importance at each longitudinal location can be assessed individually. Here the tidal advective salt transport represents the residual salt transport caused by the advection of tidal salinity by the tidal velocity, which is called tidal oscillatory salt flux in Lerczak *et al.* (2006) and Wang *et al.* (2015).

In section 3.3.1, the salt dynamics for the default experiment, representative for the Delaware estuary, will be discussed; in section 3.3.2, the influence of estuarine width convergence, Coriolis effects and estuarine bathymetry on salt dynamics are investigated using three dedicated experiments.

3.3.1 Salt dynamics for the default experiment

For the default experiment, parameters representative for the Delaware estuary are used: $L = 215$ km, $B = 39$ km (see values of all default parameters in Table 3.1). In this default experiment, the water motion is forced by an M_2 tide at the mouth with a tidal amplitude a_{M_2} (=0.75 m). A river discharge $R = 72$ m^3 s^{-1} (low discharge condition) is prescribed at the landward end of the estuary (at $x = L$), where a weir is located (Wei *et al.* 2016). The bathymetry of the Delaware estuary is characterized by a channel in the center and shallow shoals on the sides, with the lateral depth difference between the channel and the shoals decreasing landward (Aristizábal and Chant 2013). To qualitatively capture this spatial dependency, the bathymetry is described by

$$H(x,y) = H_{\mathrm{min}} + (H_{\mathrm{m}} - H_{\mathrm{min}})\frac{x}{L} + (H_{\mathrm{max}} - H_{\mathrm{min}})\left(1 - \frac{x}{L}\right)\left(1 - \frac{4y^2}{B^2}\right)e^{-C_f\frac{4y^2}{B^2}}, \tag{3.49}$$

with H_{max} (=15 m) and H_{min} (=3.6 m) the maximum and minimum water depths at the mouth. The width-averaged water depth H_{m} is longitudinally constant (H_{m} =8 m). By varying the parameter C_f, the width of the tidal flats is varied, with larger values of C_f

corresponding to wider shoals and a narrower channel, and smaller values to narrower shoals and a wider channel.

The vertical eddy viscosity A_v is assumed to be linearly proportional to the local water depth (Friedrichs and Hamrick 1996), and the same is assumed for the partial slip parameter s:

$$(A_v, s) = \frac{H}{H_\mathrm{m}} \left(A_{v_m}, s_m\right), \tag{3.50}$$

with $A_{v_m} = 0.005$ m^2 s^{-1} and $s_m = 0.039$ m s^{-1} the width-averaged friction parameters, which are the same as those used in Wei *et al.* (2016). Using these parameter settings, the leading-order tidal surface elevation obtained from the present 3D model is nearly the same as that obtained in the width-averaged model of Wei *et al.* (2016), the tidal surface gradients and velocities, however, change significantly by considering the three-dimensional effects. The horizontal eddy diffusivity has to be prescribed and is assumed to decrease from the mouth to the landward side, indicating that more unresolved processes have to be parameterized near the mouth (such as rapid depth variations, multiple channels, complex sea-estuary interactions, and tidally varying mixing effects). These unresolved processes are assumed to be proportional to the estuarine width as

$$K_h = K_h^r + K_h^m \frac{B}{B_0}, \tag{3.51}$$

with K_h^r =10 m^2 s^{-1} and K_h^e =40 m^2 s^{-1}. An overview of all default parameters is shown in Table 3.1.

Tidally averaged salinity field and longitudinal salt transport

The salinity is prescribed to be 31 psu at the seaward side, and it reduces to 2 psu at $\sim$ 120 km inside the estuary, as shown by the background colors in Fig.3.3, where the white color indicates a salinity of ~31 psu and black a vanishing salinity. Hence, the salt intrusion length L_s, which in this chapter is defined as the distance between the estuarine mouth to the location where the cross-sectionally averaged salinity is 2 psu, is 120 km. This salt intrusion length agrees well with the observed salinity profile under low river discharge (Kuijper and Van Rijn 2011, Wei *et al.* 2016), confirming that the longitudinal dependency of the horizontal diffusivity K_h as given in Eq. (3.51) is appropriate for the Delaware estuary. A lateral variation of S_0 (of ~1 psu) is found, with larger tidally averaged salinities on the left shoals than those on the right, looking seaward. This lateral distribution qualitatively agrees with the observation of the Delaware Bay near the mouth (Wong 1994).

To visualize the residual salt transport pattern, streamlines of the depth-integrated salt transport are used. Since the depth-integrated residual salt transport is divergence free (see Eq. 3.27), the amount of salt transported through any area connecting the same streamlines is constant. The streamlines of the residual salt transport are shown in Fig. 3.3a, where solid lines indicate counter-clockwise salt transport, and dashed-dotted lines indicate clockwise salt transport (looking into the paper). It is found that, in the idealized Delaware estuary, salt is mostly transported counter-clockwise, meaning the salt is

Table 3.1: Default parameters, representative for the Delaware estuary

Parameter	Value	Unit
L	215	km
L_b	42	km
B_0	39	km
H_{min}	3.6	m
H_{max}	15	m
C_f	4	
H_{m}	8	m
A_{v_m}	0.005	$\mathrm{m}^2\ \mathrm{s}^{-1}$
s_m	0.039	$\mathrm{m}\ \mathrm{s}^{-1}$
K_{h}	10-50	$\mathrm{m}^2\ \mathrm{s}^{-1}$
R	72	$\mathrm{m}^3\ \mathrm{s}^{-1}$
a_{M_2}	0.75	m
S_e	31	psu
f	1×10^{-4}	$\mathrm{rad}\ \mathrm{s}^{-1}$

transported into the estuary from the left side of the estuary, and out of the estuary from the right side of the channel looking seaward.

Since the salt transport between the same streamlines is constant, large distances between these streamlines indicate small (normal) salt transports and small distances indicate large transports. As shown in Fig. 3.3a, the distance between the two neighbouring streamlines first increases from the left bank to the mid-axis (at $y = 0$), and then decreases sharply towards the right bank. This suggests an interesting steady-state salt transport pattern: salt is transported landward from the left side of the mouth towards the mid-axis, and gets quickly transported out of the estuary on the right of the channel. To evaluate the relative importance of various longitudinal salt transport processes, the along-channel salt transport at each cross-section is calculated using Eq. (3.48). As shown in Fig. 3.3b, the seaward salt transport due to river discharge (line with upside-down triangles) is mainly balanced by the landward salt transport due to the tidal advective diffusion (line with triangles) and prescribed diffusion (line with asterisks). Gravitational circulation (solid line) and tidal rectification (dash-dotted lines) transport salt landward in the central region of salt intrusion. The residual flow due to the stress-free surface condition (line with crosses) and tidal return flow (dashed line) transport salt landward only near the mouth. The total amount of salt transport is zero (dotted line in 3.3b) by definition, as the salt content in the estuary is constant in steady state.

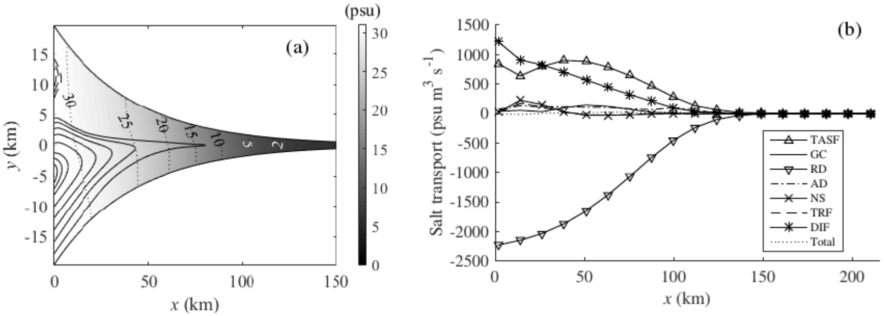

Figure 3.3: (a) Residual salinity distribution (see gray colors and dotted lines) and streamlines of the depth-integrated salt transport (see solid and dash-dotted lines). (b) The cross-sectionally integrated along-channel salt transport due to each physical process. Positive values denote landward salt transport, and negative values denote seaward salt transport.

Salt transport due to each process

In equilibrium, the divergence of the total depth-integrated salt transport is zero at every location. However, the divergence of salt transport due to each physical transport process separately is not necessarily zero, indicating a local change of the salt content due to each process. If the divergence of the salt transport due to one process has locally a negative (positive) value, it implies this process contributes to an increase (a decrease) of salt content at that location.

Figs. 3.4a-e show the divergence of the salt transport due to diffusive processes (including tidal advective diffusion and prescribed diffusion), gravitational circulation, tidal rectification, stress-free surface condition and tidal return flow, respectively. Local convergences of salt are shown in blue and divergences of salt in red. The lines in Figs. 3.4a-e show the direction of salt transport due to each process. The solid (dash-dotted) lines in Figs. 3.4b-e indicate the salt is transported in a counter-clockwise (clockwise) direction. Note that these lines are not the streamlines for the residual salt transport but for the residual water transport, since the divergence of the residual salt transport for each process individually does not vanish.

The diffusive processes transport salt from the shoals towards the channel and subsequently towards the upstream (Fig. 3.4a). The diffusive processes result in an increase of salinity on the right side of the estuary and a decrease on the left. The convergences and divergences of the diffusive salt transport is significant especially in the central region near the channel, with a salt convergence of up to 1×10^{-4} psu m s^{-1}. Moreover, the salt convergence on the right exceeds the salt decrease on the left side, resulting in an increase of salt content integrated over a cross-section. This increase in salt content agrees with the decreasing longitudinal salt transport by diffusive processes, as shown in Fig. 3.3b.

The two-cell streamlines of gravitational circulation show that the density-driven flow transports salt landward into the estuary through the channel, reverses direction in the central region, and then transports salt out of the estuary over the shoals (see Fig. 3.4b). The salt transport induced by gravitational circulation is asymmetric with respect to the

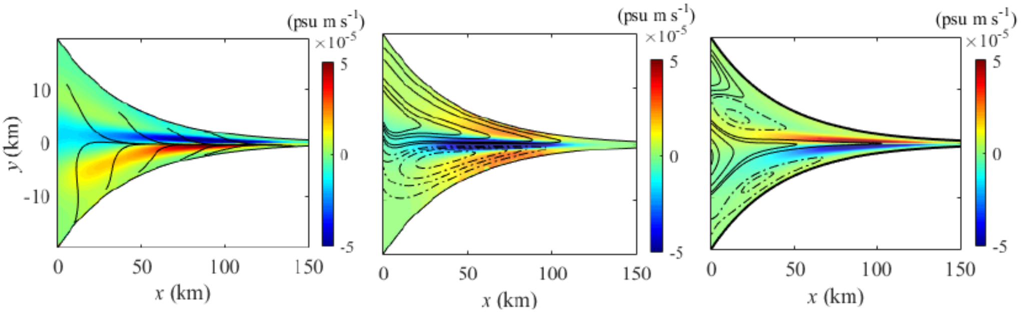

(a) Diffusive processes

(b) Gravitational circulation

(c) Tidal rectification

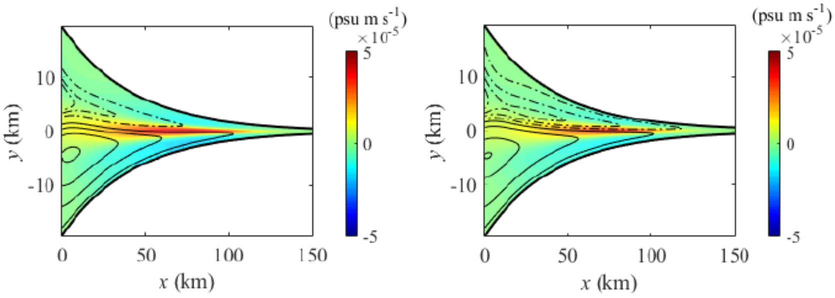

(d) Stress-free surface

(e) Tidal return flow

Figure 3.4: The divergence of residual salt transport due to each process. Positive values indicate local decreases of salt content (shown in red), while negative values indicate local increases of salt content (shown in blue). The lines show the directions of the residual salt transport due to each process.

mid-axis due to the Coriolis deflection: the landward salt transport is deflected towards the left bank, and the seaward transport is deflected towards the right bank. Even though the longitudinal salt transport (integrated over a cross-section) induced by gravitational circulation is much smaller than that induced by the diffusive processes, the gravitational circulation makes a significant contribution to local changes in salinity. The gravitational circulation induces a significant divergence of salt on the shoals, and a large increase of salt in the channel, which reaches up to 5×10^{-5} psu m s^{-1} in the central region of salt intrusion.

The salt transport induced by residual flow due to tidal rectification, stress-free surface condition, and tidal return flow all show a similar pattern, with salt transported into the estuary over the shoals and out through the channel (see Figs. 3.4c-e). The tidal rectification results in a convergence of salt on the left side of the channel, accompanied with a strong divergence of salt on the right. The stress-free surface condition and tidal return flow, however, contribute to a divergence of salt in the channel and a convergence of salt on the shoals.

3.3.2 Influence of estuarine geometry, Coriolis and bathymetry

The salt transport processes in the default experiment are affected by the interplay between estuarine geometry, Coriolis deflection, and bathymetry. To investigate the influence of estuarine width convergence on salt dynamics separately, an exponentially convergent channel with a horizontal bottom, no Coriolis, is studied in experiment I. In experiment II, the Coriolis force is added, hence the influence of the Coriolis force on salt dynamics is found by comparing the results obtained in experiment II with those found in experiment I. In experiment III, the default bathymetry profile with a lateral channel-shoal structure (see Eq. (3.49)) is used, but now the Coriolis force is neglected. Hence, the influence of bathymetric variations on salt dynamics is found by comparing the results from experiments III and I. The parameters used to define estuarine bathymetry and the Coriolis parameter are summarized in Table 3.2.

Table 3.2: Model parameters for experiments I-III

Experiments	H_{max} (m)	H_{min} (m)	f (rad s^{-1})
I	8.0	8.0	0
II	8.0	8.0	10^{-4}
III	15.0	3.6	0

Influence of estuarine width convergence (experiment I)

In a convergent channel without bathymetric variations or Coriolis force, the salt intrusion length is only 105 km, which is much smaller than that in the default experiment (120 km). The tidally averaged salinity is symmetric with respect to the mid-axis, with the salinity near the banks slightly larger than that in the middle (see Fig. 3.5a). Since no circulation cells of salt transport are formed, the depth-integrated residual salt transport is zero at each location, and no streamlines are obtained.

The residual salt balance is identical to that obtained from the width-averaged model (Wei *et al.* 2016), where the seaward salt transport induced by river discharge is balanced by the landward transport by tidal advective diffusion and prescribed diffusion (Fig. 3.5b). The residual flow induced by gravitational circulation, tidal rectification, stress-free surface and the tidal return flow, however, makes no contributions to the residual salt balance (integrated over the cross-section).

The divergence of the residual salt transport induced by the diffusive processes, as shown in Fig. 3.6, indicates that diffusion results in a convergence (increase) of salt in the central region of the estuary. The salt transport paths induced by the diffusive processes are fully adapted to the estuarine geometry, with no horizontal circulations formed.

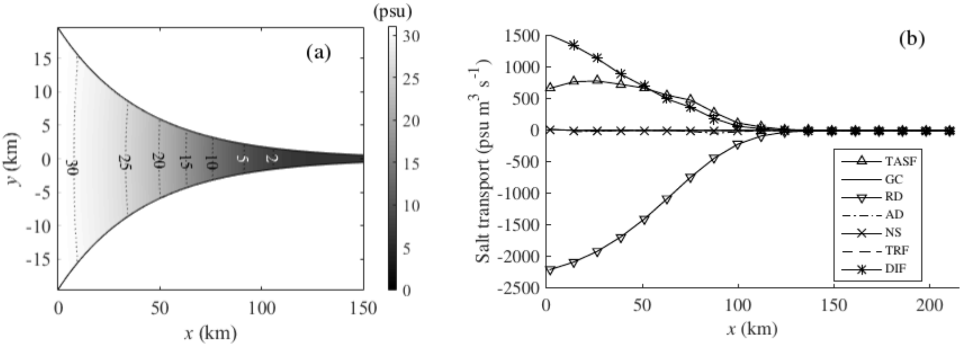

Figure 3.5: The same as Fig. 3.3, but for experiment I.

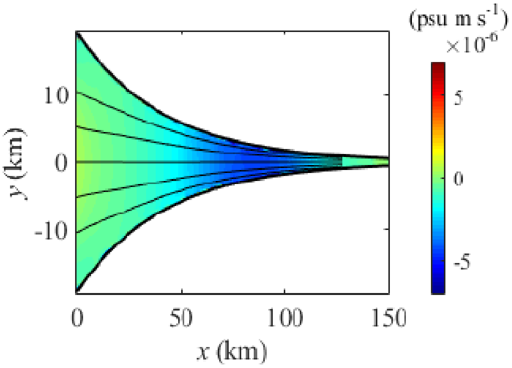

Figure 3.6: The same as Fig. 3.4, but for the divergence of salt transport induced by diffusive processes in experiment I.

Influence of Coriolis deflection (experiment II)

Including the Coriolis force in the convergent channel slightly increases the salt intrusion length to 108 km, with salinities on the left larger than that on the right (see Fig. 3.7a). The salt transport pattern is significantly changed by the Coriolis deflection, with salt transported into the estuary from the left side of the channel and out from the right. Comparing the streamlines of the total salt transport in experiments I-II, it is found that the geometry-induced salt transport pattern as found in experiment I is replaced by a Coriolis-induced pattern in experiment II by including Coriolis force. It suggests that the influence of the Coriolis deflection on the total salt transport is much stronger than that of estuarine width convergence. Due to the Coriolis deflection, the seaward salt transport induced by river discharge is mainly balanced by the landward salt transport induced by diffusive processes, while the residual flow due to the stress-free surface condition and the tidal return flow makes a small but non-negligible contribution (see Fig. 3.7b). The gravitational circulation, however, does not contribute to the residual salt balance. Due to the Coriolis force, the landward salt transport by diffusive processes, is deflected towards

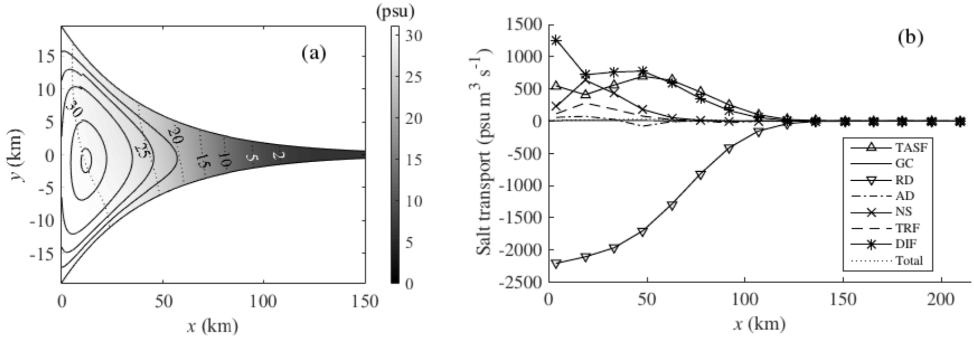

Figure 3.7: The same as Fig. 3.3, but for experiment II.

the left side of the estuary (see Fig. 3.8a), decreasing the cross-sectionally integrated longitudinal salt transport due to this contribution. It results in a significant divergence of salt on the left side and a convergence of salt on the right. The magnitude of local change in salinity induced by diffusive processes reaches up to 2×10^{-5} psu m s^{-1}, much larger than that in experiment I where no Coriolis is included. The residual flow due to the stress-free surface condition and the tidal return flow tends to transport salt landward from the left side of the estuary and seaward from the right (see solid lines in Figs. 3.8b, c). It results in a remarkable convergence of salt on the left side of the estuary and a divergence of salt on the right. The local change of salt induced by the stress-free surface condition and the tidal return flow are up to 1×10^{-5} psu m s^{-1} and 2×10^{-6} psu m s^{-1}, respectively (see color scales in Figs. 3.8b, c). The salt transport induced by tidal rectification and gravitational circulation are negligible (not shown).

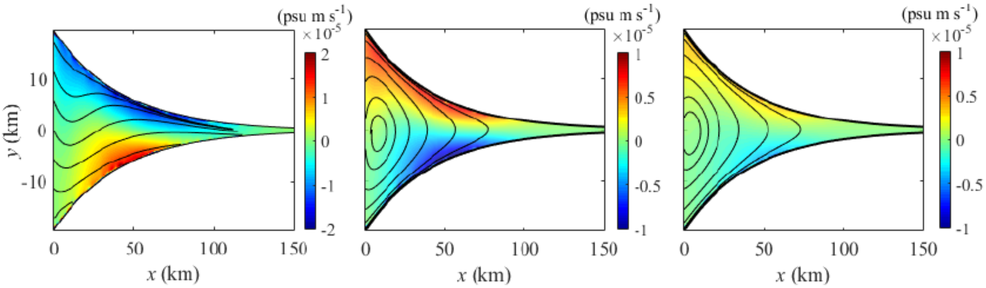

(a) Diffusive processes (b) Stress-free surface (c) Tidal return flow

Figure 3.8: The same as Fig. 3.4, but for the divergence of salt transport induced by (a) diffusive processes, (b) stress-free surface condition and (c) tidal return flow in experiment II.

Influence of estuarine bathymetry (experiment III)

By including a lateral channel-shoal structure, the salt intrusion length is significantly increased to 117 km (see Fig. 3.9a), compared to experiment I. Furthermore, the tidally averaged salinities become higher in the channel than those on the shoals. The residual salt transport patterns are also completely changed: the salt is transported landward over the shoals and seaward through the channel. This clearly shows the influence of bathymetric variations is larger than that of the estuarine width convergence. By including the bathymetric variations, the landward salt transport contributions due to tidal advective diffusion, prescribed diffusion and gravitational circulation are increased (see Fig. 3.9b). On the other hand, the residual flow induced by the stress-free surface condition and tidal return flow tends to transport salt seaward, in contrast to their landward salt transport contributions in experiment II. The salt transport due to tidal rectification is very small compared to the other processes.

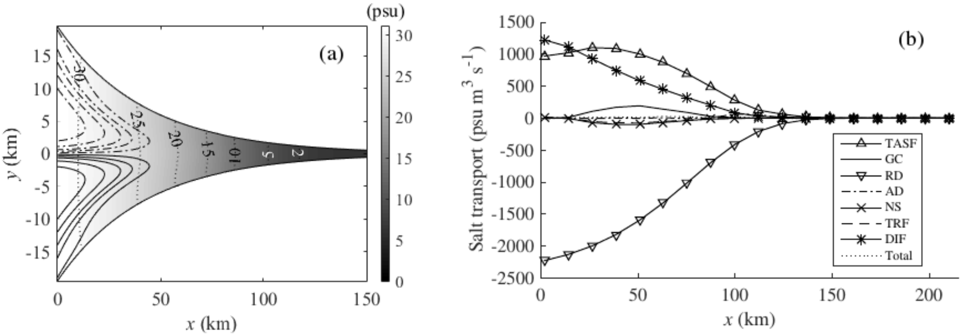

Figure 3.9: The same as Fig. 3.3, but for experiment III.

Due to the lateral channel-shoal structure, the diffusive processes transport salt from the shoals to the channel, and then transport salt landward (see Fig. 3.10a). This is accompanied with a convergence of salt in the channel and a divergence of salt on the shoals. The gravitational circulation presents a landward flow in the channel and a seaward flow on the shoals, as found by Wong (1994), transporting salt into the estuary through the channel and out over the shoals (see Fig. 3.10b). It results in a strong convergence of salt in the channel and a small divergence of salt on the shoals. The residual flow induced by tidal rectification, stress-free surface condition and tidal return flow is characterized by a net landward flow over the shoals and balanced by a return (seaward) flow in the channel (see Figs. 3.10c-e). The pattern of these three residual components is consistent with the topography-induced exchange flow as found by Li and O'Donnell (1997) (without considering density), which tends to transport salt landward over the shoals and seaward through the channel. This result in a divergence of salt in the channel and a convergence of salt on the shoals. The amount of local salt loss induced by the tidal return flow or stress-free surface condition is up to 5×10^{-5} psu m s^{-1}. The salt change induced by the tidal rectification is very small (less than 1×10^{-5} psu m s^{-1}) compared to the default experiment. This confirms that the effects of earth rotation are very important in generating the tidally rectified flow, as reported in Huijts *et al.* (2009).

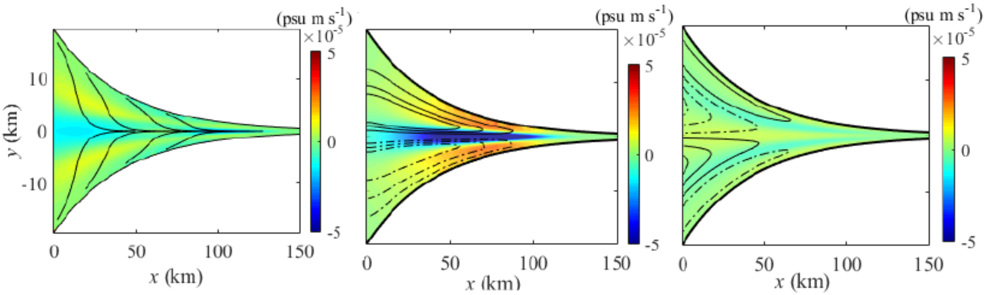

(a) Diffusive processes (b) Gravitational circulation (c) Tidal rectification

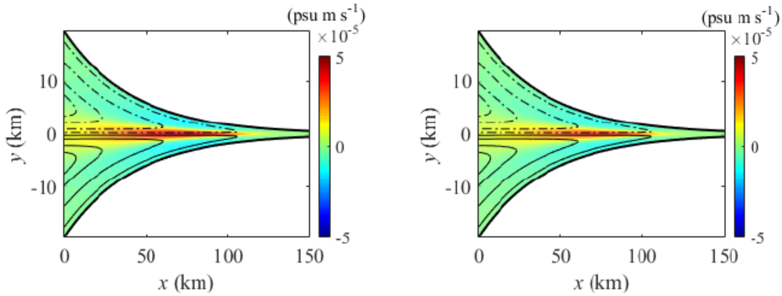

(d) Stress-free surface (e) Tidal return flow

Figure 3.10: The same as Fig. 3.4, but for experiment III.

3.4 Discussion

The importance of various physical processes on salt intrusion length is evaluated by excluding each process individually and comparing corresponding changes in the salt intrusion length. It is found that the tidal advective diffusion is the predominant physical process for longitudinal salt intrusion, which is hardly influenced by residual circulations (except for the river-induced flow). Since tidal advective diffusion is strongly influenced by many factors such as bottom friction, vertical mixing, external tidal forcing, estuarine bathymetry and geometry (Wei *et al.* 2016), it is deduced that the salt intrusion length changes significantly with these factors. Though the residual circulations make no big contributions to the salt intrusion length, they are crucial for the transverse structure of the tidally averaged salinity, which is essential for the transverse gravitational circulation and thence lateral sediment trapping in tidal estuaries (Huijts *et al.* 2006).

In section 3.4.1, the salt transport induced by tidal advective diffusion in the idealized Delaware estuary is explained by comparing results of the experiments I-III with those of the default experiment. The resulting tidal advective diffusivity coefficients are discussed in relation to estuarine geometry, bathymetry and Coriolis. The salt transport induced by the gravitational circulation, the strongest residual circulation process in the Delaware estuary, is discussed in section 3.4.2.

3.4.1 Tidal advective diffusion

Tidal advective salt flux

The salt flux induced by tidal advective diffusion (i.e., tidal advective salt flux) is a result of the temporal correlation between the tidal salinity (S_1) and the three-dimensional tidal currents (u_0, v_0, w_0). The longitudinal tidal advective salt flux can be expressed in terms of the amplitudes of u_0 and S_1 and their phase difference (Wei *et al.* 2016),

$$\overline{u_0 S_1} = \frac{1}{2}|u_0||S_1|\cos(\Phi_S - \Phi_u), \tag{3.52}$$

where Φ_S, Φ_u, $|S_1|$, and $|u_0|$ are the phases and amplitudes of S_1 and u_0, respectively. Similarly, the transverse tidal advective salt flux ($\overline{v_0 S_1}$, $\overline{w_0 S_1}$) is related to the amplitudes of the transverse tidal velocities, the tidal salinity, and their phase differences. The cross-sectional distributions of the longitudinal and transverse tidal advective salt fluxes are shown in Fig. 3.11 by gray scales and by arrows, respectively. All cross-sections are located at $x \sim 40$ km.

In experiment I, the longitudinal tidal advective salt flux is similar to that from a width-averaged model by Wei *et al.* (2016). The longitudinal tidal advective salt flux is nearly laterally uniform, with landward fluxes near the surface and seaward fluxes near the bottom (see contours in Fig. 3.11a). Moreover, the estuarine width convergence results in a lateral tidal current, which interacts with the tidal salinity and transports salt towards the mid-axis near the free surface and towards the banks near the bottom. This geometry-induced transverse tidal advective salt flux is smaller than 0.005 psu m s^{-1} (see arrows in Fig. 3.11a). When including the Coriolis effects (experiment II), $|u_0|$ and $|S_1|$ become larger on the left than the right (see Figs. 3.12a, b), while their phase differences remain almost unchanged (see Fig. 3.12c). This results in a larger longitudinal tidal advective salt flux on the left than on the right (see Fig. 3.11b). In the transverse direction, the lateral tidal current induced by the Coriolis effects interacts with the tidal salinity and yields salt fluxes towards the left near the surface and towards the right near the bottom. This Coriolis-induced circulation, together with the geometry-induced circulation, results in a slightly enhanced counter-clockwise salt transport on the right side of the estuary, and a slightly weakened clockwise transport on the left (see arrows in Fig. 3.11b).

In experiment III, tides propagate faster in the channel than on the shoal, resulting in a larger $|u_0|$ and $|S_1|$ in the channel than on the shoals (see Figs. 3.12d, e). Meanwhile, u_0 in the channel lags that on the shoals, and S_1 on the shoals lags that in the channel. Thus, in the channel, the phase difference between u_0 and S_1 is smaller than 90° near the surface, and slightly larger than 90° near the bottom; on the shoals, it is larger than 90° near the bottom, and smaller than 90° near the surface (see Fig. 3.12f). This results in an enhanced landward tidal advective salt transport near the surface (a relatively small seaward transport near the bottom) of the channel. On the shoals, since $|u_0|$ and $|S_1|$ are much smaller than those in the channel, the induced salt fluxes are much smaller (see gray scales in Fig. 3.11c). Integrated over the depth, the landward tidal advective salt transport is much stronger in the channel. Moreover, the interaction between the tidal salinity and the lateral tidal current induced by the lateral depth variations results in axial-convergent

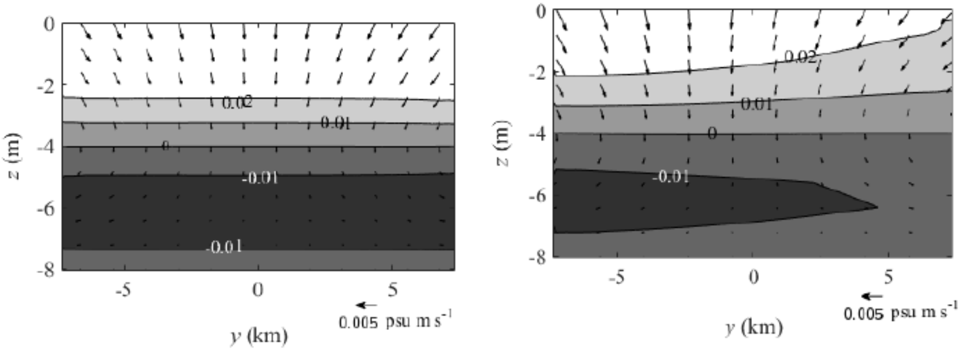

(a) Experiment I

(b) Experiment II

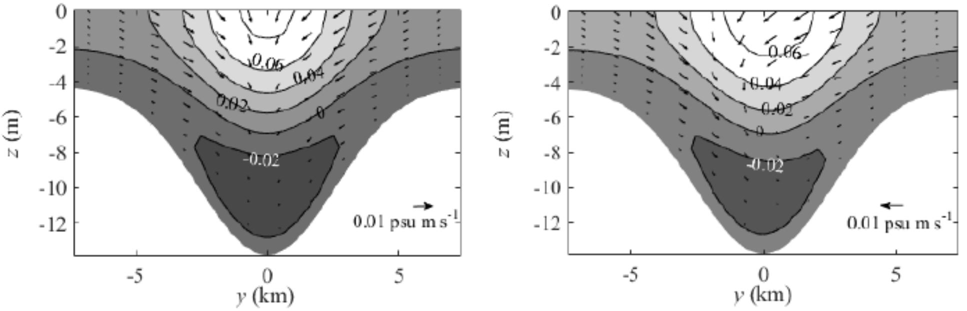

(c) Experiment III

(d) Default experiment

Figure 3.11: The transverse structure of the three-dimensional tidal advective salt flux $(\overline{u_0 S_1}, \overline{v_0 S_1}, \overline{w_0 S_1})$. Gray scales and contours show the along-channel flux, while arrows show the magnitude and direction of the transverse fluxes. Positive (negative) along-channel salt fluxes are transported landward. The vertical salt flux is scaled by a factor of 300 larger than the lateral flux. The perspective is looking seaward for all cross-sectional plots.

tidal advective salt fluxes (up to 0.01 psu m s^{-1}) towards the mid-axis at all depths (see arrows in Fig. 3.11c).

Comparing the tidal advective salt fluxes in experiments I-III with the default experiment suggests that the lateral bathymetric variations dominate the longitudinal tidal advective salt fluxes in the Delaware estuary. The lateral tidal advective salt fluxes, however, are influenced by estuarine width convergence, Coriolis and bathymetry. Due to the overall effects, the tidal advective salt fluxes towards the left on the top right of the channel, as well as the fluxes towards the right on the bottom left, are augmented (see Fig. 3.11d).

Tidal advective diffusivity

The strength of the depth-integrated salt transport due to tidal advective diffusion is measured by the tidal advective diffusion coefficients, which result from the temporal corre-

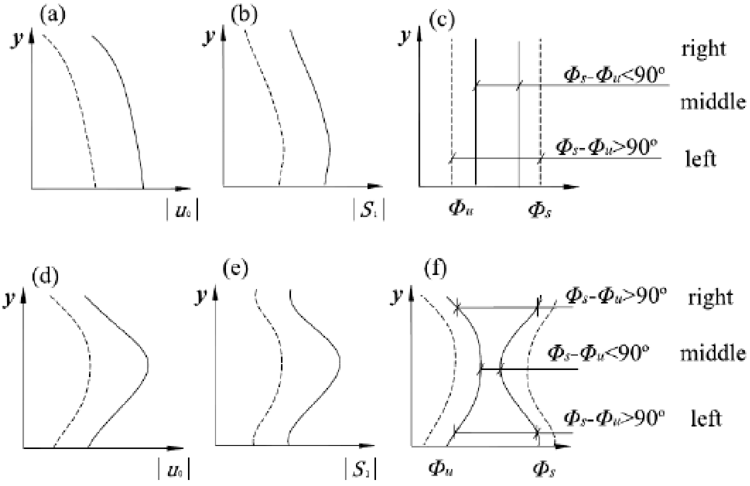

Figure 3.12: A qualitative view of the lateral profiles of $|u_0|$, $|S_1|$, and the phase difference ($\Phi_S - \Phi_u$) influenced by Coriolis effects (a-c) and lateral bathymetric variations (d-f). The amplitudes and phase difference near the surface are shown by solid lines, and those near the bottom by dashed lines.

lation between the longitudinal/lateral tidal velocities and tidal salinities (see Eqs. (3.29)-(3.32)). Since more processes are resolved in a three-dimensional model compared to a width-averaged approach, it is thus expected that the prescribed diffusion coefficient (including unresolved processes) has to be smaller compared to the values that have to be used in width-averaged models, to qualitatively reproduce the observed salt intrusion in the Delaware estuary. Figure 3.13 shows the tidal advective diffusion coefficients for all experiments. Here, only $K_{h_{11}}^{\mathrm{adv}}$, $K_{h_{12}}^{\mathrm{adv}}$ and $K_{h_{21}}^{\mathrm{adv}}$ are shown because $K_{h_{22}}^{\mathrm{adv}}$ ($\lesssim 1$ m^2 s^{-1}) is much smaller than the other diffusion coefficients.

The tidal advective diffusivity $K_{h_{11}}^{\mathrm{adv}}$ is positive in all experiments, confirming that the temporal correlation between u_0 and S_1 always results in a landward salt transport integrated over the depth (Wei *et al.* 2016). In experiment I, $K_{h_{11}}^{\mathrm{adv}}$ is almost the same as obtained from the width-averaged model in Wei *et al.* (2016) which is laterally uniform (see Fig. 3.13a). This implies that the estuarine width convergence has little influence on $K_{h_{11}}^{\mathrm{adv}}$. However, different from the width-averaged model, $K_{h_{12}}^{\mathrm{adv}}$ and $K_{h_{21}}^{\mathrm{adv}}$ become non-negligible (see Figs. 3.13b, c).

Coriolis effects significantly change the spatial pattern of $K_{h_{11}}^{\mathrm{adv}}$ compared to experiment I, with larger magnitudes on the left than on the right (see Fig. 3.13d), resulting in a larger along-channel tidal advective salt transport on the left. Moreover, $K_{h_{12}}^{\mathrm{adv}}$ and $K_{h_{21}}^{\mathrm{adv}}$ show slightly larger magnitudes near the entrance compared to experiment I (see Figs. 3.13e, f), and are almost unchanged in the landward region. In experiment III, $K_{h_{11}}^{\mathrm{adv}}$ is strongly increased in the channel and decreased on the shoals (see Fig. 3.13g). This lateral difference of $K_{h_{11}}^{\mathrm{adv}}$ contributes to a stronger along-channel tidal advective salt transport in the channel than on the shoals. The lateral bathymetric variations also significantly increase the magnitudes of $K_{h_{12}}^{\mathrm{adv}}$ and $K_{h_{21}}^{\mathrm{adv}}$ (see Figs. 3.13h-i). Comparing

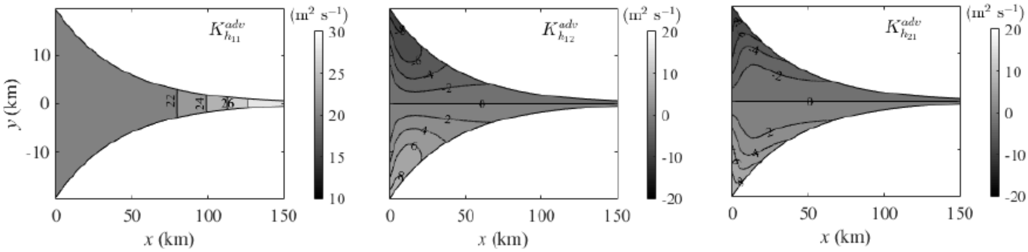

(a) $K_{h_{11}}^{\text{adv}}$ in expt. I (b) $K_{h_{12}}^{\text{adv}}$ in expt. I (c) $K_{h_{21}}^{\text{adv}}$ in expt. I

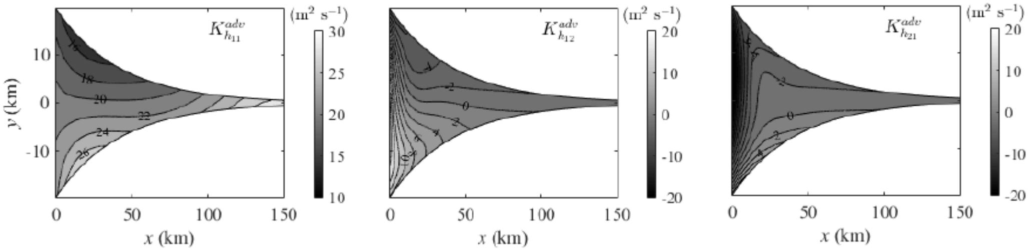

(d) $K_{h_{11}}^{\text{adv}}$ in expt. II (e) $K_{h_{12}}^{\text{adv}}$ in expt. II (f) $K_{h_{21}}^{\text{adv}}$ in expt. II

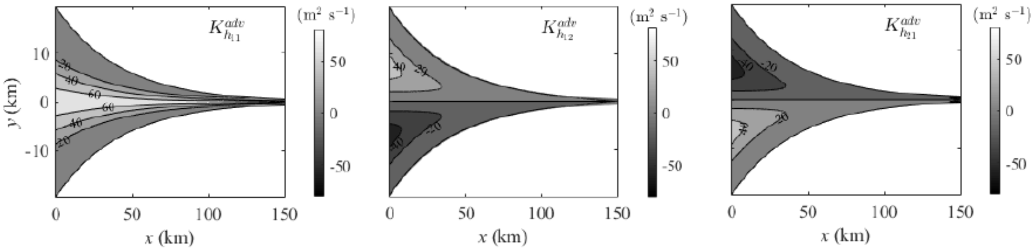

(g) $K_{h_{11}}^{\text{adv}}$ in expt. III (h) $K_{h_{12}}^{\text{adv}}$ in expt. III (i) $K_{h_{21}}^{\text{adv}}$ in expt. III

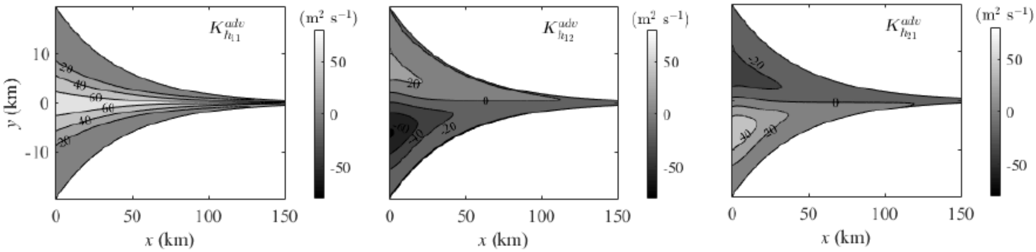

(j) $K_{h_{11}}^{\text{adv}}$ in default expt. (k) $K_{h_{12}}^{\text{adv}}$ in default expt. (l) $K_{h_{21}}^{\text{adv}}$ in default expt.

Figure 3.13: The tidal advective diffusion coefficients for all experiments.

experiments I-III with the default experiment suggests that lateral bathymetric variations dominate the magnitudes of the tidal advective diffusion coefficients. The Coriolis force hardly changes $K_{h_{11}}^{\text{adv}}$ (see Fig. 3.13j), however, it slightly increases the magnitudes of $K_{h_{12}}^{\text{adv}}$ and $K_{h_{21}}^{\text{adv}}$ on the left and decreases them on the right (see Figs. 3.13k, l). The magnitudes of the tidal advective diffusion coefficients are much larger than those of the prescribed horizontal diffusivity (K_h). It means that, by resolving the lateral processes in the three-dimensional model, the significance of the tidal advective diffusion is generally magnified, resulting in fewer processes that need to be parameterized by a prescribed horizontal diffusion coefficient than in the width-averaged model (Wei *et al.* 2016).

3.4.2 Gravitational circulation

As found by Wei *et al.* (2016), the gravitational circulation does not influence the residual salt transport in convergent estuaries with a horizontal bed (with negligible lateral processes, ignoring tidal straining effects), since the near-bottom landward salt transport is canceled by the near-surface seaward transport (see gray scales in Figs. 3.14a, b). It suggests in estuaries with no depth variations, the gravitational circulation and salinity are hardly coupled, and the gravitational circulation can be understood straightforward using the obtained salinity.

The estuarine width convergence induces a lateral gradient of the tidally averaged salinity with S_0 near the banks larger than that in the center. To balance this gradient, a barotropic pressure gradient is induced with a larger $\bar{\eta}_1^{\mathrm{GC}}$ in the center than that near the banks (see upper panel of Fig. 3.14a). These gradients result in a small but non-negligible transverse gravitational circulation, which transports salt (smaller than 0.02 psu m s^{-1}) towards the banks near the surface, and towards the mid-axis near the bottom (see arrows in Fig. 3.14a). Under the influence of Coriolis effects, however, S_0 becomes larger on the left than on the right, and $\bar{\eta}_1^{\mathrm{GC}}$ becomes larger on the right than on the left in order to balance the salinity gradient (see upper panel of Fig. 3.14b). This results in a transverse gravitational circulation which transports salt towards the left near the surface, and towards the right close to the bottom (see arrows in Fig. 3.14b). The salt fluxes induced by the Coriolis-induced transverse gravitational circulation (up to 0.1 psu m s^{-1}) are much stronger than those induced by the estuarine width convergence.

Due to the lateral bathymetric variations, the gravitational circulation transports salt landward through the channel and seaward over the shoals (see gray scales in Figs. 3.14c, d). The longitudinal gravitational circulation is qualitatively consistent with Lerczak and Geyer (2004), with the strongest landward fluxes near the bottom of the channel and the strongest seaward fluxes near the surface of the shoals. Nevertheless, there is a discrepancy: the gravitational circulation is generally landward near the bottom and seaward near the surface in Lerczak and Geyer (2004); in the present work, however, the landward flow is located at all depths of the channel with the seaward flow on the shoals. This discrepancy is probably related to different vertical mixing coefficients used in two models: Lerczak and Geyer (2004) used a relatively small A_v (0.002 m^2 s^{-1}) for their well-mixed runs, while in the present model A_v is up to 0.005 m^2 s^{-1} in the channel. It is important to note that, in presence of the channel-shoal structure, the gravitational circulation and the salinity distribution become strongly coupled, hence they can not be interpreted straightforward as in experiments I-II.

In experiments III, the diffusive processes and the residual currents act together, resulting in a larger (smaller) S_0 ($\bar{\eta}_1^{\mathrm{GC}}$) in the channel than on the shoals (see upper panel of Fig. 3.14c). This induces a two-cell transverse circulation with near-bottom salt fluxes

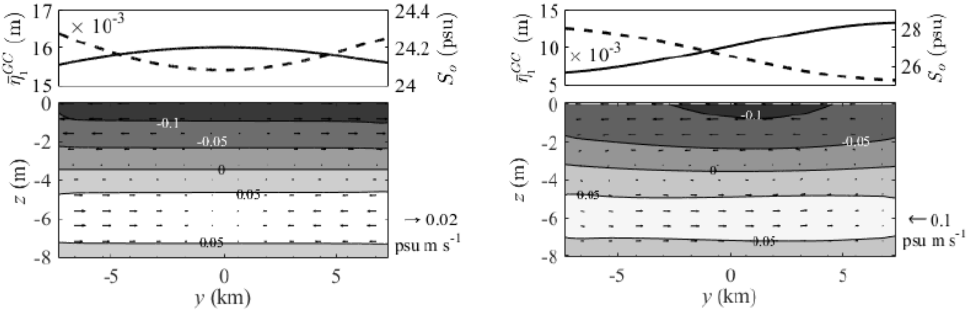

(a) Experiment I

(b) Experiment II

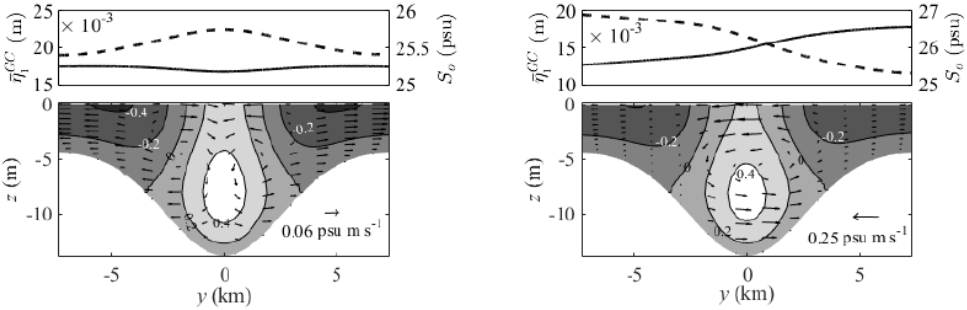

(c) Experiment III

(d) Default experiment

Figure 3.14: The upper panels show the residual water level induced by gravitational circulation ($\bar{\eta}_1^{\mathrm{GC}}$, solid lines), and the tidally averaged salinity (S_0, dashed lines) at $x \sim 40$ km. The lower panels are the same as Fig. 3.11, but for the salt fluxes induced by gravitational circulation.

towards the banks and near-surface return fluxes (up to 0.06 psu m s^{-1}) towards the mid-axis (see arrows in Fig. 3.14c). This pattern is consistent with the bathymetry-controlled secondary circulation reported by Nunes and Simpson (1985). Including the Coriolis force hardly influences the longitudinal gravitational circulation, however, it significantly enhances the transverse gravitational circulation (see arrows in Fig. 3.14d). Due to the combined effects of the estuarine width convergence, lateral bathymetric variations and Coriolis force, S_0 ($\bar{\eta}_1^{\mathrm{GC}}$) becomes larger (smaller) on the left than on the right, inducing near-surface salt fluxes (up to 0.25 psu m s^{-1}) towards the left and near-bottom fluxes towards the right (see Fig. 3.14d). The transverse salt fluxes induced by gravitational circulation have almost the same magnitude as the longitudinal fluxes, implying the transverse gravitational circulation is as significant as the longitudinal circulation.

3.4.3 Response to river discharge

To systematically explore the response of salt intrusion to river discharge, the model is applied to experiment III using three different river discharge values: 72 m^3 s^{-1}, 288 m^3 s^{-1}, 864 m^3 s^{-1}, respectively. It is found that the simulated tidally-averaged salt intrusion length varies significantly from 120 km (for $Q = 72$ m^3 s^{-1}) to 80 km ($Q = 288$ m^3 s^{-1})

and 60 km (Q =864 $\mathrm{m}^3\ \mathrm{s}^{-1}$). This strong dependency of salt intrusion length on river discharge is not consistent with observations of Garvine *et al.* (1992), who found the salt intrusion length only weakly responds to the increase of river discharge in the Delaware estuary. Earlier studies have shown that increasing river discharge can increase stratification and lead to weaker vertical mixing, consequently enhancing the residual circulation (Monismith *et al.* 2002, Ralston *et al.* 2008). This enhanced residual circulation is found to play an important role in transporting salt landward and weakening the dependency of salt intrusion on the variations of river discharge (Ralston *et al.* 2008, Lerczak *et al.* 2009). Therefore, to understand the overestimated sensitivity of the simulated salt intrusion to river discharge, the stratification (measured by the top-to-bottom salinity difference) at each location is calculated for different river discharges (not shown). It is found that the stratification in the central region of salt intrusion increases with increasing river discharge, consistent with model studies (Ralston *et al.* 2008, Lerczak *et al.* 2009) and observations (McSweeney *et al.* 2016). The top-to-bottom salinity differences (less than 1.5 psu), however, are much smaller than the observed values during large river discharges (McSweeney *et al.* 2016). This implies that the relatively strong stratification in case of large river discharges is not resolved in this model, which is probably the reason for the overestimated impact of river discharge on salt intrusion. Therefore, a larger prescribed diffusion parameter is needed in order to reproduce the observed salt intrusion for large river discharges. This is consistent with the study of Gay and O'Donnell (2009), in which the weak response of salt intrusion length in the Delaware to river discharge fluctuations is reproduced by allowing an exponential dependence of the longitudinal dispersion coefficient on river discharge.

3.5 Conclusions

A semi-analytical three-dimensional model is developed to investigate the three-dimensional salt dynamics in idealized well-mixed estuaries. The adopted perturbation method allows for a systematic decomposition of the total salt transport into contributions due to various physical processes. Each salt transport process and its relative importance are investigated in isolation.

First, the salt dynamics for a schematized estuary is investigated. The schematized estuary is exponentially converging, and the bathymetry shows a channel-shoal structure. In this experiment, the tidal advective diffusion, induced by the temporal correlation between horizontal tidal velocities and salinity (including the lateral processes), is the dominant landward salt transport process. The cross-sectionally integrated salt transport induced by residual circulations due to gravitational circulation, tidal rectification, stress-free surface condition and tidal return flow, is small compared to that induced by the tidal advective diffusion. The salt transport due to these residual circulations, however, is locally significant. The gravitational circulation transports salt landward through the channel, and seaward over the shoals. The residual circulations due to other processes are smaller, and transport salt in the opposite direction compared to the transport pattern of gravitational circulation.

The residual salt balance is influenced by the estuarine width convergence, bathymetry and Coriolis. Three experiments are conducted in order to investigate these three factors on the estuarine salt transport in separation: in experiment I, an exponentially convergent estuary is used with a horizontal bed, excluding Coriolis; in experiment II, the estuarine geometry and bathymetry are the same as in experiment I, but the Coriolis force is included; in experiment III, a channel-shoal structure is included while the Coriolis effects are excluded. The tidal advective diffusion is found to be the most dominant landward salt transport process for all experiments. The salt intrusion length slightly increases, compared to the results of experiment I, when Coriolis is included (experiment II) and increases significantly by including the channel-shoal structure (experiment III). The contribution of tidal advective diffusion to estuarine salt transport can be measured by the tidal advective diffusion coefficients, which are explicitly calculated and strongly dependent on the Coriolis effects and lateral bathymetric variations.

The residual circulations hardly influence the salt intrusion length, but are crucial for the local salt transport. In experiment I, the depth-integrated residual circulations vanish, with the river-induced seaward salt transport balanced by diffusive processes only. No significant lateral salt transport patterns are induced by the width convergence of the estuary. In experiment II (including Coriolis deflection), the residual circulations due to tidal rectification and the stress-free surface condition transport salt into the estuary from the left side of the estuary (looking seaward) and out on the right side, resulting in a significant contribution to the landward salt transport. In experiment III, salt transport due to all processes becomes stronger due to the channel-shoal structure. The gravitational circulation, as the most significant residual circulation process, is characterized by a symmetric two-cell circulation pattern. Residual circulations due to other processes are relatively weak. The residual salt transport due to residual circulations is essential for the lateral salinity structure, which can drive a strong transverse gravitational circulation within the salt intrusion region.

3.A Scaling analysis

A perturbation method is used to analytically solve the water motion and salinity. First of all, variables are scaled with their typical scales (see Table 3.3), denoted by a tilde (~). This model does not resolve the boundary layer, and processes in typical estuarine length scales are focused. The variations of water motion and salinity in the longitudinal and lateral directions are assumed to scale with the typical estuarine length scale (L_b). For estuaries with an exponentially decreasing width, L_b is equivalent to the estuarine convergence length (see Eq. (3.46)). The variations in the vertical are assumed to scale with the estuarine water depth. The scale for velocities in the horizontal directions (denoted by U) is obtained by approximately balancing the terms in the depth-averaged continuity equation:

$$a_{M_2}^m \sigma \frac{\partial \tilde{\eta}}{\partial \tilde{t}} + \frac{HU}{L_b}\frac{\partial}{\partial x}\int_{-\tilde{H}}^{0} \tilde{u}\, d\tilde{z} + \frac{HU}{L_b}\frac{\partial}{\partial y}\int_{-\tilde{H}}^{0} \tilde{v}\, d\tilde{z} = 0, \tag{3.53}$$

which yields $U = a_{M_2}^m \sigma L_b / H_0$. The scale for the vertical velocity (denoted by W) is obtained by assuming the terms in the continuity equation (3.54) to be at the same order, this yields $W = UH_0/L_b$. The river transport per unit width at the landward boundary is scaled by the width-averaged river transport: $R_i^m = R/B_L$, with B_L the estuarine width at the landward boundary.

Table 3.3: Scales of physical variables

Variable	Typical scale	Symbol	Expression
t	M_2 tidal frequency	σ	$\sigma^{-1}\tilde{t}$
η	width-averaged M_2 tidal amplitude at mouth	$a^m_{M_2}$	$a^m_{M_2}\tilde{\eta}$
x	estuarine convergence length	L_b	$L_b\tilde{x}$
y	estuarine convergence length	L_b	$L_b\tilde{y}$
(z,H)	width-averaged water depth at mouth	H^m_0	$H^m_0(\tilde{z},\tilde{H})$
u		U	$U\tilde{u}$
v		U	$U\tilde{v}$
w		W	$W\tilde{w}$
S	width-averaged salinity at mouth	S^m_e	$S^m_e\tilde{S}$
R_i	width-averaged river transport at the landward boundary	R^m_i	$R^m_i\tilde{R}_i$

Substituting these scales into the shallow water equations and the salinity equation, and replacing the density in terms of salinity in the momentum equations, the dimensionless governing equations for the water motion and salinity are derived:

$$\frac{U}{L_b}\frac{\partial\tilde{u}}{\partial\tilde{x}}+\frac{U}{L_b}\frac{\partial\tilde{v}}{\partial\tilde{y}}+\frac{W}{H^m_0}\frac{\partial\tilde{w}}{\partial\tilde{z}}=0, \tag{3.54a}$$

$$\begin{aligned}\frac{\partial\tilde{u}}{\partial\tilde{t}}+\frac{U\tilde{u}}{\sigma L_b}\frac{\partial\tilde{u}}{\partial\tilde{x}}+\frac{U\tilde{v}}{\sigma L_b}\frac{\partial\tilde{u}}{\partial\tilde{y}}+\frac{W\tilde{w}}{\sigma H^m_0}\frac{\partial\tilde{u}}{\partial\tilde{z}}=&\frac{gH^m_0\beta_s S^m_e}{U\sigma L_b}\int_{-\tilde{H}}^{\frac{\tilde{\eta}a^m_{M_2}}{H^m_0}}\frac{\partial\tilde{S}}{\partial\tilde{x}}d\tilde{z}-\frac{a^m_{M_2}g}{U\sigma L_b}\frac{\partial\tilde{\eta}}{\partial\tilde{x}}+\frac{f}{\sigma}\tilde{v}\\&+\frac{A_v}{\sigma(H^m_0)^2}\frac{\partial^2\tilde{u}}{\partial\tilde{z}^2}+\frac{A_h}{\sigma L_b^2}\frac{\partial^2\tilde{u}}{\partial\tilde{x}^2}+\frac{A_h}{\sigma L_b^2}\frac{\partial^2\tilde{u}}{\partial\tilde{y}^2},\end{aligned} \tag{3.54b}$$

$$\begin{aligned}\frac{\partial\tilde{v}}{\partial\tilde{t}}+\frac{U\tilde{u}}{\sigma L_b}\frac{\partial\tilde{v}}{\partial\tilde{x}}+\frac{U\tilde{v}}{\sigma L_b}\frac{\partial\tilde{v}}{\partial\tilde{y}}+\frac{W\tilde{w}}{\sigma H^m_0}\frac{\partial\tilde{v}}{\partial\tilde{z}}=&\frac{gH^m_0\beta_s S^m_e}{U\sigma L_b}\int_{-\tilde{H}}^{\frac{\tilde{\eta}a^m_{M_2}}{H^m_0}}\frac{\partial\tilde{S}}{\partial\tilde{y}}d\tilde{z}-\frac{a^m_{M_2}g}{U\sigma L_b}\frac{\partial\tilde{\eta}}{\partial\tilde{y}}-\frac{f}{\sigma}\tilde{u}\\&+\frac{A_v}{\sigma(H^m_0)^2}\frac{\partial^2\tilde{v}}{\partial\tilde{z}^2}+\frac{A_h}{\sigma L_b^2}\frac{\partial^2\tilde{v}}{\partial\tilde{x}^2}+\frac{A_h}{\sigma L_b^2}\frac{\partial^2\tilde{v}}{\partial\tilde{y}^2},\end{aligned} \tag{3.54c}$$

$$\frac{\partial\tilde{S}}{\partial\tilde{t}}+\frac{U\tilde{u}}{\sigma L_b}\frac{\partial\tilde{S}}{\partial\tilde{x}}+\frac{U\tilde{v}}{\sigma L_b}\frac{\partial\tilde{S}}{\partial\tilde{y}}+\frac{W\tilde{w}}{\sigma H^m_0}\frac{\partial\tilde{S}}{\partial\tilde{z}}=\frac{K_h}{\sigma L_b^2}\frac{\partial^2\tilde{S}}{\partial\tilde{x}^2}+\frac{K_h}{\sigma L_b^2}\frac{\partial^2\tilde{S}}{\partial\tilde{y}^2}+\frac{K_v}{\sigma(H^m_0)^2}\frac{\partial^2\tilde{S}}{\partial\tilde{z}^2}. \tag{3.54d}$$

The corresponding dimensionless boundary conditions at the free surface and the bottom are given by:

$$\tilde{w}=\frac{\partial\tilde{\eta}}{\partial\tilde{t}}+\frac{a^m_{M_2}\tilde{u}}{H^m_0}\frac{\partial\tilde{\eta}}{\partial\tilde{x}}+\frac{a^m_{M_2}\tilde{v}}{H^m_0}\frac{\partial\tilde{\eta}}{\partial\tilde{y}}\quad\text{and } A_v\left(\frac{\partial\tilde{u}}{\partial\tilde{z}},\frac{\partial\tilde{v}}{\partial\tilde{z}}\right)=(0,0)\ \text{ at }\ \tilde{z}=\frac{a^m_{M_2}}{H^m_0}\tilde{\eta}, \tag{3.55}$$

$$\tilde{w} = -\tilde{u}\frac{\partial \tilde{H}}{\partial \tilde{x}} - \tilde{v}\frac{\partial \tilde{H}}{\partial \tilde{y}} \quad \text{and} \quad \left(\frac{\partial \tilde{u}}{\partial \tilde{z}}, \frac{\partial \tilde{v}}{\partial \tilde{z}}\right) = \frac{sH_0^m}{A_v}(\tilde{u}, \tilde{v}) \quad \text{at } \tilde{z} = -\tilde{H}, \tag{3.56}$$

$$K_v \frac{\partial \tilde{S}}{\partial \tilde{z}} = 0 \quad \text{at } \tilde{z} = \frac{a_{M_2}}{H_0^m}\tilde{\eta} \quad \text{and } \tilde{z} = -\tilde{H}. \tag{3.57}$$

At the seaward boundary, the dimensionless boundary conditions read

$$\tilde{\eta} = \frac{a_{M_2}}{a_{M_2}^m}\cos(\sigma\tilde{t} - \phi) + \frac{a_{M_0}}{a_{M_2}^m} \quad \text{and} \quad \tilde{S} = \frac{S_e}{S_e^m} \quad \text{at } (x, y) \in \partial_S\Omega. \tag{3.58}$$

At the closed boundaries and the landward boundary, the dimensionless boundary conditions are

$$\int_{-\tilde{H}}^{\frac{a_{M_2}^m}{H_0^m}\tilde{\eta}} (\tilde{u}, \tilde{v})\, d\tilde{z} \cdot \vec{\mathbf{n}}_h = 0 \quad \text{at } (x, y) \in \partial_C\Omega, \tag{3.59}$$

$$\int_{-\tilde{H}}^{\frac{a_{M_2}^m}{H_0^m}\tilde{\eta}} (\tilde{u}, \tilde{v}) d\tilde{z} \cdot \vec{\mathbf{n}}_h = \frac{R_i^m}{H_0^m U}\tilde{R}_i \quad \text{at } (x, y) \in \partial_R\Omega, \tag{3.60}$$

$$\left[\overline{\int_{-\tilde{H}}^{\frac{a_{M_2}^m}{H_0^m}\tilde{\eta}} \left(\frac{U}{\sigma L_b}\tilde{u}\tilde{S} - \frac{K_h}{\sigma L_b^2}\frac{\partial \tilde{S}}{\partial \tilde{x}}\right) d\tilde{z}}\ ,\ \overline{\int_{-\tilde{H}}^{\frac{a_{M_2}^m}{H_0^m}\tilde{\eta}} \left(\frac{U}{\sigma L_b}\tilde{v}\tilde{S} - \frac{K_h}{\sigma L_b^2}\frac{\partial \tilde{S}}{\partial \tilde{y}}\right) d\tilde{z}}\right] \cdot \vec{\mathbf{n}}_h = 0 \quad \text{at } (x, y) \in \partial_C\Omega \text{ or } \partial_R\Omega. \tag{3.61}$$

As a next step, the magnitudes of the scaling parameters are compared with a small parameter $\varepsilon = a_{M_2}^m / H_0^m$: the ratio of the width-averaged M_2 tidal amplitude to the mean water depth at the mouth. This results in an ordering of scaling parameters of each term in the dimensionless equations, as summarized in Table 3.4.

Then, by substituting the magnitudes of these scaling parameters into (3.54)-(3.61), the dimensionless governing equations and boundary conditions are found for water motion and salinity in terms of ε. Substituting the expansions of each dimensionless variables in terms of ε and collecting the terms at the same order of ε, the dimensional governing equations and boundary conditions at different order of ε are derived. These equations will be used to calculate the water motion and salinity semi-analytically.

3.B Leading order water motion

The leading order water motion is forced by the semi-diurnal tide, thus it consists of only the M_2 tidal constituent (see details in Kumar *et al.* (2016)). The M_2 horizontal velocities u_0 and v_0 can be written in terms with the gradients of η_0,

$$u_0 = C_1\frac{\partial \eta_0}{\partial x} + C_2\frac{\partial \eta_0}{\partial y}, \quad v_0 = -C_2\frac{\partial \eta_0}{\partial x} + C_1\frac{\partial \eta_0}{\partial y}, \tag{3.62}$$

Table 3.4: Order of magnitude of scaling parameters

Dimensionless parameters	Order
$U/\sigma L_b$	$O(\varepsilon)$
$W/\sigma H_0^m$	$O(\varepsilon)$
$gH_0^m\beta_s S_e^m/U\sigma L_b$	$O(\varepsilon)$
$a_{M_2}^m g/U\sigma L_b$	$O(1)$
f/σ	$O(1)$
$A_v/\sigma(H_0^m)^2 = K_v/\sigma(H_0^m)^2$	$O(1)$
$A_h/\sigma L_b^2$	$O(\varepsilon^2)$
S_m/S_m^m	$O(1)$
$a_{M_2}/a_{M_2}^m$	$O(1)$
$a_{M_0}/a_{M_2}^m$	$O(\varepsilon)$
sH_0^m/A_v	$O(1)$
$R_i^m/H_0^m U$	$O(\varepsilon)$
$K_h/\sigma L_b^2$	$O(\varepsilon^2)$

with

$$\begin{aligned}
&C_1 = b_1(\gamma_1\cosh\alpha_1 z - 1) + b_2(\gamma_2\cosh\alpha_2 z - 1),\\
&C_2 = i\left[b_1(\gamma_1\cosh\alpha_1 z - 1) - b_2(\gamma_2\cosh\alpha_2 z - 1)\right],\\
&\alpha_1 = \sqrt{i(\sigma+f)/A_v}, \quad \alpha_2 = \sqrt{i(\sigma-f)/A_v},\\
&b_j = g/2\alpha_j^2 A_v, \quad \text{and} \quad \gamma_j = s/\left(\alpha_j A_v \sinh\alpha_j H + s\cosh\alpha_j H\right), \quad j = 1,\ 2.
\end{aligned}$$

In case of no Coriolis force ($f = 0$), it yields $C_2 = 0$, and

$$u_0 = C_1\frac{\partial\eta_0}{\partial x}, \quad v_0 = C_1\frac{\partial\eta_0}{\partial y}. \tag{3.63}$$

Substituting (3.62) into the continuity equation at O(1), integrating over depth, and applying the boundary condition of w_0 at the top and the bottom, it yields a second order partial differential equation of η_0, which is then solved numerically using a finite element method (Kumar *et al.* 2016).

3.C First order salinity equations

By solving equations (3.17)-(3.22c), it is found that the leading order salinity is independent of depth (see details in section 3.2.2), thus the salinity equation at the first order reduces to

$$\frac{\partial S_1}{\partial t} - K_v\frac{\partial^2 S_1}{\partial z^2} = -u_0\frac{\partial S_0}{\partial x} - v_0\frac{\partial S_0}{\partial y}. \tag{3.64}$$

As discussed before, the boundary condition of S_1 at the top and the bottom is required:

$$K_v \frac{\partial S_1}{\partial z}\bigg|_{z=0} = K_v \frac{\partial S_1}{\partial z}\bigg|_{z=-H} = 0 \qquad \text{at} \quad z=0 \quad \text{and}\ z=-H. \tag{3.65}$$

Since u_0, v_0 and η_0 are of M_2 tidal frequency (Kumar *et al.* 2016), $\{u_0, v_0, \eta_0\} = \Re\{(\hat{u}_0, \hat{v}_0, \hat{\eta}_0)\, e^{i\sigma t}\}$, S_1 also has the M_2 tidal frequency according to Eq. (3.64), namely, $S_1 = \Re\{\hat{S}_1 e^{i\sigma t}\}$. After that, (3.64) can be rewritten as

$$\frac{\partial^2 \hat{S}_1}{\partial z^2} - \beta^2 \hat{S}_1 = \frac{1}{K_v}\left(\hat{u}_0 \frac{\partial S_0}{\partial x} + \hat{v}_0 \frac{\partial S_0}{\partial y}\right), \tag{3.66}$$

with $\beta = \sqrt{i\sigma / K_v}$. Solving Eq. (3.66) together with the boundary condition (3.65) yields an analytical formulation of S_1, which depends on the gradients of η_0 and S_0,

$$S_1 = S_{z_1}\left(\frac{\partial \eta_0}{\partial x}\frac{\partial S_0}{\partial x} + \frac{\partial \eta_0}{\partial y}\frac{\partial S_0}{\partial y}\right) + S_{z_2}\left(\frac{\partial \eta_0}{\partial y}\frac{\partial S_0}{\partial x} - \frac{\partial \eta_0}{\partial x}\frac{\partial S_0}{\partial y}\right), \tag{3.67}$$

where S_{z_1} and S_{z_2} are known functions given by

$$S_{z_1} = \frac{b_1\gamma_1\left(\cosh\alpha_1 z - \frac{\alpha_1 \sinh\alpha_1 H}{\beta\sinh\beta H}\cosh\beta z\right)}{K_v(\alpha_1^2 - \beta^2)} + \frac{b_2\gamma_2\left(\cosh\alpha_2 z - \frac{\alpha_2 \sinh\alpha_2 H}{\beta\sinh\beta H}\cosh\beta z\right)}{K_v(\alpha_2^2 - \beta^2)} + \frac{b_1 + b_2}{i\sigma}, \tag{3.68}$$

$$S_{z_2} = \frac{i b_1\gamma_1\left(\cosh\alpha_1 z - \frac{\alpha_1 \sinh\alpha_1 H}{\beta\sinh\beta H}\cosh\beta z\right)}{K_v(\alpha_1^2 - \beta^2)} + \frac{i b_2\gamma_2\left(\frac{\alpha_2 \sinh\alpha_2 H}{\beta\sinh\beta H}\cosh\beta z - \cosh\alpha_2 z\right)}{K_v(\alpha_2^2 - \beta^2)} + \frac{b_1 - b_2}{\sigma} \tag{3.69}$$

for $f \neq 0$. In case of $f = 0$, $S_{z_2} = 0$ is found, and S_{z_1} becomes the same as S_z which is derived by Wei *et al.* (2016).

3.D First-order residual flow

3.D.1 Governing equations

The first-order residual flow follows from the first-order tidally-averaged shallow water equations

$$\frac{\partial \bar{u}_1}{\partial x} + \frac{\partial \bar{v}_1}{\partial y} + \frac{\partial \bar{w}_1}{\partial z} = 0 \tag{3.70a}$$

$$\underbrace{\Re\left\{\overline{u_0 \frac{\partial u_0}{\partial x}} + \overline{v_0 \frac{\partial u_0}{\partial y}} + \overline{w_0 \frac{\partial u_0}{\partial z}}\right\}}_{\text{AD}} - f\bar{v}_1 = -g\frac{\partial \bar{\eta}_1}{\partial x} + A_v \frac{\partial^2 \bar{u}_1}{\partial z^2} + \underbrace{g\beta z \frac{\partial S_0}{\partial x}}_{\text{GC}} \tag{3.70b}$$

$$\underbrace{\Re\left\{\overline{u_0 \frac{\partial v_0}{\partial x}} + \overline{v_0 \frac{\partial v_0}{\partial y}} + \overline{w_0 \frac{\partial v_0}{\partial z}}\right\}}_{\text{AD}} + f\bar{u}_1 = -g\frac{\partial \bar{\eta}_1}{\partial y} + A_v \frac{\partial^2 \bar{v}_1}{\partial z^2} + \underbrace{g\beta z \frac{\partial S_0}{\partial y}}_{\text{GC}}, \tag{3.70c}$$

with boundary conditions

$$\bar{\eta}_1 = 0 \qquad \text{at } (x,y) \in \partial_S\Omega, \tag{3.71a}$$

$$\left[\int_{-H}^{0}(\bar{u}_1,\bar{v}_1)dz + \underbrace{(\overline{\eta_0 u_0}|_{z=0},\overline{\eta_0 v_0}|_{z=0})}_{\text{TRF}}\right]\cdot\vec{\mathbf{n}}_h = \underbrace{R_i}_{\text{RD}} \quad \text{at } (x,y) \in \partial_R\Omega, \tag{3.71b}$$

$$\left[\int_{-H}^{0}(\bar{u}_1,\bar{v}_1)dz + \underbrace{(\overline{\eta_0 u_0}|_{z=0},\overline{\eta_0 v_0}|_{z=0})}_{\text{TRF}}\right]\cdot\vec{\mathbf{n}}_h = 0 \quad \text{at } (x,y) \in \partial_C\Omega, \tag{3.71c}$$

$$A_v\left(\frac{\partial \bar{u}_1}{\partial z},\frac{\partial \bar{v}_1}{\partial z}\right) = \underbrace{\Re\left\{A_v\left(\overline{\eta_0\frac{\partial^2 u_0}{\partial z^2}},\overline{\eta_0\frac{\partial^2 v_0}{\partial z^2}}\right)\right\}}_{\text{NS}} \quad \text{at } z=0, \tag{3.71d}$$

$$\bar{w}_1 = \underbrace{\Re\left\{-\overline{\eta_0\frac{\partial w_0}{\partial z}} + \overline{u_0\frac{\partial \eta_0}{\partial x}} + \overline{v_0\frac{\partial \eta_0}{\partial y}}\right\}}_{\text{TRF}} \quad \text{at } z=0, \tag{3.71e}$$

$$A_v\left(\frac{\partial \bar{u}_1}{\partial z},\frac{\partial \bar{v}_1}{\partial z}\right) = s(\bar{u}_1,\bar{v}_1), \quad \bar{w}_1 = -\bar{u}_1\frac{\partial H}{\partial x} - \bar{v}_1\frac{\partial H}{\partial y} \quad \text{at } z=-H. \tag{3.71f}$$

Here the underbrace $\underbrace{\cdot}$ denotes various mechanisms that force the residual flow. Eqs. (3.70)-(3.71) show that the residual flow is forced by advective contributions of the leading order M_2 tide (tidal rectification, denoted by AD), density driven gravitational circulation (GC), the stress-free surface condition (NS), river discharge (RD), and a return flow (TRF). Since the first-order water motion equations (3.70) and (3.71) are linear, the residual flow components due to these forcing mechanisms can be solved separately. Hence, the solution of the residual water motion can be written as

$$\bar{\chi}_1 = \bar{\chi}_1^{\text{RD}} + \bar{\chi}_1^{\text{TRF}} + \bar{\chi}_1^{\text{AD}} + \bar{\chi}_1^{\text{GC}} + \bar{\chi}_1^{\text{NS}}, \tag{3.72}$$

with the solution vector $\bar{\chi}_1 = \left(\bar{\eta}_1,\bar{u}_1,\bar{v}_1,\bar{w}_1\right)$. All residual contributions is calculated explicitly without information of the salinity field, except gravitational circulation, which is dependent on salinity itself.

3.D.2 Gravitational circulation

To solve the gravitational circulation, the following system of equations has to be solved:

$$\frac{\partial \bar{u}_1^{\text{GC}}}{\partial x} + \frac{\partial \bar{v}_1^{\text{GC}}}{\partial y} + \frac{\partial \bar{w}_1^{\text{GC}}}{\partial z} = 0 \quad , \tag{3.73a}$$

$$A_v\frac{\partial^2 \bar{u}_1^{\text{GC}}}{\partial z^2} + f\bar{v}_1^{\text{GC}} = g\frac{\partial \bar{\eta}_1^{\text{GC}}}{\partial x} + g\beta\frac{\partial S_0}{\partial x}z \quad , \tag{3.73b}$$

$$A_v\frac{\partial^2 \bar{v}_1^{\text{GC}}}{\partial z^2} - f\bar{u}_1^{\text{GC}} = g\frac{\partial \bar{\eta}_1^{\text{GC}}}{\partial y} + g\beta\frac{\partial S_0}{\partial y}z \quad , \tag{3.73c}$$

with boundary conditions

$$\bar{w}_1^{\mathrm{GC}}=0,\quad A_v\left(\frac{\partial \bar{u}_1^{\mathrm{GC}}}{\partial z},\frac{\partial \bar{v}_1^{\mathrm{GC}}}{\partial z}\right)=(0,0)\quad \text{at } z=0, \tag{3.74a}$$

$$\bar{w}_1^{\mathrm{GC}}=-\bar{u}_1^{\mathrm{GC}}\frac{\partial H}{\partial x}-\bar{v}_1^{\mathrm{GC}}\frac{\partial H}{\partial y},\quad A_v\left(\frac{\partial \bar{u}_1^{\mathrm{GC}}}{\partial z},\frac{\partial \bar{v}_1^{\mathrm{GC}}}{\partial z}\right)=s\left(\bar{u}_1^{\mathrm{GC}},\bar{v}_1^{\mathrm{GC}}\right)\quad \text{at } z=-H, \tag{3.74b}$$

$$\bar{\eta}_1^{\mathrm{GC}}=0\qquad \text{at } (x,y)\in\partial_C\Omega \text{ or } \partial_S\Omega, \tag{3.74c}$$

$$\int_{-H}^{0}(\bar{u}_1^{\mathrm{GC}},\bar{v}_1^{\mathrm{GC}})\,dz\cdot\vec{\mathbf{n}}_h=0\qquad \text{at } (x,y)\in\partial_C\Omega \text{ or } \partial_S\Omega. \tag{3.74d}$$

By solving the momentum equations (3.73b)-(3.73c) together with the boundary condition of $\bar{u}_1^{\mathrm{GC}}$ and $\bar{v}_1^{\mathrm{GC}}$ in (3.74a-b), the vertical structure of $\bar{u}_1^{\mathrm{GC}}$ and $\bar{v}_1^{\mathrm{GC}}$ is obtained analytically.

Introducing two rotating flow variables $\bar{R}_1$ and $\bar{R}_2$ (Kumar *et al.* 2017)

$$\bar{R}_1^{\mathrm{GC}}=\bar{u}_1^{\mathrm{GC}}+i\,\bar{v}_1^{\mathrm{GC}}\quad \text{and}\quad \bar{R}_2^{\mathrm{GC}}=\bar{u}_1^{\mathrm{GC}}-i\,\bar{v}_1^{\mathrm{GC}} \tag{3.75}$$

into (3.73) and (3.74), an analytical formulation is derived for the residual flow velocities induced by gravitational circulation:

$$\bar{u}_1^{\mathrm{GC}}=\quad C_{w1}\frac{\partial\bar{\eta}_1^{\mathrm{GC}}}{\partial x}+C_{w2}\frac{\partial\bar{\eta}_1^{\mathrm{GC}}}{\partial y}+C_{s1}\frac{\partial\bar{\rho}_0}{\partial x}+C_{s2}\frac{\partial\bar{\rho}_0}{\partial y}, \tag{3.76a}$$

$$\bar{v}_1^{\mathrm{GC}}=\quad -C_{w2}\frac{\partial\bar{\eta}_1^{\mathrm{GC}}}{\partial x}+C_{w1}\frac{\partial\bar{\eta}_1^{\mathrm{GC}}}{\partial y}-C_{s2}\frac{\partial\bar{\rho}_0}{\partial x}+C_{s1}\frac{\partial\bar{\rho}_0}{\partial y}, \tag{3.76b}$$

with

$$C_{w1}=\frac{1}{2}\left[\frac{g}{A_v\alpha_1^2}(\gamma_1\cosh\alpha_1 z-1)+\frac{g}{A_v\alpha_2^2}(\gamma_2\cosh\alpha_2 z-1)\right],$$

$$C_{w2}=\frac{i}{2}\left[\frac{g}{A_v\alpha_1^2}(\gamma_1\cosh\alpha_1 z-1)-\frac{g}{A_v\alpha_2^2}(\gamma_2\cosh\alpha_2 z-1)\right],$$

$$\begin{aligned}C_{s1}=&-\frac{g}{2\alpha_1^2\rho_c}\left(\frac{\gamma_1}{s}\cosh\alpha_1 z-\frac{H\gamma_1}{A_v}\cosh\alpha_1 z-\frac{z}{A_v}\right)-\frac{g}{2\alpha_2^2\rho_c}\left(\frac{\gamma_2}{s}\cosh\alpha_2 z-\frac{H\gamma_2}{A_v}\cosh\alpha_2 z-\frac{z}{A_v}\right)\\&+\frac{g}{2A_v\alpha_1^3\rho_c}\left[\left(\frac{A_v\alpha_1\gamma_1}{s}\cosh\alpha_1 H+\gamma_1\sinh\alpha_1 H\right)\cosh\alpha_1 z-\sinh\alpha_1 z\right]\\&+\frac{g}{2A_v\alpha_2^3\rho_c}\left[\left(\frac{A_v\alpha_2\gamma_2}{s}\cosh\alpha_2 H+\gamma_2\sinh\alpha_2 H\right)\cosh\alpha_2 z-\sinh\alpha_2 z\right],\end{aligned}$$

$$\begin{aligned}C_{s2}=&-\frac{gi}{2\alpha_1^2\rho_c}\left(\frac{\gamma_1}{s}\cosh\alpha_1 z-\frac{H\gamma_1}{A_v}\cosh\alpha_1 z-\frac{z}{A_v}\right)+\frac{gi}{2\alpha_2^2\rho_c}\left(\frac{\gamma_2}{s}\cosh\alpha_2 z-\frac{H\gamma_2}{A_v}\cosh\alpha_2 z-\frac{z}{A_v}\right)\\&+\frac{gi}{2A_v\alpha_1^3\rho_c}\left[\left(\frac{A_v\alpha_1\gamma_1}{s}\cosh\alpha_1 H+\gamma_1\sinh\alpha_1 H\right)\cosh\alpha_1 z-\sinh\alpha_1 z\right]\\&-\frac{gi}{2A_v\alpha_2^3\rho_c}\left[\left(\frac{A_v\alpha_2\gamma_2}{s}\cosh\alpha_2 H+\gamma_2\sinh\alpha_2 H\right)\cosh\alpha_2 z-\sinh\alpha_2 z\right].\end{aligned}$$

Substitute (3.76) into Eq. (3.73a), integrate it over depth, and apply corresponding boundary conditions. And then, an elliptic partial differential equation for the GC-induced residual sea surface elevation is obtained:

$$\nabla\cdot(\mathbf{B}\nabla\bar{\eta}_1^{\mathrm{GC}})-\nabla\cdot(\mathbf{C}\nabla S_0)=0, \tag{3.77}$$

with

$$\mathbf{B}=\begin{pmatrix}-D_{w1} & -D_{w2}\\ D_{w2} & -D_{w1}\end{pmatrix},\qquad \mathbf{C}=\begin{pmatrix}\rho_c\beta_s D_{s1} & \rho_c\beta_s D_{s2}\\ -\rho_c\beta_s D_{s2} & \rho_c\beta_s D_{s1}\end{pmatrix},\qquad \nabla=\begin{pmatrix}\partial/\partial x\\ \partial/\partial y\end{pmatrix},$$

and

$$\begin{aligned}
D_{w1}=&\frac{1}{2}\left[\frac{gH}{A_v\alpha_1^2}\left(\frac{\gamma_1\sinh\alpha_1 H}{\alpha_1 H}-1\right)+\frac{gH}{A_v\alpha_2^2}\left(\frac{\gamma_2\cosh\alpha_2 H}{\alpha_2 H}-1\right)\right],\\
D_{w2}=&\frac{i}{2}\left[\frac{gH}{A_v\alpha_1^2}\left(\frac{\gamma_1\cosh\alpha_1 H}{\alpha_1 H}-1\right)-\frac{gH}{A_v\alpha_2^2}\left(\frac{\gamma_2\cosh\alpha_2 H}{\alpha_2 H}-1\right)\right],\\
D_{s1}=&-\frac{gH}{2\alpha_1^2\rho_c}\left(\frac{\gamma_1\sinh\alpha_1 H}{s\alpha_1 H}-\frac{\gamma_1}{A_v\alpha_1}\sinh\alpha_1 H-\frac{1}{A_v}\right)-\frac{gH}{2\alpha_2^2\rho_c}\left(\frac{\gamma_2\sinh\alpha_2 H}{s\alpha_2 H}-\frac{\gamma_2}{A_v\alpha_2}\sinh\alpha_2 H-\frac{1}{A_v}\right)\\
&+\frac{gH}{2A_v\alpha_1^3\rho_c}\left[\left(\frac{A_v\alpha_1\gamma_1}{s}\cosh\alpha_1 H+\gamma_1\sinh\alpha_1 H\right)\frac{\sinh\alpha_1 H}{\alpha_1 H}-\frac{\cosh\alpha_1 H-1}{\alpha_1 H}\right]\\
&+\frac{gH}{2A_v\alpha_2^3\rho_c}\left[\left(\frac{A_v\alpha_2\gamma_2}{s}\cosh\alpha_2 H+\gamma_2\sinh\alpha_2 H\right)\frac{\sinh\alpha_2 H}{\alpha_2 H}-\frac{\cosh\alpha_2 H-1}{\alpha_2 H}\right],
\end{aligned}$$

$$\begin{aligned}
D_{s2}=&-\frac{gHi}{2\alpha_1^2\rho_c}\left(\frac{\gamma_1\sinh\alpha_1 H}{s\alpha_1 H}-\frac{\gamma_1}{A_v\alpha_1}\sinh\alpha_1 H-\frac{1}{A_v}\right)+\frac{gHi}{2\alpha_2^2\rho_c}\left(\frac{\gamma_2\sinh\alpha_2 H}{s\alpha_2 H}-\frac{H\gamma_2\sinh\alpha_2 H}{A_v\alpha_2 H}-\frac{1}{A_v}\right)\\
&+\frac{gHi}{2A_v\alpha_1^3\rho_c}\left[\left(\frac{A_v\alpha_1\gamma_1}{s}\cosh\alpha_1 H+\gamma_1\sinh\alpha_1 H\right)\frac{\sinh\alpha_1 H}{\alpha_1 H}-\frac{\cosh\alpha_1 H-1}{\alpha_1 H}\right]\\
&-\frac{gHi}{2A_v\alpha_2^3\rho_c}\left[\left(\frac{A_v\alpha_2\gamma_2}{s}\cosh\alpha_2 H+\gamma_2\sinh\alpha_2 H\right)\frac{\sinh\alpha_2 H}{\alpha_2 H}-\frac{\cosh\alpha_2 H-1}{\alpha_2 H}\right].
\end{aligned}$$

Definition of other parameters can be found in section 3.B.

3.E The seaward boundary condition

When solving this coupled system of equations, special care has to be taken of the seaward boundary, since numerical instabilities can occur when using an arbitrary prescribed water level at this boundary (Chen and Sanford 2009). This is because an inconsistent prescribed sea surface elevation at the mouth can result in a rapid adjustment to a consistent solution in the interior domain. This rapid adjustment will result in large unphysical gradients in the water motion close to the boundary, and thus cause numerically inaccurate solutions.

To avoid that, the computational domain is extended by 30 km in the seaward direction. At the open boundary of the computational domain, a constant M_2 tidal water level is prescribed, and the tidal water motion is calculated. This results in a physically consistent water motion within the domain of interest. Then, the resulting M_2 tidal water elevation at the seaward boundary of the physical domain is rescaled, such that the width-averaged tidal amplitude at the original open boundary (now located at $x = 30$ km) is the same as the tidal amplitude that is prescribed at the open boundary of the physical domain. This will result in a consistent M_2 water motion in the domain of interest. The extended domain is then used to calculate the residual flow using the calculated tidal water motion, except for the residual flow generated by the baroclinic pressure. To satisfy the physical boundary, a constant residual water level a_{M_0} is used at the open boundary of the computational domain such that the width-averaged residual water level is zero at the open boundary of the physical domain. After that, the calculated water motion in the physical domain is used to obtain the salinity field and gravitational circulation.

References

Aristizábal, M., and R. Chant, *A numerical study of salt fluxes in Delaware Bay estuary,* Journal of Physical Oceanography **43**, 1572–1588 (2013).

Becherer, J., M. T. Stacey, L. Umlauf, and H. Burchard, *Lateral circulation generates flood tide stratification and estuarine exchange flow in a curved tidal inlet,* Journal of Physical Oceanography **45**, 638–656 (2015).

Buijsman, M., and H. Ridderinkhof, *Variability of secondary currents in a weakly stratified tidal inlet with low curvature,* Continental Shelf Research **28**, 1711–1723 (2008).

Burchard, H., R. D. Hetland, E. Schulz, and H. M. Schuttelaars, *Drivers of residual estuarine circulation in tidally energetic estuaries: Straight and irrotational channels with parabolic cross section,* Journal of Physical Oceanography **41**, 548–570 (2011).

Chen, S.-N., W. R. Geyer, D. K. Ralston, and J. A. Lerczak, *Estuarine exchange flow quantified with isohaline coordinates: contrasting long and short estuaries,* Journal of Physical Oceanography **42**, 748–763 (2012).

Chen, S.-N., and L. P. Sanford, *Lateral circulation driven by boundary mixing and the associated transport of sediments in idealized partially mixed estuaries,* Continental Shelf Research **29**, 101–118 (2009).

Cushman-Roisin, B., and J.-M. Beckers, *Introduction to geophysical fluid dynamics: physical and numerical aspects*, Vol. 101 (Academic Press, 2011).

Dyer, K., *The salt balance in stratified estuaries,* Estuarine and coastal marine science **2**, 273–281 (1974).

Fischer, H., *Mass transport mechanisms in partially stratified estuaries,* Journal of Fluid Mechanics **53**, 671–687 (1972).

Friedrichs, C. T., and J. M. Hamrick, *Effects of channel geometry on cross sectional variations in along channel velocity in partially stratified estuaries,* Buoyancy Effects on Coastal and Estuarine Dynamics , 283–300 (1996).

Garvine, R. W., R. K. McCarthy, and K.-C. Wong, *The axial salinity distribution in the Delaware estuary and its weak response to river discharge,* Estuarine, Coastal and Shelf Science **35**, 157–165 (1992).

Gay, P., and J. O'Donnell, *Buffering of the salinity intrusion in estuaries by channel convergence,* Hydrology and Earth System Sciences Discussions **6**, 6007–6033 (2009).

Geyer, W. R., and P. MacCready, *The estuarine circulation,* Annual Review of Fluid Mechanics **46**, 175 (2014).

Gockenbach, M. S., *Understanding and implementing the finite element method* (Siam, 2006).

Guymer, I., and J. West, *Longitudinal dispersion coefficients in estuary,* Journal of Hydraulic Engineering **118**, 718–734 (1992).

Hansen, D. V., and M. Rattray, *Gravitational circulation in straits and estuaries,* Estuarine and Coastal Marine Science **23**, 104–122 (1965).

Hughes, F., and M. Rattray, *Salt flux and mixing in the Columbia River estuary,* Estuarine and Coastal Marine Science **10**, 479–493 (1980).

Huijts, K., H. M. Schuttelaars, H. E. de Swart, and C. Friedrichs, *Analytical study of the transverse distribution of along-channel and transverse residual flows in tidal estuaries,* Continental Shelf Research **29**, 89–100 (2009).

Huijts, K., H. M. Schuttelaars, H. E. de Swart, and A. Valle-Levinson, *Lateral entrapment of sediment in tidal estuaries: An idealized model study,* Journal of Geophysical Research: Oceans **111** (2006).

Huijts, K. M., H. E. de Swart, G. P. Schramkowski, and H. M. Schuttelaars, *Transverse structure of tidal and residual flow and sediment concentration in estuaries,* Ocean Dynamics **61**, 1067–1091 (2011).

Jay, D., and J. Smith, *Residual circulation in shallow, stratified estuaries. II. weakly-stratified and partially-mixed systems,* Journal of Geophysical Research **95**, 733–748 (1990).

Kuijper, K., and L. C. Van Rijn, *Analytical and numerical analysis of tides and salinities in estuaries; part II: salinity distributions in prismatic and convergent tidal channels,* Ocean Dynamics **61**, 1743–1765 (2011).

Kumar, M., H. M. Schuttelaars, and P. C. Roos, *Three-dimensional semi-idealized model for estuarine turbidity maxima in tidally dominated estuaries,* Ocean Modelling **113**, 1–21 (2017).

Kumar, M., H. M. Schuttelaars, P. C. Roos, and M. Möller, *Three-dimensional semi-idealized model for tidal motion in tidal estuaries,* Ocean Dynamics **66**, 99–118 (2016).

Lacy, J. R., and S. G. Monismith, *Secondary currents in a curved, stratified, estuarine channel,* Journal of Geophysical Research: Oceans **106**, 31283–31302 (2001).

Lerczak, J. A., and W. R. Geyer, *Modeling the lateral circulation in straight, stratified estuaries,* Journal of Physical Oceanography **34**, 1410–1428 (2004).

Lerczak, J. A., W. R. Geyer, and R. J. Chant, *Mechanisms driving the time-dependent salt flux in a partially stratified estuary,* Journal of Physical Oceanography **36**, 2296–2311 (2006).

Lerczak, J. A., W. R. Geyer, and D. K. Ralston, *The temporal response of the length of a partially stratified estuary to changes in river flow and tidal amplitude,* Journal of Physical Oceanography **39**, 915–933 (2009).

Li, C., and J. O'Donnell, *Tidally driven residual circulation in shallow estuaries with lateral depth variation,* Journal of Geophysical Research: Oceans **102**, 27915–27929 (1997).

MacCready, P., *Toward a unified theory of tidally-averaged estuarine salinity structure,* Estuaries **27**, 561–570 (2004).

MacCready, P., and W. R. Geyer, *Advances in estuarine physics,* Annual Review of Marine Science **2**, 35–58 (2010).

McCarthy, R. K., *Residual currents in tidally dominated, well-mixed estuaries,* Tellus A **45**, 325–340 (1993).

McSweeney, J. M., R. J. Chant, and C. K. Sommerfield, *Lateral variability of sediment transport in the Delaware estuary,* Journal of Geophysical Research: Oceans (2016).

Monismith, S. G., W. Kimmerer, J. R. Burau, and M. T. Stacey, *Structure and flow-induced variability of the subtidal salinity field in northern San Francisco Bay,* Journal of Physical Oceanography **32**, 3003–3019 (2002).

Nunes, R., and J. Simpson, *Axial convergence in a well-mixed estuary,* Estuarine, Coastal and Shelf Science **20**, 637–649 (1985).

Oey, L.-Y., G. L. Mellor, and R. I. Hires, *A three-dimensional simulation of the Hudson-Raritan estuary. Part I: Description of the model and model simulations,* Journal of Physical Oceanography **15**, 1676–1692 (1985).

Ralston, D. K., W. R. Geyer, and J. A. Lerczak, *Subtidal salinity and velocity in the Hudson River estuary: Observations and modeling,* Journal of Physical Oceanography **38**, 753–770 (2008).

Ralston, D. K., W. R. Geyer, and J. A. Lerczak, *Structure, variability, and salt flux in a strongly forced salt wedge estuary,* Journal of Geophysical Research: Oceans **115** (2010).

Ralston, D. K., and M. T. Stacey, *Longitudinal dispersion and lateral circulation in the intertidal zone,* Journal of Geophysical Research: Oceans **110** (2005).

Schramkowski, G. P., and H. E. de Swart, *Morphodynamic equilibrium in straight tidal channels: combined effects of coriolis force and external overtides,* Journal of Geophysical Research: Oceans (1978–2012) **107**, 20–1 (2002).

Schulz, E., H. M. Schuttelaars, U. Gräwe, and H. Burchard, *Impact of the depth-to-width ratio of periodically stratified tidal channels on the estuarine circulation,* Journal of Physical Oceanography **45**, 2048–2069 (2015).

Smith, R., *Long-term dispersion of contaminants in small estuaries,* Journal of Fluid Mechanics **82**, 129–146 (1977).

Valle-Levinson, A., *Contemporary issues in estuarine physics* (Cambridge University Press, 2010).

Valle-Levinson, A., C. Reyes, and R. Sanay, *Effects of bathymetry, friction, and rotation on estuary-ocean exchange,* Journal of Physical Oceanography **33**, 2375–2393 (2003).

Valle-Levinson, A., K.-C. Wong, and K. M. Lwiza, *Fortnightly variability in the transverse dynamics of a coastal plain estuary,* Journal of Geophysical Research: Oceans **105**, 3413–3424 (2000).

Wang, T., W. R. Geyer, P. Engel, W. Jiang, and S. Feng, *Mechanisms of tidal oscillatory salt transport in a partially stratified estuary,* Journal of Physical Oceanography **45**, 2773–2789 (2015).

Wei, X., G. P. Schramkowski, and H. M. Schuttelaars, *Salt dynamics in well-mixed estuaries: importance of advection by tides,* Journal of Physical Oceanography **46**, 1457-1475 (2016).

West, J., R. Uncles, J. Stephens, and K. Shiono, *Longitudinal dispersion processes in the upper Tamar estuary,* Estuaries **13**, 118–124 (1990).

Winant, C. D., *Three-dimensional residual tidal circulation in an elongated, rotating basin,* Journal of Physical Oceanography **38**, 1278–1295 (2008).

Wong, K.-C., *On the nature of transverse variability in a coastal plain estuary,* Journal of Geophysical Research: Oceans **99**, 14209–14222 (1994).

Chapter 4

Three-dimensional sediment transport and trapping mechanisms in well-mixed estuaries

To investigate the dominant sediment transport and trapping mechanisms, a semi-analytical three-dimensional model is developed resolving the dynamic effects of salt intrusion on sediment in well-mixed estuaries in morphodynamic equilibrium. As a study case, a schematized estuary with a converging width and a channel-shoal structure representative for the Delaware estuary is considered. When neglecting Coriolis effects, sediments downstream of the estuarine turbidity maximum (ETM) are imported into the estuary through the channel and exported over the shoals. Within the ETM region, sediments are transported seaward through the channel and transported landward over the shoals. The largest contribution to the cross-sectionally integrated seaward residual sediment transport is attributed to the advection of the tidally-averaged sediment concentration by river-induced flow and tidal return flow. This contribution is mainly balanced by the residual landward sediment transport due to temporal correlations between the suspended sediment concentrations and velocities at the M_2 *tidal frequency. The* M_2 *sediment concentration mainly results from spatial settling lag effects and asymmetric bed shear stresses due to interactions of* M_2 *bottom velocities and the internally-generated* M_4 *tidal velocities, as well as the salinity-induced residual currents. Residual advection of tidally-averaged sediment concentrations also plays an important role in the landward sediment transport. Including Coriolis effects hardly changes the cross-sectionally integrated sediment balance, but results in a landward (seaward) sediment transport on the right (left) side of the estuary (looking seaward), consistent with recent observations from literature. The sediment transport/trapping processes change significantly by changing sediment properties or the river discharge. For example, gravitational circulation plays an important role in trapping fine-grained sediment in the lower estuary, and trapping* *coarse-grained sediment near the salt intrusion limit. Moreover, the relative importance of the gravitational circulation significantly increases with river discharge.* [1]

4.1 Introduction

An estuarine turbidity maximum (ETM) is a region where the suspended sediment concentration is elevated compared to concentrations upstream or downstream of that region. Estuarine turbidity maxima can have strong implications for estuarine morphology, ecology and biology, because of a continuous deposition of particulate matter that often contains contaminants (Jay *et al.* 2015). Furthermore, these high turbidity levels result in reduced light availability and oxygen levels (Talke *et al.* 2009, de Jonge *et al.* 2014, McSweeney *et al.* 2016b), thus significantly affecting the productivity of ecosystems. ETM's are often located at regions of low salinities (Grabemann *et al.* 1997), but they are also found in regions with larger salinities (Gibbs *et al.* 1983, Lin and Kuo 2001) or even at fixed locations independent of salinity (Jay and Musiak 1994, Lin and Kuo 2001). This large variability in sediment trapping locations highlights the importance to identify the dominant processes resulting in the ETM formation.

Process-based models have been intensively used to investigate sediment transport and trapping mechanisms. Complex process-based models (e.g., Ralston *et al.* (2012), Van Maren *et al.* (2015)) are often used to investigate a specific estuary in detail. These models take into account observed estuarine bathymetry, geometry and forcing conditions and include all known physical processes and state-of-the-art parameterization, thus allowing for a quantitative comparison of the model results with observations. Due to their complexity, nevertheless, these models are often solved numerically, which complicates the assessment of the influence of physical processes in isolation. Furthermore, due to their long run-time, these models are not commonly used for systematic sensitivity studies.

Idealized process-based models, which focus on specific processes using idealized geometries and bathymetries, are effective tools to systematically investigate the dominant trapping processes and study the sensitivity of these processes to model parameters. Idealized models have been developed to investigate the cross-sectionally averaged (1D) processes (Friedrichs *et al.* 1998, de Swart and Zimmerman 2009, Winterwerp 2011), width-averaged (longitudinal-vertical, 2DV) processes (Geyer 1993, Jay and Musiak 1994, Burchard and Baumert 1998, Talke *et al.* 2009, Chernetsky *et al.* 2010, Schuttelaars *et al.* 2013, de Jonge *et al.* 2014), or lateral processes (e.g., assuming along-channel uniform conditions (Huijts *et al.* 2006, 2011, Yang *et al.* 2014)). The results of the width-averaged models show that the formation and maintenance of the ETM can often be attributed to the convergence of residual seaward sediment transport upstream of the ETM induced by river discharge, and residual landward sediment transport downstream of the ETM resulting from various processes. These processes include the salinity-induced gravitational circulation (Postma 1967, Festa and

---

[1] This chapter is based on:
Wei, X., Kumar, M., Schuttelaars, H.M., under review. Three-dimensional sediment trapping mechanisms in well-mixed estuaries: importance of the internally-generated overtide, spatial settling lag and gravitational circulation.

Hansen 1978), settling lag effects and tidal asymmetry (Friedrichs *et al.* 1998, Lin and Kuo 2001, de Swart and Zimmerman 2009, Chernetsky *et al.* 2010, Winterwerp and Wang 2013), tidal straining (Burchard and Baumert 1998, Burchard *et al.* 2004, Scully and Friedrichs 2007), stratification induced by salinity (Geyer 1993) and suspended sediment concentration (Winterwerp 2011), sediment-induced current (Talke *et al.* 2009), flocculation and hindered settling (Winterwerp 2011), etc. Focusing on the lateral sediment trapping processes, Huijts *et al.* (2006, 2011) showed that the lateral density gradient was crucial for the lateral sediment trapping, and trapping due to the Coriolis effects was less important. Extending the work of Huijts *et al.* (2006, 2011), Yang *et al.* (2014) found that the effects of the lateral density gradient, M_4 tidal flow and spatial settling lag all played an important role in the lateral sediment trapping. The above-mentioned references clearly show that most idealized models either focus on longitudinal or lateral processes, even though observational studies have shown that both lateral and longitudinal processes, especially their interaction, are important to the along-channel and cross-channel sediment transport and trapping in estuaries (Fugate *et al.* 2007, Sommerfield and Wong 2011, McSweeney *et al.* 2016a, Becherer *et al.* 2016). To investigate the importance of the three-dimensional (3D) sediment trapping processes, Kumar *et al.* (2017) developed a semi-analytical three-dimensional model combining the longitudinal and lateral approaches of Chernetsky *et al.* (2010) and Huijts *et al.* (2006) in a consistent way. However, the resulting model is still diagnostic in salinity, thus the dynamic effects of salinity-induced gravitational circulation on sediment transport and trapping, which are potentially important, are not included.

The aim of this chapter is to develop a three-dimensional semi-analytical model that allows for a systematical analysis of the sediment trapping and transport processes, explicitly resolving the dynamic effects of salt intrusion. First, the coupled water motion and salinity are obtained using the model introduced in Chapter 3. Using this information, the sediment transport and distribution are calculated using the model of Kumar *et al.* (2017). This approach allows for a systematical analysis of the three-dimensional sediment trapping processes and the importance of each individual process for the ETM formation. In this chapter, a schematized estuary is considered, with characteristics representative for the Delaware estuary, in which both lateral and longitudinal circulations are significant (McSweeney *et al.* 2016a,b). Moreover, since the location of sediment trapping can change significantly with varying settling velocity and river discharge (Aubrey 1986, Uncles and Stephens 1993, de Jonge *et al.* 2014, Jay *et al.* 2015), a sensitivity study of the three-dimensional sediment trapping locations and processes for these two factors is conducted.

The structure of this chapter is as follows: in section 4.2, the idealized model is introduced, including the governing equations and corresponding boundary conditions (section 4.2.1), a brief introduction of the adopted semi-analytical method (section 4.2.2) and an analytical decomposition of the sediment transport processes (section 4.2.3). In section 4.3, the default experiment using parameters representative for the Delaware estuary, but neglecting Coriolis effects, is studied to show the 3D sediment trapping processes. The influence of Coriolis deflection is investigated in section 4.4. Next, a sensitivity study of the sediment trapping processes for the sediment settling velocity and river discharge is presented in section 4.5. The above-mentioned sensitivity and the limitations of the present idealized model are discussed in section 4.6. Conclusions are drawn in section 4.7.

4.2 Model description

The semi-analytical idealized three-dimensional (3D) model presented in this paper consists of the shallow water equations, dynamically coupled to the salinity module described in Wei *et al.* (in press), and the sediment module of Kumar *et al.* (2017). The estuary is assumed to be well-mixed and tidally dominated. Since the coupled water motion and salinity are calculated simultaneously, the salinity effects on the water motion and sediment transport are dynamically obtained.

In section 4.2.1, the systems of equations governing the water motion, salinity and sediment dynamics, together with the corresponding boundary conditions are introduced; the solution method is briefly introduced in section 4.2.2; the analytical decomposition of the sediment transport processes is introduced in section 4.2.3.

4.2.1 Governing equations and boundary conditions

The estuary under consideration is forced by tides at the seaward boundary ($\partial_S\Omega$) and a river discharge at the landward boundary ($\partial_R\Omega$), where a weir is located (see Fig. 4.1). The closed boundaries ($\partial_C\Omega$) are impermeable. The undisturbed water level is located at $z = 0$, and the free surface elevation is denoted by $z = \eta$. The estuarine bathymetry varies in the horizontal directions $z = -H(x, y)$, with H an arbitrary function of the horizontal coordinates (x, y).

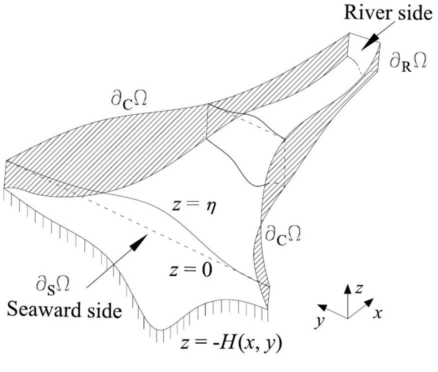

Figure 4.1: A three-dimensional sketch of the estuary, with x and y the horizontal coordinates, and z the vertical coordinate, positive in the upward direction. The seaward, river and closed boundaries are denoted by $\partial_S\Omega$, $\partial_R\Omega$ and $\partial_C\Omega$, respectively. The free surface elevation and the estuarine bottom are located at $z = \eta$ and $z = -H(x, y)$, respectively. This sketch is the same as that is shown in Chapter 3.

The water motion is governed by the 3D shallow water equations assuming hydrostatic equilibrium and using the Boussinesq approximation:

$$\frac{\partial u}{\partial x}+\frac{\partial v}{\partial y}+\frac{\partial w}{\partial z}=0, \tag{4.1}$$

$$\frac{\partial u}{\partial t}+\nabla\cdot(\mathbf{U}u)-fv=-g\frac{\partial \eta}{\partial x}-\frac{g}{\rho_c}\int_z^{\eta}\frac{\partial \rho}{\partial x}dz'+\frac{\partial}{\partial z}\left(A_v\frac{\partial u}{\partial z}\right), \tag{4.2}$$

$$\frac{\partial v}{\partial t}+\nabla\cdot(\mathbf{U}v)+fu=-g\frac{\partial \eta}{\partial y}-\frac{g}{\rho_c}\int_z^{\eta}\frac{\partial \rho}{\partial y}dz'+\frac{\partial}{\partial z}\left(A_v\frac{\partial v}{\partial z}\right). \tag{4.3}$$

Here t denotes time, $\mathbf{U}=(u,v,w)$ is the velocity vector, with u, v and w the velocity components in x, y and z directions, respectively. The acceleration of gravity is denoted by g, with a value of 9.8 $\mathrm{m}^2\ \mathrm{s}^{-1}$, and the vertical eddy viscosity coefficient is denoted by A_v. Following Winant (2008) and Kumar *et al.* (2017), the horizontal viscous effects are neglected. The Coriolis parameter is denoted by f. The estuarine water density ρ is assumed to depend only on the salinity S as $\rho=\rho_c(1+\beta_s S)$, with β_s =7.6×10^{-4} psu^{-1} and ρ_c the background density, taken to be 1000 kg m^{-3}. To dynamically calculate the density, the salinity equation needs to be solved:

$$\frac{\partial S}{\partial t}+\nabla\cdot(\mathbf{U}S)=\frac{\partial}{\partial x}\left(K_h\frac{\partial S}{\partial x}\right)+\frac{\partial}{\partial y}\left(K_h\frac{\partial S}{\partial y}\right)+\frac{\partial}{\partial z}\left(K_v\frac{\partial S}{\partial z}\right), \tag{4.4}$$

with K_h and K_v (assumed to be equal to A_v) the horizontal and vertical diffusivity coefficients, respectively. The suspended sediment concentration (SSC) equation reads

$$\frac{\partial C}{\partial t}+\nabla\cdot(\mathbf{U}C)-\frac{\partial(w_s C)}{\partial z}=\frac{\partial}{\partial x}\left(K_h\frac{\partial C}{\partial x}\right)+\frac{\partial}{\partial y}\left(K_h\frac{\partial C}{\partial y}\right)+\frac{\partial}{\partial z}\left(K_v\frac{\partial C}{\partial z}\right), \tag{4.5}$$

where w_s is the sediment settling velocity and strongly depends on the sediment grain size (Fredsøe and Deigaard 1992).

At the closed boundaries, $\partial_C\Omega$, the normal depth-integrated water transport and the tidally-averaged salt and sediment transports are required to vanish. At the river boundary $\partial_R\Omega$, a river discharge R is prescribed, while the normal tidally-averaged salt and sediment transports have to vanish, for details see Wei *et al.* (in press) and Kumar *et al.* (2017). At the seaward boundaries, the water motion is forced by a prescribed sea surface elevation that consists of a semi-diurnal tidal constituent (M_2), its first overtide (M_4), and a residual sea surface elevation (M_0):

$$\begin{aligned}\eta(x,y,t)=&\,a_{M_2}(x,y)\cos[\sigma_{M_2}t-\varphi_{M_2}(x,y)]\\&+a_{M_4}(x,y)\cos[2\sigma_{M_2}t-\varphi_{M_4}(x,y)]\\&+a_{M_0}(x,y)\quad\text{at }(x,y)\in\partial_S\Omega,\end{aligned} \tag{4.6}$$

where a_{M_2}, a_{M_4}, φ_{M_2} and φ_{M_4} are the prescribed amplitude and phase of the semi-diurnal and its first overtide at the seaward boundary $\partial_S\Omega$, respectively. Here $\sigma_{M_2}\sim 1.4\times10^{-4}s^{-1}$ denotes the M_2 tidal frequency. The prescribed residual sea surface elevated at $\partial_S\Omega$ is denoted by $a_{M_0}(x,y)$. The tidally averaged salinity and suspended sediment concentration are prescribed at $\partial_S\Omega$,

$$\bar{S}=S_e(x,y),\qquad \bar{C}=C_m(x,y)\quad\text{at }(x,y)\in\partial_S\Omega, \tag{4.7}$$

with the overbar $\bar{\cdot}$ denoting a tidal average. Note that the seaward boundary condition for the sediment concentration in (4.7) is different from that used in Kumar *et al.* (2017), where the normal (depth-integrated) sediment transport is required to vanish at each location of the seaward boundary. Using boundary condition (4.7) allows a pointwise nonzero sediment transport over the seaward boundary. In equilibrium, the cross-sectionally integrated sediment transport has to vanish due to the no-transport condition at the closed and river boundaries.

For the water motion, the kinematic and stress-free boundary conditions are prescribed at the free surface ($z = \eta$):

$$w = \frac{\partial \eta}{\partial t} + u\frac{\partial \eta}{\partial x} + v\frac{\partial \eta}{\partial y}, \tag{4.8}$$

$$A_v\frac{\partial u}{\partial z} = A_v\frac{\partial v}{\partial z} = 0. \tag{4.9}$$

At the bottom ($z = -H$), the normal velocity is required to vanish and a partial slip condition is applied (Schramkowski and de Swart 2002):

$$w = -\frac{\partial H}{\partial x}u - \frac{\partial H}{\partial y}v, \tag{4.10}$$

$$A_v\left(\frac{\partial u}{\partial z}, \frac{\partial v}{\partial z}\right) = \frac{\tau_{\mathbf{b}}^{\mathbf{h}}}{\rho_c} = s(u, v). \tag{4.11}$$

The slip parameter s depends on the bed roughness, and follows from linearizing the horizontal component of the bed shear stress $\tau_{\mathbf{b}}^{\mathbf{h}}$. Here the horizontal bed shear stress is used because the depth gradients are assumed to be small, thus the vertical component of the bed shear stress is negligible. Concerning the salinity dynamics, the salt flux is required to vanish at the free surface and the bottom.

The normal sediment flux is required to vanish at the surface,

$$\left(K_h\frac{\partial C}{\partial x}, K_h\frac{\partial C}{\partial y}, K_v\frac{\partial C}{\partial z} + w_sC\right)\cdot \vec{n}_\eta = 0 \qquad \text{at } z = \eta, \tag{4.12}$$

with $\vec{n}_\eta$ the normal vector at the free surface, pointing upwards: $\vec{n}_\eta = \left(-\frac{\partial \eta}{\partial x}, -\frac{\partial \eta}{\partial y}, 1\right)$. The normal component of the diffusive sediment flux at the bottom is related to the erosion flux $E = w_sC_{\text{ref}}$ by

$$\left(K_h\frac{\partial C}{\partial x}, K_h\frac{\partial C}{\partial y}, K_v\frac{\partial C}{\partial z}\right)\cdot \vec{n}_b = w_sC_{\text{ref}} \qquad \text{at } z = -H(x, y), \tag{4.13}$$

with $\vec{n}_b = \left(-\frac{\partial H}{\partial x}, -\frac{\partial H}{\partial y}, -1\right)$ the normal vector at the bottom pointing downwards. The reference concentration is denoted by C_{ref}, and is proportional to the bed shear stress and the sediment availability a:

$$C_{\text{ref}} = \frac{\rho_s a|\tau_{\mathbf{b}}^{\mathbf{h}}|}{\rho_0 g' d_s}. \tag{4.14}$$

Here ρ_s denotes the sediment density, $g' = g(\rho_s - \rho_0)/\rho_0$ denotes the reduced gravity and d_s the sediment grain size. The mean water density ρ_0 takes into account the effects of salinity on water density and is assumed to be a constant. The sediment availability a is an erosion coefficient that accounts for the amount of easily erodible sediment available in a mud reach (Friedrichs *et al.* 1998, Huijts *et al.* 2006, Chernetsky *et al.* 2010).

At this point, the sediment availability a is still unknown. By assuming the estuary to be in morphodynamic equilibrium (the tidally-averaged sediment deposition and erosion balance each other, for details see Friedrichs *et al.* (1998) and Kumar *et al.* (2017)), the spatial distribution of a follows from solving the tidally-averaged and depth-integrated sediment equation

$$\frac{\partial}{\partial x}\overline{\int_{-H}^{\eta}\left(uC-K_h\frac{\partial C}{\partial x}\right)dz}+\frac{\partial}{\partial y}\overline{\int_{-H}^{\eta}\left(vC-K_h\frac{\partial C}{\partial y}\right)dz}=0, \tag{4.15}$$

using boundary conditions (4.7), (4.12), (4.13), and the vanishing normal sediment transport conditions at the closed and landward boundaries.

4.2.2 Solution method

To identify the relative importance of different processes governing the sediment dynamics, a semi-analytical approach is used to solve Eqs. (4.1)-(4.15). In this approach, we employ a perturbation method to get an ordered system of equations which are partly solved analytically and partly numerically using a finite element method. As a first step, all physical variables are scaled by their typical values, resulting in a non-dimensional system of equations. The dimensionless numbers that indicate the relative importance of the various terms are then compared to the small parameter ε, the ratio of the M_2 tidal amplitude to the water depth averaged over the seaward boundary. Next, terms at the same order of ε are collected, resulting in a system of equations at each order of ε that can be solved separately. The vertical structures of all physical variables describing the water motion, salinity and sediment concentration are obtained analytically, while their horizontal structures have to be calculated numerically. Here we use a finite element method (for details see Kumar *et al.* (2016, 2017) and Wei *et al.* (in press)) to get the horizontal dependencies. Using this approach, the residual (M_0) flow components which are independent of salinity, and the M_2 and M_4 tidal flow can be explicitly calculated. However, since the baroclinic residual flow (i.e., gravitational circulation) is dynamically coupled to salinity, an iterative approach is needed to simultaneously calculate the gravitational circulation and the salinity field (for details see Wei *et al.* (in press)). After calculating the necessary water motion constituents (M_0, M_2, M_4), the suspended sediment concentration at each order of ε can be expressed in terms of the sediment availability, which follows from the morphodynamic equilibrium condition (Kumar *et al.* 2017).

4.2.3 An analytical decomposition

Using the solution method sketched above and neglecting terms of $O(\varepsilon^2)$ and higher, the flow velocity can be analytically decomposed into two tidal constituents and a residual component:

$$\mathbf{U}=\underbrace{\mathbf{U}_{M_2}}_{O(1)}+\underbrace{\mathbf{U}_{M_4}+\mathbf{U}_{M_0}}_{O(\varepsilon)}. \tag{4.16}$$

Here $\mathbf{U}_{M_2}$ is the leading-order tidal velocity at the M_2 tidal frequency (at $O(1)$), $\mathbf{U}_{M_4}$ is the first-order tidal velocity at the M_4 tidal frequency (at $O(\varepsilon)$), and $\mathbf{U}_{M_0}$ is the $O(\varepsilon)$ subtidal flow velocity. The M_2 component of the flow velocity $\mathbf{U}_{M_2}$ is externally forced by a prescribed M_2 tide at the entrance. Its first overtide $\mathbf{U}_{M_4}$ consists of various contributions:

$$\mathbf{U}_{M_4} = \mathbf{U}_{M_4}^{\mathrm{EF}} + \mathbf{U}_{M_4}^{\mathrm{AC}} + \mathbf{U}_{M_4}^{\mathrm{NS}} + \mathbf{U}_{M_4}^{\mathrm{TRF}}. \tag{4.17}$$

The first contribution $\mathbf{U}_{M_4}^{\mathrm{EF}}$ results from an external M_4 forcing prescribed at the mouth, while other contributions are generated internally by nonlinear interactions of the M_2 tidal constituent: tidal rectification ($\mathbf{U}_{M_4}^{\mathrm{AC}}$), the stress-free condition ($\mathbf{U}_{M_4}^{\mathrm{NS}}$, as the shear stress is required to vanish at $z = \eta$ instead of $z = 0$) and tidal return flow ($\mathbf{U}_{M_4}^{\mathrm{TRF}}$).

The residual flow $\mathbf{U}_{M_0}$ is analytically decomposed into different components as well:

$$\mathbf{U}_{M_0} = \mathbf{U}_{M_0}^{\mathrm{RD}} + \mathbf{U}_{M_0}^{\mathrm{GC}} + \mathbf{U}_{M_0}^{\mathrm{AC}} + \mathbf{U}_{M_0}^{\mathrm{NS}} + \mathbf{U}_{M_0}^{\mathrm{TRF}}. \tag{4.18}$$

Here $\mathbf{U}_{M_0}^{\mathrm{RD}}$ results from the externally prescribed river discharge. Other contributions are related to the salinity-induced gravitational circulation ($\mathbf{U}_{M_0}^{\mathrm{GC}}$), the nonlinear interactions due to tidal rectification ($\mathbf{U}_{M_0}^{\mathrm{AC}}$), the stress-free surface condition ($\mathbf{U}_{M_0}^{\mathrm{NS}}$) and tidal return flow ($\mathbf{U}_{M_0}^{\mathrm{TRF}}$).

Substituting Eq. (4.16) into (4.11) and making a Taylor expansion with respect to the small parameter ε, it follows that $|\tau_{\mathbf{b}}^{\mathbf{h}}|$ consists of a residual component and all frequencies that are a multiple of the M_2 tidal frequency,

$$|\tau_{\mathbf{b}}^{\mathbf{h}}| = \rho s\sqrt{u_b^2 + v_b^2} = \underbrace{\left(|\tau_{\mathbf{b}_{\mathbf{M_0}}}| + |\tau_{\mathbf{b}_{\mathbf{M_4}}}| + |\tau_{\mathbf{b}_{\mathbf{M_8}}}| + ...\right)}_{O(1)} + \underbrace{\left(|\tau_{\mathbf{b}_{\mathbf{M_2}}}| + |\tau_{\mathbf{b}_{\mathbf{M_6}}}| + ...\right)}_{O(\varepsilon)} + ... \quad . \tag{4.19}$$

A careful analysis shows that the residual bed shear stress $\tau_{\mathbf{b}_{\mathbf{M_0}}}$, and all bed shear stresses of frequencies which are even multiples of the M_2 tidal frequency ($\tau_{\mathbf{b}_{\mathbf{M_4}}}$, $\tau_{\mathbf{b}_{\mathbf{M_8}}}$, ...) result from the M_2 bottom velocity, and are leading-order contributions. The other components ($\tau_{\mathbf{b}_{\mathbf{M_2}}}$, $\tau_{\mathbf{b}_{\mathbf{M_6}}}$, ...) result from the interactions of the M_2 bottom velocity with the residual and M_4 bottom velocities, and are of $O(\varepsilon)$. From Eqs. (4.13) and (4.14), it follows that the resulting suspended sediment concentration is given by

$$\mathbf{C} = \underbrace{\left(\mathbf{C}_{M_0} + \mathbf{C}_{M_4} + \mathbf{C}_{M_8} + ...\right)}_{O(1)} + \underbrace{\left(\mathbf{C}_{M_2} + \mathbf{C}_{M_6} + ...\right)}_{O(\varepsilon)} + ... \quad , \tag{4.20}$$

i.e., it consists of contributions at different tidal frequencies. It can be shown that C_{M_0}, C_{M_4} (and C_{M_8}, ...) are leading-order concentrations, and C_{M_2} (and C_{M_6}, ...) are first-order concentrations. The leading-order concentrations are induced by the bed shear stress due to M_2 bottom velocity. The first-order concentrations, however, are caused both by the asymmetric bed shear due to the combined M_2 and M_0/M_4 bottom velocities, and by the advection of the leading-order concentrations by the M_2 tidal velocity ($\mathbf{U}_{M_2}$). Moreover, the vanishing normal sediment flux prescribed at the free surface introduces a first-order sediment flux at $z = 0$, which also results in a first-order contribution in the sediment concentrations C_{M_2} (Kumar *et al.* 2017). It is important to note that to obtain the dominant sediment transport balance, only the leading-order concentrations C_{M_0} and C_{M_4}, and the first-order concentration C_{M_2} are needed. Using this information, substituting Eqs. (4.16), (4.18), (4.20) into (4.15), the depth-integrated, tidally averaged sediment transport equation becomes

$$\nabla\cdot\underbrace{\begin{pmatrix} \int_{-H}^{0} u_{M_0} C_{M_0}\, dz + \overline{\eta_{M_2} u_{M_2}}\big|_{z=0}\; C_{M_0}\big|_{z=0} \\ \int_{-H}^{0} v_{M_0} C_{M_0}\, dz + \overline{\eta_{M_2} v_{M_2}}\big|_{z=0}\; C_{M_0}\big|_{z=0} \end{pmatrix}}_{\mathbf{T}_{M_0}} + \nabla\cdot\underbrace{\begin{pmatrix} \int_{-H}^{0} \overline{u_{M_2} C_{M_2}}\, dz \\ \int_{-H}^{0} \overline{v_{M_2} C_{M_2}}\, dz \end{pmatrix}}_{\mathbf{T}_{M_2}}$$

$$+\nabla\cdot\underbrace{\begin{pmatrix} \int_{-H}^{0} \overline{u_{M_4} C_{M_4}}\, dz + \overline{\eta_{M_2}\;\, u_{M_2}|_{z=0} C_{M_4}\big|_{z=0}} \\ \int_{-H}^{0} \overline{v_{M_4} C_{M_4}}\, dz + \eta_{M_2}\;\, v_{M_2}|_{z=0} C_{M_4}\big|_{z=0} \end{pmatrix}}_{\mathbf{T}_{M_4}} + \nabla\cdot\underbrace{\begin{pmatrix} -\int_{-H}^{0} K_h \frac{\partial C_{M_0}}{\partial x}\, dz \\ -\int_{-H}^{0} K_h \frac{\partial C_{M_0}}{\partial y}\, dz \end{pmatrix}}_{\mathbf{T}_{DIFF}} = 0. \tag{4.21}$$

In Eq. (4.21), $\mathbf{T}_{M_0}$, $\mathbf{T}_{M_2}$ and $\mathbf{T}_{M_4}$ represent the depth-integrated residual sediment transport contributions due to different advective transport processes, and $\mathbf{T}_{DIFF}$ denotes transport due to diffusive processes. Here, $\mathbf{T}_{M_2}$ is the depth-integrated residual sediment transport due to the advection of the M_2 tidal concentration C_{M_2} by M_2 tidal velocities. The depth-integrated residual sediment transports due to the advection of the residual concentration C_{M_0} by the residual velocities, and the advection of the M_4 tidal concentration C_{M_4} by the M_4 tidal velocities, are included in $\mathbf{T}_{M_0}$ and $\mathbf{T}_{M_4}$, respectively.

Following Eqs. (4.17)-(4.20), the depth-integrated sediment transport contributions can be further decomposed into different processes as listed in Table 4.1 (see a more detailed decomposition in Kumar *et al.* (2017)). The sediment transport $\mathbf{T}_{M_0}$ includes transport contributions due to the advection of the residual concentration C_{M_0} by the gravitational circulation ($\mathbf{T}_{M_0}^{\mathrm{GC}}$), and the other barotropic residual flow components ($\mathbf{T}_{M_0}^{\mathrm{BR}}$) as a result of the river-induced flow ($\mathbf{T}_{M_0}^{\mathrm{RD}}$), tidal rectification ($T_{M_0}^{\mathrm{AC}}$), the stress-free surface boundary condition ($\mathbf{T}_{M_0}^{\mathrm{NS}}$), and tidal return flow ($\mathbf{T}_{M_0}^{\mathrm{TRF}}$). The depth-integrated transport $\mathbf{T}_{M_2}$ includes the M_2 tidal advection of SSC at the M_2 tidal frequency, which is partly a result of the asymmetric bed shear stress due to the interaction of the M_2 tidal velocity and the salinity-induced baroclinic residual current ($\mathbf{T}_{M_2}^{\mathrm{GC}}$) and the internally-generated barotropic residual current ($\mathbf{T}_{M_2}^{\mathrm{BR}}$) at the bottom. Moreover, the asymmetric bed shear stress due to interactions of the M_2 bottom velocity and the externally-forced ($\mathbf{T}_{M_2}^{\mathrm{EF}}$) or internally-generated ($\mathbf{T}_{M_2}^{\mathrm{IN}}$) M_4 tidal currents at the bottom also induce an M_2 tidal concentration, which temporally correlates with the M_2 tidal velocity, and results in a residual sediment transport. Besides, the first-order correction of the leading-order vertical sediment fluxes at the free-surface boundary results in a first-order SSC at the M_2 tidal frequency and thence a sediment transport ($\mathbf{T}_{M_2}^{\mathrm{SC}}$), which is called the surface contribution (Kumar *et al.* 2017). Finally, the advection of the residual and M_4 tidal components of SSC by the M_2 tidal currets also results in a SSC at the M_2 tidal frequency. Advection of this concentration component by the M_2 tidal currents again results in a residual sediment transport, and is denoted as spatial settling lag contribution ($\mathbf{T}_{M_2}^{\mathrm{SSL}}$). The transport contribution $\mathbf{T}_{M_4}$ is caused by advection of SSC at the M_4 tidal frequency by M_4 tidal flow as a result of both the M_4 tidal flow generated internally ($\mathbf{T}_{M_4}^{\mathrm{IN}}$) and the externally forced

M_4 tide ($\mathbf{T}_{M_4}^{\mathrm{EF}}$). Owing to the semi-analytical solution method and the analytic approach of decomposition, all decomposed processes listed above can be calculated individually.

Table 4.1: Decomposition of the depth-integrated sediment transports due to different contributions. The same decomposition can be made for the cross-sectionally integrated transport contributions (not shown).

transport	decomposition	concentration	velocity
$\mathbf{T}_{M_0}$	$\mathbf{T}_{M_0}^{\mathrm{GC}}$	C_{M_0}	$\mathbf{U}_{M_0}^{\mathrm{GC}}$
	$\mathbf{T}_{M_0}^{\mathrm{RD}}$		$\mathbf{U}_{M_0}^{\mathrm{RD}}$
	$\mathbf{T}_{M_0}^{\mathrm{AC}}$		$\mathbf{U}_{M_0}^{\mathrm{AC}}$
	$\mathbf{T}_{M_0}^{\mathrm{TRF}}$		$\mathbf{U}_{M_0}^{\mathrm{TRF}}$
	$\mathbf{T}_{M_0}^{\mathrm{NS}}$		$\mathbf{U}_{M_0}^{\mathrm{NS}}$
$\mathbf{T}_{M_2}$	$\mathbf{T}_{M_2}^{\mathrm{GC}}$	C_{M_2} due to $\mathbf{U}_{M_2}$+$\mathbf{U}_{M_0}^{\mathrm{GC}}$	$\mathbf{U}_{M_2}$
	$\mathbf{T}_{M_2}^{\mathrm{BR}}$	C_{M_2}due to $\mathbf{U}_{M_2}$+$\mathbf{U}_{M_0}^{\mathrm{RD}}$+$\mathbf{U}_{M_0}^{\mathrm{AC}}$+$\mathbf{U}_{M_0}^{\mathrm{NS}}$+$\mathbf{U}_{M_0}^{\mathrm{TRF}}$	
	$\mathbf{T}_{M_2}^{\mathrm{EF}}$	C_{M_2} due to $\mathbf{U}_{M_2}$+$\mathbf{U}_{M_4}^{\mathrm{EF}}$	
	$\mathbf{T}_{M_2}^{\mathrm{IN}}$	C_{M_2} due to $\mathbf{U}_{M_2}+\mathbf{U}_{M_4}^{\mathrm{AC}}+\mathbf{U}_{M_4}^{\mathrm{NS}}+\mathbf{U}_{M_4}^{\mathrm{TRF}}$	
	$\mathbf{T}_{M_2}^{\mathrm{SC}}$	C_{M_2} due to surface contribution	
	$\mathbf{T}_{M_2}^{\mathrm{SSL}}$	C_{M_2} due to spatial settling lag	
$\mathbf{T}_{M_4}$	$\mathbf{T}_{M_4}^{\mathrm{IN}}$	C_{M_4}	$\mathbf{U}_{M_4}^{\mathrm{AC}}+\mathbf{U}_{M_4}^{\mathrm{NS}}+\mathbf{U}_{M_4}^{\mathrm{TRF}}$
	$\mathbf{T}_{M_4}^{\mathrm{EF}}$		$\mathbf{U}_{M_4}^{\mathrm{EF}}$

Integrating Eq. (4.21) from the left bank of the channel ($y = y_1$) to the right bank ($y = y_2$), and subsequently integrating from the weir (at $x = L$) to any longitudinal location x, the (cross-sectionally integrated) longitudinal residual sediment balance is found:

$$\begin{aligned}&\underbrace{\int_{y_1}^{y_2}\left(\int_{-H}^{0} u_{M_0}C_{M_0}\,dz+\overline{\eta_{M_2}u_{M_2}}\big|_{z=0}\,C_{M_0}\big|_{z=0}\right)dy}_{T_{M_0}}+\underbrace{\int_{y_1}^{y_2}\int_{-H}^{0}\overline{u_{M_2}C_{M_2}}\,dzdy}_{T_{M_2}}\\&+\underbrace{\int_{y_1}^{y_2}\left(\int_{-H}^{0}\overline{u_{M_4}C_{M_4}}\,dz+\overline{\eta_{M_2}\;u_{M_2}|_{z=0}C_{M_4}\big|_{z=0}}\right)dy}_{T_{M_4}}+\underbrace{\int_{y_1}^{y_2}\int_{-H}^{0}-K_h\frac{\partial C_{M_0}}{\partial x}\,dzdy}_{T_{\mathrm{DIFF}}}=0.\end{aligned}\tag{4.22}$$

Equation (4.22) shows that the cross-sectionally integrated along-channel residual sediment balance is maintained by T_{M_0}, T_{M_2}, T_{M_4}, and T_{DIFF}. These transport contributions can be further decomposed in the same way as the depth-integrated sediment transport contribution (not shown).

4.3 Default experiment

In section 4.3.1, a default experiment with parameter values representative for the Delaware estuary (neglecting Coriolis effects) is defined. In section 4.3.2, the three-dimensional structure of the resulting ETM, the depth-integrated residual sediment transport and trapping patterns due to different contributions, and their relative importance to the cross-sectionally integrated residual sediment balance are demonstrated.

4.3.1 Parameters setting for the default experiment

The default experiment considers a schematized, well-mixed estuary, with an estuarine length (L) of 215 km and a width (B) exponentially converging up-estuary,

$$B = B_0 e^{-x/L_b}. \tag{4.23}$$

Here B_0 = 39 km is the estuarine width at the mouth, and L_b = 42 km is the estuarine convergence length (representative for the Delaware estuary). Following Wei *et al.* (in press), the bathymetry exhibits a lateral channel-shoal structure, and is given by

$$H(x,y) = H_{\mathrm{min}} + (H_{\mathrm{m}} - H_{\mathrm{min}})\frac{x}{L} + (H_{\mathrm{max}} - H_{\mathrm{min}})\left(1 - \frac{x}{L}\right)\left(1 - \frac{4y^2}{B^2}\right)e^{-C_f\frac{4y^2}{B^2}}, \tag{4.24}$$

with the maximum water depth H_{max} =15 m and the minimum water depth H_{min} = 3.6 m on the shoals of the estuarine mouth. The width-averaged water depth H_{m} = 8 m and the tidal flat parameter C_f = 4 are constant along the channel.

In order to obtain a physically consistent solution for the salinity, and to make the sediment distribution at the seaward boundary consistent with that in the interior, the barotropic water motion will be calculated in a domain which is extended 30 km towards the open sea (see gray rectangle in Fig. 4.2). A constant barotropic sea surface elevation is prescribed at the seaward boundary of the extended domain ($x' = 0$) such that the width-averaged sea surface elevation η^m at the seaward boundary of the physical domain ($x = 0$)

$$\eta^m = a^m_{M_2}\cos(\sigma_{M_2} t) + a^m_{M_4}\cos(2\sigma_{M_2} t - \Delta\varphi^m) + a^m_{M_0} \tag{4.25}$$

is in agreement with the observations of the Delaware estuary by Walters (1997). Here $a^m_{M_2}$, $a^m_{M_4}$, and $\Delta\varphi^m$ denote the width-averaged M_2 and M_4 tidal amplitudes and the phase difference between the M_2 and M_4 tidal constituents at $x = 0$, respectively. The mean residual water level at $x = 0$, $a^m_{M_0}$, is required to vanish. Following Wei *et al.* (in press), the residual salinity S_m is prescribed to be 31 psu at $x = 0$, and the horizontal diffusivity K_h is assumed to be proportional to B, varying from 50 m^2 s^{-1} at the mouth to 10 m^2 s^{-1} at the landward side.

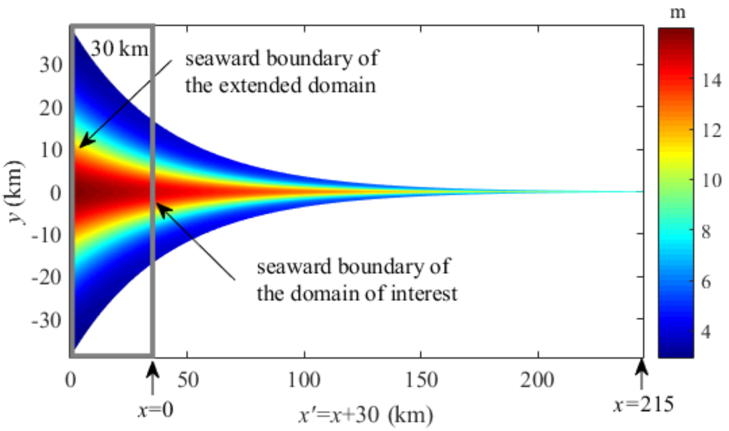

Figure 4.2: The bathymetry and geometry of the extended domain, and the (non-extended) domain of interest.

After calculating the barotropic water motion in the extended domain, the (baroclinic) gravitational circulation and salinity distribution are calculated for the domain of interest (between $x = 0$ and $x = L$). Then, using the resulting water motion, the sediment concentration for the (non-extended) domain of interest is calculated. The suspended sediment concentration at the seaward boundary of the physical domain (C_m) is prescribed to be constant. The value of C_m is determined by prescribing the averaged sediment availability a_* in the physical domain

$$a_* = \frac{\int_0^L \int_{y_1}^{y_2} a \; dydx}{\int_0^L \int_{y_1}^{y_2} dydx} \tag{4.26}$$

to be constant, such that a maximum residual SSC of ~200 mg l^{-1} representative for the observed ETM in the Delaware estuary under a river discharge of ~ 288 m^3 s^{-1} (McSweeney *et al.* 2016a) is obtained.

The vertical eddy viscosity A_v is assumed to be constant in time. Both the vertical eddy viscosity A_v and the slip parameter s are assumed to be proportional to the local water depth (Friedrichs and Hamrick 1996, Wei *et al.* in press),

$$A_v = A_{v_m}\frac{H}{H_m}, \qquad s = s_m\frac{H}{H_m}. \tag{4.27}$$

Here H_m is the width-averaged water depth, A_{v_m} and s_m are prescribed friction parameters which are obtained from calibrating the M_2 tidal water motion with observations in the Delaware estuary (values taken from Wei *et al.* (2016, in press)). A constant settling velocity is used, $w_s = 0.5$ mm s^{-1}, representative for sediments in the lower Delaware bay (Gibbs *et al.* 1983). The grain size of sediments, the mean water density, and sediment density are also assumed to be constant: $d_s = 20$ μm, $\rho_0 = 1020$ kg m^3, $\rho_s = 2650$ kg m^3. For clarity, the Coriolis force is neglected in the default experiment, its effect will be discussed in detail in section 4.4. All above-mentioned parameters defining the default experiment are listed in Table 4.2.

Table 4.2: Parameters for the default experiment.

Physical parameter	symbol	Value
length	L	215 km
convergence length	L_b	42 km
width at the mouth	B_0	39 km
minimum water depth	H_{min}	3.6 m
maximum water depth	H_{max}	15 m
average water depth	H_m	8 m
tidal flat parameter	C_f	4
average vertical eddy viscosity	A_{v_m}	0.005 $\text{m}^2\ \text{s}^{-1}$
average slip parameter	s_m	0.039 m s^{-1}
horizontal diffusivity	K_{h}	10-50 $\text{m}^2\ \text{s}^{-1}$
river discharge	R	288 $\text{m}^3\ \text{s}^{-1}$
average M_2 tidal amplitude	$a_{M_2}^m$	0.75 m
average M_4 tidal amplitude	$a_{M_4}^m$	0.012 m
average residual water level	$a_{M_0}^m$	0
M_2 tidal frequency	σ_{M_2}	$1.4 \times 10^{-4}\ \text{s}^{-1}$
average phase difference	$\Delta\varphi^m$	-247°
Coriolis parameter	f	0
salinity at the mouth	S_m	31 psu
mean water density	ρ_0	1020 kg m^{-3}
sediment grain size	d_s	20 μm
sediment density	ρ_s	2650 kg m^{-3}
settling velocity	w_s	0.5 mm s^{-1}
average sediment availability	a_*	0.1228

4.3.2 Three-dimensional suspended sediment concentration

Since no Coriolis force is considered, and the bed profile and geometry are laterally symmetric, the sediment availability and sediment concentrations are symmetric with respect to the central axis of the estuary ($y = 0$). As shown in Fig. 4.3a, the maximum sediment availability is found at about 100 km up-estuary from the mouth, with larger values on the shoals than in the channel. To illustrate the three-dimensional structure of the ETM and its position with respect to the tidally-averaged salinity structure, the longitudinal-vertical distribution of the residual suspended sediment concentration at $y =$

0 and a lateral-vertical (cross-sectional) distribution within the ETM region (at $x = 100$ km) are depicted in Figs. 4.3b-c. The residual salinities are vertically uniform (see white lines), however, the residual suspended sediment concentrations are generally larger near the bottom than near the top (see color scales). The ETM is centered at ~ 100 km, with the turbidity zone stretching between 55 km and 130 km from the mouth (see Fig. 4.3b). The maximum residual suspended sediment concentration is found at a salinity of about 0.05 psu, coinciding with the residual salt intrusion limit. Due to larger sediment availabilities on the shoals and larger residual salinities in the channel (see Fig. 4.3c), the residual suspended sediment concentrations are larger on the shoals than in the channel (even though the bed shear stress in the channel is larger). The lateral distributions of the residual salinity and suspended sediment concentration confirm the results of Huijts *et al.* (2006), that salinity gradients tend to trap sediment in regions of the cross-section with lower salinities.

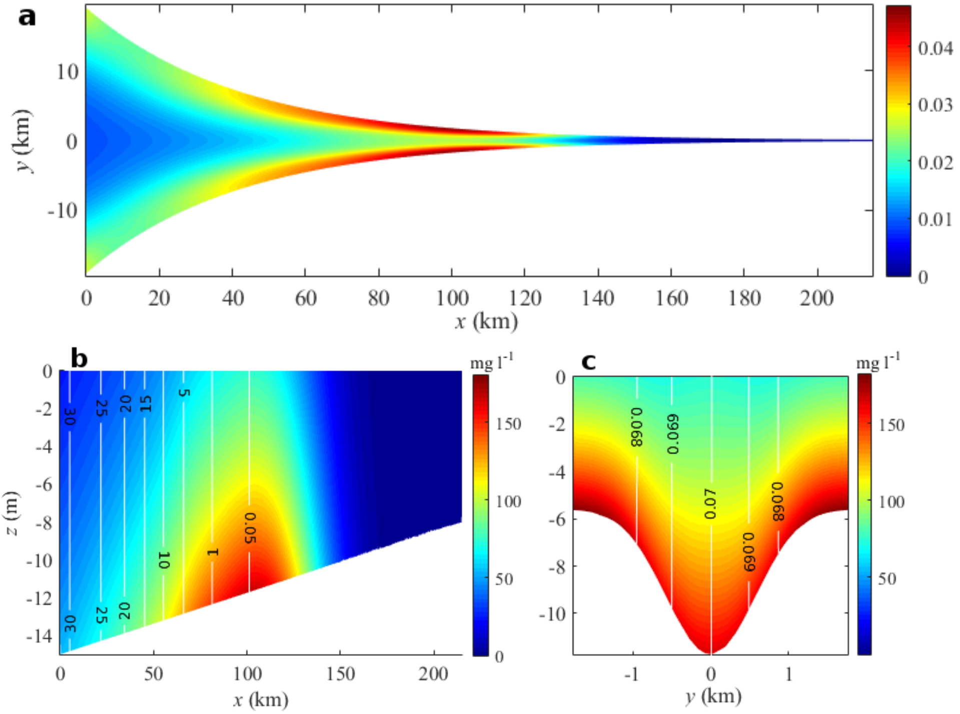

Figure 4.3: (a) The spatial distribution of sediment availability. (b) The longitudinal-vertical profile at $y = 0$ and (c) lateral-vertical distributions of the residual concentration at $x = 100$ km for the default experiment. The white contour lines show the vertically uniform residual salinities.

4.3.3 Depth-integrated sediment transport and trapping processes

To identify the longitudinal and lateral sediment transport patterns and the depth-averaged sediment trapping patterns, the depth-integrated residual sediment transport and the depth-averaged residual sediment concentration are shown in Fig. 4.4. The maximum depth-averaged residual sediment concentration is located at x = 100 km, with the depth-averaged ETM region extending from 70 km to 120 km up-estuary from the mouth. Four circulation cells of residual sediment transport are identified (see arrows in Fig. 4.4): seaward of the ETM, sediments are transported towards the ETM through the channel, next move laterally towards the flanks and are transported seaward over the shoal; within the ETM region, sediments are transported seaward through the channel and landward over the shoals. The longitudinal residual sediment transport (integrated over the depth) reaches its maximum (up to 24 g m^{-1} s^{-1}) in the channel within the ETM region at the central estuary, while the maximum lateral transport (less than 3 g m^{-1} s^{-1}) is found on the shoals near the mouth. To investigate the physical mechanisms behind the residual sediment transport and trapping, the depth-integrated residual sediment transport contributions due to advection of residual concentrations by residual velocities ($\mathbf{T}_{M_0}$), advection of tidal components of sediment concentrations by tidal velocities ($\mathbf{T}_{M_2}+\mathbf{T}_{M_4}$) and diffusive processes ($\mathbf{T}_{DIFF}$) are shown in Fig. 4.5. The divergence (convergence) of the depth-integrated residual sediment transport due to each contribution is shown in red (blue), with the magnitude and direction of the sediment transport shown by arrows. Upstream of the seaward edge of the ETM, the residual sediment transport contribution $\mathbf{T}_{M_0}$ tends to transport sediment seaward. This results in a divergence of sediment transport in the upper estuary (x > 120 km) and a convergence in the central region (70 km

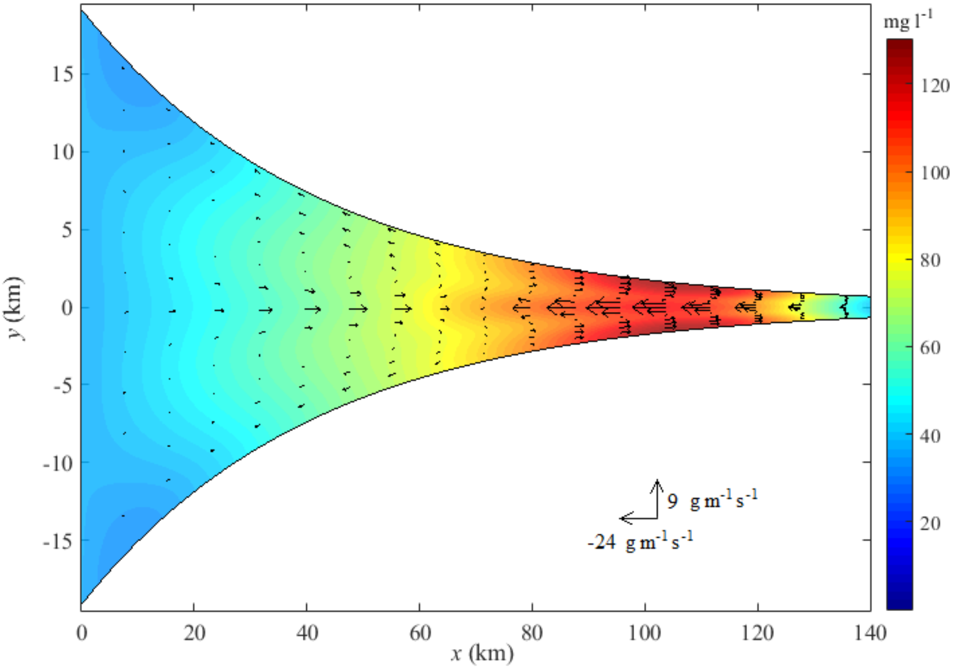

Figure 4.4: The depth-averaged residual suspended sediment concentration (see background color scales) and the depth-integrated sediment transport (see arrows). The length of the arrow measures the magnitudes of the depth-integrated residual suspended sediment transport at each location (x, y), and the direction of the arrow measures the direction of the transport at this location.

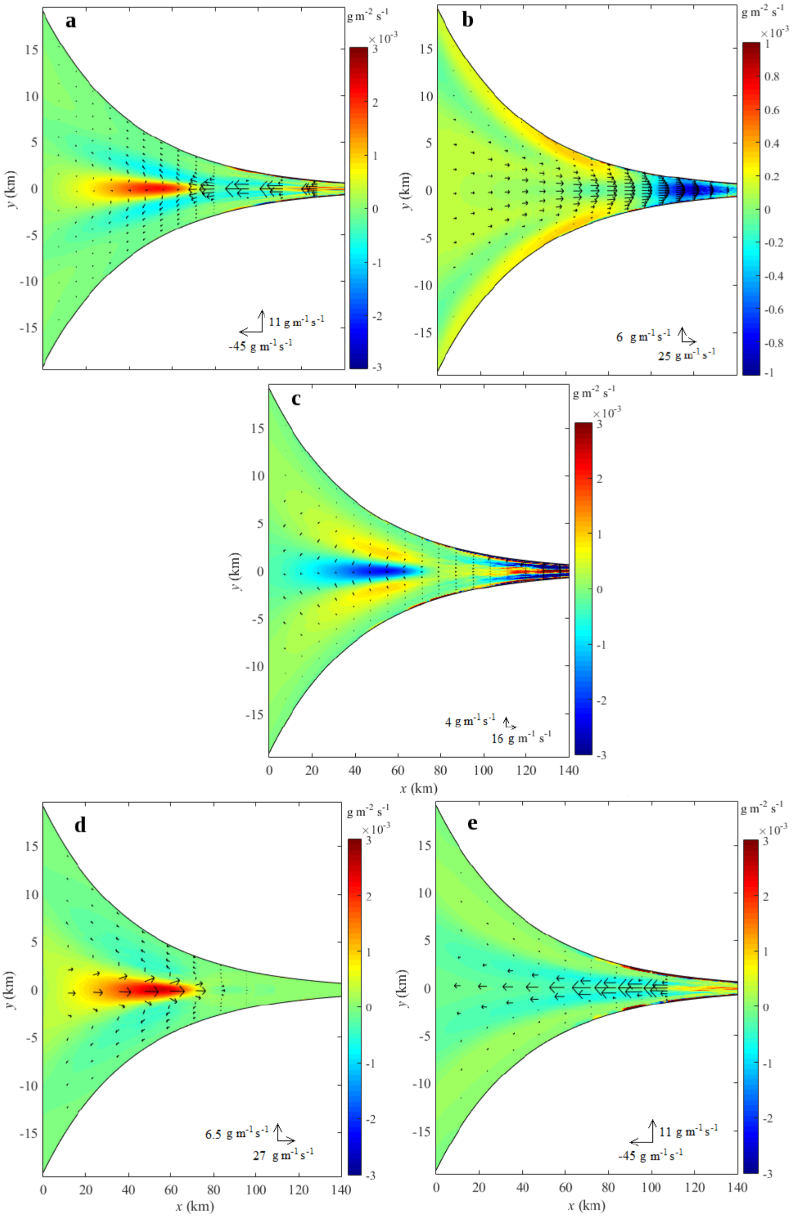

Figure 4.5: The divergence of the depth-integrated residual sediment transport (color scales) due to (a) residual advection of residual concentrations ($\mathbf{T}_{M_0}$), (b) tidal pumping ($\mathbf{T}_{M_2} + \mathbf{T}_{M_4}$), (c) diffusion ($\mathbf{T}_{DIFF}$), (d) transport due to advection of residual suspended sediment concentration by gravitational circulation ($\mathbf{T}^{GC}_{M_0}$) and (e) barotropic residual currents ($\mathbf{T}^{BR}_{M_0}$). The direction and magnitude of the transport vectors is shown by arrows.

$< x < 120$ km) of about 1 mg m^{-2} s^{-1} (see Fig. 4.5a). Downstream of the ETM ($x < 70$ km), $\mathbf{T}_{M_0}$ tends to transport sediments landward through the channel. Next, sediments are transported towards the flanks and subsequently exported over the shoals. This results in a strong divergence of sediment transport in the channel (up to 3 mg m^{-2} s^{-1}) and a convergence on the shoals (up to 1 mg m^{-2} s^{-1}). The residual sediment transport contributions $\mathbf{T}_{M_2}$ and $\mathbf{T}_{M_4}$ represent the depth-integrated sediment transport due to the temporal correlations between sediment concentrations and velocities at the M_2 and M_4 tidal frequencies. These contributions, which are called tidal pumping contribution hereafter, significantly contribute to the depth-integrated residual sediment transport and trapping, with $\mathbf{T}_{M_2}$ much larger than $\mathbf{T}_{M_4}$. The tidal pumping contribution plays an important role in transporting sediments from the seaward side towards the ETM. while its contribution to the lateral sediment transport is negligible (Fig. 4.5b). Tidal pumping results in a divergence of sediment transport at the seaward side of the ETM and a convergence within the ETM region of less than 1 mg m^{-2} s^{-1}. Diffusive processes contribute to a transport of sediments from the shoals towards the channel (Fig. 4.5c), which is consistent with the model results that sediment concentrations are larger on the shoals than in the channel. As a result, the diffusive contribution results in a significant convergence of the depth-integrated residual sediment transport in the channel (up to 3 mg m^{-2} s^{-1}) and a divergence on the shoals (up to 1 mg m^{-2} s^{-1}). Note that the divergence of the total depth-integrated residual sediment transport vanishes, as we assume the estuaries to be in morphodynamic equilibrium. It is clear that, downstream of the ETM, the landward sediment transport in the channel (see Fig. 4.4) is mainly due to $\mathbf{T}_{M_0}$ and tidal pumping, while the seaward sediment transport over the shoals is predominantly controlled by $\mathbf{T}_{M_0}$.

To assess the relative importance of the advection of residual sediment concentrations by gravitational circulation ($\mathbf{T}_{M_0}^{GC}$) and the other barotropic residual currents ($\mathbf{T}_{M_0}^{BR}$), the sediment transport due to these two contributions is shown in Figs. 4.5d-e, respectively, together with the resulting divergence of the transport. It is found that the largest contribution to the divergence of the residual sediment transport $\mathbf{T}_{M_0}$ in the seaward side of the ETM is related to the advection of the residual concentrations by the gravitational circulation ($\mathbf{T}_{M_0}^{GC}$). The convergence of the residual sediment transport $\mathbf{T}_{M_0}$ on the shoals downstream of the ETM is due to the combined effects of $\mathbf{T}_{M_0}^{GC}$ and $\mathbf{T}_{M_0}^{BR}$. The convergence of the residual sediment transport $\mathbf{T}_{M_0}$ in the ETM region, however, is mainly resulting from the advection of residual concentrations by the barotropic residual currents ($\mathbf{T}_{M_0}^{BR}$) (see Fig. 4.5e). The transport contribution $\mathbf{T}_{M_0}^{GC}$ tends to transport sediments landward through the deeper channel and seaward over the shoals (see Fig. 4.5d). The contribution $\mathbf{T}_{M_0}^{BR}$, however, transports sediments seaward at each location, especially in the channel. In the channel downstream of the ETM, the landward residual sediment transport contribution $\mathbf{T}_{M_0}^{GC}$ exceeds the seaward transport contribution $\mathbf{T}_{M_0}^{BR}$; while on the shoals, both $\mathbf{T}_{M_0}^{GC}$ and $\mathbf{T}_{M_0}^{BR}$ contribute to a seaward sediment transport. As a result, the landward sediment transport contribution $\mathbf{T}_{M_0}$ in the channel is smaller than the seaward transport on the shoals, as is visible in Fig. 4.5a.

4.3.4 Cross-sectionally integrated residual sediment balance

Integrating the sediment transport over the cross-section results in the cross-sectionally integrated residual sediment balance due to different processes. In Fig. 4.6a, it is shown that T_{M_2} and T_{M_0} are the dominant landward and seaward residual sediment transport contributions, respectively, while the residual sediment transport contributions T_{M_4} and T_{DIFF} are much smaller. To obtain the dominant sediment importing and exporting processes, the sediment transport contributions T_{M_2} and T_{M_0} are further decomposed into contributions related to specific processes listed in Table 4.1. The largest contribution to the landward residual sediment transport contribution T_{M_2} is caused by the M_2 tidal advection of the suspended sediment concentrations at the M_2 tidal frequency ($T_{M_2}^{\mathrm{IN}}$), as a result of the asymmetric bed shear stress due to interactions of the M_2 bottom velocity and the internally-generated M_4 bottom velocity. The M_2 tidal advection of the M_2 tidal concentration as a result of the spatial settling lag effects also results in a significant landward residual sediment transport contribution ($T_{M_2}^{\mathrm{SSL}}$). The tidal advection of the tidal concentrations as a result of the asymmetric bed shear stress due to the combined salinity-induced bottom residual velocity and the M_2 bottom flow also contributes to a small but non-negligible landward sediment transport ($T_{M_2}^{\mathrm{GC}}$). The M_2 tidal advection of the M_2 tidal concentration as a result of the asymmetric bed shear stress due to interactions between the M_2 tidal velocities and the externally-generated M_4 tidal velocities ($T_{M_2}^{\mathrm{EF}}$), however, is negligible for the residual sediment balance integrated over the cross-section. The M_2 tidal advection of the M_2 tidal concentration as a result of the asymmetric bed shear stress due to interactions between the M_2 tidal velocities and the barotropic residual currents ($T_{M_2}^{\mathrm{BR}}$) and transport due to surface contribution ($T_{M_2}^{\mathrm{SC}}$) result in a significant seaward residual transport of sediment. In Fig. 4.6c, it is shown that

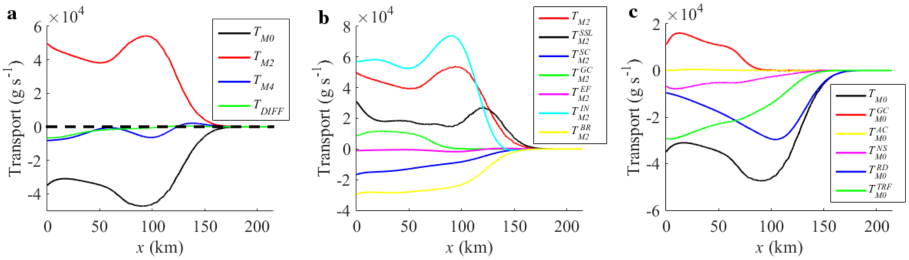

Figure 4.6: (a) Cross-sectionally integrated residual sediment transport contributions T_{M_0}, T_{M_2}, T_{M_4} and T_{DIFF}. Decomposed cross-sectionally integrated sediment transport contributions of (b) T_{M_2} and (c) T_{M_0}.

the advection of the residual sediment concentration by gravitational circulation ($T_{M_0}^{\mathrm{GC}}$) contributes to a landward sediment transport. The advection of residual sediment concentration by all barotropic residual velocities ($T_{M_0}^{\mathrm{RD}}$, $T_{M_0}^{\mathrm{AC}}$, $T_{M_0}^{\mathrm{NS}}$, $T_{M_0}^{\mathrm{TRF}}$), however, result in a seaward sediment transport (see Fig. 4.6c), with $T_{M_0}^{\mathrm{RD}}$ and $T_{M_0}^{\mathrm{TRF}}$ the dominant seaward sediment transport contributions.

4.3.5 Contributions to the ETM

In this section, the significance of residual sediment transport contributions due to M_2 tidal advection of the M_2 tidal concentration related to the internally-generated M_4 overtide, spatial settling lag effects, and the residual and M_2 tidal advective transport by gravitational circulation to the ETM formation is studied. Three dedicated experiments, in which one of these contribution is excluded, are used to show the differences of the characteristics of the resulting ETM in comparison with those in the default experiment.

In experiments I-II, the sediment transport contributions related to the internally-generated M_4 overtide ($\mathbf{T}_{M_2}^{\mathrm{IN}}$) and the spatial settling lag effects ($\mathbf{T}_{M_2}^{\mathrm{SSL}}$) are excluded, respectively. In both experiments, the ETM moves to the seaward boundary (see Figs. 4.7a-b). This implies that both $\mathbf{T}_{M_2}^{\mathrm{IN}}$ and $\mathbf{T}_{M_2}^{\mathrm{SSL}}$ are essential for the sediment trapping and the occurrence of the ETM in the central estuary. In experiment III, the transport contribution related to gravitational circulation ($\mathbf{T}_{M_2}^{\mathrm{GC}} + \mathbf{T}_{M_0}^{\mathrm{GC}}$) is excluded. Compared to the default experiment, the longitudinal location of the ETM is hardly changed, but the residual sediment concentration is reduced in the ETM (less than 90 mg l^{-1}, see Fig. 4.7c). This implies that even though the residual sediment transport contribution involving gravitational circulation results in a much more efficient trapping of sediments in the ETM and thence a much larger maximum sediment concentration (up to 130 mg l^{-1}, see Fig. 4.4), it is not essential for the formation of the ETM in the central estuary. It is worth noting that, by excluding this contribution, the sediment concentrations become larger in the channel than on the shoals. In conclusion, the sediment transports related to gravitation circulation play an important role in redistributing the trapped sediments in both longitudinal and lateral directions.

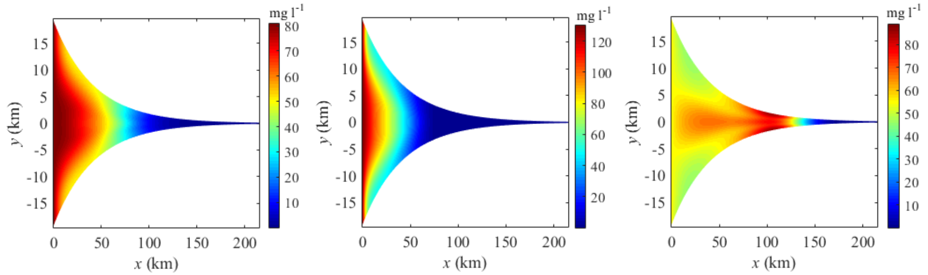

(a) no internal M_4 (b) no spatial settling lag (c) no gravitational circulation

Figure 4.7: The depth-averaged residual suspended sediment concentration after excluding the sediment transport contributions due to (a) the internally generated M_4 overtide, (b) the spatial settling lag effects, and (c) the gravitational circulation, respectively.

4.4 Influence of earth rotation

To investigate the influence of earth rotation on the sediment transport and trapping (necessary to compare the results with observations in the Delaware estuary), the Coriolis force is included in a dedicated experiment with $f = 1 \times 10^{-4}$ rad s^{-1}.

Comparing Fig. 4.8a with Fig. 4.3a shows that the location of the maximum sediment availability (~ 100 km from the seaward boundary) hardly changes by including the Coriolis force. The sediment availability, however, becomes laterally asymmetric, with larger values on the right shoal than on the left, looking seaward. In Figs. 4.8b-c, the 2DV distributions of the residual SSC and isohalines at the central axis of the estuary and the cross-sectional distribution of them at x = 100 km are shown, respectively. Comparing Figs. 4.8b-c with Fig. 4.3 reveals that the inclusion of the Coriolis forcing hardly change the longitudinal and vertical patterns of the residual SSC or salt intrusion (though the magnitudes of the residual SSC and salinity are slightly changed), but the lateral patterns of both the residual SSC and salinity are significantly changed. The Coriolis effects result in larger residual salinities on the left side of the estuary than on the right (see white lines in Fig. 4.8c). This lateral salinity gradients contribute to a lateral gravitational circulation transporting sediments from the left side of the estuary to the right shoal, thus resulting in larger sediment concentrations on the right shoal than the shoal on the left (see Fig. 4.8c). This lateral sediment trapping pattern in relation to the lateral salinity gradients is consistent with results in Huijts *et al.* (2006).

Figure 4.8d shows that the depth-integrated sediment transport patterns are significantly changed by the Coriolis force: sediments are transported landward from the left side of the estuary and transported seaward from the right side. The depth-integrated residual sediment transport in both longitudinal and lateral directions are increased, with the maximum longitudinal sediment transport of 35 g m^{-1} s^{-1} on the right shoal in the ETM region and a maximum lateral sediment transport of up to ~5 g m^{-1} s^{-1} on the left side of the channel near the mouth. The relative importance of different processes for the depth-integrated and cross-sectionally integrated residual sediment transport is hardly changed by Coriolis deflection (not shown).

By comparing the model results with observations of McSweeney *et al.* (2016a), it is found that the main features of the ETM in the Delaware estuary are qualitatively reproduced. First of all, the ETM is centered around 100 km for the river discharge used here (288 m^3 s^{-1}), with the region of elevated SSC distributed between approximately 80 km and 120 km from the mouth. Secondly, the lateral distribution of the simulated SSC is also consistent with observations, with larger sediment concentrations at the Delaware (right) side of the estuary than at the New Jersey (left) side. Moreover, the spatial sediment transport patterns observed by McSweeney *et al.* (2016a) are qualitatively reproduced, with sediments transported into the estuary from the left side of the deep channel, and transported down-estuary on the right flanks. Finally, the model confirms that the lateral depth-integrated residual sediment transport is mainly due to the advection of the residual SSC by the residual currents, while sediment transport contributions due to both tidal pumping and residual advection of residual concentration contribute significantly to the longitudinal residual sediment transport.

4.5 Sensitivity to sediment grain size and river discharge

To investigate the sensitivity of the sediment trapping locations and processes to particle size and river discharge, four experiments considering different grain sizes and river discharges are performed. In section 4.5.1, the sensitivity to the sediment grain size is studied by considering a grain size of 10 μm (fine-grained sediments) and 40 μm (relatively coarse-grained sediments), corresponding to a settling velocities of w_s =0.2 mm s^{-1} and w_s =1 mm s^{-1} (Fredsøe and Deigaard 1992), respectively. In section 4.5.2, the sensitivity to river discharge is investigated considering two different river discharges, R=72 m^3 s^{-1}, 864 m^3 s^{-1}. In these experiments, all other parameters including the av-

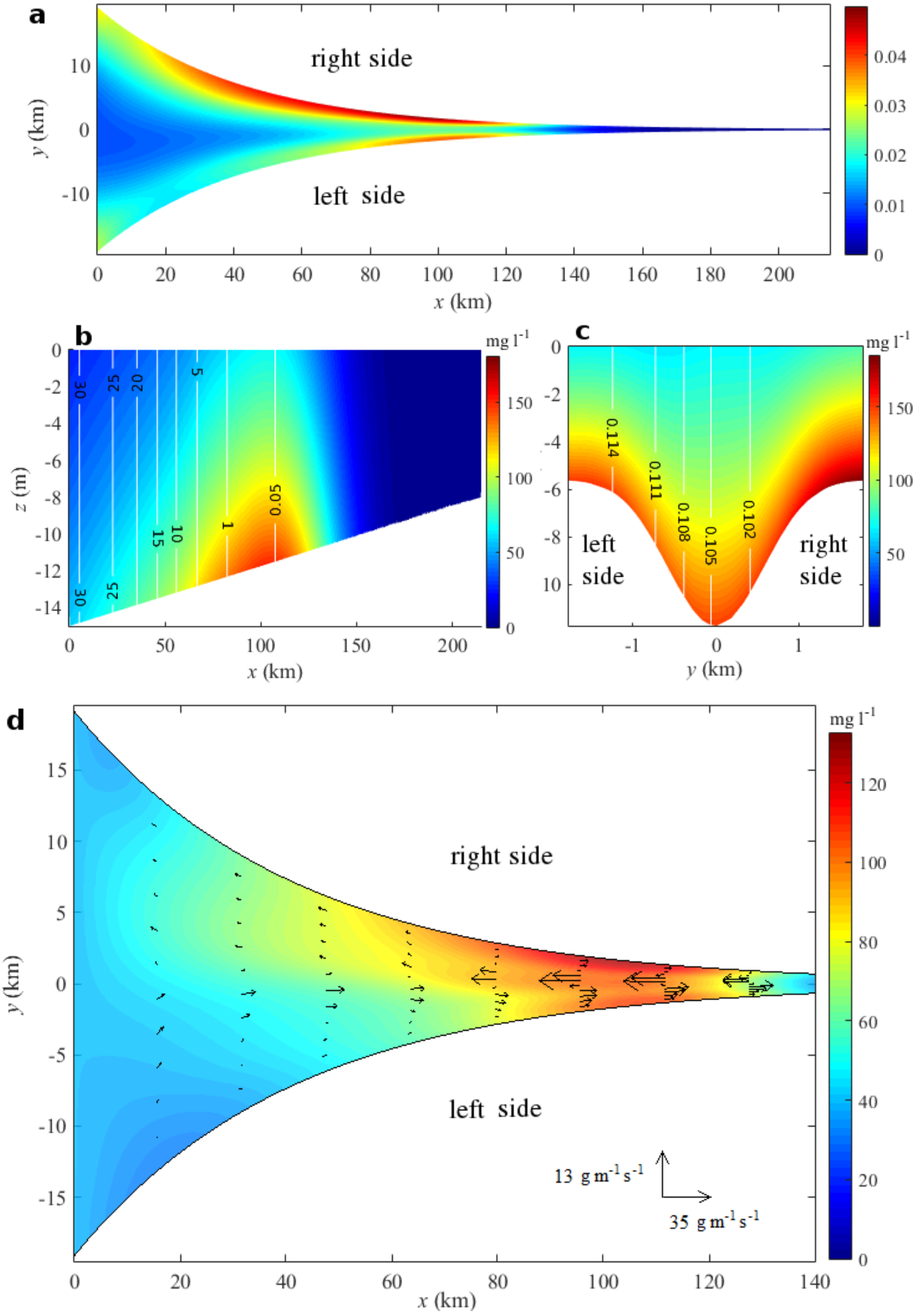

Figure 4.8: The same as Fig. 4.3 and Fig. 4.4, but for $f = 1 \times 10^{-4}$ rad s^{-1}.

eraged sediment availability a_*, are the same as those used in the default experiment. The differences of the sediment trapping and residual transport patterns, and the relative importance of different processes to the ETM formation, will be discussed in comparison with those in the default experiment.

4.5.1 Sensitivity to sediment grain size

Fine-grained sediments

For fine-grained sediments (w_s =0.2 mm s^{-1}, d_s =10 μm), the sediment availability, the three-dimensional structure of the residual SSC, and the depth-integrated sediment transport patterns change significantly (see Fig. 4.9) compared to those in the default experiment. The maximum sediment availability moves towards the seaward side, and is found at x ~30 km (see Fig. 4.9a). The residual SSC becomes more vertically uniform, and the ETM occurs at relatively large salinities in the downstream region (see Fig. 4.9b). Moreover, the lateral difference of the residual SSC between the shoals and the channel becomes more pronounced, with more strongly elevated residual sediment concentrations on the shallow shoals at all depths (Fig. 4.9c). In the region with elevated depth-averaged residual sediment concentrations (x < 70 km), the depth-integrated residual sediment transport circulation cells are enhanced with a significant landward transport through the channel and seaward transports over the shoals (see Fig. 4.9d).

The cross-sectionally integrated residual transport contributions T_{M_2} and T_{M_0} remain the dominant sediment sediment contributions (Fig. 4.10a), but the transport processes are significantly changed (Figs. 4.10b-c) compared to those in the default experiment. The sediment transport contributions due to the M_2 tidal advection of M_2 tidal concentrations related to the internally-generated M_4 overtide ($T_{M_2}^{\mathrm{IN}}$) and the gravitational circulation ($T_{M_2}^{\mathrm{GC}}$) are both reduced, while that related to spatial settling lag effects ($T_{M_2}^{\mathrm{SSL}}$) is significantly increased (Fig. 4.10b). The transport due to advection of residual SSC by gravitational circulation $T_{M_0}^{\mathrm{GC}}$ results in a significant seaward sediment transport for fine-grained sediments (Fig. 4.10c), contrasting the landward transport contribution $T_{M_0}^{\mathrm{GC}}$ in the default experiment (Fig. 4.6c).

The contribution of the sediment transports related to the internally-generated M_4 tide ($\mathbf{T}_{M_2}^{\mathrm{IN}}$), spatial settling lag effects ($\mathbf{T}_{M_2}^{\mathrm{SSL}}$) and gravitational circulation ($\mathbf{T}_{M_2}^{\mathrm{GC}} + \mathbf{T}_{M_0}^{\mathrm{GC}}$) to the trapping patterns of fine-grained sediments are strongly influenced by the sediment grain-size. For fine-grained sediments, excluding the sediment transport contributions caused by the spatial settling lag effects and the internally generated M_4 overtide results in an ETM at the seaward boundary (Figs. 4.10a-b), as was found in the default experiment. However, different from the default experiment, excluding the sediment transport contribution induced by gravitational circulation, results in a noticeable landward shift of the ETM (up to ~30 km, see Fig. 4.10c). This again illustrates that gravitational circulation plays an important role in transporting fine-grained sediments seaward and trapping them in the downstream region.

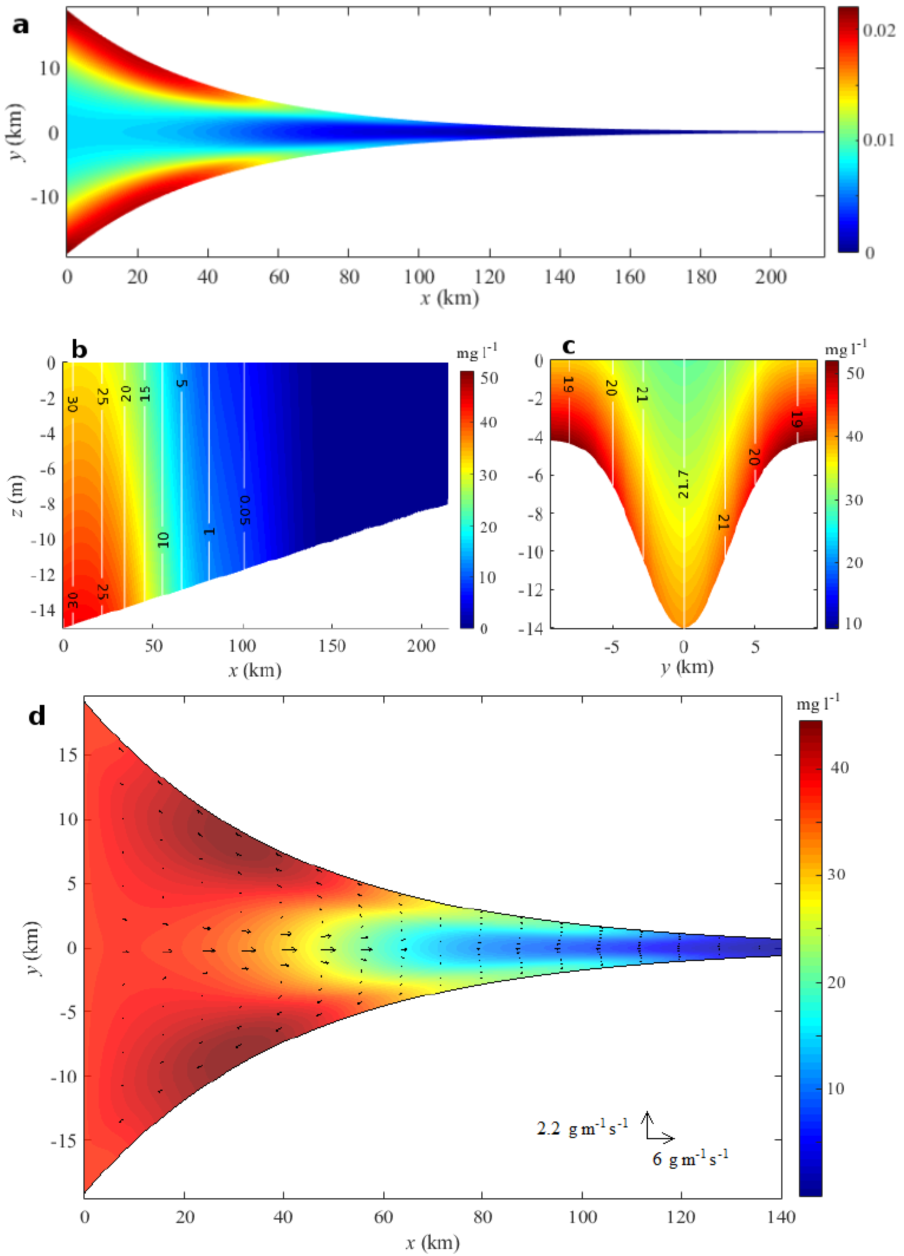

Figure 4.9: The same as Fig. 4.8, but for $f = 0$, w_s =0.2 mm s^{-1} and d_s =10 μm. The cross-section in Fig. 4.9c is taken at $x = 30$ km.

Coarse-grained sediments

For more coarse-grained sediments (w_s = 1 mm s^{-1}, d_s =40 μm), the longitudinal locations of the maximal sediment availability a hardly changes compared to those in the

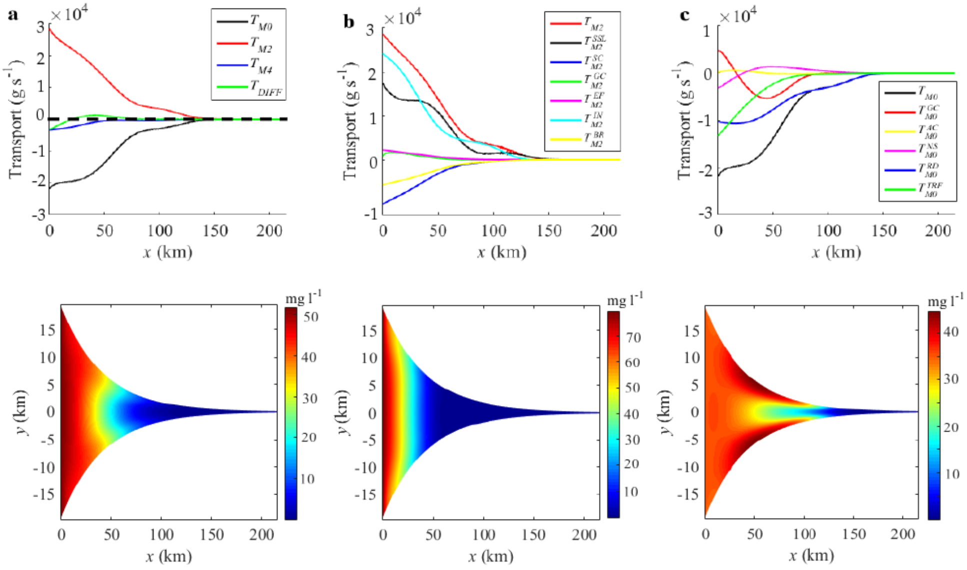

(d) no internal M_4 (e) no spatial settling lag (f) no gravitational circulation

Figure 4.10: The same as Fig. 4.6 (upper panels) and Fig. 4.7 (lower panels), but for w_s = 0.2 mm s^{-1} and d_s =10 μm.

default experiment, but the maximum a is now found in the channel (see Fig. 4.11a). The longitudinal location of the maximum residual SSC is nearly the same as that in the default experiment (coinciding with the ~0.5 psu isohaline, see Fig. 4.11b). Considering a larger settling velocity, however, results in a much larger residual SSC near the bottom than in the upper layers. Moreover, the sediment concentrations of coarse-grained sediments are much larger in the channel than on the shoals (see Fig. 4.11c). The depth-integrated residual transport of coarse-grained sediments is most significant in the ETM region between 70 km and 120 km up-estuary from the mouth (see color scales in Fig. 4.11d), where sediments are efficiently transported seaward through the channel and landward over the shoals (see arrows).

By considering sediments of a larger grain size, the landward transport contribution due to M_2 tidal advection of the M_2 tidal concentrations related to the internally-generated M_4 overtide ($T_{M_2}^{\mathrm{IN}}$) becomes more significant, while that related to spatial settling lag effects ($T_{M_2}^{\mathrm{SSL}}$) decreases within the ETM region and contributes to a seaward transport of sediments downstream of the ETM (for $x < 70$ km). The landward sediment transport contributions due to advective transport by gravitational circulation ($T_{M_2}^{\mathrm{GC}}$ and $T_{M_2}^{\mathrm{GC}}$) are increased (see Figs. 4.12b-c). These transport contribution changes have a strong influence on the ETM: the ETM shifts seaward (for ~ 30 km) by excluding the M_2 tidal advection of M_2 tidal concentrations related to to the internally-generated M_4 tide (Fig. 4.12d); excluding the contribution related to the spatial settling lag effects also results in a seaward shift of the ETM (for ~ 20 km), and the width of the region with elevated concentrations significantly decreases (Fig. 4.12e). Excluding the residual sedi-

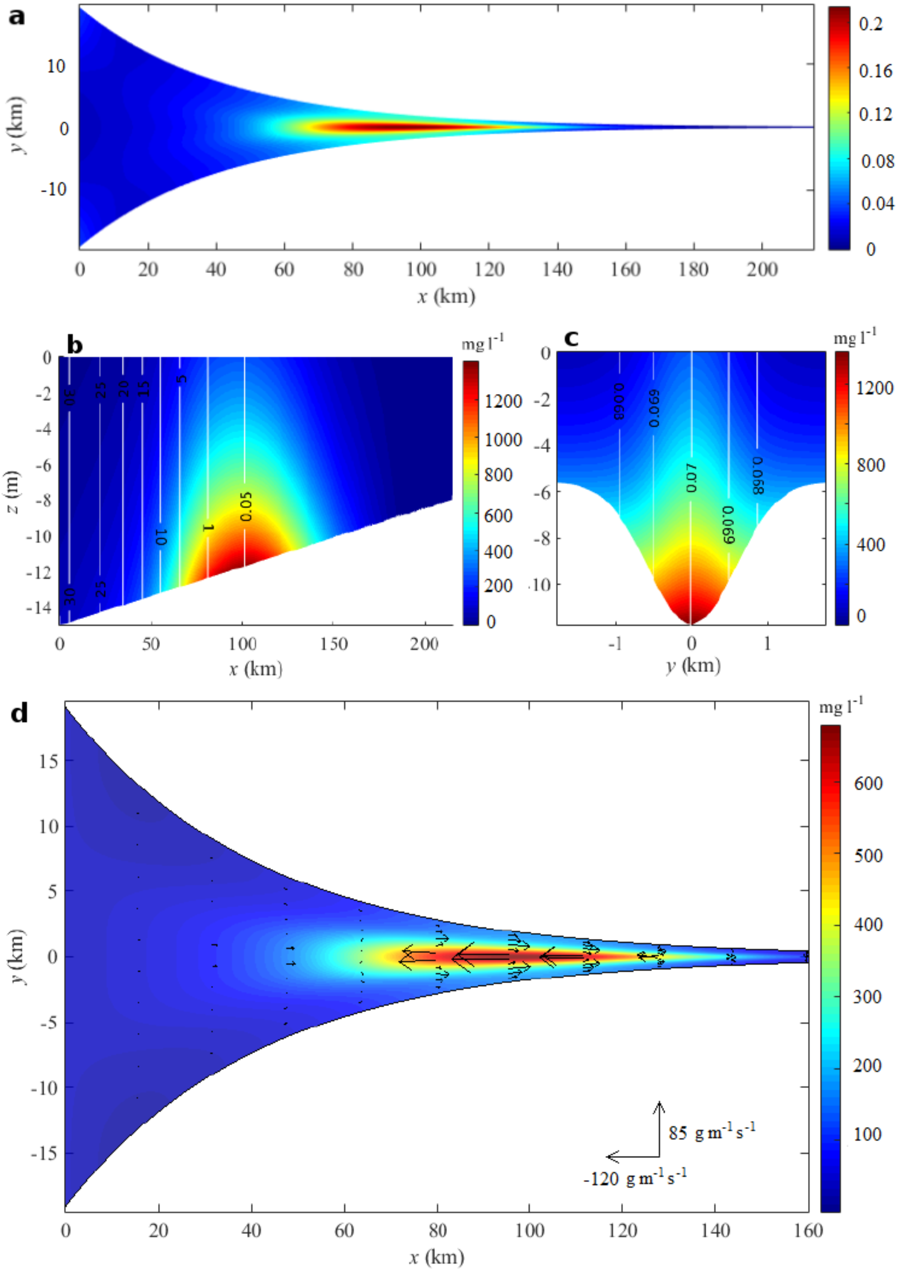

Figure 4.11: The same as Fig. 4.8, but for $w_s = 1$ mm s^{-1} and d_s =40 μm. The cross-section in Fig. 4.11c is taken at $x = 100$ km.

ment transport due to advection of residual SSC by gravitational circulation again results in an ETM near the seaward boundary (Fig. 4.12f).

The changes of the relative importance of the main cross-sectionally integrated residual sediment transport contributions are summarized in Table 4.3. Here " + " indicates the importance of the transport contribution is increased compared to that in the default experiment, " − " indicates the contribution becomes less important, and " ∗ " indicates that the direction of the sediment transport is changed. The qualitative changes (relative importance) of these transport contributions are mainly related to different settling velocities. By considering more fine-grained sediments with smaller settling velocities, it allows particles to travel longer distances in both longitudinal and lateral directions before settling to the bottom, which results in a more important sediment transport contribution due to the spatial settling lag effects ($T_{M_2}^{\mathrm{SSL}}$). Small settling velocities are also responsible for a more uniform suspended sediment concentration over the cross-section (see for example Fig. 4.9c). This results in less important contributions due to advection of residual SSC by residual circulation ($T_{M_0}^{\mathrm{GC}}$, $T_{M_0}^{\mathrm{NS}}$, $T_{M_0}^{\mathrm{TRF}}$), and less important contributions due to tidal advection of tidal concentrations related to asymmetric bed shear stresses ($T_{M_2}^{\mathrm{GC}}$, $T_{M_2}^{\mathrm{BR}}$, $T_{M_2}^{\mathrm{IN}}$), as shown in Table 4.3. The advection of residual SSC by river-induced flow ($T_{M_0}^{\mathrm{RD}}$) becomes more dominant in the seaward residual sediment transport as a result of the increased residual SSC in the upper water column where the maximum river-induced flow occurs. The seaward residual transport due to advection of residual SSC by gravitational circulation integrated over the cross-section ($T_{M_0}^{\mathrm{GC}}$) is caused by much larger residual concentrations on the shoals than in the channel, and the seaward residual sediment transport on the shoals exceeds the landward transport in the channel.

By considering a larger sediment grain size with larger settling velocity, sediments can settle to the bed faster, resulting in a more concentrated region near the bottom of the channel (see Fig. 4.11c), where the bed shear stress is largest. As a result, the residual sediment transport contribution related to the spatial settling lag effects ($T_{M_2}^{\mathrm{SSL}}$) becomes less important, and a seaward residual sediment transport is induced downstream of the ETM. The residual sediment transport contributions related to the advection of residual SSC by residual circulation ($T_{M_0}^{\mathrm{GC}}$, $T_{M_0}^{\mathrm{NS}}$, $T_{M_0}^{\mathrm{TRF}}$) and the M_2 tidal advection of M_2 tidal concentrations related to asymmetric bed shear stress ($T_{M_2}^{\mathrm{GC}}$, $T_{M_2}^{\mathrm{BR}}$, $T_{M_2}^{\mathrm{IN}}$), however, become more important (see Table 4.3). The sediment transport contribution $T_{M_0}^{\mathrm{RD}}$ is decreased because of the reduced surface concentration.

4.5.2 Sensitivity to river discharge

Low river discharge

By decreasing the river discharge from 288 to 72 $\mathrm{m}^3\ \mathrm{s}^{-1}$, the largest sediment availability moves landward by ~30 km, and is now located at x ~130 km (Fig. 4.13a). The residual salt intrusion at the central axis of the estuary is enhanced, reaching its landward limit at ~ 130 km up-estuary from the mouth, where the maximum residual suspended sediment concentration is found (Fig. 4.13b). At the cross-section at $x = 130$ km, salinities are larger in the channel than on the shoals, and the residual sediment concentrations are larger on the shoals than in the middle (Fig. 4.13c). The depth-integrated residual sedi-

Table 4.3: Changes of the relative importance of main residual sediment transport contributions integrated over the cross-section by varying settling velocities and river discharges. Here " + " and " – " indicate the relative importance of the sediment transport contribution is increased and decreased, respectively, and " ∗ " indicates the resulting residual sediment transport changes from a seaward transport contribution to a landward transport contribution, or vice versa.

	component	w_s =0.2 mm s^{-1} d_s =10 μm	w_s =1 mm s^{-1} d_s =40 μm	$R = 72$ m^3 s^{-1}	$R = 864$ m^3 s^{-1}
T_{M_2}	$T_{M_2}^{\mathrm{GC}}$	−	+	−	+
	$T_{M_2}^{\mathrm{BR}}$	−	+	−	+
	$T_{M_2}^{\mathrm{IN}}$	−	+	+	−
	$T_{M_2}^{\mathrm{SSL}}$	+	∗	∗	+
T_{M_0}	$T_{M_0}^{\mathrm{GC}}$	∗	+	−	+
	$T_{M_0}^{\mathrm{NS}}$	−	+	+	−
	$T_{M_0}^{\mathrm{TRF}}$	−	+	+	−
	$T_{M_0}^{\mathrm{RD}}$	+	−	−	+

ment transport is significantly reduced, with a small seaward sediment transport through the channel and landward transport over the shoals within the ETM region (Fig. 4.13d).

By decreasing the river discharge, T_{M_2} and T_{M_0} remain the most dominant sediment transport contributions integrated over the cross-section (Fig. 4.14a). The dominance of sediment transport contribution related to the internally-generated M_4 overtide ($T_{M_2}^{\mathrm{IN}}$) becomes more pronounced, and the transport due to the spatial settling lag effects ($T_{M_2}^{\mathrm{SSL}}$) results in a more important landward sediment transport downstream of the ETM and seaward transport upstream of the ETM. The sediment transports due to both river discharge ($T_{M_0}^{\mathrm{RD}}$) and gravitational circulation ($T_{M_0}^{\mathrm{GC}}$ and $T_{M_2}^{\mathrm{GC}}$) decrease significantly (see Figs. 4.14b-c).

Excluding the M_2 tidal advection of the M_2 tidal component of concentrations related to either the internally-generated M_4 tide or gravitational circulation results in a significant seaward shift of the ETM from the central estuary to the mouth (see Fig. 4.14a). By excluding the sediment transport due to the spatial settling lag effects, the ETM slightly shifts towards the sea (for less than 10 km), with most sediments trapped in a small region in the central estuary (see Fig. 4.14b). Excluding the gravitational circulation hardly changes longitudinal location of the ETM, but the maximum sediment concentration is reduced (see Fig. 4.14c).

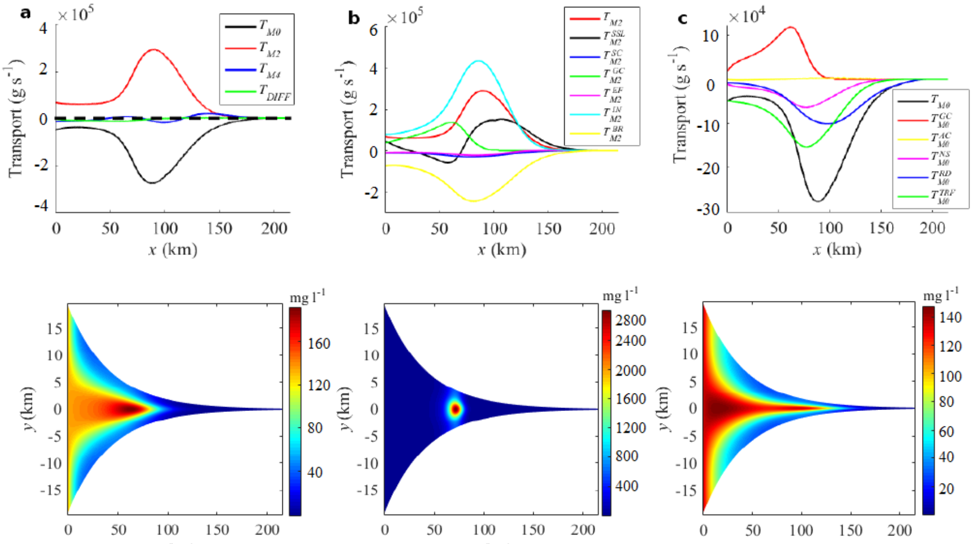

(d) no internal M_4 (e) no spatial settling lag (f) no gravitational circulation

Figure 4.12: The same as Fig. 4.6 (upper panels) and Fig. 4.7 (lower panels), but for w_s = 1 mm s^{-1} and d_s =40 μm.

High river discharge

By increasing the river discharge from 288 to 864 m^3 s^{-1}, the maximum sediment availability is found near the mouth (Fig. 4.15a). The salt intrusion is dramatically reduced, with the 1 psu isohaline at the central axis of the estuary shifting from ~ 125 km to ~ 55 km from the mouth (see white lines in Fig. 4.15b). The maximum residual suspended sediment concentration at the central axis of the estuary is found at x ~50 km (Fig. 4.15b), coinciding the 5 psu isohaline. The residual SSC at x = 50 km is larger in the channel than on the shoals, and the sediment concentrations become more laterally uniform (Fig. 4.15c). Within the ETM region (x < 60 km), sediments are transported landward through the channel, laterally transporting towards the flanks, and subsequently transported seaward over the shoals (see arrows in Fig. 4.15d). Moreover, it is found that the maximum depth-averaged residual concentrations are located in the center of the transport circulation cells.

For R = 864 m^3 s^{-1}, the sediment transport contributions T_{M_2} and T_{M_0} still dominate the cross-sectionally integrated residual sediment balance (Fig. 4.16a). The major changes in this balance are that, the sediment transport contributions due to M_2 tidal advection of the M_2 tidal concentrations related to the internally-generated M_4 overtide ($T^{\mathrm{IN}}_{M_2}$) decreases and that related to the spatial settling lag effects ($T^{\mathrm{SSL}}_{M_2}$) increases. The landward sediment transport contributions induced by gravitational circulation ($T^{\mathrm{GC}}_{M_2}$ and $T^{\mathrm{GC}}_{M_0}$) are also increased. As a result, excluding the sediment transport related to any of these three contributions results in an ETM at the seaward entrance (see Figs. 4.16d-f).

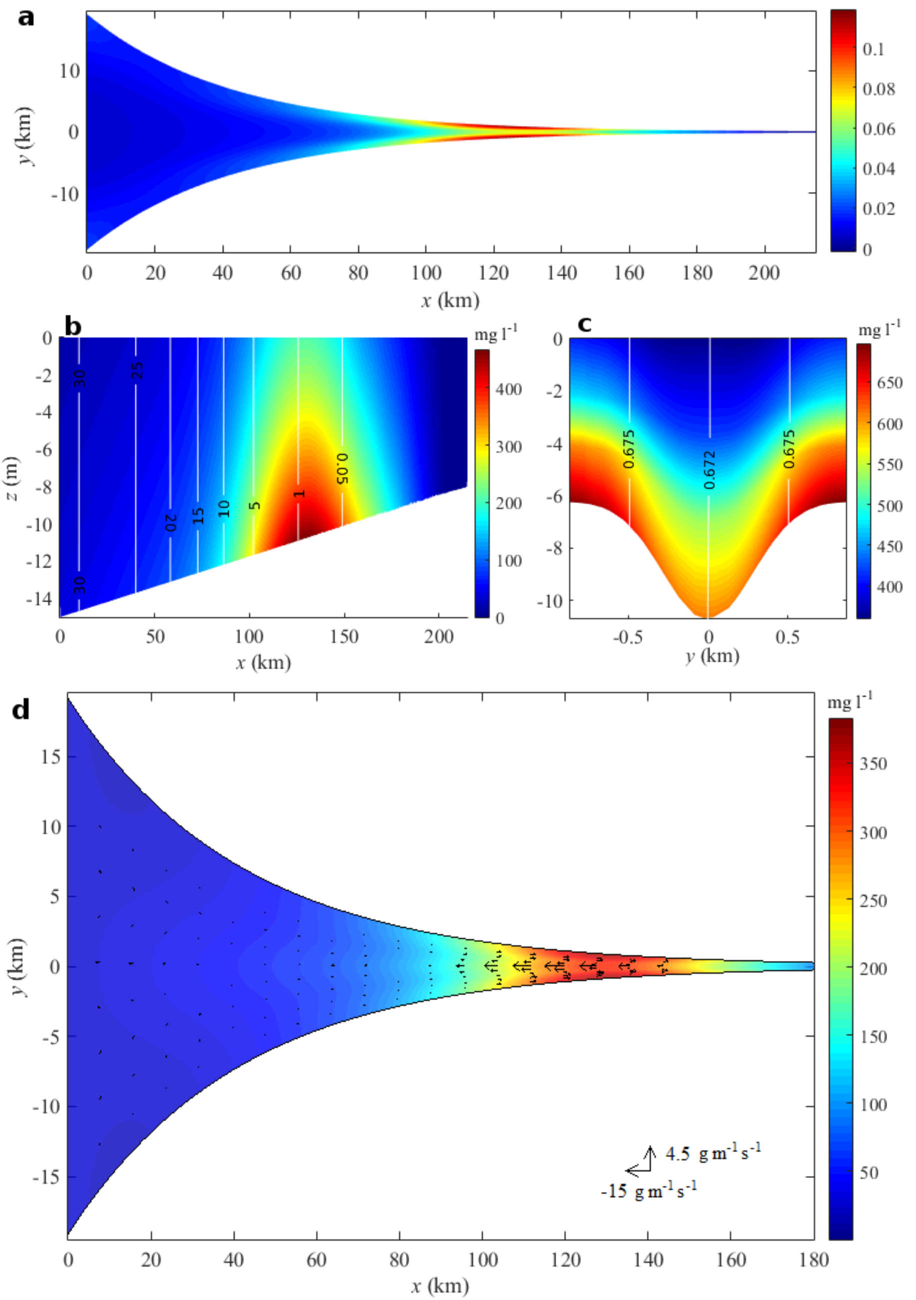

Figure 4.13: The same as Fig. 4.8, but for $R = 72$ m^3 s^{-1}. The cross-section in Fig. 4.13c is taken at $x = 130$ km.

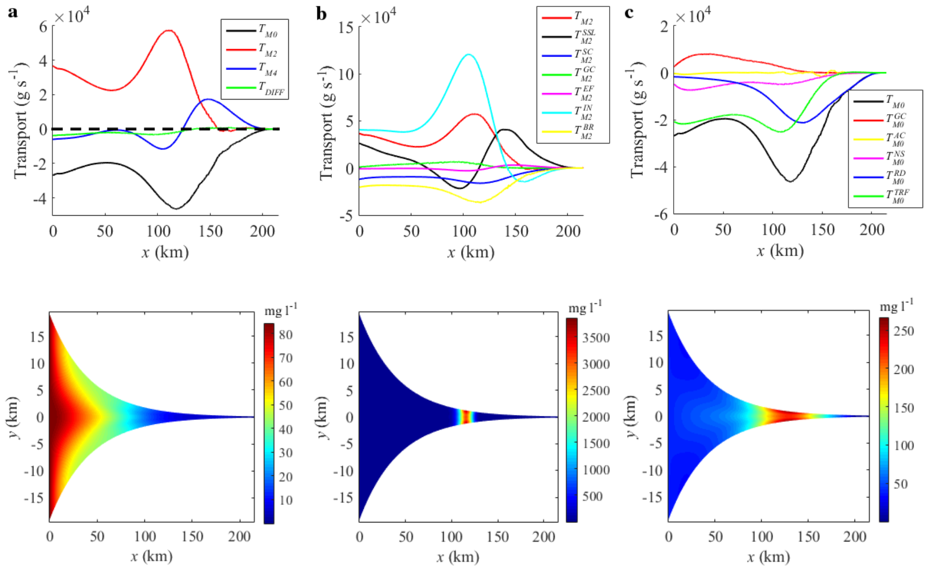

(d) no internal M_4 (e) no spatial settling lag (f) no gravitational circulation

Figure 4.14: The same as Fig. 4.6 (upper panels) and Fig. 4.7 (lower panels), but for $R = 72$ m^3 s^{-1}.

The main changes of the relative importance of residual sediment transport contributions by varying river discharge are summarized in Table 4.3. By decreasing (increasing) river discharge, the river-induced residual flow is decreased (increased), and the ebb-dominant bed shear stress becomes less (more) significant. This results in a reduced (increased) residual sediment transport contribution due to advection of residual SSC by river-induced flow ($T^{\mathrm{RD}}_{M_0}$) and a reduced (increased) residual transport due to M_2 tidal advection of the M_2 tidal concentration as a result of the river-induced ebb-dominant bed shear stress (included in $T^{\mathrm{BR}}_{M_2}$). Moreover, decreasing (increasing) river discharge results in smaller (larger) longitudinal and lateral salinity gradients, hence decreasing (increasing) the residual sediment transport contributions related to gravitational circulation ($T^{\mathrm{GC}}_{M_2}$, $T^{\mathrm{GC}}_{M_0}$), see Table 4.3. Decreasing (increasing) river discharge also results in a narrower (wider) ETM region, which results in a more (less) important residual sediment transport contribution due to spatial settling lag effects ($T^{\mathrm{SSL}}_{M_2}$). The residual sediment transport contributions due to other processes ($T^{\mathrm{IN}}_{M_2}$, $T^{\mathrm{TRF}}_{M_0}$) become more (less) dominant, maintaining the balance of the residual sediment transport over the cross-section at steady states.

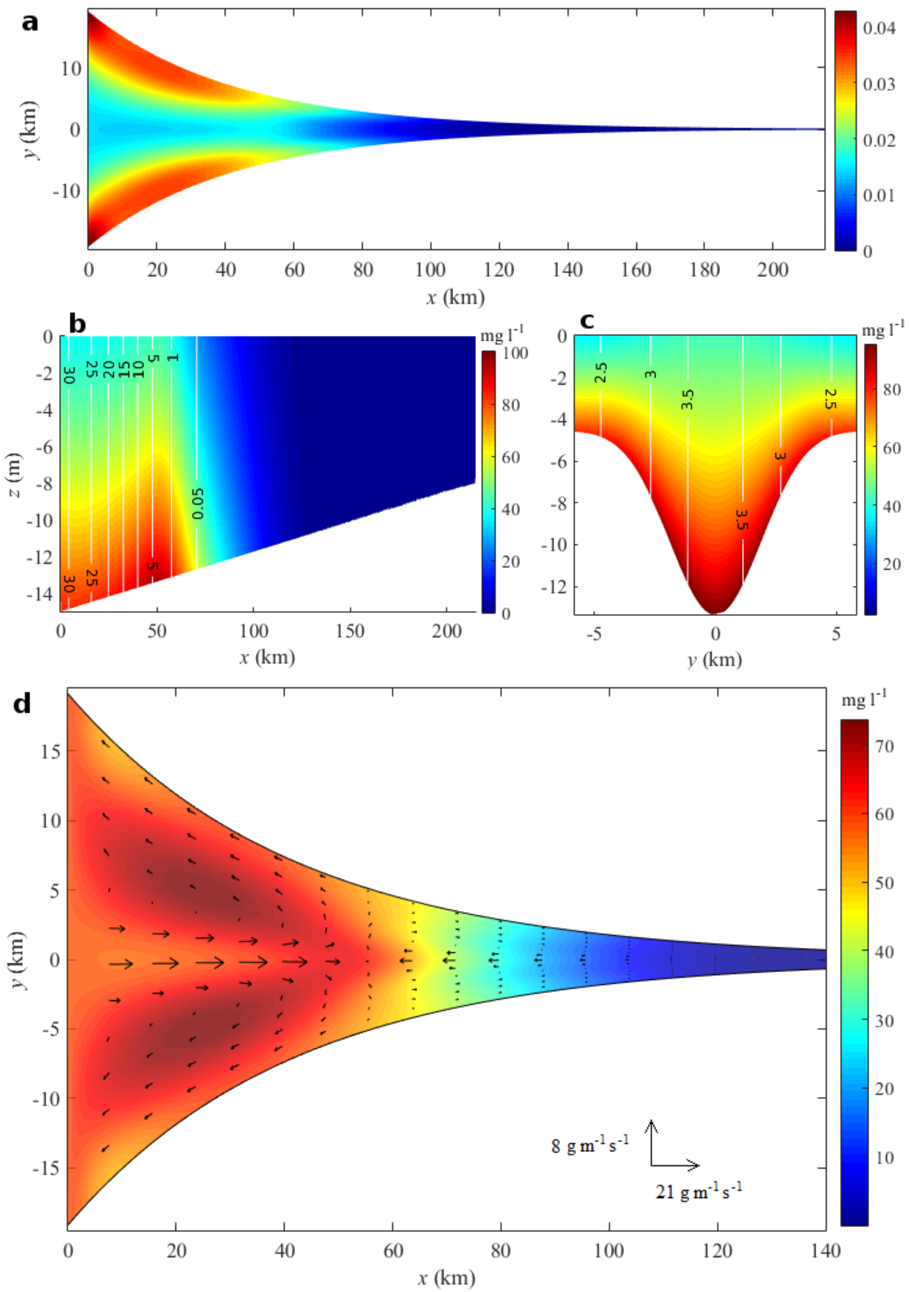

Figure 4.15: The same as Fig. 4.8, but for $R = 864$ m^3 s^{-1}. The cross-section in Fig. 4.15c is taken at $x = 50$ km.

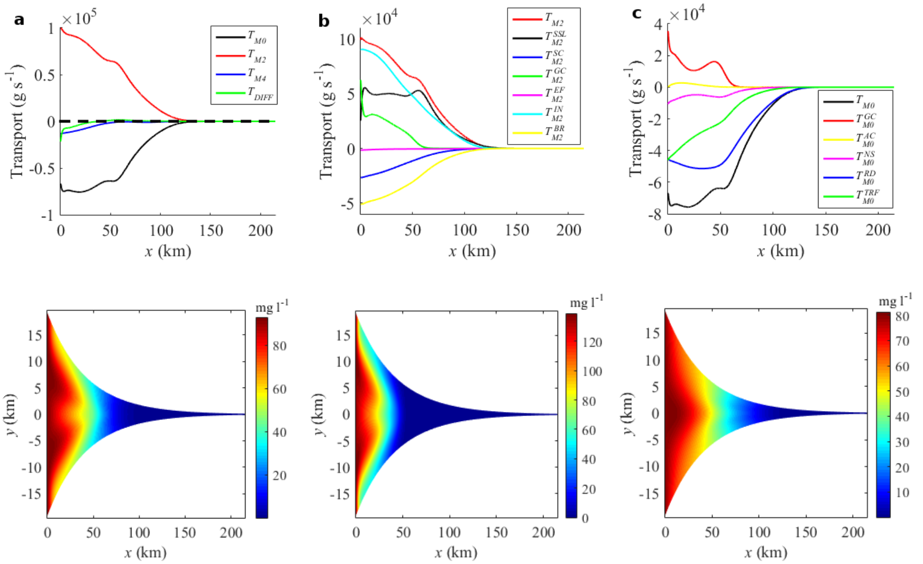

(d) no internal M_4 (e) no spatial settling lag (f) no gravitational circulation

Figure 4.16: The same as Fig. 4.6 (upper panels) and Fig. 4.7 (lower panels), but for $R = 864$ m^3 s^{-1}.

4.6 Model limitations

4.6.1 Deviations from observations

A major difference between the model results and the observational results of McSweeney *et al.* (2016a) is that, in the observations, the cross-sectionally integrated tidally-averaged sediment transport due to tidal pumping can vary from up-estuary to down-estuary with increasing river discharges, while in the present model tidal pumping always results in a landward sediment transport. This inconsistency can be understood by noting that the sediment transport in the model is obtained by assuming the estuary to be in morphodynamic equilibrium, while the observed sediment transport is obtained under non-equilibrium conditions with time-varying forcing conditions such as river discharge and tides. The observed transport patterns may thus deviate from those in morphodynamic equilibrium. This hypothesis is tested by recalculating the residual sediment transport contribution due to tidal pumping under a large river discharge condition using the sediment availability which is obtained under a small river discharge condition. Test results show that the tidal pumping contribution results in a significant seaward residual sediment transport. This suggests that by increasing river discharge, the tidal pumping contribution tends to transport sediment seaward to reach a new morphodynamic equilibrium.

4.6.2 Unresolved processes

Even though many processes contributing to sediment transport and trapping are resolved in the model presented in this chapter, there are a number of processes which are potentially important but not taken into account. Among these processes are the sediment transport related to the residual flow due to the covariance between the temporally varying eddy viscosity and shear (Jay and Musiak 1994, Burchard and Hetland 2010, Burchard *et al.* 2011, Burchard and Schuttelaars 2012), constrained sediment resuspension in case of strong salinity-induced stratifications in the lower water column (Geyer 1993, Scully and Friedrichs 2003, 2007) and sediment-induced residual currents (Talke *et al.* 2009). For example, in case of the Delaware estuary, the simulated ETM for a river discharge of $R = 864$ m^3 s^{-1} is located at a much more seaward position compared to the observations of Sommerfield and Wong (2011). This deviation may be related to the salinity-induced stratification, which is significant in the Delaware estuary in case of large river discharges (Aristizábal and Chant 2014, McSweeney *et al.* 2016a,b), but is ignored in the present model. Beyond that, the effects of the critical bed shear stress and hindered settling are not considered. Last but not least, flocculation, which is evidenced to be important in the region of low salinities in the Delaware estuary (Gibbs *et al.* 1983), is also excluded in the model.

4.7 Conclusions

The sediment transport and trapping in estuaries are important to estuarine morphology, ecology and economy, but the dominant physical processes behind the three-dimensional sediment dynamics are not well understood. This chapter introduces a semi-analytical 3D model to identify the dominant processes governing the sediment transport and trapping in well-mixed estuaries. This model resolves the three-dimensional dynamic effects of salinity on water motion and sediment transport. As a study case, the sediment dynamics in a schematized estuary with a channel-shoal structure and an exponentially decreasing width is studied. A river discharge of 288 m^3 s^{-1} is considered and a constant sediment settling velocity of 0.5 mm s^{-1} is used, which are representative for the Delaware estuary. As a first step, Coriolis is ignored. The maximum suspended sediment concentration (SSC) is found near the salt intrusion limit, with larger concentrations in the channel than on the shoals. The depth-integrated residual sediment transport shows remarkable symmetric circulation cells: downstream of the ETM, sediments are transported from the seaward region to the ETM through the channel and transported from the ETM towards the sea over the shoals. Within the ETM region, sediments are transported landward over the shoals and transported from the landward regions to the ETM through the channel. The longitudinal component of these transports is dominated by the advection of (mainly M_2) tidal suspended sediment concentrations by tidal currents (tidal pumping contribution), and advection of residual concentrations by residual currents. The lateral transport component, however, is controlled by advection of the residual concentrations by the gravitational circulation.

The cross-sectionally integrated residual seaward sediment transport is dominated by advection of the residual suspended sediment concentration by river-induced flow and the tidal return flow. The landward sediment transport is mainly controlled by advection of the M_2 tidal concentrations by M_2 tidal currents. This transport contribution is accomplished through many different processes. Among these the most important ones are related to the internally-generated M_4 tidal currents, spatial settling lag effects and gravitational circulation. First of all, the asymmetric bed shear stress due to interactions of the internally-generated M_4 bottom current and the M_2 bottom current results in an M_2 tidal component of the suspended sediment concentration which temporally correlates with the M_2 tidal currents and results in a residual sediment transport. This is the most important mechanism contributing to the landward residual sediment transport. Moreover, the temporal correlation between M_2 tidal velocities and the residual and M_4 tidal components of concentrations also results in an M_2 tidal concentration, which interacts with the M_2 tidal currents and results in a significant landward sediment transport. Besides, the advection of the residual concentrations by gravitational circulation, and the M_2 tidal advection of the M_2 tidal concentration (which is originated from the asymmetric bed shear stress due to the combined M_2 tidal and salinity-induced residual bottom currents), also contribute significantly to the landward residual sediment transport. The former two sediment transport contributions related to the internally-generated M_4 overtide and spatial settling lag effects are essential for the formation of the ETM in the central region of the estuary. The transport contributions due to gravitational circulation, however, mainly affects the lateral distribution of the suspended sediments.

Including Coriolis force results in an asymmetric SSC distribution with respect to the central axis of the estuary, with larger residual concentrations on the right shoal than on the left, looking seaward. The depth-integrated sediment transport shows one circulation cell with sediments transported landward from the left side of the estuary and seaward from the right. These results are qualitatively consistent with the observations of McSweeney *et al.* (2016a) for the river discharge considered here. The relative importance of different sediment contributions is not significantly influenced by the Coriolis effects.

The characteristics of the ETM and the relative importance of different residual sediment transport contributions are significantly influenced by sediment settling velocity. By decreasing the settling velocity from 0.5 mm s^{-1} to 0.2 mm s^{-1}, the ETM moves downstream of the salt intrusion limit, with much larger residual suspended sediment concentrations on the shoals than in the channel. Residual sediment transport is significant within the ETM region, where sediments are transported landward through the channel and seaward over the shoals. The M_2 tidal advection of the M_2 tidal component of concentrations related to the internally-generated M_4 tide and spatial settling lag effects dominates the cross-sectionally integrated landward residual sediment transport. The advection of the M_2 tidal concentrations (which is related to the gravitational circulation) by the M_2 tidal currents results in a seaward sediment transport integrating over the cross-section. This process contributes significantly to trapping sediments in the downstream region. By increasing the settling velocity to 1 mm s^{-1}, the ETM remains near the salt intrusion limit in the central region of the estuary, while the residual suspended sediment concentrations become larger in the channel than on the shoals. Significant residual sediment transports are found within the ETM with sediments transported seaward through the channel and landward over the shoals. The M_2 tidal advection of M_2 tidal concentrations related to the internally-generated M_4 tide predominates the landward residual sediment transport integrated over the cross-section, while that related to spatial settling lag effects controls the width of the ETM by transporting sediments from the ETM to regions further downstream or upstream. The suspended sediment transport related to the gravitational circulation makes a more significant contribution to the landward residual sediment transport.

The ETM moves slightly landward by decreasing the river discharge to 72 m^3 s^{-1}. For this river discharge, the landward residual sediment transport is predominantly controlled by the M_2 tidal advection of the M_2 tidal concentrations related to the internally-generated M_4 tide. The residual sediment transport due to the spatial settling lag effects contributes significantly in transporting sediments from the ETM region and controls the width of the ETM. By increasing the river discharge to 864 m^3 s^{-1}, the ETM moves significantly towards the sea. The sediment transport contributions due to the M_2 tidal advection of the M_2 tidal concentrations related to the internally-generated M_4 tide and spatial settling lag effects, and the advective transport related to the gravitational circulation, are all essential to the landward residual sediment transport and the formation of the ETM.

References

Aristizábal, M., and R. Chant, *Mechanisms driving stratification in Delaware Bay estuary,* Ocean Dynamics **64**, 1615–1629 (2014).

Aubrey, D., *Hydrodynamic controls on sediment transport in well-mixed bays and estuaries,* Physics of Shallow Estuaries and Bays , 245–258 (1986).

Becherer, J., G. Flöser, L. Umlauf, and H. Burchard, *Estuarine circulation versus tidal pumping: Sediment transport in a well-mixed tidal inlet,* Journal of Geophysical Research: Oceans **121**, 6251–6270 (2016).

Burchard, H., and H. Baumert, *The formation of estuarine turbidity maxima due to density effects in the salt wedge: A hydrodynamic process study,* Journal of Physical Oceanography **28**, 309–321 (1998).

Burchard, H., K. Bolding, and M. R. Villarreal, *Three-dimensional modelling of estuarine turbidity maxima in a tidal estuary,* Ocean Dynamics **54**, 250–265 (2004).

Burchard, H., and R. D. Hetland, *Quantifying the contributions of tidal straining and gravitational circulation to residual circulation in periodically stratified tidal estuaries,* Journal of Physical Oceanography **40**, 1243–1262 (2010).

Burchard, H., R. D. Hetland, E. Schulz, and H. M. Schuttelaars, *Drivers of residual estuarine circulation in tidally energetic estuaries: Straight and irrotational channels with parabolic cross section,* Journal of Physical Oceanography **41**, 548–570 (2011).

Burchard, H., and H. M. Schuttelaars, *Analysis of tidal straining as driver for estuarine circulation in well-mixed estuaries,* Journal of Physical Oceanography **42**, 261–271 (2012).

Chernetsky, A. S., H. M. Schuttelaars, and S. A. Talke, *The effect of tidal asymmetry and temporal settling lag on sediment trapping in tidal estuaries,* Ocean Dynamics **60**, 1219–1241 (2010).

Festa, J. F., and D. V. Hansen, *Turbidity maxima in partially mixed estuaries: A two-dimensional numerical model,* Estuarine and Coastal Marine Science **7**, 347–359 (1978).

Fredsøe, J., and R. Deigaard, *Mechanics of coastal sediment transport*, Vol. 3 (World scientific, 1992).

Friedrichs, C. T., B. Armbrust, and H. E. de Swart, *Hydrodynamics and equilibrium sediment dynamics of shallow, funnel-shaped tidal estuaries,* Physics of Estuaries and Coastal Seas , 315–327 (1998).

Friedrichs, C. T., and J. M. Hamrick, *Effects of channel geometry on cross sectional variations in along channel velocity in partially stratified estuaries,* Buoyancy Effects on Coastal and Estuarine Dynamics , 283–300 (1996).

Fugate, D. C., C. T. Friedrichs, and L. P. Sanford, *Lateral dynamics and associated transport of sediment in the upper reaches of a partially mixed estuary, Chesapeake Bay, USA,* Continental Shelf Research **27**, 679–698 (2007).

Geyer, W. R., *The importance of suppression of turbulence by stratification on the estuarine turbidity maximum,* Estuaries **16**, 113–125 (1993).

Gibbs, R. J., L. Konwar, and A. Terchunian, *Size of flocs suspended in Delaware Bay,* Canadian Journal of Fisheries and Aquatic Sciences **40**, s102–s104 (1983).

Grabemann, I., R. Uncles, G. Krause, and J. Stephens, *Behaviour of turbidity maxima in the Tamar (UK) and Weser (FRG) estuaries,* Estuarine, Coastal and Shelf Science **45**, 235–246 (1997).

Huijts, K., H. M. Schuttelaars, H. E. de Swart, and A. Valle-Levinson, *Lateral entrapment of sediment in tidal estuaries: An idealized model study,* Journal of Geophysical Research: Oceans **111** (2006).

Huijts, K. M., H. E. de Swart, G. P. Schramkowski, and H. M. Schuttelaars, *Transverse structure of tidal and residual flow and sediment concentration in estuaries,* Ocean Dynamics **61**, 1067–1091 (2011).

Jay, D., S. Talke, A. Hudson, and M. Twardowski, *Estuarine turbidity maxima revisited: Instrumental approaches, remote sensing, modeling studies, and new directions,* Developments in Sedimentology **68**, 49-109 (2015).

Jay, D. A., and J. D. Musiak, *Particle trapping in estuarine tidal flows,* Journal of Geophysical Research: Oceans **99**, 20445–20461 (1994).

de Jonge, V. N., H. M. Schuttelaars, J. E. van Beusekom, S. A. Talke, and H. E. de Swart, *The influence of channel deepening on estuarine turbidity levels and dynamics, as exemplified by the Ems estuary,* Estuarine, Coastal and Shelf Science **139**, 46–59 (2014).

Kumar, M., H. M. Schuttelaars, and P. C. Roos, *Three-dimensional semi-idealized model for estuarine turbidity maxima in tidally dominated estuaries,* Ocean Modelling **113**, 1–21 (2017).

Kumar, M., H. M. Schuttelaars, P. C. Roos, and M. Möller, *Three-dimensional semi-idealized model for tidal motion in tidal estuaries,* Ocean Dynamics **66**, 99–118 (2016).

Lin, J., and A. Y. Kuo, *Secondary turbidity maximum in a partially mixed microtidal estuary,* Estuaries **24**, 707–720 (2001).

McSweeney, J. M., R. J. Chant, and C. K. Sommerfield, *Lateral variability of sediment transport in the Delaware estuary,* Journal of Geophysical Research: Oceans (2016a).

McSweeney, J. M., R. J. Chant, J. L. Wilkin, and C. K. Sommerfield, *Suspended-sediment impacts on light-limited productivity in the Delaware estuary,* Estuaries and Coasts , 1–17 (2016b).

Postma, H., *Sediment transport and sedimentation in the estuarine environment,* (1967).

Ralston, D. K., W. R. Geyer, and J. C. Warner, *Bathymetric controls on sediment transport in the Hudson River estuary: lateral asymmetry and frontal trapping,* Journal of Geophysical Research: Oceans **117** (2012).

Schramkowski, G. P., and H. E. de Swart, *Morphodynamic equilibrium in straight tidal channels: combined effects of coriolis force and external overtides,* Journal of Geophysical Research: Oceans (1978–2012) **107**, 20–1 (2002).

Schuttelaars, H. M., V. N. de Jonge, and A. Chernetsky, *Improving the predictive power when modelling physical effects of human interventions in estuarine systems,* Ocean & Coastal Management **79**, 70–82 (2013).

Scully, M. E., and C. T. Friedrichs, *The influence of asymmetries in overlying stratification on near-bed turbulence and sediment suspension in a partially mixed estuary,* Ocean Dynamics **53**, 208-219 (2003).

Scully, M. E., and C. T. Friedrichs, *Sediment pumping by tidal asymmetry in a partially mixed estuary,* Journal of Geophysical Research: Oceans **112** (2007).

Sommerfield, C. K., and K.-C. Wong, *Mechanisms of sediment flux and turbidity maintenance in the Delaware estuary,* Journal of Geophysical Research: Oceans **116** (2011).

de Swart, H. E., and J. Zimmerman, *Morphodynamics of tidal inlet systems,* Annual review of fluid mechanics **41**, 203–229 (2009).

Talke, S. A., H. E. de Swart, and H. M. Schuttelaars, *Feedback between residual circulations and sediment distribution in highly turbid estuaries: an analytical model,* Continental Shelf Research **29**, 119–135 (2009).

Uncles, R., and J. Stephens, *Nature of the turbidity maximum in the Tamar estuary, UK,* Estuarine, Coastal and Shelf Science **36**, 413–431 (1993).

Van Maren, D., T. Van Kessel, K. Cronin, and L. Sittoni, *The impact of channel deepening and dredging on estuarine sediment concentration,* Continental Shelf Research **95**, 1–14 (2015).

Walters, R. A., *A model study of tidal and residual flow in Delaware Bay and River,* Journal of Geophysical Research: Oceans **102**, 12689–12704 (1997).

Wei, X., M. Kumar, and H. M. Schuttelaars, *Three-dimensional salt dynamics in well-mixed estuaries: influence of estuarine convergence, coriolis and bathymetry,* Journal of Physical Oceanography (in press).

Wei, X., G. P. Schramkowski, and H. M. Schuttelaars, *Salt dynamics in well-mixed estuaries: importance of advection by tides,* Journal of Physical Oceanography **46**, 1457-1475 (2016).

Winant, C. D., *Three-dimensional residual tidal circulation in an elongated, rotating basin,* Journal of Physical Oceanography **38**, 1278–1295 (2008).

Winterwerp, J. C., *Fine sediment transport by tidal asymmetry in the high-concentrated Ems River: indications for a regime shift in response to channel deepening,* Ocean Dynamics **61**, 203–215 (2011).

Winterwerp, J. C., and Z. B. Wang, *Man-induced regime shifts in small estuaries-I: theory,* Ocean Dynamics **63**, 1279–1292 (2013).

Yang, Z., H. E. de Swart, H. Cheng, C. Jiang, and A. Valle-Levinson, *Modelling lateral entrapment of suspended sediment in estuaries: The role of spatial lags in settling and M4 tidal flow,* Continental Shelf Research **85**, 126–142 (2014).

Chapter 5

Conclusions

This thesis aims for a good understanding of the physical mechanisms controlling the salt intrusion, sediment transport and trapping in well-mixed estuaries. To reach that, the tidal and residual water motion, salinity and suspended sediment concentrations are calculated using process-based idealized semi-analytical models, allowing for a systematical investigation of the dominant processes of salt transport, sediment transport and trapping. In section 5.1, the main conclusions of this thesis are summarized, addressing each of the research questions as presented in Chapter 1. Some recommendations for future research are given in section 5.2.

5.1 Main conclusions

- $Q1$: Can we quantify the residual salt transport contribution induced by processes at the tidal timescale in well-mixed estuaries of an arbitrary geometry and bathymetry? How does this contribution vary with estuarine bathymetry, geometry and friction parameters? How significant is this contribution in natural well-mixed estuaries?

Chapter 2 aims to address the research question $Q1$. In this chapter, a width-averaged semi-analytical model is developed to calculate the coupled water motion and salinity at tidal timescale for well-mixed estuaries of an arbitrary geometry and bathymetry, extending the model of McCarthy (1993). A perturbation method is used to analytically calculate the vertical distribution of water motion and salinity, and a finite difference method is employed to numerically obtain their horizontal distributions. Using this model, the contribution of the residual salt transport due to the temporal correlation between the width-averaged along-channel tidal velocities and the tidal salinities, is explicitly identified. This contribution behaves like diffusion, and is called tidal advective diffusion in this thesis. The tidal advective diffusivity strongly depends on friction parameters, and estuarine bathymetry and geometry. Large values of tidal advective diffusivity are found in case of strong bottom friction, small vertical eddy viscosities, moderate water depths and estuarine convergence lengths. The tidal advective diffusion strongly dominates the residual salt transport in the Scheldt estuary. This contribution is significant to the landward residual salt transport in the Delaware estuary and the Columbia estuary in well-mixed conditions, but not dominant. The salt transport contributions due to other mechanisms such as lateral processes seem to dominate in these systems.

- *Q*2: Under what conditions are lateral processes important for the residual salt transport in well-mixed estuaries? Can we identify the three-dimensional structure of residual salt fluxes induced by each physical process?

In Chapter 3, the research question *Q*2 is addressed. The width-averaged model in Chapter 2 is extended to a three-dimensional semi-analytical model by using a perturbation method and a finite element method. Lateral processes and the interactions between longitudinal and lateral processes, which are probably important in the Delaware and Columbia estuaries, are resolved. This model resolves the dynamic coupling effects of the water motion and salinity using an iterative approach, thus it can be used to systematically investigate the relative importance of various processes controlling the residual salt balance. In a schematized system representative for the Delaware estuary, the laterally varying tidal advective diffusion is found to dominate the residual landward salt transport integrated over the cross-section. This confirms the importance of lateral processes for the along-channel salt transport in the Delaware estuary. The estuarine circulations due to tidal rectification, stress-free surface condition, tidal return flow and gravitational circulation are locally significant, but their contributions to the cross-sectionally integrated salt transport are small. The gravitational circulation transports salt into the estuary through the channel and exports salt over the shoals, while the other residual flow components transport salt in the opposite pattern, with salt imported over the shoals and exported through the channel. All processes contributing to the residual salt transport are strongly affected by the estuarine geometry, bathymetry and Coriolis force. No horizontal estuarine circulations are generated in convergent estuaries with a horizontal bed, neglecting Coriolis force, where the tidal advective diffusion is the only landward salt transport process. Including Coriolis force in the convergent estuary results in an estuarine circulation as a result of the stress-free surface condition and tidal return flow, with salt imported from the left side of the estuary and exported from the right side (looking seaward). By including a lateral channel-shoal structure in the estuary and excluding Coriolis force, the gravitational circulation becomes the dominant estuarine circulation, transporting salt landward through the channel and seaward over the shoals. Residual circulations due to other processes tend to transport salt in an opposite direction. The tidal advective diffusion accounts for most of the landward salt transport in all experiments, and is the primary process controlling the salt intrusion length. Estuarine circulation plays a minor role in the along-channel salt intrusion, but it strongly influences the lateral salinity distribution.

- *Q*3: What is the influence of salt intrusion on sediment transport and trapping in well-mixed estuaries? What are other potentially important processes governing the occurrence and variations of estuarine turbidity maximum? How do the sediment transport processes change with different sediment properties (such as settling velocity) and forcing conditions (such as river discharge)?

Research question $Q3$ is addressed in Chapter 4, where the three-dimensional sediment transport and trapping mechanisms in well-mixed estuaries are investigated by incorporating the salinity module introduced in Chapter 3 with the sediment module of Kumar *et al.* (2017). In this way, the dynamical effects of salt intrusion on sediment transport and trapping are resolved, including both longitudinal and lateral processes. As a first step, the sediment dynamics in an idealized estuary (representative for the Delaware estuary, but excluding Coriolis force) is studied. The estuarine turbidity maxima (ETM) is found near the salt intrusion limit, and larger concentrations are found on the shoals than in the channel. Remarkable circulation cells of the depth-integrated sediment transport are found. Downstream of the ETM, sediments are imported towards the ETM through the channel and exported over the shoals. Within the ETM region, sediments are transported from the upper estuary towards the ETM through the channel, and transported landward over the shoals. The cross-sectionally integrated seaward sediment transport mainly results from the advection of residual concentrations by the river-induced flow and tidal return flow. The landward sediment transport is mainly due to the M_2 tidal advection of the M_2 tidal concentrations, which are resulted from the asymmetric bed shear stress due to the internally-generated M_4 overtide and the salinity-induced gravitational circulation. The M_2 tidal advection of the M_2 tidal concentrations resulted from spatial settling lag effects also results in a significant landward sediment transport. Including Coriolis force hardly influences the longitudinal location of the ETM or the residual sediment balance integrated over the cross-section, but the lateral distributions of the suspended sediment concentration and the sediment transport patterns are greatly affected. Larger sediment concentrations are found on the right shoal, with sediments transported into the estuary from the left side of the channel and seaward from the right (looking seaward). The relative importance of processes contributing to residual sediment transport and trapping is strongly influenced by the sediment settling velocity and river discharge. The ETM is significantly moved towards the landward boundary by increasing settling velocity or decreasing river discharge. The sediment transport contribution related to the internally-generated M_4 tide increases by increasing settling velocity or decreasing river discharge, but that related to spatial settling lag effects increases by decreasing settling velocity or increasing river discharge. The gravitational circulation significantly contributes to transporting sediments of small settling velocities seaward and trapping them on the shoals. For sediments of large settling velocities or under large river discharges, however, gravitational circulation contributes significantly to transporting sediments landward and trapping them near the salt intrusion limit.

5.2 Recommendations

This thesis provides fundamental insight into the dominant mechanisms driving salt intrusion, sediment transport and trapping in well-mixed estuaries, resolving longitudinal and lateral processes, and processes varying at the tidal timescale. Nevertheless, there are many possibilities to extend the semi-analytical three dimensional model so that other processes, which are potentially important for the maintenance of the salt intrusion and ETM but are unresolved in this thesis, can be better understood.

5.2.1 Impact of stratification

In this thesis, estuaries are assumed to be well-mixed in all experiments. In reality, strong stratifications can occur when river discharge is strong (see section 3.4.3) or during neap tides, and estuaries can change from a well-mixed condition to partially-mixed or even strongly-stratified conditions. In case of strong stratification, the ordering used in this thesis is no longer suitable as the leading-order salinity is not vertically homogeneous and the gravitation circulation is as significant as the M_2 tidal flow. To study the impact of stratification on the estuarine dynamics, the model presented in Chapter 3 can be extended by including a dependence of the vertical mixing coefficients (vertical viscosity and diffusivity) on stratification. For example, the vertical mixing coefficients can be related to the Simpson number: the ratio of potential energy change to the rate of production of turbulent kinetic energy (Geyer and MacCready 2014). This would provide insight into the dominant physical mechanisms controlling the adjustment of estuaries between different mixing conditions, and help in pursuing a unified theory.

5.2.2 From morphodynamic equilibrium to morphological evolution

This thesis focuses on idealized estuaries in morphodynamic equilibrium, and the influence of sediment deposition or erosion on the water depth is assumed to be negligible. In reality, the sediment budget in estuaries can be highly variable due to varying sediment sources from the landward/seaward boundaries and river/tide forcing conditions. Moreover, the estuarine bathymetry can be constantly varying due to sediment accretion/erosion, resulting in non-negligible morphological evolution. To include this aspect, the interactions between the three-dimensional water motion, sediment transport and trapping, and the changes of estuarine bathymetry should be taken into account. This may be realized by extending the one-dimensional model of Schuttelaars and de Swart (1996) to a three-dimensional model, and allowing the total sediment availability to vary in time (Brouwer *et al.* 2016).

5.2.3 Other processes

One of the most important processes which is not considered in this thesis is the time-variability of the vertical eddy viscosity and eddy diffusivity. As a result of vertical or lateral density variations (due to differences in salinity or suspended sediment concentration), the intensity of turbulence can vary significantly over a tidal cycle, hence affecting the vertical eddy viscosity and eddy diffusivity in time. The variation of the vertical eddy viscosity, for example, can temporally interact with the vertical shear and contributes to a residual circulation, thus strongly affecting the salt intrusion and ETM in estuaries. To take this process into account, the temporal variability of the vertical eddy viscosity and diffusivity should be considered in future research in accordance with the tidally varying salinity and sediment concentration. Other processes, such as flocculation and hindered settling, can be studied by extending the model to consider cohesive sediments and effects of large sediment concentrations.

5.2.4 Improve numerical performance

The three-dimensional models developed in Chapter 3 and Chapter 4 use a perturbation method to analytically obtain the vertical structures of all physical variables (water motion, salinity, SSC), which provides a very good vertical resolution for the model results. However, since the horizontal distributions of those variables are numerically calculated using a classical Galerkin finite element method, the accuracy strongly depends on the mesh-size and the adopted numerical scheme. This can be problematic as the accuracy of the residual water motion, salinity and sediment concentration is strongly related to the second-order, even the third-order derivatives of the tidal surface elevation, which has a poor accuracy using the current numerical scheme. Consequently, the model results close to the lateral boundaries of the estuary, especially in narrow reaches where high resolutions are required, are not very accurate. To take care of this problem, a new numerical scheme needs to be developed to solve the shallow water equations with higher rates of convergence.

References

Brouwer, R. L., G. P. Schramkowski, Y. M. Dijkstra, and H. M. Schuttelaars, *Using dynamic availability to model inter-annual variation of sediment dynamics in a well-mixed tidally dominated estuary,* Abstract for the 18th Physics of Estuaries and Coastal Seas Conference (2016).

Geyer, W. R., and P. MacCready, *The estuarine circulation,* Annual Review of Fluid Mechanics **46**, 175 (2014).

Kumar, M., H. M. Schuttelaars, and P. C. Roos, *Three-dimensional semi-idealized model for estuarine turbidity maxima in tidally dominated estuaries,* Ocean Modelling **113**, 1–21 (2017).

McCarthy, R. K., *Residual currents in tidally dominated, well-mixed estuaries,* Tellus A **45**, 325–340 (1993).

Schuttelaars, H. M., and H. E. de Swart, *Idealized long-term morphodynamic model of a tidal embayment,* European Journal of Mechanics, B Fluids **15**, 55–80 (1996).

Acknowledgements

My PhD would not be possible without the help from others. Below I express my gratitudes to many, but not all who have contributed greatly to my phd work and life.

First of all, I would like to express my full gratitude to my co-promotor and daily supervisor, Dr. Henk M. Schuttelaars. Henk, you have shown a very good example of a great scientist. It is such an honor and pleasure working with you. I could not have finished my PhD project successfully without your endless support and encouragement. Every time I got stuck, you were there to help, and always so patient to answer my (basic, sometimes stupid) questions clearly and comprehensively. I have enjoyed and learned a lot during our discussions, especially your passion for research. As I said to you once, I would hope one day I will be able to supervise my future students like you do. I am also deeply in debt to your extremely detailed feedback and comments for my thesis, journal papers, conference abstracts, presentations, CV (basically everything I sent to you), and all efforts you made to cover our publication costs in JPO. As a supervisor, you were happy to spend your time coding (and debugging) and reading articles in my favor, although your emails at mid-nights sometimes confused me about the real Dutch way of working. I guess your endless energy must originate from your true love for research, not coffee!

Secondly, I would like to thank my promotor Prof. Arnold W. Heemink, who has been always supportive and helpful during my PhD application, researching, thesis preparation, and job searching. I also truly appreciate for your encouraging feedback during our meetings and all your advice and suggestion to my thesis.

I am grateful to Prof. Wei Zhang, my master supervisor, for encouraging me to study abroad. I appreciate Prof. Wenping Gong for hosting me when I first met Henk in Guangzhou in early 2012, to discuss about my PhD application, and for inviting me as a young scientist to present my PhD work in Sun Yat-sen University in December 2015.

I want to say "thank you" to Kees Lemmens for helping me with all problems I encountered using my PC and the cluster. I also owe a great debt to Dorothee and Evelyn, who have been always friendly and helpful. All your support has made my PhD life so much easier than it could be. Mohit, thanks for explaining me how the 3D hydrodynamic model works in the very beginning, which has saved me a lot of time and efforts in completing my PhD project. It is a great pleasure working with you. I want to thank George for your constructive advice and suggestion in our analytical work. Yoeri, thanks a lot for translating my summary to the Dutch version so efficiently, and hosting me for our excursion to the Ems.

Life would be dull without friends or entertainments. I am lucky to have two sweet girls as officemates, Tugce and Corine. Doing a PhD in a ladies-only office in the department of mathematics is an exceptionally lovely experience, where daily conversation topics ranged from solving complex PDE's to raising a baby (or cat). I would also like to thank my other colleagues, Kaihua, Guangliang, Sha, Atif, Hyder, Bijan, Nick, Mahya, Rajab, Changyu, Adelaide, Isabel, Alberto, Jianbin, Haochuan, Jie, Senlei, Cong for all your support and company especially during lunch breaks.

My gratitude also goes to my housemates, Yu Sun, Lijian Qi, Tao Zou, Zilong Wei, Yan Zhou. It has been such a pleasure sharing the same house with you, I will miss all funs we had playing badminton, board games, and those amazing hotpot nights. I want to also thank my friends Qujiang Lei, Xiangming Liu, Jia Xu, Xiaowei Ouyang for all your help and pleasant moments we shared in Delft.

I am lucky to meet and become best friends with Huarong Zheng and Xiangrong Wang during my PhD. It has been so comforting and cheering to have you to share my happiness and sorrow with. The time we spent together for sight-seeing, shopping, movie nights, cooking/eating and a lot of chatting, has been a precious memory for me which will never fade.

Finally, I am greatly in debt to my fiance Zaibin Lin, my parents, my sister and brother for your unconditional love and consistent support during my PhD. I love you so much!!

Xiaoyan Wei

January, 2017

Curriculum Vitæ

Xiaoyan Wei was born on 6 November, 1988 in Anhua, China. From September 2006 to June 2010, she majored in Harbour, Waterway and Coastal Engineering in Hohai University, China. After that, she continued her study on Harbour, Coastal and Offshore Engineering, Hohai University. Her master thesis focuses on mechanisms of salt intrusion in the Pearl River estuary and the influence of water division on salt intrusion, which was conducted mainly using state-of-the-art numerical models. After obtaining her master degree on November, 2012, she started her role as a PhD candidate in the Department of Applied Mathematics, TU Delft, the Netherlands. Her PhD project aims to improve understanding of dominant mechanisms of salt and sediment dynamics in well-mixed estuaries, such that salt intrusion length and locations of estuarine turbidity maxima can be better predicted. This was carried out by developing idealized, process-based semi-analytical models, which resolve the three-dimensional estuarine dynamics including the interactions of water motion, salt and suspended sediment. Using these models, she systematically investigated the contributions of different physical mechanisms to the transport of salt and suspended sediment, which has resulted in this thesis.

List of Publications

- **Wei, X.**, Kumar, M., Schuttelaars, H.M., under review. Three-dimensional sediment trapping mechanisms in well-mixed estuaries: importance of the internally-generated overtide, spatial settling lag and gravitational circulation.
- **Wei, X.**, Kumar, M., Schuttelaars, H.M., in press. Three-dimensional salt dynamics in well-mixed estuaries: influence of estuarine convergence, Coriolis and bathymetry. Journal of Physical Oceanography.
- **Wei, X.**, Schramkowski, G.P., Schuttelaars, H.M., 2016. Salt dynamics in well-mixed estuaries: importance of advection by tides. Journal of Physical Oceanography, 46(5), pp. 1457-1475.